

## DTIC FILE COPY

SECURITY CLASSIFICATION OF THIS PAGE

## REPORT DOCUMENTATION PAGE

Form Approved  
OMB No. 0704-0188

1a. REPORT SECURITY CLASSIFICATION <b>UNCLASSIFIED</b>			1b. RESTRICTIVE MARKINGS <b>NONE</b>		
2a. SECURITY CLASSIFICATION AUTHORITY			3. DISTRIBUTION/AVAILABILITY OF REPORT APPROVED FOR PUBLIC RELEASE; DISTRIBUTION UNLIMITED.		
2b.			5. MONITORING ORGANIZATION REPORT NUMBER(S) AFIT/CI/CIA- 89-155		
4. <b>AD-A218 025</b>			7a. NAME OF MONITORING ORGANIZATION AFIT/CIA		
6a. NAME OF PERFORMING ORGANIZATION AFIT STUDENT AT Univ of IL/ Urbana-champaign		6b. OFFICE SYMBOL (If applicable)	7b. ADDRESS (City, State, and ZIP Code) Wright-Patterson AFB OH 45433-6583		
6c. ADDRESS (City, State, and ZIP Code)		9. PROCUREMENT INSTRUMENT IDENTIFICATION NUMBER			
8a. NAME OF FUNDING/SPONSORING ORGANIZATION	8b. OFFICE SYMBOL (If applicable)	10. SOURCE OF FUNDING NUMBERS			
8c. ADDRESS (City, State, and ZIP Code)		PROGRAM ELEMENT NO.	PROJECT NO.	TASK NO.	WORK UNIT ACCESSION NO.
11. TITLE (Include Security Classification) (UNCLASSIFIED) DESIGN AND PERFORMANCE ANALYSIS OF ADAPTIVE OPTICAL TELESCOPES USING LASER GUIDE STARS					
12. PERSONAL AUTHOR(S) BYRON MACMASTER WELSH					
13a. TYPE OF REPORT THESIS/DISSEMINATION	13b. TIME COVERED FROM TO	14. DATE OF REPORT (Year, Month, Day) 1989		15. PAGE COUNT 272	
16. SUPPLEMENTARY NOTATION APPROVED FOR PUBLIC RELEASE IAW AFR 190-1 ERNEST A. HAYGOOD, 1st Lt, USAF Executive Officer, Civilian Institution Programs					
17. COSATI CODES			18. SUBJECT TERMS (Continue on reverse if necessary and identify by block number)		
FIELD	GROUP	SUB-GROUP			
19. ABSTRACT (Continue on reverse if necessary and identify by block number)					
<div style="text-align: center;"> <b>DTIC</b>  <b>ELECTE</b>  <b>S FEB 15 1990 D</b>  <b>D CR</b> </div> <div style="text-align: right; font-size: 2em; margin-top: 20px;">90 02 14 048</div>					
20. DISTRIBUTION/AVAILABILITY OF ABSTRACT <input checked="" type="checkbox"/> UNCLASSIFIED/UNLIMITED <input type="checkbox"/> SAME AS RPT. <input type="checkbox"/> DTIC USERS			21. ABSTRACT SECURITY CLASSIFICATION <b>UNCLASSIFIED</b>		
22a. NAME OF RESPONSIBLE INDIVIDUAL ERNEST A. HAYGOOD, 1st Lt, USAF			22b. TELEPHONE (Include Area Code) (513) 255-2259	22c. OFFICE SYMBOL AFIT/CI	

DESIGN AND PERFORMANCE ANALYSIS OF  
ADAPTIVE OPTICAL TELESCOPES USING LASER GUIDE STARS

BY

BYRON MACMASTER WELSH

B.S., Virginia Military Institute, 1982  
M.S., Air Force Institute of Technology, 1983

THESIS

Submitted in partial fulfillment of the requirements  
for the degree of Doctor of Philosophy in Electrical Engineering  
in the Graduate College of the  
University of Illinois at Urbana-Champaign, 1989

Urbana, Illinois

Accession For	
PHS - CR-1	<input checked="" type="checkbox"/>
PHS - CR-2	<input type="checkbox"/>
PHS - CR-3	<input type="checkbox"/>
PHS - CR-4	
By	
Date	
For	
Date	
A-1	

## ABSTRACT

Atmospheric turbulence severely limits the resolution of ground-based astronomical telescopes. In good seeing conditions at the best observatory sites, resolution at visible wavelengths is typically limited to  $\sim 1$  sec of arc. During the past 15 years adaptive optical systems using electrically deformable mirrors have been developed to compensate for turbulence effects. Unfortunately, these systems require bright reference sources adjacent to the object of interest and can be used to observe only the brightest stars. Artificial guide stars suitable for controlling an adaptive imaging system can be created in the upper atmosphere by using a laser to excite either Rayleigh backscattering in the stratosphere or resonance backscattering in the mesospheric Na layer. The design requirements of a laser-guided adaptive telescope, as well as the expected imaging performance, are discussed in detail in this thesis.

Analytical expressions giving the performance of a class of adaptive optics systems using slope sensors are derived. The unique analysis takes into account the nonideal characteristics of the wavefront sensor and wavefront correction device, as well as the effects of anisoplanatism. Performance measures include the mean square residual phase error across the aperture of the optical system and the optical transfer function. We show that a two-meter, ground-based, laser-guided telescope can achieve imaging performance levels at visible wavelengths nearly matching those of the Hubble Space Telescope

(HST). The laser power requirement for Rayleigh and Na guide stars is on the order of 33 W and 6 W, respectively, for zenith viewing and  $r_0 = 20$  cm. Both systems will achieve near diffraction limited imaging with a Strehl ratio of  $\sim 0.73$  and an angular resolution of approximately 0.07 arcsec for an observation wavelength of  $0.5 \mu\text{m}$ .

In the case of guide stars created in the mesospheric Na layer, saturation effects may significantly reduce the backscattered signal expected for resonance fluorescence lidar systems. The level of saturation is determined by the laser's pulse length, pulse energy, beamwidth and linewidth. Design examples, including lidar systems for atmospheric research and laser-guided telescopes, are studied in detail. (f-10)\*

**DEDICATION**

to Andrew and Kathryn

# ACKNOWLEDGMENTS

I thank Dr. Chester Gardner for the invaluable guidance and assistance that made the completion of this thesis possible. I also thank the members of the Electro-Optics Systems Laboratory for their support and friendship. Special thanks to Tim Kane for his friendship, the many enlightening discussions about the guide star project, and also for reading and critiquing selected chapters of this thesis. Finally I thank Nancyanne for her unending support and love.

This work was supported in part by National Science Foundation grant ATM 88-11771.

## TABLE OF CONTENTS

	PAGE
1. INTRODUCTION . . . . .	1
2. DESIGN AND PERFORMANCE ANALYSIS OF ADAPTIVE OPTICAL TELESCOPES USING LASER GUIDE STARS . . . . .	8
2.1 Introduction: Qualitative Discussion of Design Issues . . . . .	8
2.2 Atmospheric Turbulence Effects . . . . .	21
2.3 Guide Star Brightness . . . . .	30
2.4 Rayleigh Laser Guide Stars . . . . .	50
2.5 Sodium Resonance Fluorescence Laser Guide Stars . . . . .	62
2.6 Design Ssummaries for Rayleigh and Na Guide Star Systems . . . . .	83
2.7 Optical Interferometric Imaging . . . . .	89
2.8 Summary . . . . .	91
3. PERFORMANCE ANALYSIS OF ADAPTIVE OPTICS SYSTEMS USING LASER GUIDE STARS AND SLOPE SENSORS . . . . .	94
3.1 Introduction . . . . .	94
3.2 Definitions and Assumptions . . . . .	98
3.3 Mean-Square Residual Phase Error . . . . .	101
3.4 Optical Transfer Function . . . . .	104
3.5 Wavefront Phase Statistics . . . . .	108
3.6 Slope Measurement Noise . . . . .	110
3.7 Computational Results for Continuous Mirrors . . . . .	111
3.8 Summary . . . . .	139
4. NONLINEAR RESONANT ABSORPTION EFFECTS ON THE DESIGN OF RESONANCE FLUORESCENCE LIDARS AND LASER GUIDE STARS . . . . .	142
4.1 Introduction . . . . .	142
4.2 Population State Rate Equation and Specific Solutions . . . . .	144
4.3 Interpretation and Comparison of Results . . . . .	160
4.4 Design of Pulsed Lidar Systems . . . . .	166
4.5 Summary . . . . .	179
5. EFFECTS OF TURBULENCE INDUCED ANISOPLANATISM ON THE IMAGING PERFORMANCE OF ADAPTIVE ASTRONOMICAL TELESCOPES USING LASER GUIDE STARS . . . . .	180
5.1 Introduction . . . . .	180
5.2 Geometry . . . . .	184
5.3 Adaptive Optics System Definitions and Assumptions . . . . .	188
5.4 Mean-Square Residual Phase Error over the Corrected Aperture . . . . .	191
5.5 Optical Transfer Function . . . . .	194
5.6 Wavefront Phase Statistics . . . . .	196
5.7 Phase Structure Function . . . . .	198
5.8 Computational Results . . . . .	200
5.9 Summary . . . . .	229

## PAGE

6. THE BISTATIC IMAGING LIDAR TECHNIQUE FOR UPPER ATMOSPHERIC	
STUDIES . . . . .	231
6.1 Introduction . . . . .	231
6.2 Analysis . . . . .	232
6.3 Discussion . . . . .	238
6.4 Factors Affecting Resolution . . . . .	242
6.5 Experimental Data . . . . .	247
6.6 Summary . . . . .	259
7. CONCLUSIONS . . . . .	261
REFERENCES . . . . .	264
VITA . . . . .	271



## LIST OF TABLES

TABLE	PAGE
2.1 Optimum Design Parameters and Expected Performance for the Wavefront Sensor and Adaptive Mirror . . . . .	38
2.2 Assumptions for the Rayleigh Laser Guide Star Pulse Energy Calculations . . . . .	57
2.3 Assumptions for the Na Laser Guide Star Pulse Energy Calculations . . . . .	76
2.4 Rayleigh Laser Guide Star Design Requirements for 2 and 4 m Adaptive Telescopes . . . . .	84
2.5 Na Laser Guide Star Design Requirements for 2 and 4 m Adaptive Telescopes . . . . .	85
4.1 Saturation Effects ( $N_R/N_{Ro}$ ) for the Laser Beam Cross Sections and Pulse Shapes Assumed in Cases 1, 2 and 3 . . . .	161
4.2 CEDAR Lidar Specifications . . . . .	170
6.1 Atmospheric and Imaging System Parameters . . . . .	246

## LIST OF FIGURES

FIGURE	PAGE
1.1. Photocount contour plot of a Na guide star image taken on January 21, 1987. The guide star was generated by the University of Illinois lidar system and imaged by the University of Hawaii 2.2 meter telescope. The contours are 150, 200, 300, 400, 500, 600, 800 and 900 counts per pixel. The pixel size is 3.4 $\mu$ rad. . . . .	3
2.1a. Small diameter telescope geometry. . . . .	9
2.1b. Large diameter adaptive telescope. . . . .	10
2.2. Laser-guided adaptive telescope system diagram. . . . .	12
2.3. Single Hartmann tilt sensor and section of CCD array surface. . . . .	17
2.4. Geometry of the isoplanatic angle superimposed on a cross section of the telescope aperture. . . . .	27
2.5. Optimum subaperture diameter versus the residual RMS wavefront phase error over the aperture. . . . .	35
2.6. Required photon flux density (photons/ $r_o^2$ ) versus the residual RMS phase error over the aperture. The detector efficiency parameter $\eta_c$ is assumed to be 1.35. . . . .	36
2.7. Required number of subapertures versus telescope diameter for three values of $\Delta\phi$ : $\lambda/15$ , $\lambda/17.5$ , and $\lambda/20$ . . . . .	39
2.8. Wavefront sensor and mirror actuator configuration. . . . .	41
2.9. RMS residual phase error versus photon flux (photons/ $r_o^2$ ) for the wavefront sensor and mirror configuration shown in Figure 2.8. The aperture size is $D = 4d$ and the subaperture size takes on values of $d = 0.83r_o$ , $0.69r_o$ and $0.59r_o$ . . . . .	43
2.10. Ensemble average OTF for the wavefront sensor and mirror configuration shown in Figure 2.8. The photon flux ranges from $10/r_o^2$ to $500/r_o^2$ . The aperture size is $D = 4d$ and the subaperture size is $d = 0.69r_o$ . . . . .	45
2.11. One dimensional ensemble average PSF for the wavefront sensor and mirror configuration shown in Figure 2.8. The photon flux ranges from $10/r_o^2$ to $500/r_o^2$ . The aperture size is $D = 4d$ and the subaperture size is $d = 0.69r_o$ . . . . .	46

FIGURE	PAGE
2.12. Normalized FWHM angular resolution versus photon flux (photons/ $r_o^2$ ). The resolution is normalized by the FWHM angular resolution of the unaberrated system. Curves are shown for three values of $d_o$ : $0.83r_o$ , $0.69r_o$ and $0.59r_o$ . . . . .	48
2.13. Strehl ratio versus photon flux (photons/ $r_o^2$ ). Curves are shown for three values of $d_o$ : $0.83r_o$ , $0.69r_o$ and $0.59r_o$ . . . . .	49
2.14. Geometry of the telescope and laser light path. . . . .	52
2.15. Total Rayleigh laser pulse energy requirements versus the residual RMS phase error over the aperture. Curves are shown for $r_o = 10$ cm, 20 cm and 30 cm. The aperture diameter is assumed to be 2 m. . . . .	58
2.16. Total Rayleigh laser pulse energy requirements versus the normalized telescope diameter. The residual RMS phase error over the aperture is assumed to be $\lambda/17.5$ . . . . .	59
2.17. Factor increase of the Rayleigh pulse energy requirements versus zenith angle. . . . .	61
2.18. Seasonal variation of the Na layer column abundance at Urbana, Illinois. The symbol marks the average value for the night while the line represents the range of values measured during the night. . . . .	63
2.19. Seasonal variation of the centroid height of the Na layer at Urbana, Illinois. The symbol marks the average value for the night while the line represents the range of values measured during the night. . . . .	64
2.20. Na density profile measured by Beatty et al. <sup>39</sup> with the CEDAR lidar on March 4, 1988 at Urbana, Illinois. The integration period was 27 s and the vertical resolution was 75 m. The dense narrow layer at 82.4 km is a meteor ablation trail. . . . .	65
2.21. Homogeneously and inhomogeneously broadened Na $D_2$ absorption line versus wavelength. . . . .	67
2.22. Geometry between the laser, receiver, and Na layer. . . . .	69
2.23. Scattering cross section $\sigma_s$ versus laser line width. Curves are shown for $\tau_s/\tau_n$ ranging from 0.5 to 10. . . . .	75
2.24. Total Na laser pulse energy requirements versus residual RMS phase error over the aperture. Curves are shown for $r_o = 10$ cm, 20 cm and 30 cm. The aperture diameter is assumed to be 2 m. . . . .	78

FIGURE	PAGE
2.25. Na laser pulse length requirements versus residual RMS phase error over the aperture. . . . .	79
2.26. Total Na laser pulse energy requirements versus telescope diameter. The value of residual RMS phase error over the aperture is assumed to be $\lambda/17.5$ and $r_0$ ranges from 10 cm to 30 cm. . . . .	80
2.27. Factor increase of the Na laser pulse energy requirements versus zenith angle. . . . .	82
2.28. Optimum subaperture diameter versus zenith angle for the adaptive telescope designs summarized in Tables 2.4 and 2.5. . . . .	86
2.29. Required number of subapertures versus zenith angle for the adaptive telescope designs summarized in Tables 2.4 and 2.5. . . . .	87
3.1. Membrane mirror and actuator pad configuration. . . . .	113
3.2. Membrane actuator response for actuators positioned along the x axis. The center of the membrane is at $x = 0$ and the edge is at $x = 10$ . . . . .	115
3.3. Wavefront sensor configuration. . . . .	117
3.4. Single Hartmann tilt sensor. . . . .	118
3.5a. Average RMS residual phase error versus photocounts/subaperture for the Gaussian mirror response function. The aperture size ranges from $D = 6d$ to $2d$ . The other parameters are constant: $d = r_0$ and $\tau = 0$ . . . . .	122
3.5b. Average RMS residual phase error versus photocounts/subaperture for the membrane mirror response function. The aperture size ranges from $D = 6d$ to $2d$ . The other parameters are constant: $d = r_0$ and $\tau = 0$ . . . . .	123
3.6a. Average RMS residual phase error versus photocounts/subaperture for the Gaussian mirror response function. The subaperture size ranges from $d = 1.5r_0$ to $0.5r_0$ . The other parameters are constant: $D = 4d$ and $\tau = 0$ . . . . .	125
3.6b. Average RMS residual phase error versus photocounts/subaperture for the membrane mirror response function. The subaperture size ranges from $d = 1.5r_0$ to $0.5r_0$ . The other parameters are constant: $D = 4d$ and $\tau = 0$ . . . . .	126

FIGURE	PAGE
3.7. Average RMS residual phase error versus subaperture photon count. The dimensionless quantity $v\tau/r_o$ ranges from 0 to 2.5. The other parameters are constant: $D = 4L$ , and $L = r_o$ .	128
3.8a. OTF for the system using the Gaussian mirror response function. The photocounts/subaperture ranges from 10 to 500. The other parameters are constant: $D = 4d$ , $d = r_o$ , $\tau = 0$ .	130
3.8b. OTF for the system using the membrane mirror response function. The photocounts/subaperture ranges from 10 to 500. The other parameters are constant: $D = 4d$ , $d = r_o$ , $\tau = 0$ .	131
3.9a. PSF for the system using the Gaussian mirror response function. The photocounts/subaperture ranges from 10 to 500. The other parameters are constant: $D = 4d$ , $d = r_o$ , $\tau = 0$ .	133
3.9b. PSF for the system using the membrane mirror response function. The photocounts/subaperture ranges from 10 to 500. The other parameters are constant: $D = 4d$ , $d = r_o$ , $\tau = 0$ .	134
3.10. Strehl ratio versus photocounts/subaperture for either the Gaussian or membrane mirror response functions. The other parameters are constant: $D = 4d$ , $d = r_o$ , $\tau = 0$ .	135
3.11. OTF for the system using the Gaussian mirror response function. The subaperture size ranges from $d = 1.5r_o$ to $0.5r_o$ . The other parameters are constant: $D = 4d$ , $\tau = 0$ , $N = 500$ .	137
3.12. PSF for the system using the Gaussian mirror response function. The subaperture size ranges from $d = 1.5r_o$ to $0.5r_o$ . The other parameters are constant: $D = 4d$ , $\tau = 0$ , $N = 500$ .	138
3.13. Strehl ratio versus $d/r_o$ for the Gaussian response function. The other parameters are constant: $D = 4d$ , $\tau = 0$ , $N = 500$ .	140
4.1. Geometry between the laser, receiver, and scattering layer.	145
4.2. Realistic pulse shape, $t_r = 1$ .	159
4.3. Saturation effects for broad and narrow laser linewidths: $N_R/N_{R0}$ versus $t_s/t_n$ for cases 1, 2 and 3.	164

FIGURE	PAGE
4.4. Minimum allowed beam divergence versus rms pulse length for the CEDAR lidar system (daytime configuration). . . . .	172
4.5. Minimum allowed beam divergence versus rms pulse length for the narrow line width (0.13 $\mu\text{m}$ ) CEDAR lidar system (atmospheric temperature measurement configuration). . . . .	175
4.6. Off zenith geometry. . . . .	177
5.1. Geometry between point sources and optical aperture. . . . .	185
5.2. Wavefront sensor and mirror actuator configuration. . . . .	205
5.3. Normalized plot of $C_n^2$ versus altitude. . . . .	209
5.4. Residual RMS phase error over the aperture versus $D_1/D_0$ for the single layer turbulence model. Curves are shown for aperture dimensions ranging from $D_1 = 2d$ to $5d$ . . . . .	212
5.5. Residual RMS phase error over the aperture versus $D_1/D_0$ for the Hufnagel turbulence model. Curves are shown for aperture dimensions ranging from $D_1 = 2d$ to $5d$ . . . . .	213
5.6. Strehl ratio versus $D_1/D_0$ for both turbulence models. . . . .	215
5.7. OTF of the phase corrected aperture for $D_1/D_0$ ranging from 0.2 to 2.0 and the single layer turbulence model. . . . .	220
5.8. OTF of the phase corrected aperture for $D_1/D_0$ ranging from 0.2 to 2.0 and the Hufnagel turbulence model. . . . .	221
5.9. PSF of the phase corrected aperture for $D_1/D_0$ ranging from 0.2 to 2.0 and the single layer turbulence model. . . . .	222
5.10. PSF of the phase corrected aperture for $D_1/D_0$ ranging from 0.2 to 2.0 and the Hufnagel turbulence model. . . . .	223
5.11. Normalized angular resolution of the phase corrected aperture versus $D_1/D_0$ . The normalizing resolution is $0.88\lambda/r_0$ and is computed from the unaberrated PSF in Figure 5.10. . . . .	225
5.12. Residual rms phase error versus $\theta_x/\theta_0$ for $D_1/D_0$ ranging from 0.0 to 2.0. $\theta_x$ is the angular offset in the x direction between the object and axis of the telescope. . . . .	227
5.13. Change in the residual rms phase error $\Delta\epsilon$ versus $\theta_x/\theta_0$ for $D_1/D_0$ ranging from 0.0 to 2.0. $\theta_x$ is the angular offset in the x direction between the object and axis of the telescope. . . . .	228

FIGURE	PAGE
6.1. Imaging lidar configuration. . . . .	233
6.2. Vertical resolution of the imaging lidar versus laser beam divergence for several values of the separation distance $d$ . . . . .	240
6.3. Vertical resolution of the imaging lidar versus separation distance $d$ for several values of the laser beam divergences. . . . .	241
6.4. Minimum vertical resolution versus the atmospheric cell size $r_0$ for several values of the separation distance $d$ . . . . .	244
6.5. Photocount contour plot of the laser spot image taken on January 20. The contours are 350, 400, 500, 600, 700, 800, 900, 1000, 1100, 1200 and 1400 counts per pixel. The pixel size is 3.4 $\mu$ rad. . . . .	248
6.6. Photocount contour plot of the laser spot image taken on January 21. The contours are 150, 200, 300, 400, 500, 600, 800 and 900 counts per pixel. The pixel size is 3.4 $\mu$ rad. . . . .	249
6.7. Integrated azimuth ( $\alpha$ ) angle profile through the image in Figure 6.5. . . . .	251
6.8. Integrated zenith ( $\phi$ ) angle profile through the image in Figure 6.5. . . . .	252
6.9. Na density profiles computed from the azimuthally integrated data shown in Figure 6.5 and from simultaneous monostatic lidar data. The imaging lidar had a vertical resolution of 16.6 km, while the monostatic lidar had a resolution of 150 m. . . . .	253
6.10. Na density profiles computed from the azimuthally integrated data shown in Figure 6.6 and from simultaneous monostatic lidar data. The imaging lidar had a vertical resolution of 16.6 km, while the monostatic lidar had a resolution of 150 m. . . . .	254
6.11. Power spectra of the Na density profiles in Figure 6.9. . . . .	256
6.12. Power spectra of the Na density profiles in Figure 6.10. . . . .	257

## 1. INTRODUCTION

It is well-known that the resolution of large ground-based telescopes is limited by random wave front distortion caused by atmospheric turbulence. Real time wave front reconstruction systems, commonly called adaptive optics systems, have been shown to improve significantly the image resolution of these telescopes.<sup>1</sup> With the use of adaptive optics techniques it should be possible to achieve nearly diffraction limited imaging performance. The operation of an adaptive optics system consists of two basic functions: wave front sensing and wave front correction. By using the light from either the object being observed or a nearby guide star, a wave front sensor measures the turbulence induced phase perturbations across the telescope aperture. The measurements are in turn used to adjust an electrically deformable mirror to compensate for the phase distortions. This general class of adaptive optics system has been shown to work if 1) the reference wave front from the guide star is within the isoplanatic angle of the object being observed and 2) if the guide star is bright enough to provide an adequate signal for the wave front sensor. For astronomical imaging, these two requirements imply that bright guide stars must be available within the isoplanatic angle for all observation directions. As described by Beckers,<sup>2</sup> the size of the isoplanatic angle is least restrictive at longer wavelengths. For wavelengths longer than  $4\text{ }\mu\text{m}$  the isoplanatic angle is large enough to allow wave front correction of the entire sky using natural guide stars, yet less than 0.003% of the sky can be corrected at visible wavelengths using natural guide stars.<sup>2</sup>



Obviously an adaptive telescope based on natural guide stars does not provide adequate sky coverage for astronomical imaging at the visible wavelengths. In 1985 Foy and Labeyrie<sup>3</sup> suggested that it may be possible to create a suitable artificial guide star with a laser in the upper atmosphere. Laser guide stars would allow access to the entire sky, even at visible wavelengths, since the laser could be pointed in any desired direction. In 1987 Thompson and Gardner<sup>4</sup> further advanced the laser guide star concept by demonstrating experimentally the feasibility of creating a laser guide star in the mesospheric Na layer. They made detailed engineering calculations to determine the necessary laser power to create a sufficiently bright guide star for zenith observations. They subsequently verified their analytical expressions by predicting the brightness of an experimental guide star produced at Mauna Kea Observatory.<sup>4</sup> Figure 1.1 is a contour plot of an image obtained by Thompson and Gardner of a Na guide star created with the University of Illinois lidar system. The image was obtained using a low-noise CCD detector array positioned at the Cassegrain focal plane of the University of Hawaii 2.2 meter telescope. For this experiment no attempt was made to decrease the size of the guide star to that required for an adaptive telescope system. The analytic and experimental results of Thompson and Gardner suggest that full adaptive correction for ground-based telescopes is within reasonable grasp of current laser technology.

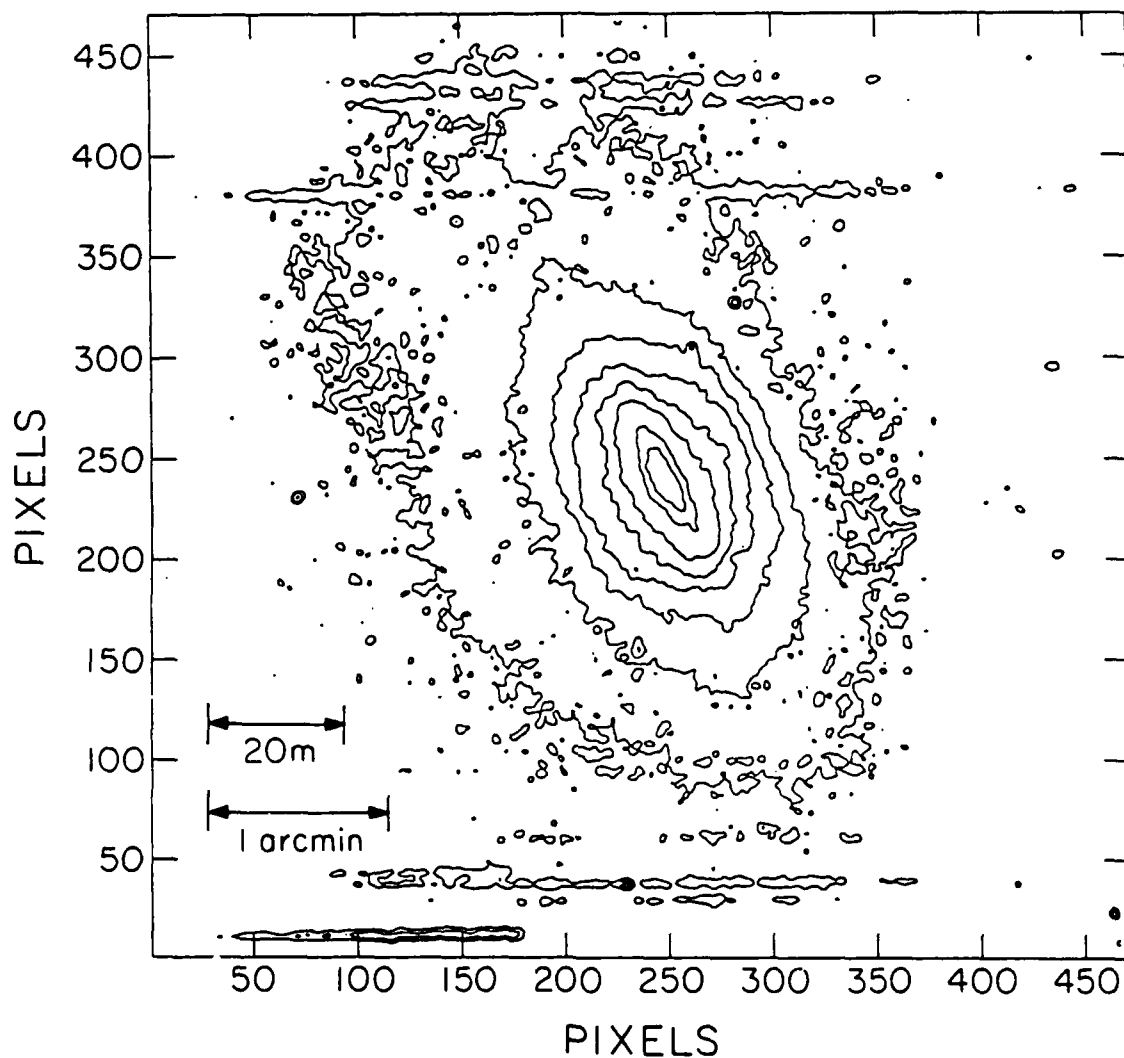


Figure 1.1. Photocount contour plot of a Na guide star image taken on January 21, 1987. The guide star was generated by the University of Illinois lidar system and imaged by the University of Hawaii 2.2 meter telescope. The contours are 150, 200, 300, 400, 500, 600, 800 and 900 counts per pixel. The pixel size is  $3.4 \mu\text{rad}$ .

If natural guide stars are available for the entire sky at infrared wavelengths, why consider the laser guide star technique? There are three important reasons. First, astronomers have an interest in observing astrophysical phenomena at all wavelengths. Second, the performance of imaging detectors and the associated sky background noise are both worse in the infrared. Third, even if an adaptive optics system corrects the wave front to the diffraction limit, this diffraction limit at infrared wavelengths is not nearly as good as that possible at visible wavelengths. For example, a 4 m telescope working at  $10\text{ }\mu\text{m}$  (where guide stars are easily found) has a diffraction limit of 0.63 arcsec. If the telescope is operated at  $5\text{ }\mu\text{m}$  (where only 50% of the sky has acceptable guide stars) the diffraction limit is still only 0.32 arcsec, while at visible wavelengths the diffraction limit is less than 0.03 arcsec. To reach these limits of resolution in the infrared will, no doubt, be a great advance. However, the infrared diffraction limits do not match the limiting resolution of the Hubble Space Telescope (HST). A laser guide star system operating at a large ground-based telescope with a full adaptive optics system will produce images in the visible wavelength region close to or even better than those expected from the HST.

Described in the remaining chapters are the results of a detailed study of the design and performance of laser-guided telescopes. In addition to the actual design and performance issues, much of the material in the following chapters encompasses the analytical design tools developed over the course of the study. One of these tools is a

unique performance analysis of a class of adaptive optics systems using wavefront slope sensors. Unlike past analyses, the performance analysis takes into account the nonideal characteristics of the wavefront sensor and wavefront correction device, as well as the effects of anisoplanatism. Performance measures include the mean square residual phase error across the aperture of the optical system and the optical transfer function (OTF). These performance measures are ultimately used to determine the key design parameters for the laser, wavefront sensor and wavefront correction device. One of the most important design tasks is determining the required laser parameters. The required brightness, size and number of laser guide stars are dependent on the desired imaging performance of the adaptive telescope. These requirements in turn directly impact the design of the laser. In the case of guide stars created in the mesospheric Na layer, the choice of the laser pulse energy, pulse length, and linewidth is complicated by the nonlinear absorption (saturation) effects. Saturation effects may significantly reduce the backscattered signal (and thus the brightness of the guide star). Characterizing the effects of saturation for a pulsed Na laser is a necessary step in the process of specifying the laser parameters.

In Chapter 2 the basic concepts and engineering design issues of laser-guided adaptive telescopes are introduced and discussed. Computing the required brightness of the guide star is one of the major design tasks. The brightness issue is addressed by investigating the imaging performance of an adaptive optics system as a function of the

photon flux density at the wavefront sensor. Other design issues include the method of forming the guide star, the positional stability of the guide star, the required size of the guide star, and the number of guide stars needed for a given telescope diameter. Some of these design issues have significantly different implications, depending on the altitude at which the guide star is formed. We consider guide stars created at a relatively low altitude within the stratosphere, using Rayleigh scattering from air molecules and guide stars created using resonance-fluorescence scattering at a relatively high altitude within the mesospheric sodium (Na) layer. Both techniques have their own unique advantages and disadvantages. The material in this chapter closely parallels that found in Reference 5.

The imaging performance of the adaptive telescope calculated in Chapter 2 is based on the analysis described in Chapter 3. Chapter 3 introduces a method of analyzing the performance of a general class of adaptive optical systems using wavefront slope sensors. Unlike past performance analyses, this analysis takes into account the nonideal characteristics inherent in any real system. The material in this chapter closely follows that of Reference 6. In Chapter 4 the effects of nonlinear resonant absorption are characterized for the pulsed lidar system. The results from this chapter are used in Chapter 2 to calculate the required Na laser parameters. The material in this chapter closely follows that of Reference 7.

The effects of anisoplanatism on the performance of laser-guided telescopes are addressed in Chapter 5. Anisoplanatism degrades the imaging performance of systems that use a reference source (i.e., a guide star) separate from the object being imaged. Due to the finite altitude of laser guide stars and the effects of anisoplanatism, multiple guide stars are required to fully sample a large telescope aperture.<sup>3</sup> The analysis presented in this chapter is critical for determining how many guide stars are required for a given telescope size and how imaging performance degrades as the observation direction is separated in angle from that of the laser guide stars. The required number of guide stars calculated in Chapter 2 is based on the results of this chapter. The material in this chapter closely parallels that found in Reference 8.

Finally, in Chapter 6, a new remote sensing technique for the study of the upper atmospheric metal layers is presented. This technique holds in common many of the design issues related to laser guide stars. The bistatic imaging lidar technique is fundamentally different from traditional monostatic lidar techniques. The vertical density of an atmospheric layer, such as the mesospheric sodium layer, is measured by imaging an illuminated spot within the layer. The spot is illuminated with a laser and imaged with a telescope in a bistatic configuration. Profiles through the image contain information about the vertical structure of the layer as well as the laser beam cross section. The material in this chapter closely follows that of Reference 9.

## 2. DESIGN AND PERFORMANCE ANALYSIS OF ADAPTIVE OPTICAL TELESCOPES USING LASER GUIDE STARS

### 2.1 Introduction: Qualitative Discussion of Design Issues

Consider a small diameter telescope as illustrated in Figure 2.1a. A diffraction limited image is focused onto the image plane of the telescope if the pupil diameter  $D$  is less than the Fried<sup>10</sup> coherence cell size  $r_0$ . The angular resolution of the telescope in the short exposure limit is  $1.22\lambda/D$ , where  $\lambda$  is the optical wavelength. However, for long exposures, random wavefront tilts cause the image to dance around in the focal plane and image blurring occurs. If the object is bright enough, a simple tip-tilt mirror arrangement can be used to compensate for the random wavefront tilt.<sup>11</sup> Such a system would consist of three main components: an image centroid detector, a tip-tilt mirror, and a control algorithm connecting the two.

For a telescope diameter larger than  $r_0$ , the angular resolution is limited to  $1.22\lambda/r_0$ . Each subaperture of size  $r_0$  within the telescope pupil generates a subimage of angular radius  $1.22\lambda/r_0$ . A random wavefront tilt over each  $r_0$  subaperture causes the subimages to dance around in the image plane. The motion of a single subimage is nearly independent of the motion of every other subimage. Modern adaptive optics telescopes of the type illustrated in Figure 2.1b use a wavefront sensor to measure the wavefront tilts over each  $r_0$  subaperture. A typical wavefront sensor consists of a lenslet array and detector array. The detector array measures the centroid displacement of the image spot under each lenslet. These

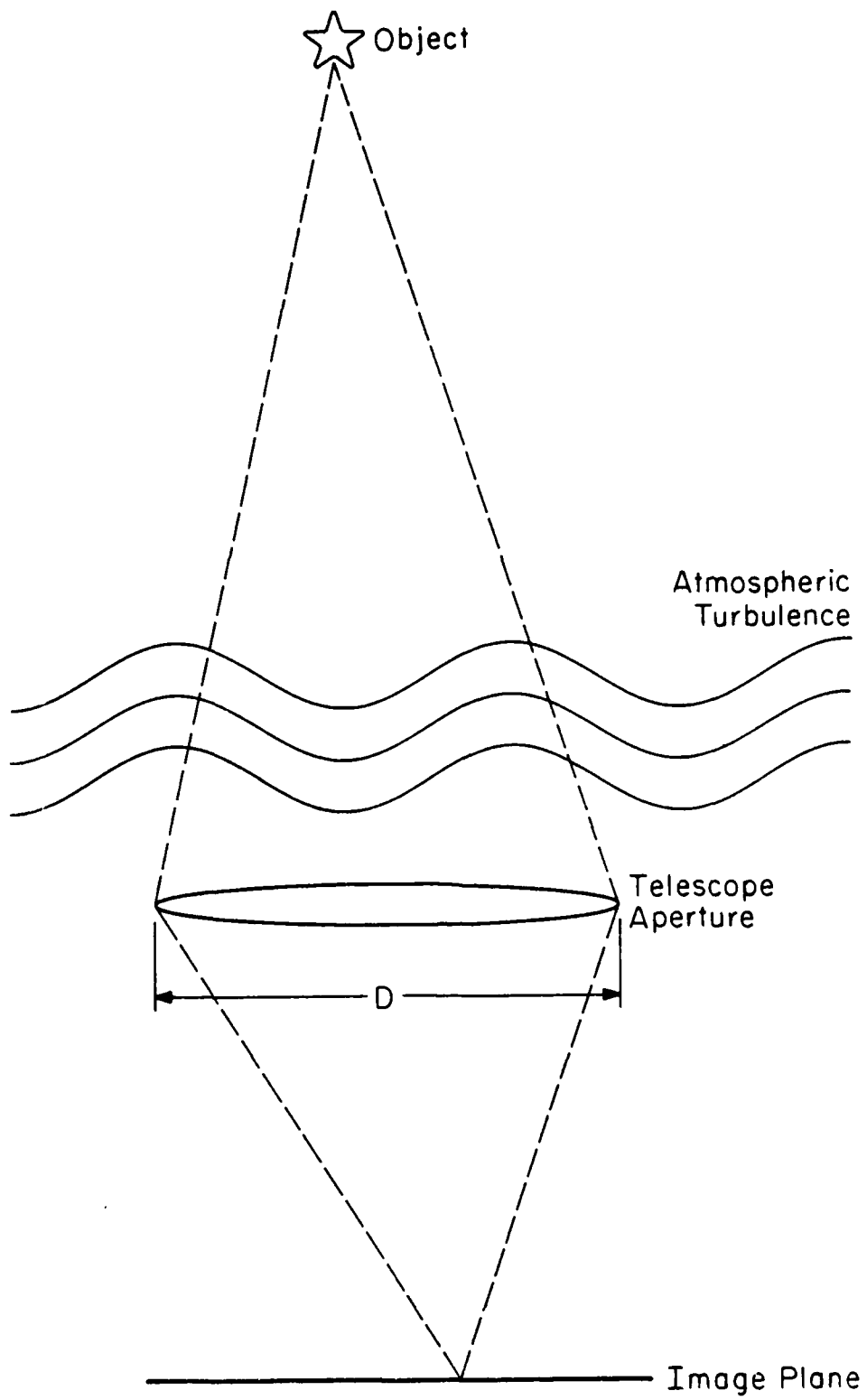


Figure 2.1a. Small diameter telescope geometry.



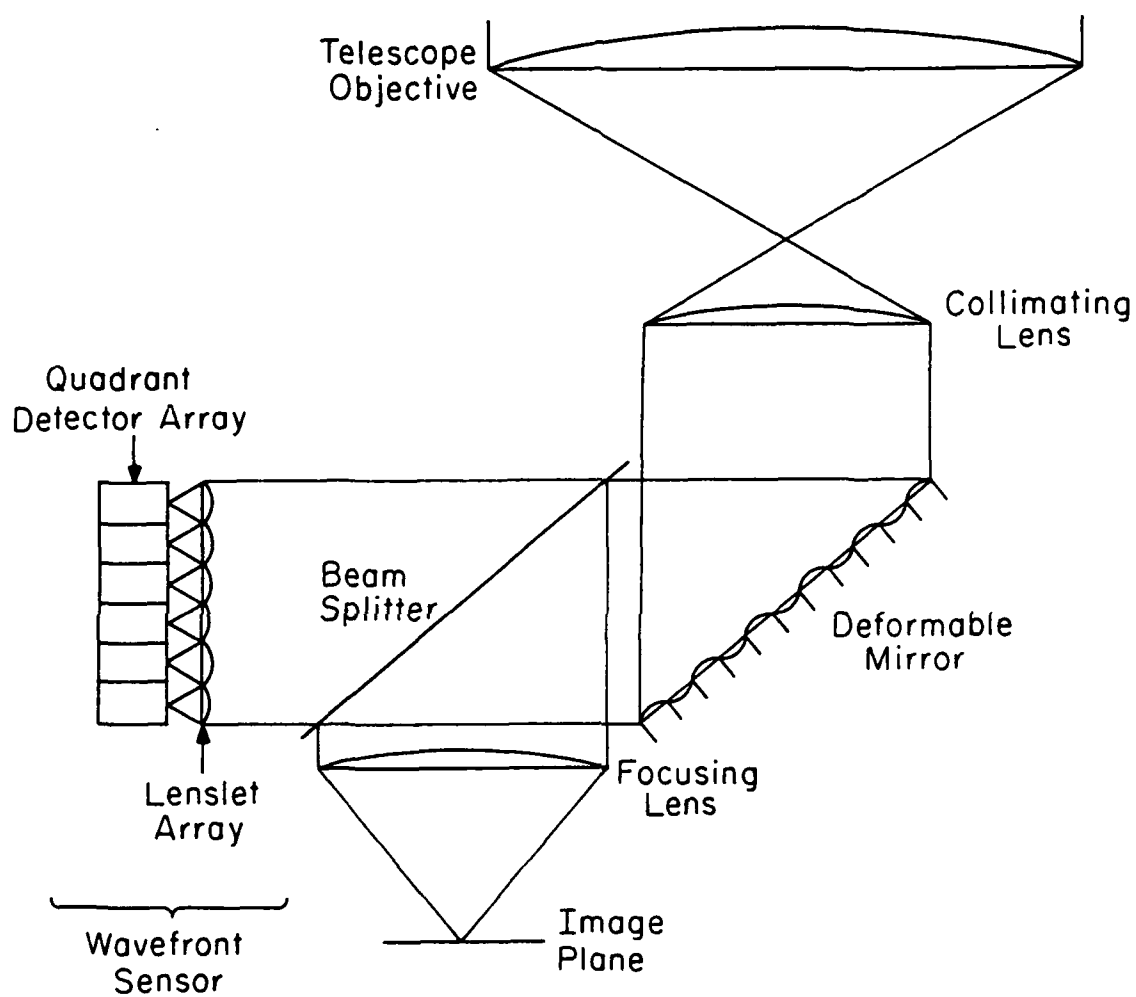


Figure 2.1b. Large diameter adaptive telescope.

measurements are in turn used to cancel the tilts by controlling the shape of a deformable mirror. If the tilts are removed from each  $r_0$  subaperture, nearly diffraction limited imaging performance can be achieved.

Figure 2.2 illustrates the optical design of a laser guided adaptive telescope. The major components include the telescope aperture, laser, laser beam jitter sensor, low frequency motion sensor, deformable mirror, tip-tilt mirror, wavefront sensor, imaging module and control module. In the remainder of this section we discuss the basic operation of these components and how the nonideal characteristics of the components affect imaging performance. Throughout we concentrate on phase correcting systems, and assume that turbulence induced amplitude perturbations are negligible.<sup>12</sup>

The laser beam is expanded and transmitted through a projection telescope behind the Cassegrain secondary mirror. The beam is focused at the altitude of the selected atmospheric scattering region. Before leaving the projection telescope, part of the beam is sampled for use by the jitter sensor. The jitter sensor measures the propagation angle of the laser beam, and this information is fed back into the control module to null out effects of beam jitter.

The backscattered light from the laser guide star, after being focused by the telescope, is passed through the central hole of a 45° turning mirror. The mirror reflects the light from a set of widely

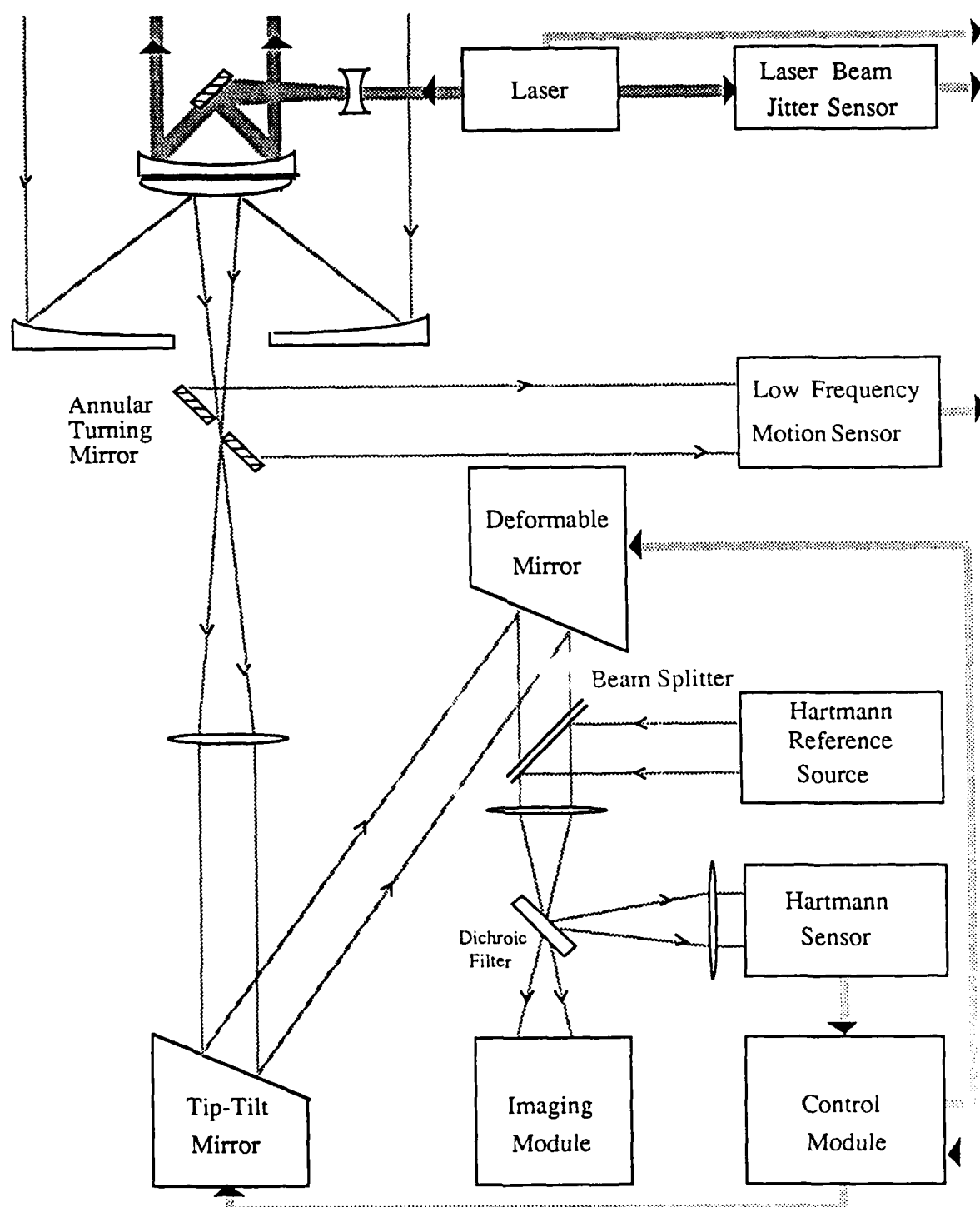


Figure 2.2. Laser guided adaptive telescope system diagram.

spaced natural stars which are used for low frequency motion compensation. The low frequency motion sensor locks onto the location of these widely spaced stars and sends a signal to the control module where the low frequency motions of the laser guide star and telescope are nulled. The requirement for low frequency motion compensation is discussed in more detail below. Once passing through the annular turning mirror the light from the laser guide star is collimated and is reflected first off the tip-tilt mirror and then off the deformable mirror. The tip-tilt mirror removes overall wavefront tilt while the deformable mirror removes subaperture tilts. The light is then reflected off a dichroic beamsplitter to the wavefront sensor, and the remaining light is directed to the imaging module. The subaperture tilts detected by the wavefront sensor are processed and sent to the deformable mirror as actuator control signals. The imaging module captures the corrected image reflected from the deformable mirror and these data are saved as the final astronomical image.

Consider the problem (first discussed by Thompson and Gardner in Reference 13) of creating the guide star by transmitting the laser beam with a projection aperture of diameter  $r_0$ . Except for the tilt induced by the turbulence, the beam is relatively unperturbed as it goes up through the atmosphere. Because the round-trip travel time for light scattered in the upper atmosphere is  $\leq 600 \mu s$ , the refractive index perturbations in the atmosphere remain essentially unchanged, so the laser light received within the  $r_0$  aperture returns along the same path traversed during transmission. In this case the random tilt over the

$r_0$  aperture does not cause the guide star to move. Consequently, the image of the guide star does not dance around in the image plane of the  $r_0$  aperture, while natural stars--whose light traverses the atmosphere only once--do. Such an arrangement yields no information about the turbulence effects within the  $r_0$  aperture. Next consider the case where the transmitting aperture contains  $M$  cells each of diameter  $r_0$ . Since  $M$  separate beams are deflected at independent angles due to the tilt components in each  $r_0$  cell, the resulting guide star, when viewed from below, contains  $M$  small sources which are spread over a patch of angular diameter  $\sim \sqrt{2}(1.22\lambda/r_0)$ . The  $\sqrt{2}$  factor arises because of the double pass through the atmosphere. The centroid of the multiple-speckled guide star provides a stationary point of reference which can be used by the wavefront sensor to measure the subaperture tilts. However, if the atmosphere contains wavefront perturbations of the same size as (or larger than) the transmitting aperture, these low spatial frequency wavefront errors are not detected for reasons directly analogous to the single  $r_0$  case. These low frequency wavefront perturbations cause the position of the laser guide star to move relative to the natural stars.

Low frequency wavefront perturbations are one of three effects which will cause the centroid of the laser guide star to move in unexpected ways, and thereby to lose reference with respect to the background stars. The other two effects include 1) jitter in the laser beam and 2) nonsidereal motion of the transmitting telescope. The problem of laser beam jitter is easily solved by monitoring the angular

orientation of the beam at the output of the laser. Any detected beam jitter can simply be measured and nulled within the computer analyzing the wavefront. The other two sources of error--telescope jitter and low frequency atmospheric refraction--are more difficult to remove, especially at the required level of precision. To first order, both of the latter image motion effects can be removed by building a tracking system that locks onto nearby natural guide stars. These stars do not have to lie in the isoplanatic patch of the adaptive mirror since only first order effects must be corrected. The error signal from the tracking system can be sent to a tip-tilt mirror capable of moving at high frequency, and this will remove most, if not all, of the detected image motion.

In an ideal system the wavefront compensation would result in perfect cancellation of the phase perturbations of the aberrated wavefront. In reality, though, there are many factors which prevent us from achieving the ideal diffraction limit. These factors can be summarized as our inability to build perfect wavefront sensors and deformable mirrors. Hardy<sup>1</sup> presents a thorough review of the types of wavefront sensors and deformable mirrors used in modern adaptive optics. The two most important limiting factors are 1) the spacing of the sensors and mirror actuators within the aperture of the optical system, 2) and photon noise. Sensor and actuator spacing determine the response of the adaptive optics system to the highest spatial frequency of the phase perturbations. From the discussion above we indicate that tilt sensors and tilt correctors spaced at intervals of  $r_0$  can result

in nearly diffraction limited imaging performance. Even with this spacing the accuracy of the reconstructed wave can be severely degraded if photon noise effects are significant. Photon noise arises because of the finite flux available from the guide star reference wavefront. In the simplest case the signal-to-noise ratio for sensors based on photon counting techniques is proportional to  $1/\sqrt{N}$  where  $N$  is the total photon count per subaperture during the measurement integration time. Depending on the efficiency of the sensor, a weak reference wavefront can significantly degrade performance. Quantifying the effects of photon noise is particularly important for the design of laser-guided adaptive telescopes, since the laser requirements are derived directly from guide star brightness requirements.

One of the more common wavefront sensors is the Hartmann sensor, the performance of which is analyzed in detail by Kane et al.<sup>14,15</sup> The Hartmann wavefront sensor falls under the general category of a slope or tilt sensor. The aperture of the optical system is segmented into subapertures and within each subaperture the wavefront tilt is measured. The Hartmann sensor uses a lenslet array to translate the task of wavefront tilt detection to one of centroid detection in the image plane. Figure 2.3 illustrates a diagram of a single cell of a Hartmann sensor. A tilt  $\psi$  (rad) is detected by measuring the centroid offset of the diffraction limited spot in the focal plane ( $x,y$  plane) of a single lenslet. The offset is measured by a sensor array capable

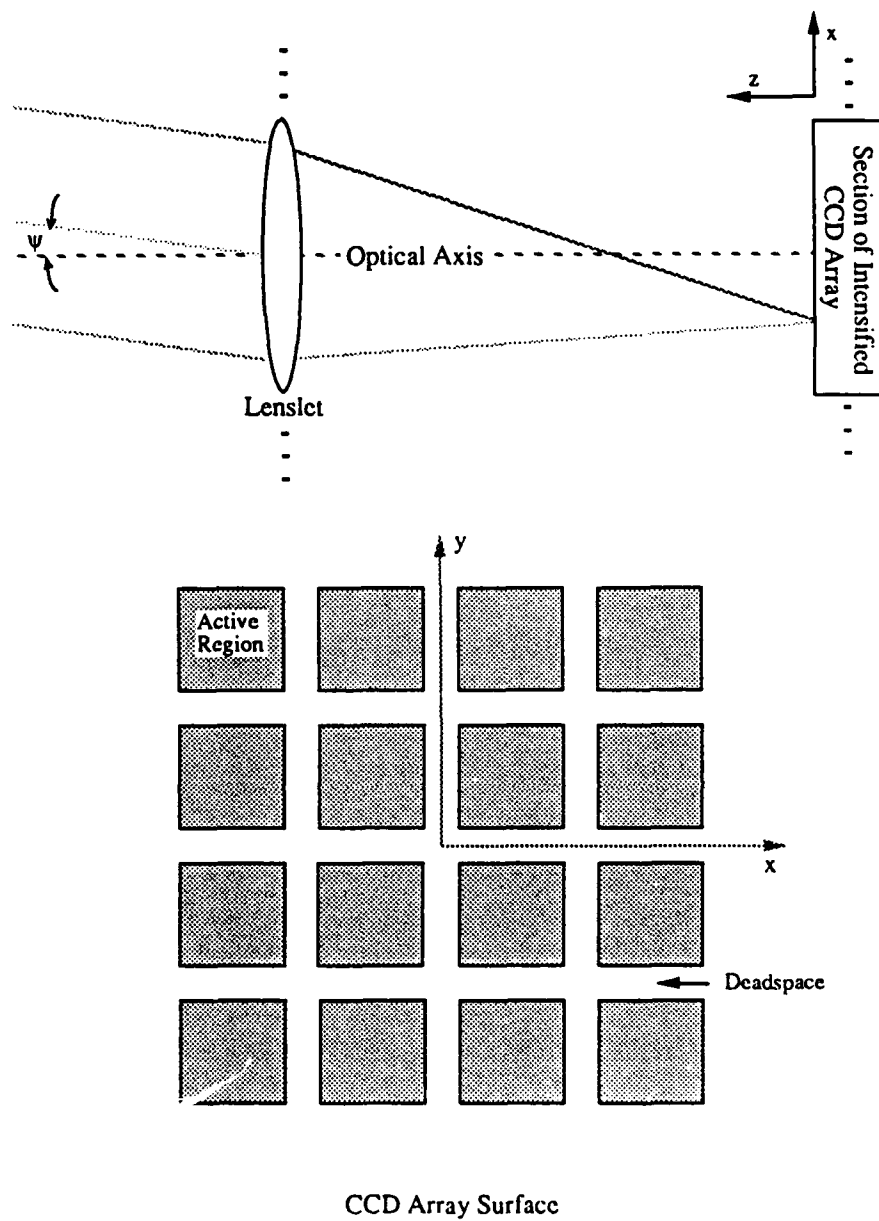


Figure 2.3. Single Hartmann tilt sensor and section of CCD array surface.



of photon counting. For an ideal centroid detector the rms tilt measurement error in the x or y directions  $\Delta\psi_{x,y}$  is given by<sup>14,15</sup>

$$\Delta\psi_x = \Delta\psi_y = \begin{cases} \frac{0.431 \lambda}{\sqrt{N} d} & d \leq r_o \\ \frac{0.431 \lambda}{\sqrt{N} r_o} & d > r_o \end{cases} \quad (2.1)$$

where N is the total photon count for the single Hartmann cell. The factor 0.431 arises because the Airy spot distribution in the image plane is equated to a Gaussian spot distribution by matching the spot diameter at the  $e^{-1}$  points. Kane et al.<sup>14,15</sup> present a more detailed analysis and find that the total tilt measurement accuracy  $\Delta\psi$  of this type of sensor can be written

$$\Delta\psi = [\Delta\psi_x^2 + \Delta\psi_y^2]^{1/2} = \begin{cases} \frac{0.61 \lambda \eta_c}{\sqrt{N} d} & d \leq r_o \\ \frac{0.61 \lambda \eta_c}{\sqrt{N} r_o} & d > r_o \end{cases} \quad (2.2)$$

where  $\eta_c$  is an efficiency factor that includes the effects of an imperfect detector array in the image plane (i.e., dead space in the detector surface, finite pixel size, and finite pixel spacing), the effects of spot size and spot location within the focal plane, and the effects of an image intensifier in front of the array. In an analysis similar to that of Winick,<sup>16</sup> Kane finds that the efficiency factor  $\eta_c$  can be minimized with respect to the size of the focal plane spot. For typical CCD array and image intensifier parameters he finds that the

minimum value of  $\eta_c$  ranges from 1.35 to 1.50. In Section 2.3 we use the accuracy specified in Equation (2.2) to calculate the guide star brightness requirement for a Hartmann type wavefront sensor.

The size of the guide star also affects wavefront sensor accuracy. For maximum centroiding accuracy it is reasonable to assume that the full angular resolution of a subaperture lenslet should be employed. For a given lenslet focal length, this angular resolution determines the smallest possible spot size in the focal plane. If the subaperture diameter  $d$  is less than  $r_0$ , the smallest angular diameter of the spot is  $2.44\lambda/d$  (i.e., diameter at the  $e^{-2}$  intensity points). For  $d > r_0$ , turbulence restricts the smallest angular diameter to  $2.44\lambda/r_0$ . To take advantage of these resolution limits, the angular size of guide star  $\Delta\alpha$  should be no larger than the angular resolution of the subaperture. There is virtually no advantage to making the laser guide star smaller; in fact, for Na laser guide stars there is a significant disadvantage to making the angular diameter smaller.<sup>7</sup> Thus we require the diameter of the laser guide star to equal the angular resolution of the subaperture

$$\Delta\alpha = \begin{cases} 2.44\lambda/d & d \leq r_0 \\ 2.44\lambda/r_0 & d > r_0 \end{cases} \quad (2.3)$$

For the case of  $d \geq r_0$  the width given in Equation (2.3) corresponds to the apparent size of natural stars. If an adaptive optics telescope is designed to work at a wavelength of  $0.5 \mu\text{m}$  in conditions where  $d = r_0 = 20 \text{ cm}$ , the laser guide star should have a diameter at the  $e^{-2}$  intensity

points of  $\sim 1.26$  arcsec. Achieving this angular size is likely to be quite easy even in the presence of the double pass through the atmosphere. If there is a need to make the guide star smaller, the beam wander induced by each of the  $r_0$  projection cells could be compensated by projecting the laser beam through the phase corrected telescope.

Nonisoplanicity represents another fundamental limitation to imaging performance. The effects of nonisoplanicity arise because of the distribution of turbulence along the optical path. Effective wavefront compensation is limited to an angular region surrounding the guide star. The size of the region is defined by the isoplanatic angle. The isoplanatic angle is commonly defined as the largest field of view (FOV) for which the OTF of the optical system does not change significantly. Due to the small size of the isoplanatic angle at visible wavelengths and the finite altitude of the laser guide star, several guide stars are required to fully correct a large telescope aperture. The actual number required is derived in Chapter 5.

In Sections 2.2 - 2.5 we provide a more quantitative discussion of the design issues by deriving the key design equations for a laser-guided adaptive telescope. To aid in deriving these equations, we first review, in Section 2.2, the basic concepts and terminology used to describe the effects of atmospheric turbulence on ground-based imaging systems. The required brightness of the guide star is addressed next in Section 2.3. Design equations are derived giving

overall imaging performance as a function of guide star brightness. In Sections 2.4 and 2.5 we discuss adaptive telescope systems based on Rayleigh and Na resonance fluorescence guide stars. The results of Section 2.3 are used to compute the laser characteristics required to generate sufficiently bright guide stars. In Section 2.6 we present the key design parameters of 2- and 4-meter laser-guided adaptive telescope systems. We specify the required laser characteristics and compute the expected imaging performance. Finally, in Section 2.7, we briefly discuss the application of laser guide star systems to optical interferometric imaging.

## 2.2 Atmospheric Turbulence Effects

During the past 15 years many authors have studied the effects of atmospheric turbulence on ground-based imaging systems.<sup>10,17-24</sup> In 1966 Fried<sup>10</sup> wrote a seminal paper describing the performance of an optical system in the presence of atmospheric turbulence. He characterizes performance in terms of the OTF. From the OTF Fried derives a single parameter, now called the Fried coherence diameter  $r_0$ , that concisely characterizes the performance of an aperture in the presence of atmospheric turbulence. Fried defines  $r_0$  as

$$r_0 = 0.185 \left[ \frac{\lambda^2}{\int_0^h \left[ 1 - \frac{\xi}{h} \right]^{5/3} C_n^2(\xi) d\xi} \right]^{3/5} \quad (2.4)$$

where  $\lambda$  is the optical wavelength,  $C_n$  is the structure constant of the refractive index fluctuations, and  $h$  is the length of the optical path

from the aperture entrance plane to the light source. The parameter  $C_n$  is a general measure of the severity of the turbulence-induced phase distortions and is a function of location. By using a measure of resolution equivalent to the Strehl ratio, Fried showed that for a telescope diameter  $D$  much less than  $r_0$ , resolution is proportional to the square of  $D$ . As  $D$  becomes larger than  $r_0$ , resolution asymptotically approaches a constant value slightly greater than the resolution of an aperture of diameter  $r_0$ .

The dependence of  $r_0$  on wavelength goes as  $\lambda^{6/5}$ . As the wavelength is increased, the effects of atmospheric turbulence decrease. At the best observatory sites, and in conditions of good seeing,  $r_0$  can range from 10 to 30 cm for visible wavelengths. For infrared wavelengths ( $\sim 2 \mu\text{m}$ ) Beckers et al.<sup>2</sup> find that  $r_0$  can range from 50 to 200 cm. The dependence of  $r_0$  on the structure parameter  $C_n(\xi)$  is related to the length of the optical path through the turbulence and on the actual strength of the turbulence. If the value of  $r_0$  for vertical viewing is used as a reference, it is easy to show using Equation (2.4) that  $r_0$  varies with the zenith angle  $\theta$  as

$$r_0(\theta) = 0.185 (\cos\theta)^{3/5} \left[ \frac{\lambda^2}{\int_0^h \left[ 1 - \frac{\xi}{h} \right]^{5/3} C_n^2(\xi) d\xi} \right]^{3/5}. \quad (2.5)$$

This decrease in  $r_0$  with the zenith angle is caused by the increased path length through the turbulence.

The dominant effect of atmospheric turbulence for an aperture of diameter  $r_0$  is a random wavefront tilt. This assertion was quantified by Fried.<sup>25</sup> He derived the statistics of the phase fluctuation across an aperture by characterizing the fluctuations as an infinite sum of orthogonal geometric representations. The first few terms used in the representation include easily visualized phase surfaces: a constant phase shifted surface, a tilted surface, a spherical surface, and a hyperbolic surface. Fried finds that the average rms value of the phase  $\Delta\phi$  (m) over an aperture of diameter  $d$  is given by<sup>25</sup>

$$\Delta\phi = \left( \frac{d}{r_0} \right)^{5/6} \frac{\lambda}{6.2}. \quad (2.6)$$

He then approximates the wavefront phase with the first two terms in the geometric representation, which include the constant phase shift and tilted wavefront surfaces. The average rms difference between the phase of the actual and approximate wavefront is given by<sup>25</sup>

$$\Delta\phi' = \left( \frac{d}{r_0} \right)^{5/6} \frac{\lambda}{17.4}. \quad (2.7)$$

This rms difference is equivalent to the residual phase variation obtained for an adaptive optics system capable of achieving perfect tilt compensation. Equation (2.7) indicates that a large part of the phase distortions across an aperture can be attributed to wavefront tilt. In fact nearly 90 percent of the power in the phase fluctuations is due to tilt. This is an important result, since it indicates that an adaptive optics system correcting only for wavefront tilt can remove

a large percentage of the phase distortions. The smaller the aperture over which the tilt is removed, the smaller the residual uncorrected phase variation. Consider an aperture segmented into subapertures of diameter  $r_0$ . If the overall aperture and subaperture tilts are removed, the resulting rms phase variation over the entire aperture will be  $\lambda/17.4$ . This wavefront phase variation yields a Strehl ratio of 0.88. By comparison, the HST is designed for a figure error not to exceed  $\lambda/20$ , which corresponds to a Strehl ratio of 0.91. This simple example demonstrates that it is possible to achieve near diffraction limited performance simply by removing wavefront tilt over subapertures of diameter  $r_0$ .

The isoplanatic angle represents a significant limitation for adaptive telescope systems that rely on guide stars which are separated in angle from the object of interest. The offset results in two optical paths traversing different regions in the turbulence. The turbulence effects in one path are only partially correlated with the turbulence effects in the other path. This decorrelation degrades the accuracy of the wavefront compensation. Many papers<sup>26-30</sup> have addressed the effects of anisoplanatism on adaptive optical systems. Most of these characterize the effects in terms of the degradation of the OTF as a function of angular separation between the reference light source and object of interest. A common definition of the isoplanatic angle is the largest field of view (FOV) for which the OTF of the optical system does not change significantly. Fried<sup>28</sup> gives the following expression for the isoplanatic angle:

$$\theta_{IP} = \frac{r_o}{(6.88)^{5/3}} \left[ \frac{\int_0^h \left[ 1 - \frac{\xi}{h} \right]^{5/3} C_n^2(\xi) d\xi}{\int_0^h C_n^2(\xi) \xi^{5/3} d\xi} \right]^{3/5}. \quad (2.8)$$

For computational purposes it is common to approximate the effects of the atmosphere by assuming the turbulence is confined primarily to a single layer at a height of  $h_t$ . In this case Equation (2.8) reduces to

$$\theta_{IP} \approx \frac{r_o}{3} \left( \frac{1}{h_t} - \frac{1}{h} \right). \quad (2.9)$$

For the case of astronomical imaging,  $h_t \ll h$  and Equation (2.9) reduces to

$$\theta_{IP} \approx \frac{r_o}{3 h_t}. \quad (2.10)$$

For  $r_o = 20$  cm and  $h_t = 10$  km, we find that  $\theta_{IP}$  is  $\sim 1.38$  arcsec.

Due to the small size of the isoplanatic angle at visible wavelengths, multiple laser guide stars are required to fully correct a large telescope aperture. This was first pointed out by Foy and Labeyrie.<sup>3</sup> In an ideal situation the guide star would be in the far field of the telescope aperture, giving rise to a plane wave reference wavefront at the telescope entrance pupil. Due to the finite altitude of the laser guide star the effects of nonisoplanicity must be considered. The wavefront corrections are effective only for those



points in the aperture that lie within the isoplanatic angle of the guide star. Figure 2.4 illustrates a diagram of the isoplanatic angle superimposed on a cross section of the telescope aperture. The points in the aperture that lie within the isoplanatic angle are encircled by an area of diameter  $D_{IP}$  where  $D_{IP}$  is given by<sup>31</sup>

$$D_{IP} \approx 2 z_g \theta_{IP}, \quad (2.11)$$

and  $z_g$  is the height of the guide star above the telescope entrance plane. For apertures larger than  $D_{IP}$ , the number of guide stars required  $N_{gs}$  is approximately<sup>5, 31</sup>

$$N_{gs} \sim \frac{D^2}{D_{IP}^2} \approx \frac{D^2}{4 z_g^2 \theta_{IP}^2}. \quad (2.12)$$

If the effects of the turbulence are well modeled by a single turbulent layer at a height of  $h_t$ , Equation (2.10) can be substituted into Equation (2.12) to obtain

$$N_{gs} \sim 2.25 \frac{D^2 h_t^2}{z_g^2 r_o^2}. \quad (2.13)$$

Equation (2.13) is obtained by choosing, rather arbitrarily, Fried's definition of  $\theta_{IP}$ . More recently Welsh and Gardner<sup>8</sup> presented an analysis of the effects of anisoplanatism on laser-guided telescopes. This analysis is summarized in Chapter 5. In this analysis, Welsh and Gardner take into account the nonideal characteristics of the wavefront sensor and deformable mirror, as well

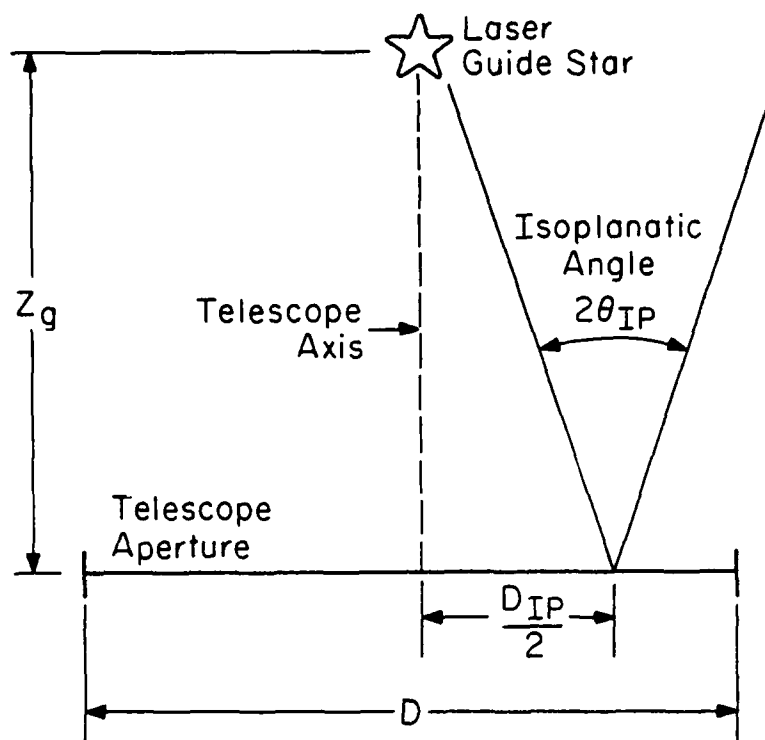


Figure 2.4. Geometry of the isoplanatic angle superimposed on a cross section of the telescope aperture.

as the spherical nature of the wavefront from the laser guide star. They quantify the imaging performance of the adaptive telescope as a function of the height and number of guide stars. The results of their numerical computations indicate that  $N_{gs}$  can be substantially reduced from that given by Equation (2.13) without significantly degrading the imaging performance of the adaptive telescope. This is a significant result, since the laser power requirements for the laser-guided adaptive telescope are directly proportional to  $N_{gs}$ . They find that

$$N_{gs} \sim \frac{D^2 h_t^2}{z_g^2 r_o^2}, \quad (2.14)$$

which is a factor of 2.25 reduction of that given by Equation (2.13). In the remainder of this chapter, Equation (2.14) will be used for all calculations involving  $N_{gs}$ . Consider, for example, a telescope diameter of 2 m,  $r_o = 20$  cm,  $h_t = 10$  km, and a guide star height of  $z_g = 92$  km. The number of guide stars required for these parameters is  $\sim 1$ . For a 4 m diameter telescope the number of guide stars required increases to  $\sim 5$ . The height  $z_g = 92$  km corresponds to the nominal altitude of the mesospheric Na layer.<sup>32</sup> The required number of guide stars increases when the guide star is formed at lower altitudes. If a Rayleigh guide star is formed at a height of 12 km, the required number of guide stars is  $\sim 69$  for a 2 m telescope and  $\sim 278$  for a 4 m telescope.

Up to this point we have addressed only the spatial nature of the turbulence effects. Temporal fluctuations of the wavefront phase are

caused by the relative motion of the turbulence with respect to the aperture of the optical system. For vertical viewing through the atmosphere it is common to think of the turbulence as stratified into horizontal layers, each with a characteristic velocity. Several authors<sup>6, 33-35</sup> have characterized the effects of temporal fluctuations on adaptive optics systems by assuming either the turbulence is confined to one layer with a characteristic velocity and  $C_n$  value, or that the turbulence consists of several layers, each with a characteristic velocity and  $C_n$  value. The impact of temporal fluctuations is a constraint on the minimum frequency at which the wavefront must be corrected. The required frequency is dictated primarily by the correlation time of the atmosphere. For a single layer of turbulence with a speed of  $v$ , Tyler<sup>35</sup> shows that the required 3 dB bandwidth of the adaptive optics servo loop is on the order of  $v/r_0$ . Using this relationship and substituting in  $v = 10$  m/s and  $r_0 = 20$  cm, the required correction rate is 50 Hz. Welsh and Gardner<sup>6</sup> investigated the effects of the correction rate on the performance of an adaptive optics system using slope sensors. For the same layer velocity assumed above, they found that correction rates of 100 Hz or larger resulted in minimal degradation of the performance. For zenith viewing through the atmosphere it is generally accepted that the required correction rate will be on the order of 50 to 100 Hz. The guide star must be bright enough to provide the required flux within the cycle time of the adaptive optics system. This requirement specifies that the laser be pulsed at a rate greater than or equal to the sampling rate of the adaptive optics system and that the pulse

energy be large enough to insure that the required photon flux density is achieved per cycle period.

### 2.3 Guide Star Brightness

The brightness of the guide star determines the ultimate accuracy of the wavefront sensor and consequently the performance of the adaptive telescope. To discuss the brightness requirement (and in later sections the power requirements of the laser), we must first discuss the desired performance of the adaptive telescope. In the analysis to follow we calculate performance in terms of the rms residual phase error over the telescope aperture and the Strehl ratio. These performance measures are related to the spacing of the wavefront sensors and the tilt measurement accuracy. The wavefront sensor is modeled after the basic design of the Hartmann sensor described in Section 2.1. The deformable mirror is assumed to be perfect in the sense that it removes the measured tilt in each subaperture of the telescope pupil. The effects of misalignment of the individually tilted mirror segments are ignored. The analysis yields very simple formulae that can be used to obtain estimates of the required photon flux. The section is concluded by comparing the results obtained from this analysis to the results from a more sophisticated analysis technique presented by Welsh and Gardner<sup>6</sup> and summarized in Chapter 3. They analyzed the performance of a complete wavefront compensation system based on slope sensors. Included in their analysis are the effects of photon noise and realistic models of the wavefront sensor and deformable mirror.

Equation (2.7) gives the rms wavefront phase variation over a circular aperture of diameter  $d$  for the case of perfect tilt removal. This phase variation is designated  $\Delta\phi'$ . If tilt is removed over subapertures of diameter  $r_o$ , the total residual rms phase variation over the entire aperture  $\Delta\phi$  will be  $\Delta\phi = \Delta\phi' \sim \lambda/17$ . This small residual phase variation results in nearly diffraction limited imaging. Another useful performance measure is the Strehl ratio, which compares the peak amplitude of the point spread function (PSF) to the peak amplitude theoretically possible in an unaberrated system. The Strehl ratio is a general indication of how well the peak intensity in the image plane can be discerned from the surrounding intensity distribution. For  $\Delta\phi < \lambda/10$  the Strehl ratio  $S$  can be approximated by<sup>1</sup>

$$S(\Delta\phi) = \exp\left\{-\left[\frac{2\pi\Delta\phi}{\lambda}\right]^2\right\}. \quad (2.15)$$

In the case of perfect tilt removal,  $\Delta\phi'$  given by Equation (2.7) is substituted for  $\Delta\phi$  in Equation (2.15) to give

$$S(\Delta\phi') = \exp\left\{-0.1301 \left[\frac{d}{r_o}\right]^{5/3}\right\}. \quad (2.16)$$

For  $d = r_o$ ,  $S$  is approximately 0.88.

To achieve perfect tilt compensation the tilt measurement error in the wavefront sensor must go to zero. The tilt measurement accuracy  $\Delta\psi$  given by Equation (2.2) indicates that the guide star would have to

be infinitely bright to achieve zero measurement error. Since it is impossible to remove the subaperture tilts perfectly, the contribution of the uncorrected tilt must be included in the computation of the total rms phase variation  $\Delta\phi$ . Let  $\Delta\phi_{\text{tilt}}$  (m) be this contribution. In a straightforward geometric calculation it is easy to show, for a circular aperture of diameter  $d$ , that  $\Delta\psi$  (rad) is related to  $\Delta\phi_{\text{tilt}}$  by

$$\Delta\phi_{\text{tilt}} = \frac{\Delta\psi d}{4}. \quad (2.17)$$

Substituting  $\Delta\psi$  given by Equation (2.2) into Equation (2.17) gives

$$\Delta\phi_{\text{tilt}} = \begin{cases} \frac{0.153 \lambda \eta_c}{\sqrt{N}} & d \leq r_o \\ \frac{0.153 \lambda \eta_c d}{\sqrt{N} r_o} & d > r_o \end{cases}. \quad (2.18)$$

Assuming  $\Delta\phi_{\text{tilt}}$  is statistically independent of the residual phase variation for perfect tilt removal,  $\Delta\phi'$ , the total rms phase variation  $\Delta\phi$  can be written

$$\Delta\phi = (\Delta\phi'^2 + \Delta\phi_{\text{tilt}}^2)^{1/2}. \quad (2.19)$$

Note that the effect of a time delay between wavefront sensing and wavefront correction has been ignored in the derivation of Equation (2.19). Preliminary results from ongoing research indicate that the degradation to imaging performance caused by the time delay can be incorporated into the analysis by letting  $\Delta\phi'^2$  be a sum of two terms: the residual phase variation for perfect tilt removal (Equation (2.7))

and the phase variation due to a nonzero time delay between wavefront sensing and correction. For the remainder of the analysis we assume the time delay is small enough to insure that the additional phase variation is negligible.

Restricting our attention to the case where  $d \leq r_o$  and substituting Equations (2.7) and (2.18) into Equation (2.19) and then solving for the required photon flux density  $F$  (photons/m<sup>2</sup>) we obtain

$$F = \frac{8.99 \eta_c^2}{d^2 \left\{ \left( \frac{\Delta\phi}{0.0574\lambda} \right)^2 - \left( \frac{d}{r_o} \right)^{5/3} \right\}} \quad (2.20)$$

where  $F$  is related to the subaperture photon count  $N$  by  $F = 4N/\pi d^2$ . Equation (2.20) is valid for  $\Delta\phi > \Delta\phi'$ . Using Equations (2.19) and (2.15) we can also solve for the required flux as a function of the Strehl ratio  $S(\Delta\phi)$ :

$$F = \frac{1.17 \eta_c^2}{d^2 \left\{ -\ln \left[ S(\Delta\phi) \right] - 0.1301 \left( \frac{d}{r_o} \right)^{5/3} \right\}} \quad (2.21)$$

Recall the approximation for  $S(\Delta\phi)$  given by Equation (2.15) is valid for  $\Delta\phi < \lambda/10$ . This restriction implies Equation (2.21) is valid for  $S(\Delta\phi) > 0.674$ .

Equations (2.20) and (2.21) give the required flux density  $F$  to achieve a specified level of phase error ( $\Delta\phi$ ) or Strehl ratio ( $S(\Delta\phi)$ )



as a function of subaperture size  $d$ . The flux density  $F$  can be minimized with the proper choice of  $d$ . Let  $d_0$  designate the value of  $d$  that minimizes  $F$ . Minimization of Equations (2.20) or (2.21) gives

$$d_0 = 21.45 r_0 (\Delta\phi/\lambda)^{6/5} \quad (2.22)$$

and

$$F_{\min} = \frac{1.42 \times 10^{-4} \eta_c^2}{r_0^2 (\Delta\phi/\lambda)^{22/5}} \quad (2.23)$$

where  $F_{\min}$  is the minimized photon flux density. The restriction that  $d \leq r_0$  implies that Equations (2.22) and (2.23) are valid for  $\Delta\phi \leq \lambda/12.9$ . Figures 2.5 and 2.6 are plots of  $d_0$  and  $F_{\min}$  as a function of  $\Delta\phi$ . Equation (2.23) is plotted for a detector efficiency factor of  $\eta_c = 1.35$ . This value is typical for currently available intensified CCD detector arrays.<sup>14,15</sup> Consider, for example, a value of  $\Delta\phi = \lambda/17.5$ . For this phase error the optimum subaperture size is  $0.69r_0$  and the minimized flux requirement is  $76.3/r_0^2$  photons/m<sup>2</sup>. If  $r_0 = 20$  cm, the optimum subaperture size is 13.8 cm and the required flux is 1907 photons/m<sup>2</sup> per cycle of the adaptive optics system. If the cycle time of the adaptive optics system is on the order of 10 ms, a natural star producing this same photon flux when observed through a filter with a 100 nm bandwidth centered at the visible wavelengths (0.55  $\mu$ m) would have an apparent magnitude of  $M_v = 11.9$ .

In Sections 2.4 and 2.5 we compute the required laser characteristics to generate guide stars in the stratosphere and in the

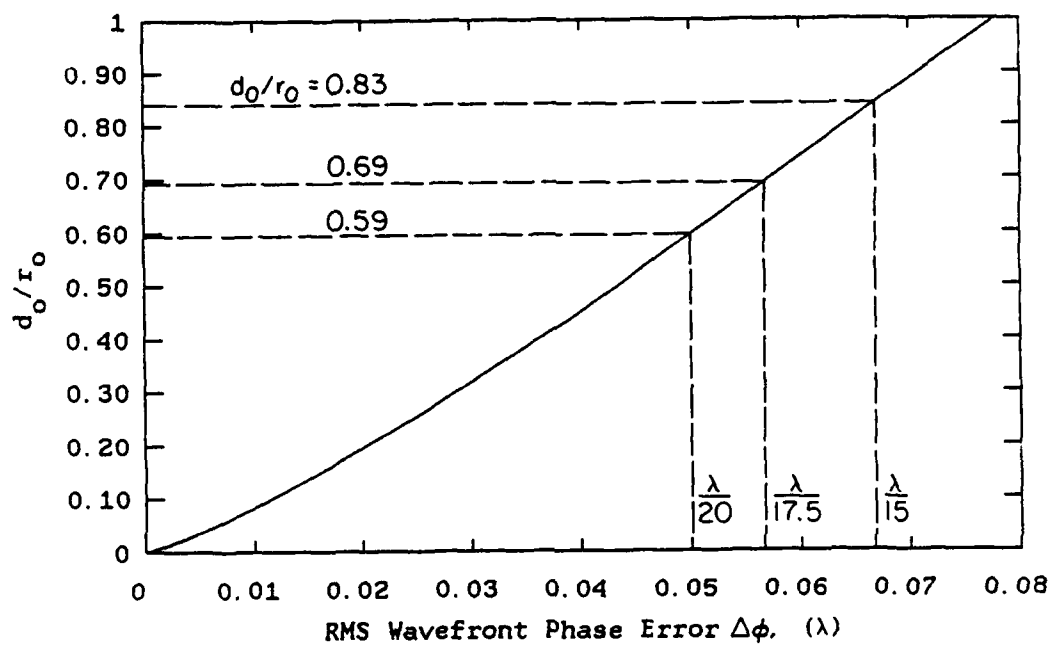


Figure 2.5. Optimum subaperture diameter versus the residual RMS wave front phase error over the aperture.

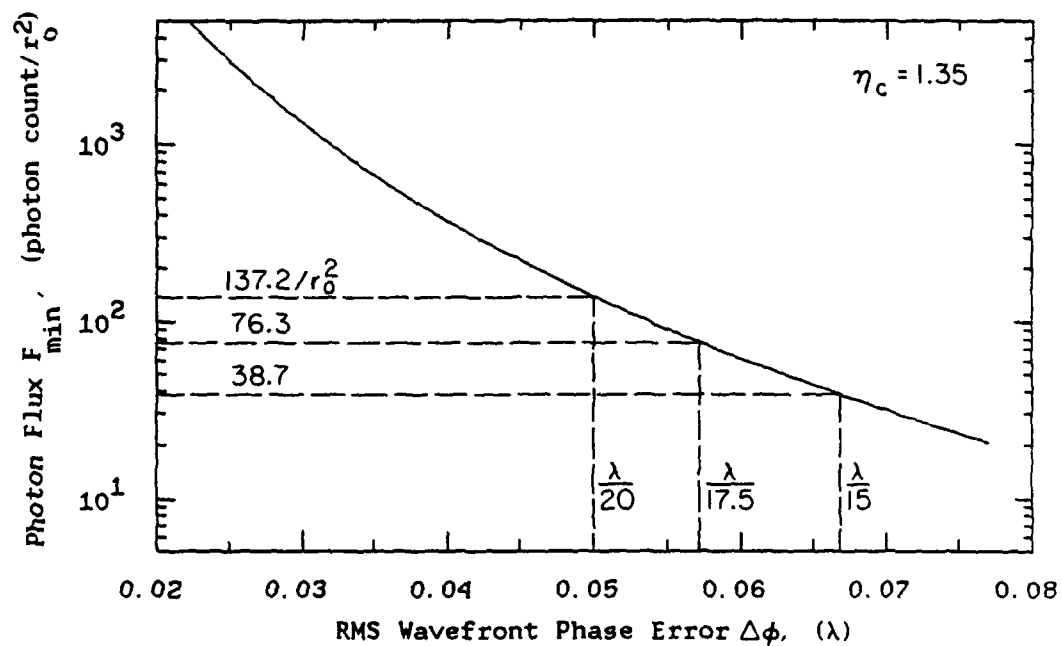


Figure 2.6. Required photon flux density (photons/ $r_0^2$ ) versus the residual RMS phase error over the aperture. The detector efficiency parameter  $\eta_c$  is assumed to be 1.35.

mesospheric Na layer. In order to perform these computations the design curves shown in Figures 2.5 and 2.6 are used to specify the subaperture size  $d$  and the required photon flux density  $F$  to achieve a desired level of imaging performance specified by  $\Delta\phi$  (or  $S(\Delta\phi)$ ). In particular we will consider three levels of imaging performance:  $\Delta\phi = \lambda/15$ ,  $\lambda/17.5$  and  $\lambda/20$ . The corresponding values of the Strehl ratio for these values of  $\Delta\phi$  are  $S(\Delta\phi) = 0.84$ ,  $0.88$ , and  $0.91$ , respectively. Table 2.1 summarizes the subaperture size and photon flux density requirements for the three performance levels. In addition to the design curves giving  $d_0$  and  $F_{min}$ , the number of required subapertures over the telescope pupil is also of interest. Using the subaperture size specified by Equation (2.22), the approximate number of subapertures required to fully sample the telescope pupil  $N_{s.a.}$  is given by

$$N_{s.a.} \sim \frac{D^2}{d_0^2} = \frac{2.17 \times 10^{-3} D^2}{r_0^2 (\Delta\phi/\lambda)^{12/5}} \quad (2.24)$$

where  $\Delta\phi \leq \lambda/12.9$ . Figure 2.7 illustrates a plot of  $N_{s.a.}$  as a function of  $D/r_0$  for the three levels of imaging performance specified in Table 2.1.

In the remainder of this section we compare the results obtained with the formulae given above to the results from a more sophisticated performance analysis technique presented by Welsh and Gardner in Reference 6 and summarized in Chapter 3. They consider a wavefront correction system consisting of an aperture, a deformable mirror, a

Table 2.1

Optimum Design Parameters and Expected Performance for the  
Wavefront Sensor and Adaptive Mirror

Design Parameters		Simplified Analysis		Simulated Performance <sup>6</sup> (Welsh and Gardner)		
Optimum Subaperture Size $d_o$	Photon Flux Density $F_{min}$	RMS Phase Variation $\Delta\phi$ (m)	Strehl Ratio $S(\Delta\phi)$	RMS Phase Variation $\Delta\phi$ (m)	Strehl Ratio $S(\Delta\phi)$	FWHM Resolution
$0.83r_o$	$38.7/r_o^2$	$\lambda/15.0$	0.84	$\lambda/9.35$	0.64	$0.98\lambda/D$
$0.69r_o$	$76.3/r_o^2$	$\lambda/17.5$	0.88	$\lambda/11.1$	0.73	$0.95\lambda/D$
$0.59r_o$	$137.2/r_o^2$	$\lambda/20.0$	0.91	$\lambda/14.3$	0.82	$0.90\lambda/D$

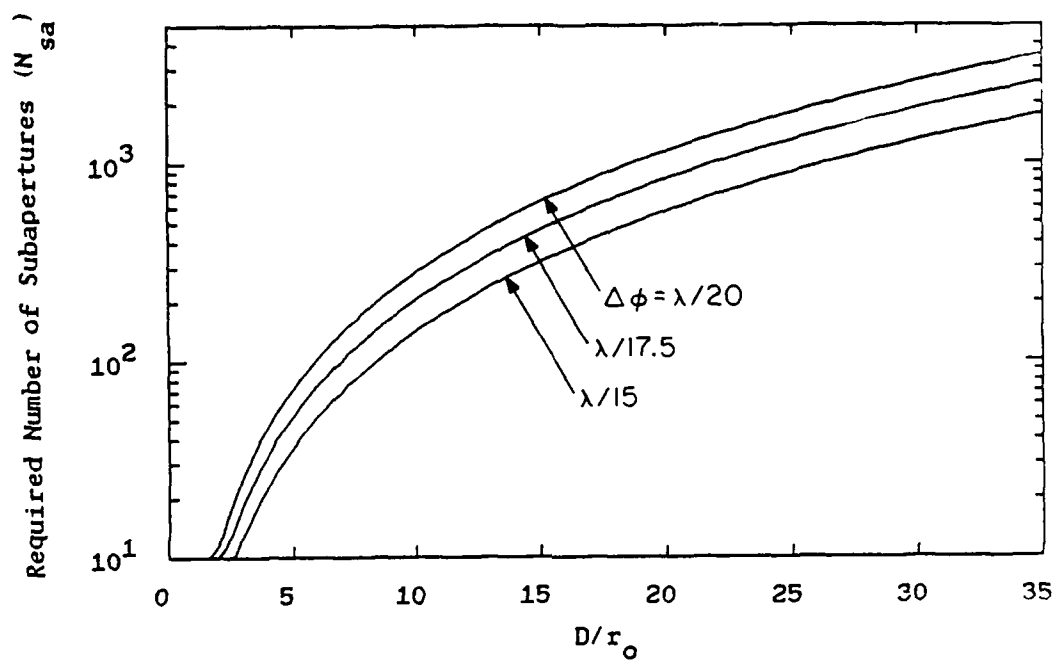


Figure 2.7. Required number of subapertures versus telescope diameter for three values of  $\Delta\phi$ :  $\lambda/15$ ,  $\lambda/17.5$ , and  $\lambda/20$ .

wavefront sensor and a control law. The mirror surface is controlled by a finite number of actuators which can effect zonal or modal surface deformations. The aperture is segmented into subapertures, and the wavefront sensor measures the average wavefront slope within each. The control law uses the measured wavefront slope information to position the actuators of the deformable mirror. In contrast to the simple analysis presented above, this analysis incorporates realistic models of both the wavefront sensor and deformable mirror. The analysis also takes into account the statistical correlations of the subaperture tilt measurements, as well as the influence of the mirror actuator deformations over adjacent subapertures. Consider a wavefront sensor configuration such as that shown in Figure 2.8. The square aperture has a dimension  $D$ . The wavefront phase slope is sensed in both the  $x$  and  $y$  directions within square subapertures of dimension  $d$ . The tilt measurement accuracy for a subaperture slope sensor is described by an expression nearly identical to Equation (2.2).<sup>6</sup> The deformable mirror is modeled with Gaussian deformations having an influence radius  $d$ . The influence radius corresponds, in this case, to the  $e^{-1}$  points on the Gaussian deformation. The mirror actuators are located at positions corresponding to the corners of the subapertures. A control algorithm uses a linear combination of the sensor measurements to drive the mirror actuators. The optimum drive signals are computed by minimizing the mean-square difference between the actual wavefront phase and the reconstructed wavefront phase.

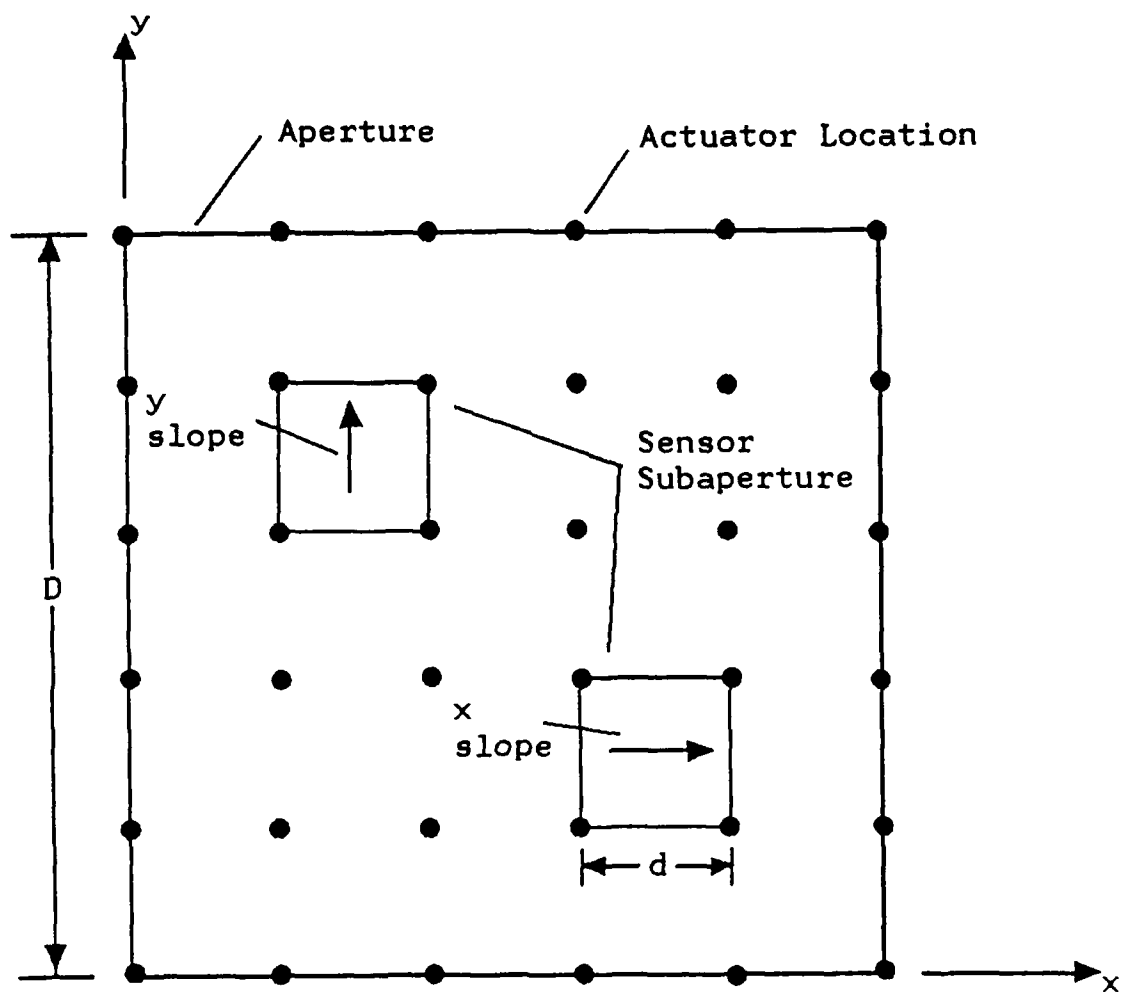


Figure 2.8. Wavefront sensor and mirror actuator configuration.



Figure 2.9 illustrates a plot of the average residual phase error over the corrected aperture as a function of photon flux density. The subaperture size ranges from  $d = 0.83r_0$  to  $0.59r_0$  (corresponding to the sizes given in Table 2.1) and  $D = 4d$ . As the photon count increases, the effects of the slope measurement noise become negligible and the errors introduced by the finite actuator and sensor spacing establish the minimum possible phase error. In all three cases  $\Delta\phi$  begins to asymptotically approach its minimum value in the 100 to 200 photon count range. Consider the required flux levels listed in Table 2.1 for the cases of  $d = 0.83r_0$ ,  $0.69r_0$  and  $0.59r_0$ . The corresponding values of  $\Delta\phi$  found from Figure 2.9 are  $\sim \lambda/9.3$ ,  $\lambda/11.1$ , and  $\lambda/14.3$ . Note that these values of  $\Delta\phi$  are slightly larger than those given by the simplified analysis in Table 2.1. The error is larger for two reasons. First, the analysis presented above is for circular subapertures of diameter  $d$ , whereas the subapertures in Figure 2.9 are square of dimension  $d$ . The residual phase variation for a tilt corrected circular aperture is smaller than the corresponding value for tilt corrected square aperture. Second, the limited response of the deformable mirror is realistically modeled in Welsh and Gardner's analysis, whereas the deformable mirror is assumed ideal in the analysis presented above. Inherent in the simplified analysis is the assumption that the phase variation over the entire aperture is equal to the phase variation of a tilt corrected subaperture. Due to the limitations of the deformable mirror this assumption will not be true for any system consisting of more than one subaperture. Finally note that the results presented in Figure 2.9 are for a fixed aperture size,

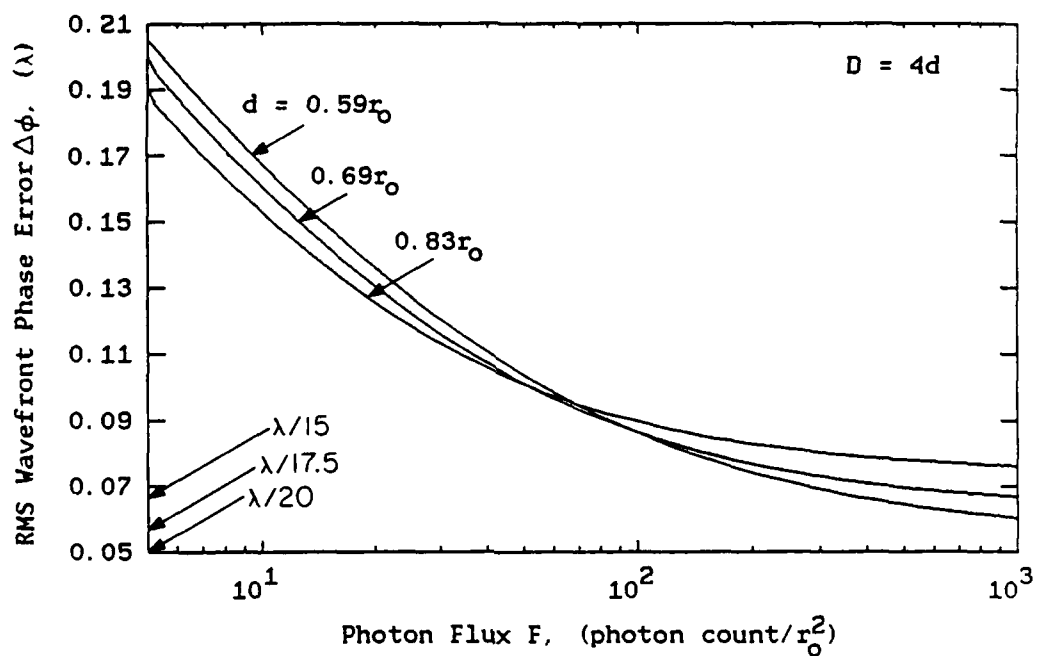


Figure 2.9. RMS residual phase error versus photon flux (photons/ $r^2$ ) for the wave front sensor and mirror configuration shown in Figure 2.8. The aperture size is  $D=4d$  and the subaperture size takes on values of  $d = 0.83r_0$ ,  $0.69r_0$  and  $0.59r_0$ .

$D = 4d$ . Welsh and Gardner also investigate other aperture sizes. They show that  $\Delta\phi$  is nearly independent of  $D$  for photon count levels greater than  $\sim 100$ . This photon count range corresponds to the range in which the slope measurement noise becomes negligible, and the errors introduced by the finite actuator and sensor spacing establish the minimum possible phase error.

In addition to the residual phase error, Welsh and Gardner<sup>6</sup> also present analysis techniques for investigating performance in terms of the OTF, PSF, and Strehl ratio. Figures 2.10 and 2.11 illustrate the ensemble average OTF and PSF for the phase corrected aperture shown in Figure 2.8. In Figure 2.10 the magnitude of the OTF is plotted versus  $\rho_x/D$  where  $\rho_x$  is related to spatial frequency  $\nu_x$  (cycles/m) by  $\nu_x = \rho_x/\lambda f_D$  and  $f_D$  (m) is the focal length of the telescope primary. The  $\rho_x$  direction corresponds to the x-direction in Figure 2.8. For this plot  $d = 0.69r_0$  and  $D = 4d$ . Each curve corresponds to a photon flux ranging from  $10/r_0^2$  to  $500/r_0^2$ . The uppermost curve is the OTF of the unaberrated system. The bottom-most curve is the OTF for the aberrated system assuming no wavefront correction. Even for flux levels as low as  $10/r_0^2$  the improvement in the OTF response is substantial. Figure 2.11 illustrates the corresponding one-dimensional (1D) PSFs for the OTF's illustrated in Figure 2.10. The 1D PSF is calculated by taking the Fourier transform of the 1D cross section of the OTF<sup>6</sup> (as shown in Figure 2.10). The amplitude of the 1D PSF is plotted versus the dimensionless quantity  $uD/\lambda f_D$ , where  $u$  is the image plane coordinate. One-dimensional PSFs are also shown for the unaberrated and aberrated

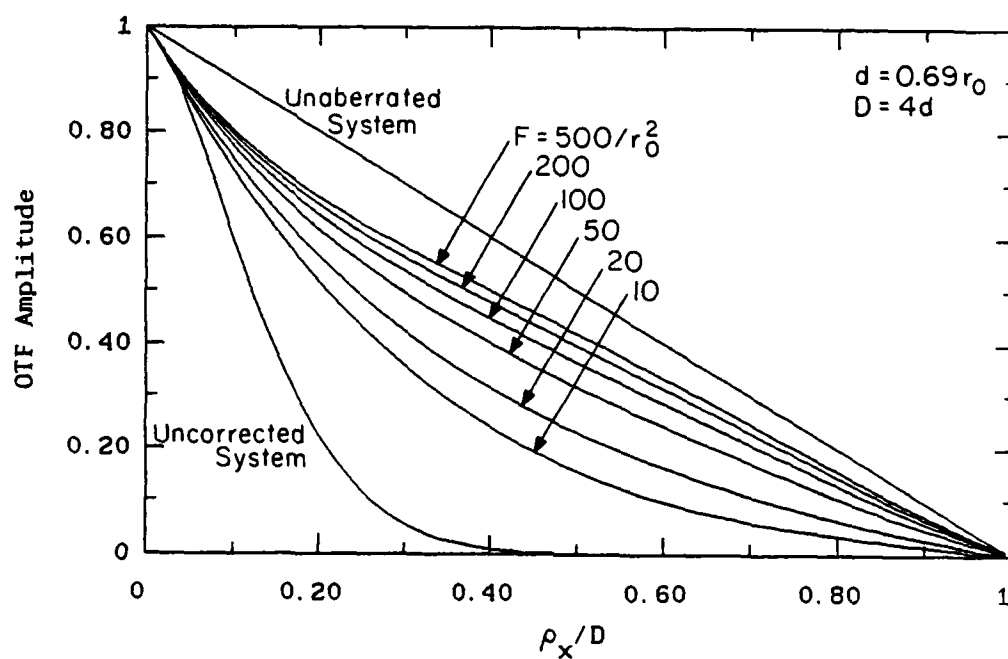


Figure 2.10. Ensemble average OTF for the wavefront sensor and mirror configuration shown in Figure 2.8. The photon flux ranges from  $10/r_0^2$  to  $500/r_0^2$ . The aperture size is  $D = 4d$  and the subaperture size is  $d = 0.69r_0$ .

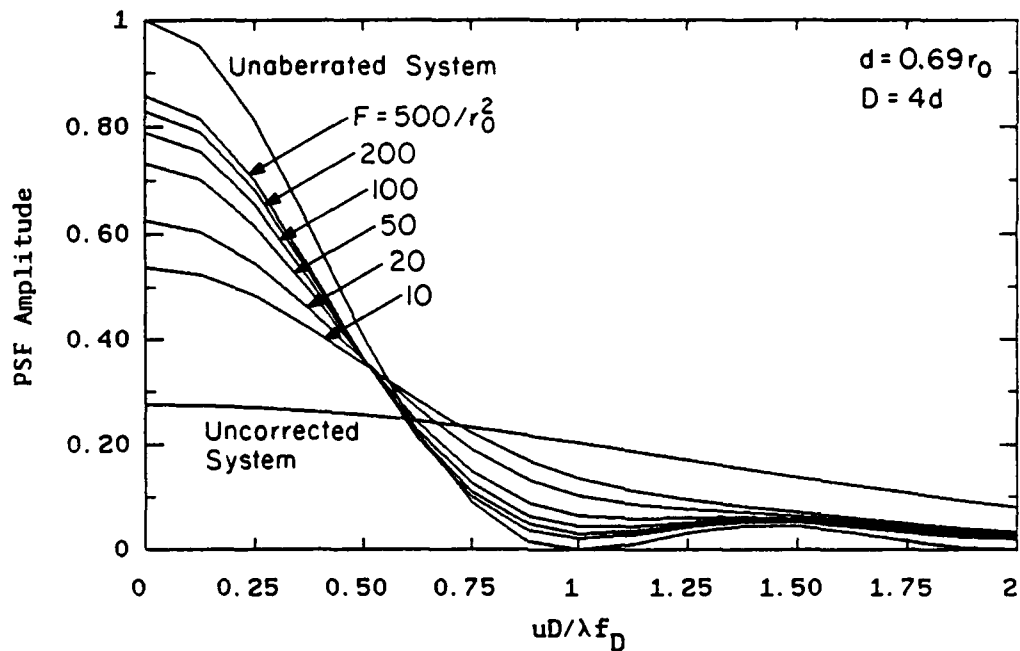


Figure 2.11. One-dimensional ensemble average PSF for the wave front sensor and mirror configuration shown in Figure 2.8. The photon flux ranges from  $10/r_0^2$  to  $500/r_0^2$ . The aperture size is  $D=4d$  and the subaperture size is  $d = 0.69r_0$ .

systems. These curves again indicate the substantial improvement in performance even for a flux as low as  $10/r_0^2$ . It is also interesting to note that resolution, as measured by the FWHM of the 1D PSF main lobe, does not rapidly degrade from that of the unaberrated system for decreasing photon flux levels. Figure 2.12 illustrates a plot of angular resolution as a function of photon flux for subaperture sizes of  $d = 0.83r_0$ ,  $0.69r_0$ , and  $0.59r_0$ . The angular resolution is normalized by the FWHM angular resolution of the unaberrated system. The FWHM angular resolution is found to be  $0.88\lambda/D$  from the unaberrated PSF shown in Figure 2.11 (recall this value is calculated from the 1D PSF). Even for a flux as low as  $10/r_0^2$  and  $d = 0.69r_0$ , the resolution is only 1.47 times worse than that possible for diffraction limited imaging. The Strehl ratio, on the other hand, shows considerable degradation in performance as the photon noise level increases.

The Strehl ratio is calculated by substituting the values of  $\Delta\phi$  shown in Figure 2.9 into Equation (2.15). Figure 2.13 is a plot of the Strehl ratio versus photon flux. The ratio shows a significant decrease as the flux decreases. For the case of  $d = 0.69r_0$ , the ratio drops from a value of  $\sim 0.83$  for  $1000 \text{ counts}/r_0^2$  to  $\sim 0.66$  for  $50 \text{ counts}/r_0^2$ .

Consider an adaptive telescope design based on a subaperture size  $d$  of  $0.69r_0$  and a required photon flux density  $F$  of  $76.3/r_0^2$ . These two requirements correspond to an imaging performance of  $\Delta\phi = \lambda/17.5$  as

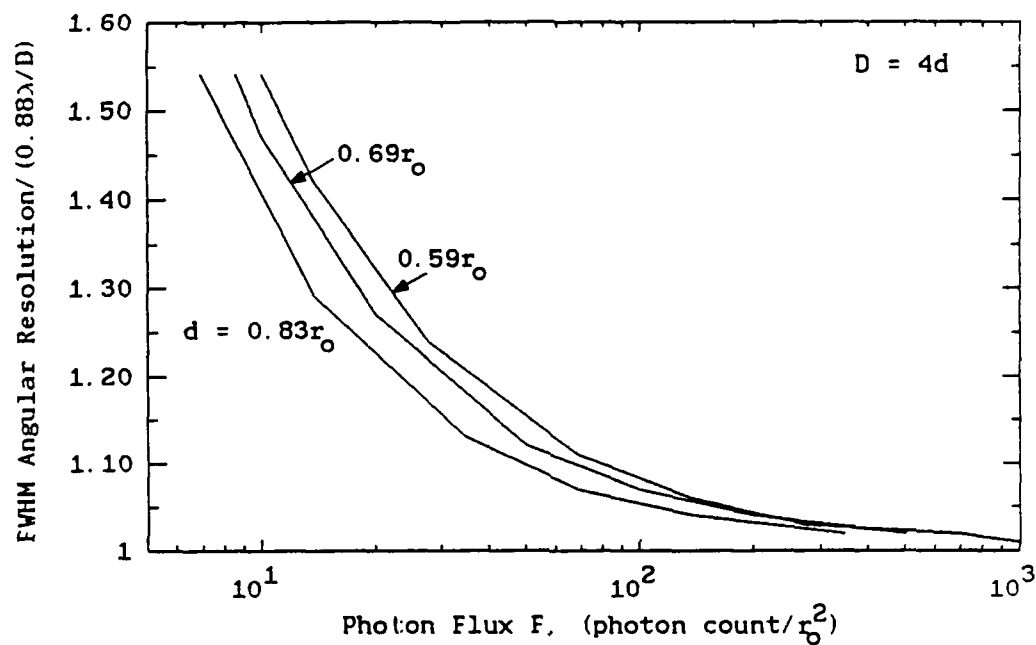


Figure 2.12. Normalized FWHM angular resolution versus photon flux (photons/r<sub>0</sub><sup>2</sup>). The resolution is normalized by the FWHM angular resolution of the unaberrated system. Curves are shown for three values of d: 0.83r<sub>0</sub>, 0.69r<sub>0</sub> and 0.59r<sub>0</sub>.

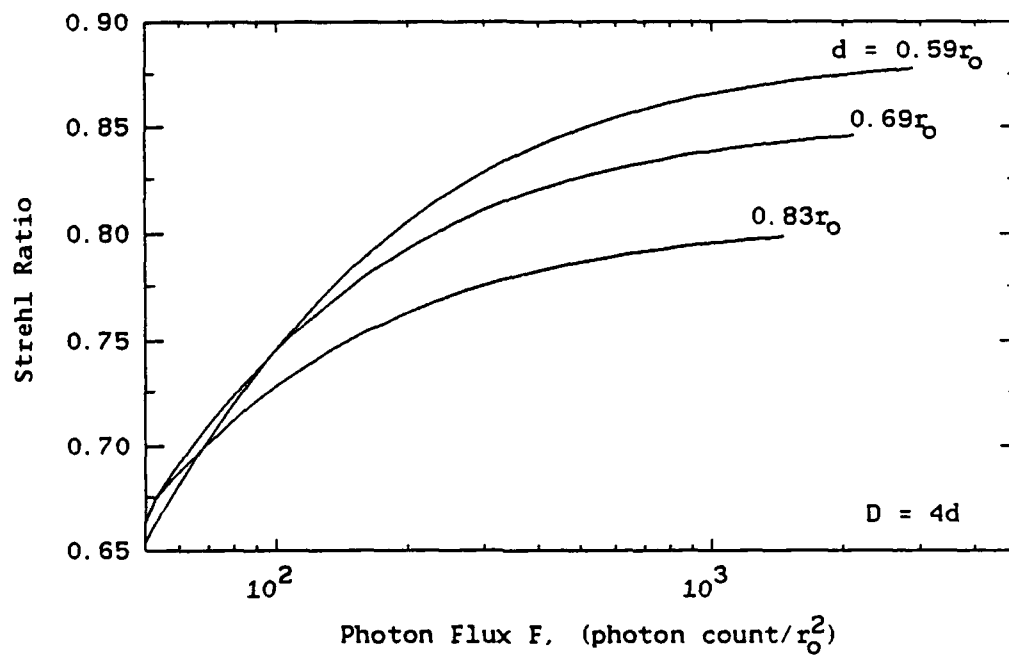


Figure 2.13. Strehl ratio versus photon flux (photons/ $r_0^2$ ). Curves are shown for three values of  $d_0$ :  $0.83r_0$ ,  $0.69r_0$  and  $0.59r_0$ .



predicted by the simplified analysis in Equation (2.20). For the wavefront sensor and deformable mirror shown in Figure 2.8, Welsh and Gardner's<sup>6</sup> analysis technique shows that the average residual wavefront phase error over the aperture will be  $\sim \lambda/11.1$  and the Strehl ratio will be  $\sim 0.73$ . Additionally, the resolution of the system, as measured by the FWHM of the 1D PSF, will be  $\sim 1.09$  times that of the unaberrated system. Table 2.1 summarizes the performance predictions obtained from the simplified analysis technique and those obtained from Welsh and Gardner's<sup>6</sup> analysis technique for each of the listed subaperture sizes and flux requirements.

In Sections 2.4 and 2.5 we address the design of laser guide star systems based on Rayleigh scattering in the stratosphere and on resonance scattering in the mesospheric Na layer. We use the results from this section as a starting point for computation of the laser power requirements.

## 2.4 Rayleigh Laser Guide Stars

Laser guide stars can be created by Rayleigh scattering off air molecules in the stratosphere. This problem is discussed in detail by Thompson and Gardner.<sup>31</sup> One of the principal advantages of Rayleigh guide stars is that lasers can be purchased today with many of the required characteristics. These characteristics include 1) pulsed operation with repetition rates up to 200 pulses per second, 2) high average output power, 3) excellent beam quality, and 4) long term reliability. In particular, excimer lasers have these characteristics

and would be ideal for producing Rayleigh guide stars in the lower atmosphere.

For a given laser energy the brightness of a Rayleigh guide star is proportional to the density of the atmosphere within the illuminated volume. Because atmospheric density decreases exponentially with altitude, Rayleigh guide stars must be produced at a relatively low altitude. Consider the geometry of the laser projection telescope and the laser light path shown in Figure 2.14. If the laser energy is focused at a height of  $z_g$  above the telescope entrance pupil, the beam diverges for altitudes above and below  $z_g$ . To insure that the size of the guide star is equal to  $\Delta\alpha$ , the wavefront sensor must be gated so that only the backscattered energy from the altitude region  $\Delta z$  is sampled by the wavefront sensor. From the geometry shown in Figure 2.14 the maximum allowable scattering layer thickness is<sup>31</sup>

$$\Delta z = \Delta z_u + \Delta z_L = \frac{2 \Delta\alpha z_g^2 / D_p}{[1 + (z_g \Delta\alpha / D_p)^2]}, \quad (2.25)$$

where  $\Delta z_u$  and  $\Delta z_L$  are defined in Figure 2.14 and  $D_p$  is the projection telescope diameter. Assume  $\Delta\alpha$  takes on a value equivalent to the angular size of a natural guide star as given in Equation (2.3). Using the fact that  $\Delta\alpha$  is small, Equation (2.25) can be approximated by

$$\Delta z = \frac{4.88 \lambda z_g^2}{D_p r_o}. \quad (2.26)$$

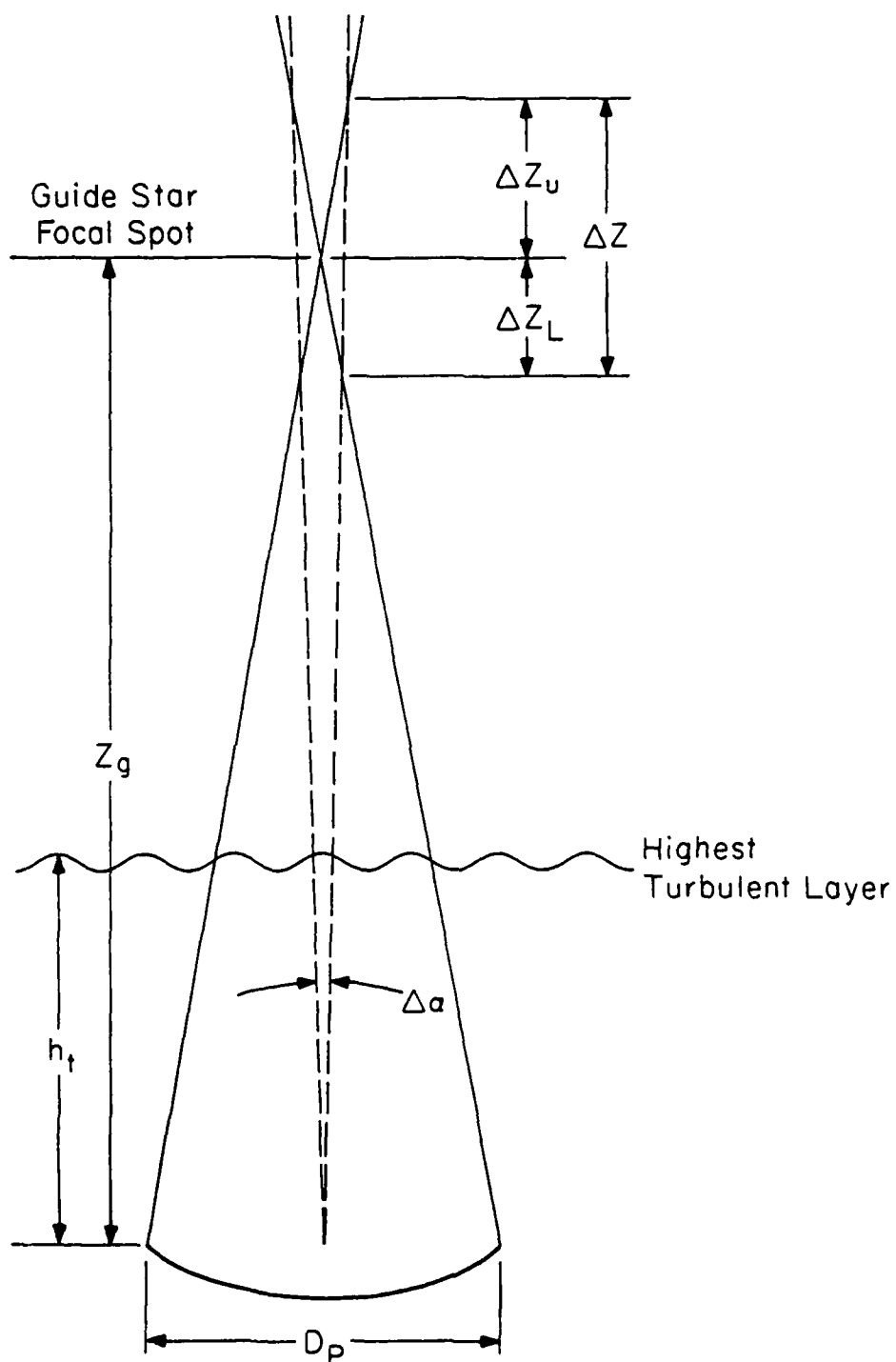


Figure 2.14. Geometry of the telescope and laser light path.

The detected Rayleigh photon flux density  $F$  from an atmospheric layer of thickness  $\Delta z$  is given by the lidar equation<sup>32, 36</sup>

$$F = \eta T_A^2 \frac{\sigma_R n_R(z_g + z_t) \Delta z}{4 \pi z_g^2} \frac{\lambda_L E}{h c}, \quad (2.27)$$

where  $\eta$  = efficiency of telescope and detector,  
 $T_A$  = one-way atmospheric transmission,  
 $\sigma_R$  = Rayleigh backscatter cross section ( $m^2$ ),  
 $z_g$  = height of the focused guide star above the telescope entrance plane (m),  
 $z_t$  = altitude of the telescope entrance plane above sea level (m),  
 $n_R(z)$  = atmospheric density at altitude  $z$  ( $m^{-3}$ ),  
 $E$  = laser energy per pulse (J),  
 $\lambda_L$  = optical wavelength of the laser (m),  
 $h$  = Planck's constant,  $6.63 \times 10^{-34}$  (J s),  
 $c$  = speed of light,  $3 \times 10^8$  (m/s).

Note that the value of  $\lambda_L$  is different from the value of the observation wavelength  $\lambda$ . The product of the Rayleigh backscatter cross section  $\sigma_R$  and the atmospheric density  $n_R$  is<sup>32, 36</sup>

$$\sigma_R n_R(z) = 3.6 \times 10^{-31} \frac{P(z)}{T(z)} \lambda_L^{-4.0117}, \quad (2.28)$$

where  $P(z)$  = atmospheric pressure at altitude  $z$  (mbar),  
 $T(z)$  = atmospheric temperature at altitude  $z$  (K).

Substituting Equation (2.26) for  $\Delta z$  into Equation (2.27) and solving for the required laser pulse energy  $E$  gives

$$E = \frac{2.58 h c F D_p r_o}{\eta T_A^2 \lambda \lambda_L \sigma_R n_R(z_g + z_t)}, \quad (2.29)$$

where  $D_p$  is the diameter of the laser projection aperture which need not correspond to the full aperture of the telescope. Since  $E$  is directly proportional to  $D_p$ , it should be chosen to be as small as possible. However,  $D_p$  must be large enough that the guide star centroid is reasonably stable, as discussed in Section 2.1. We assume

$$D_p \approx 5 r_o. \quad (2.30)$$

Substituting Equation (2.30) into Equation (2.29) gives

$$E = \frac{12.88 h c F r_o^2}{\eta T_A^2 \lambda \lambda_L \sigma_R n_R(z_g + z_t)}. \quad (2.31)$$

The energy requirement  $E$  is for a single guide star. For multiple guide stars Equation (2.31) must be multiplied by the required number of guide stars  $N_{gs}$  given in Equation (2.14):

$$E_T = \frac{12.88 h c F D^2 h_t^2}{\eta T_A^2 \lambda \lambda_L \sigma_R z_g^2 n_R(z_g + z_t)}, \quad (2.32)$$

where  $E_T$  is the total required energy to create  $N_{gs}$  stars. For an optimum wavefront sensor design, the subaperture size  $d$  will be given by  $d_o$  in Equation (2.22), and the required photon flux density  $F$  will

be given by  $F_{min}$  in Equation (2.23). Substituting  $F_{min}$  into Equation (2.32) gives

$$E_T = \frac{1.83 \times 10^{-3} \eta_c^2 h c D^2 h_t^2}{r_o^2 (\Delta\phi/\lambda)^{22/5} \eta T_A^2 \lambda \lambda_L \sigma_R z_g^2 n_R(z_g + z_t)}. \quad (2.33)$$

Equation (2.33) gives the total required energy  $E_T$  per atmospheric sampling time. Note that  $E_T$  is inversely proportional to  $r_o^2$ . This dependence highlights the importance of choosing an observatory site with good seeing in order to minimize the required laser pulse energy.

In the stratosphere, the atmospheric density decreases approximately exponentially with increasing altitude

$$\sigma_R n_R \propto e^{-z/H}, \quad (2.34)$$

where  $H$  is the atmospheric scale height.  $H$  is given approximately by

$$H \approx 30 T \text{ (meters)}, \quad (2.35)$$

where  $T$  is the atmospheric temperature in  $^{\circ}\text{K}$ . The temperature of the stratosphere varies geographically and seasonally but is typically on the order of  $200^{\circ}\text{K}$  so that  $H \sim 6 \text{ km}$ . From Equations (2.33) and (2.34) we see that the required pulse energy can be minimized by maximizing the expression

$$z_g^2 \exp[-(z_g + z_t)/H]. \quad (2.36)$$

The laser pulse energy is minimized for a guide star height of  $z_g = 2H = 12 \text{ km}$ . Note that  $z_g$  must be selected so that the majority of the

turbulence occurs at altitudes less than  $(z_g + z_t) - \Delta z_L$  to insure effective wavefront compensation.

For an excimer laser operating at a wavelength of  $\lambda_L = 351$  nm, the approximate value of  $\sigma_R n_R(z)$  as a function of altitude is given by

$$\sigma_R n_R(z) \approx 2 \times 10^{-4} \exp(-z/H). \quad (2.37)$$

By substituting Equation (2.37) into Equation (2.33) and assuming the typical atmospheric and laser parameters listed in Table 2.2, we are able to compute the required pulse energy  $E_T$  as a function of the imaging performance specified by  $\Delta\phi$ . Figure 2.15 is a plot of  $E_T$  versus  $\Delta\phi$  for a telescope diameter  $D$  of 2m and  $r_o = 10, 20$ , and 30 cm. Figure 2.16 is a plot of  $E_T$  versus  $D/r_o$  for a constant value of  $\Delta\phi = \lambda/17.5$ . Consider, for example, the following parameter values:  $\Delta\phi = \lambda/17.5$ ,  $D = 2$  m, and  $r_o = 20$  cm. For these conditions the total required pulse energy  $E_T$  is 330 mJ/cycle. According to Equation (2.14) this energy is divided among 69 guide stars. The amount of energy sent to each guide star per cycle is  $\sim 4.8$  mJ. If the atmospheric sampling rate is 100 Hz, the total laser power required is 33 W.

The calculations given above are for a zenith pointing guide star. As the guide star is pointed away from zenith, the energy requirement increases due to increasing propagation path loss, decreasing atmospheric transmission and decreasing  $r_o$ . From straightforward geometrical considerations we find that the factor increase in the required pulse energy as a function of zenith angle  $\theta$  is

Table 2.2

Assumptions for the Rayleigh Laser Guide Star  
Pulse Energy Calculations

**ATMOSPHERE:**


---

Atmospheric transmission, $T_A$	0.4
Turbulence layer height, $h_t$	10 km
Atmospheric scale height, $H$	6 km
Optimal guide star height, $z_g$	12 km
Telescope entrance plane altitude, $z_t$	2 km
$\sigma_R n_R(z)$	$2 \times 10^{-4} \exp(-z/H)$

**LASER AND RECEIVER SYSTEM:**

Observation wavelength, $\lambda$	500 nm
Laser wavelength, $\lambda_L$	351 nm
Laser pulse repetition rate	100 Hz
Overall optical efficiency, $\eta$	7.5 %
Centroid detector efficiency factor, $\eta_c$	1.35



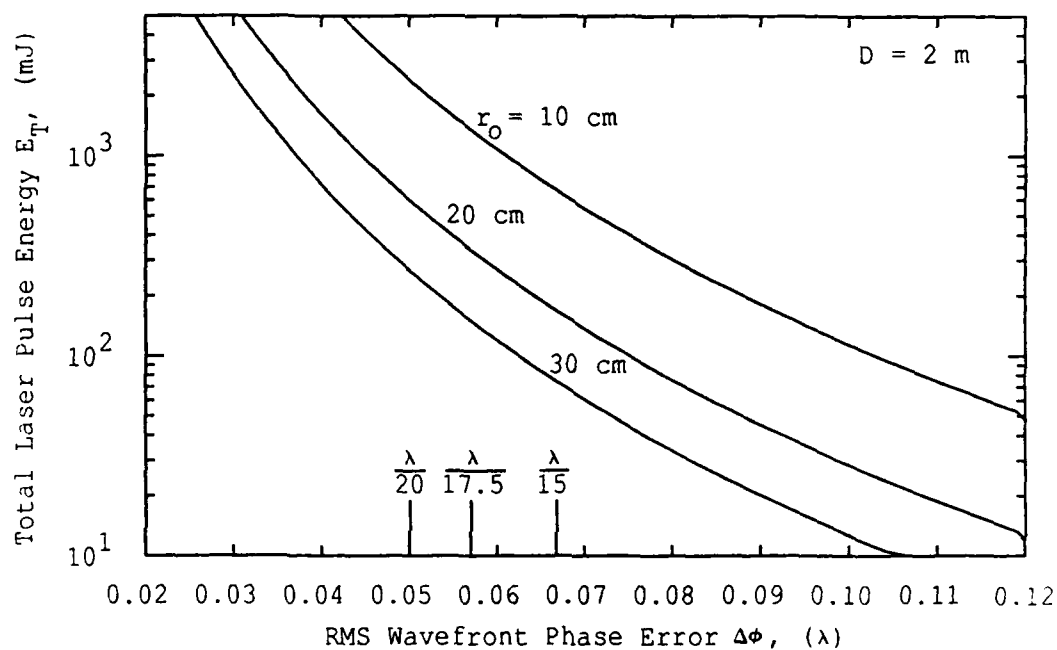


Figure 2.15. Total Rayleigh laser pulse energy requirements versus the residual RMS phase error over the aperture. Curves are shown for  $r_0 = 10$  cm, 20 cm and 30 cm. The aperture diameter is assumed to be 2 m.

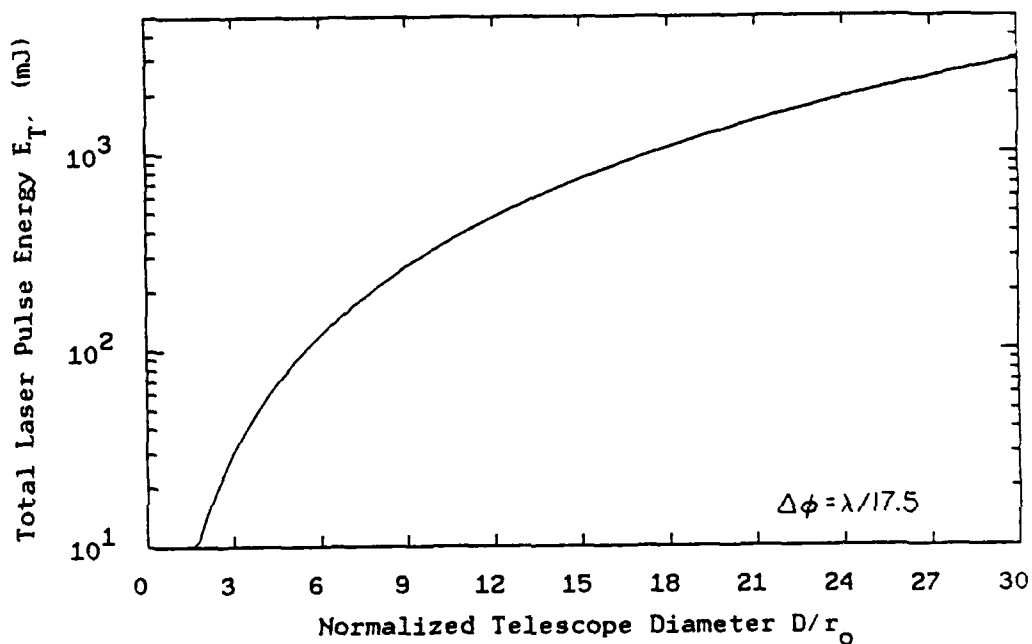


Figure 2.16. Total Rayleigh laser pulse energy requirements versus the normalized telescope diameter. The residual RMS phase error over the aperture is assumed to be  $\lambda/17.5$ .

$$\frac{E_T(\theta)}{E_T(0)} = \exp\left[-2\sigma_d\left(1 - \frac{1}{\cos\theta}\right)\right] \frac{1}{(\cos\theta)^{12/5}} \quad (2.38)$$

where  $E_T(\theta)$  is the required pulse energy as a function of  $\theta$ , and  $\sigma_d$  is the optical depth of the lower atmosphere. Atmospheric transmission  $T_A(\theta)$  is related to optical depth by  $T_A(\theta) = \exp(-\sigma_d/\cos\theta)$ . Equation (2.38) is derived assuming the laser projection aperture diameter  $D_p$  and the guide star angular width  $\Delta\alpha$  are held constant as a function of zenith angle. Equation (2.38) is plotted in Figure 2.17 as a function of zenith angle for  $T_A(0) = 0.4$ . For astronomical observing at zenith angles out to 30 degrees the factor increase in the required pulse energy is 1.88. At this angle the total required pulse energy  $E_T$  increases to 622 mJ/cycle, which corresponds to a laser power of 62 W at 100 pps. By substituting  $r_o(\theta)$  given by Equation (2.5) into the expression for  $N_{gs}$  given by Equation (2.14) we find the number of guide stars required increases to  $\sim 82$ .

The feasibility of using Rayleigh guide stars is dependent on the availability of lasers powerful enough to create the guide stars and on our ability to create a large array of stars. Available today are commercial excimer lasers which can deliver the output power required to produce zenith guide stars for telescopes of 2 m diameter or smaller.<sup>31</sup> Since the laser power requirements scale with the square of the telescope aperture, larger telescopes may require a multiple laser system.

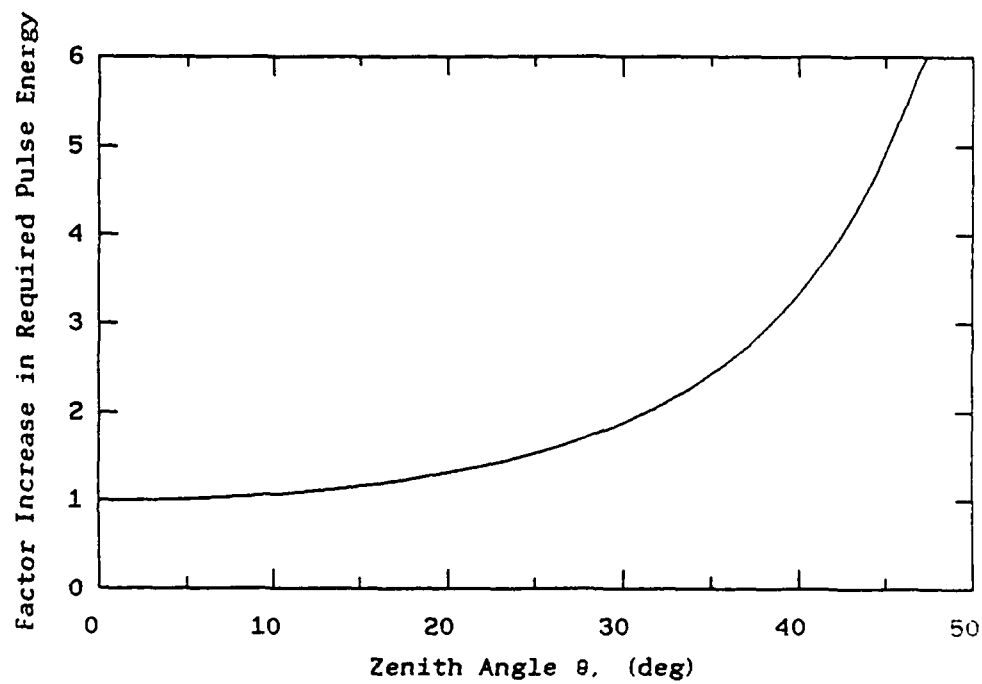


Figure 2.17. Factor increase of the Rayleigh pulse energy requirements versus zenith angle.

## 2.5 Sodium Resonance Fluorescence Laser Guide Stars

The mesospheric Na layer provides an excellent scattering medium for the creation of laser guide stars because of its high altitude and its large resonant backscattering coefficient. The layer was discovered in the late 1920s and has been explored extensively since the late 1960s with lidar techniques. The Na layer is believed to be created by meteoric ablation, and depleted at its lower boundary by chemical processes. The layer lies at a mean altitude of 92 km, and its average thickness is about 10 km FWHM. The Na column density varies on both diurnal and annual time scales. The column abundance at mid-latitudes in the Northern Hemisphere shows a summer minimum of about  $3 \times 10^9 \text{ cm}^{-2}$  and a winter maximum of about  $10^{10} \text{ cm}^{-2}$  in December and January. The seasonal and geographical variations are believed to be related to changes in mesopause temperatures that affect the main chemical reaction rates at the lower boundary of the Na layer. Diurnal variations in the Na abundance are caused primarily by the influence of atmospheric tides and gravity waves.<sup>37,38</sup> Gardner et al.<sup>32</sup> provide a good review of nocturnal and seasonal variations of the Na layer structure at Urbana, Illinois. Figures 2.18 and 2.19 illustrate the seasonal variation of the Na layer column abundance and centroid height as measured at Urbana, Illinois. Figure 2.20 is a Na density profile measured by Beatty et al.<sup>39</sup> The thin dense layer near 82 km altitude is a meteor ablation trail.

In addition to Na, numerous other atomic species are deposited in the thick layers near the mesopause by meteoric ablation. Several have

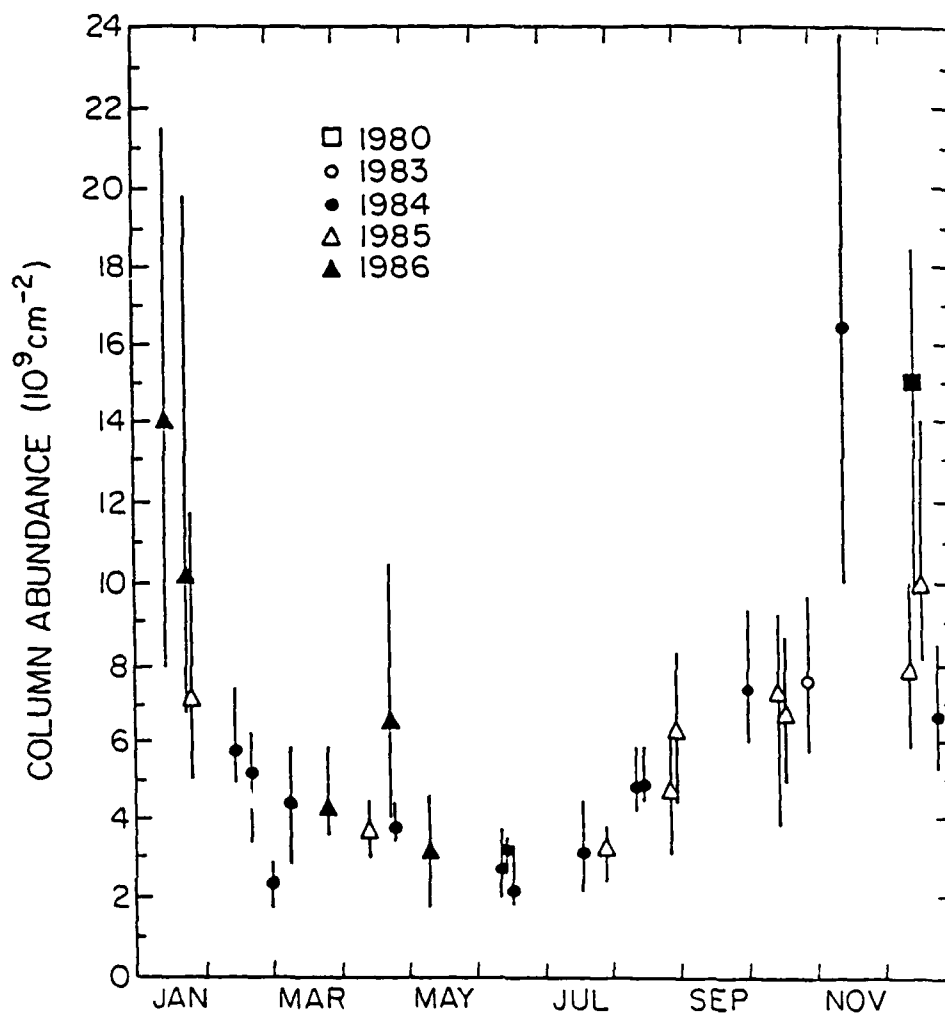


Figure 2.18. Seasonal variation of the Na layer column abundance at Urbana, Illinois. The symbol marks the average value for the night while the line represents the range of values measured during the night.

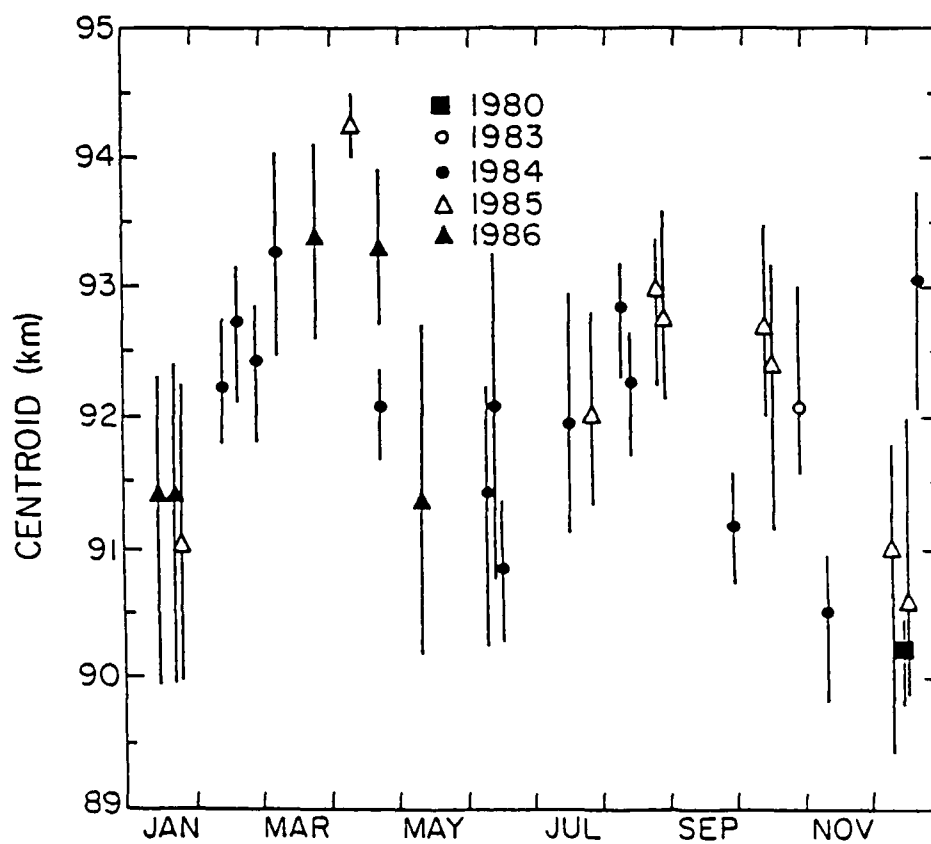


Figure 2.19. Seasonal variation of the centroid height of the Na layer at Urbana, Illinois. The symbol marks the average value for the night while the line represents the range of values measured during the night.

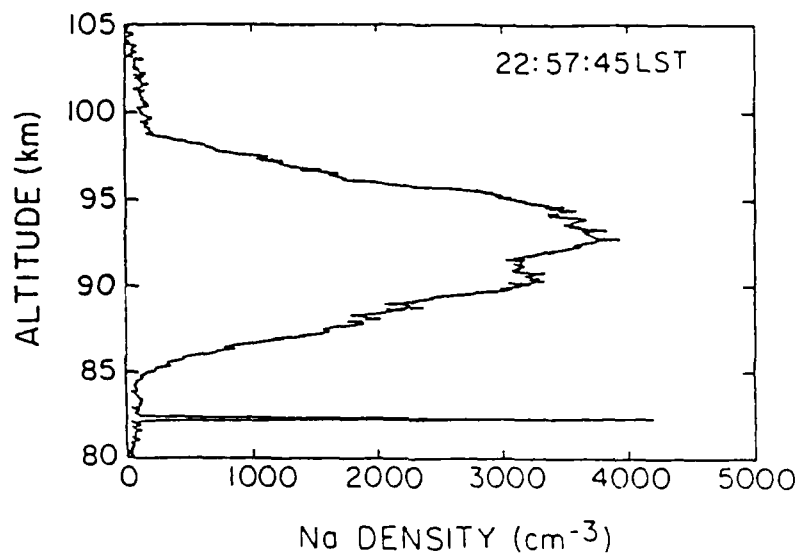


Figure 2.20. Na density profile measured by Beatty et al.<sup>39</sup> with the CEDAR lidar on March 4, 1988 at Urbana, Illinois. The integration period was 27 s and the vertical resolution was 75 m. The dense narrow layer at 82.4 km is a meteor ablation trail.



resonant backscatter cross sections in the visible and near UV wavelength region where atmospheric transmission is reasonably high and have been studied using lidar techniques. These include potassium (769.9 nm), lithium (670.8 nm), calcium (422.7 nm), aluminum (396.2 nm), calcium ions (393.4 nm), and iron (372.0 nm). However, because of the combination of lower densities and/or lower resonant backscatter cross sections, the laser pulse energies required to create sufficiently bright guide stars by scattering from these other species are significantly larger than for Na. For this reason we restrict our attention to Na laser guide stars.

In contrast to the molecular scattering of Rayleigh guide stars, the scattering mechanism for Na guide stars is resonance fluorescence scattering. The backscattered energy from the Na layer is maximized by tuning the laser to the peak of the Na D<sub>2</sub> resonance line. The Doppler broadened resonance line for the Na layer is shown in Figure 2.21 for atmospheric temperatures ranging from 150° to 500° K. At high latitudes in the northern hemisphere the mesopause temperature varies from a summer minimum of 130 to 150 K to a winter maximum of 210 to 230 K.<sup>40</sup>

The process of selecting the laser pulse energy, pulse length and linewidth to achieve the guide star brightness requirements given in Section 2.3 is not straightforward, because absorption by the Na layer is nonlinear (i.e., it saturates). Saturation arises when the energy density within the Na layer is large enough to significantly alter the

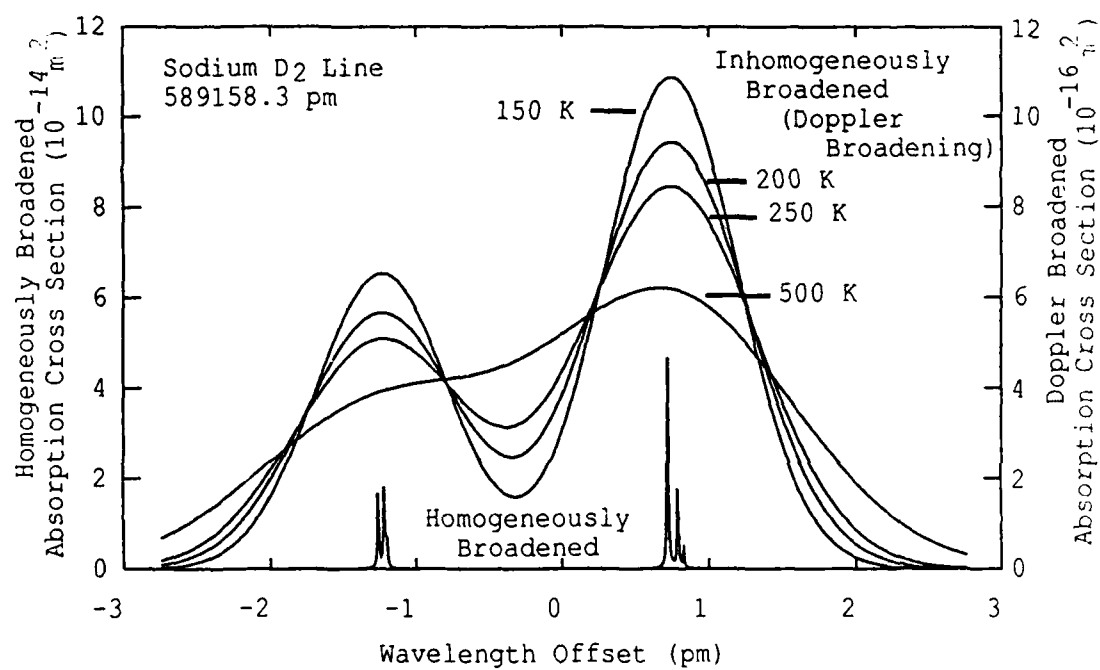


Figure 2.21. Homogeneously and inhomogeneously broadened Na D<sub>2</sub> absorption line versus wavelength.

population densities of the atomic states. In terms of a simple two-state system, a large energy density can significantly reduce the number of lower state atoms while increasing the number of excited state atoms. These altered state populations lead to nonlinear absorption of the laser energy, which results in an increased rate of stimulated emission and a reduced rate of fluorescence. The combined effect is a reduction in the backscattered energy from the guide star. To achieve the required guide star brightness, the laser pulse energy must be relatively large. This large pulse energy, in combination with the small size of the guide star, may contribute to significant saturation effects unless the laser parameters are chosen carefully. Welsh and Gardner present a thorough investigation of saturation effects for pulsed lasers in References 7 and 41. This analysis is summarized in Chapter 4. Their analysis takes into account the cross-sectional shape of the laser beam, the temporal shape of the laser pulse, the line shape of the laser, and off-zenith effects. The analysis shows that the laser design can be optimized in terms of the pulse energy, pulse length, and linewidth.

To compute the required laser characteristics we consider the laser backscattering geometry shown in Figure 2.22. The photon flux density  $F$  (photons/m<sup>2</sup>) detected from the Na layer per laser pulse is<sup>32, 36</sup>

$$F = \eta T_A^2 \frac{C_s \sigma_t}{4 \pi z_g^2} \frac{\lambda_L E}{h c}, \quad (2.39)$$

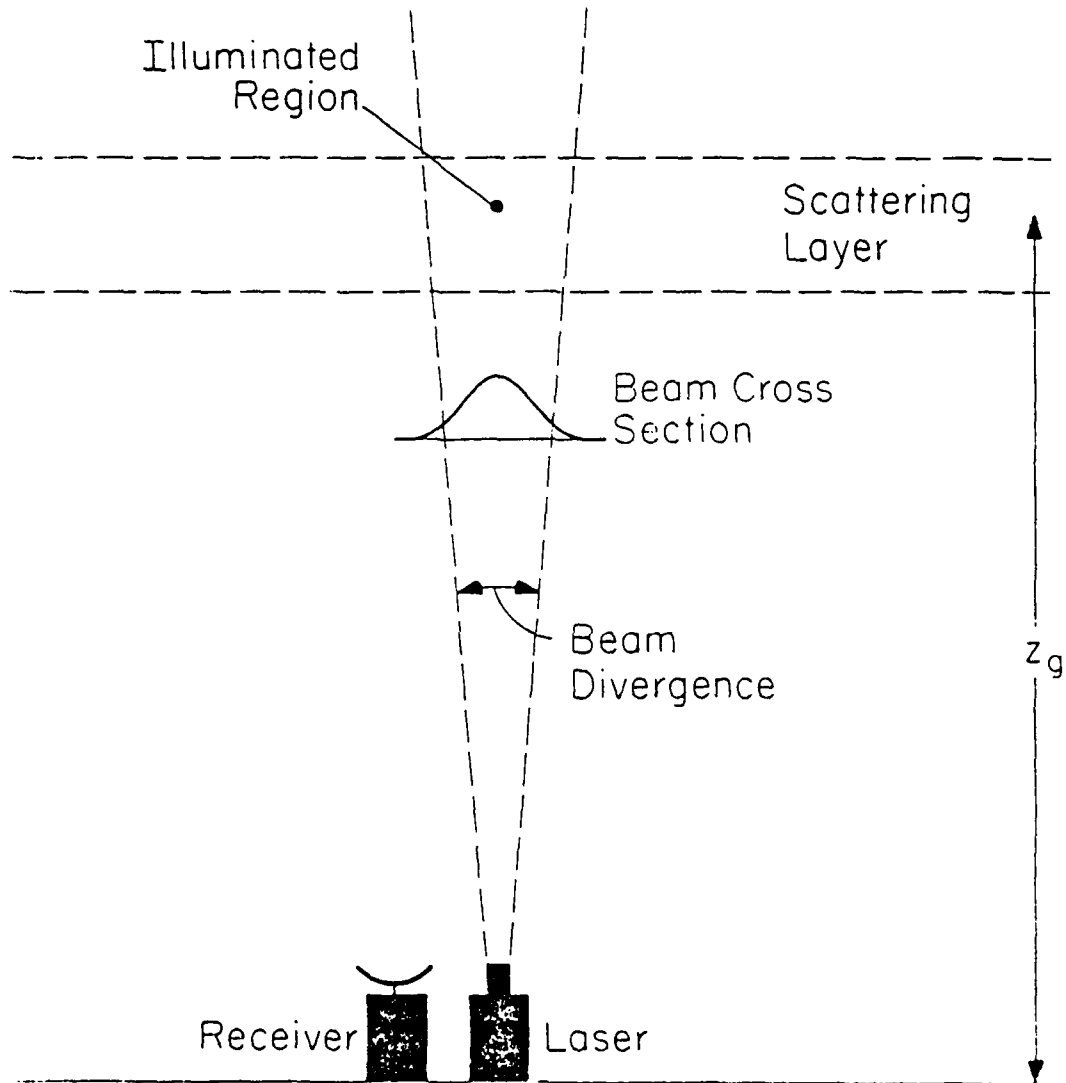


Figure 2.22. Geometry between the laser, receiver, and Na layer.

where  $\eta$  = efficiency of telescope and detector,  
 $T_A$  = one-way atmospheric transmission,  
 $\sigma_t$  = total Na backscattering cross section ( $\text{m}^2$ ),  
 $C_s$  = Na column abundance ( $\text{m}^{-2}$ ),  
 $z_g$  = height of the guide star above the telescope entrance  
 plane (m),  
 $E$  = laser energy per pulse (J),  
 $\lambda_L$  = optical wavelength of the laser (m),  
 $h$  = Planck's constant,  $6.63 \times 10^{-34}$  (J s),  
 $c$  = speed of light,  $3 \times 10^8$  (m/s).

In the case of negligible saturation the total scattering cross section  $\sigma_t$  is given by

$$\sigma_t = \int_{-\infty}^{\infty} \frac{n(\omega_d)}{n_o} \sigma_{eff}(\omega_d) d\omega_d, \quad (2.40)$$

where  $\omega_d$  = Doppler angular frequency shift associated with a given  
 atom (rad/s)  
 $n(\omega_d)$  = density of Na atoms per unit Doppler angular  
 frequency shift ( $\text{m}^{-3} \text{rad}^{-1} \text{s}$ ),  
 $n_o$  = total integrated density of Na atoms ( $\text{m}^{-3}$ ),  
 $\sigma_{eff}(\omega_d)$  = scattering cross section as a function of Doppler  
 frequency ( $\text{m}^2$ ).

The scattering cross section  $\sigma_{eff}(\omega_d)$  is a function of the natural  
 absorption spectrum of Na and the laser line shape:

$$\sigma_{eff}(\omega_d) = \int_{-\infty}^{\infty} \sigma(\omega - \omega_d) g(\omega) d\omega, \quad (2.41)$$

where  $\omega$  = angular frequency (rad/s),  
 $\sigma(\omega)$  = homogeneously broadened absorption cross section of Na  
 $(m^2)$ ,  
 $g(\omega)$  = distribution of the laser photon flux per unit angular  
frequency (rad<sup>-1</sup>s).

Figure 2.21 illustrates a plot of  $\sigma(\omega)$  for the Na resonance D<sub>2</sub> line.

In the case of saturation, we can generalize the backscattering equation given in Equation (2.39) by incorporating the effects of saturation into the calculation of a generalized scattering cross section  $\sigma_s$ . Assuming the laser beam cross section is Gaussian with an rms radius of  $\Delta\rho_{rms}$  (m), and the laser temporal pulse shape is rectangular with a length of  $\Delta t$  (s), Welsh and Gardner<sup>7</sup> find that  $\sigma_s$  is given by

$$\sigma_s = \int_{-\infty}^{\infty} \frac{\tau_s \sigma_t n(\omega_d)}{2\tau_n n_o} \ln \left( \frac{2\tau_n \sigma_{eff}(\omega_d)}{\tau_s \sigma_t} + 1 \right) d\omega_d, \quad (2.42)$$

where  $\tau_n$  is the natural decay time of Na and  $\tau_s$  is the saturation time which is defined by

$$\tau_s = \frac{2 \Delta t \pi \Delta \rho_{rms}^2 h c}{E \lambda_L T_A \sigma_t} . \quad (2.43)$$

The saturation time  $\tau_s$  is a measure of the characteristic time of stimulated emission. The ratio  $\tau_s/\tau_n$  indicates the level of saturation within the layer. A large ratio implies that the natural decay time is much shorter than the characteristic time of stimulated emission. In this case, the rate of stimulated emission is much lower than the rate of spontaneous emission, which results in negligible saturation effects (i.e.,  $\sigma_s \sim \sigma_t$ ). On the other hand, a small ratio implies the rate of stimulated emission is much larger than the rate of natural decay, which results in significant saturation effects (i.e.,  $\sigma_s < \sigma_t$ ). Note that in the limit as  $\tau_s/\tau_n \rightarrow 0$ ,  $\sigma_s$  given by Equation (2.42) reduces to  $\sigma_t$  given by Equation (2.40).

Using Equations (2.39) and (2.43), two design equations are derived giving the required pulse energy  $E$  and pulse length  $\Delta t$  as a function of the required photon flux density  $F$ :

$$E = \frac{12.57 F z_g^2 h c}{\eta T_A^2 \lambda_L C_s \sigma_s} , \quad (2.44)$$

$$\Delta t = \frac{2 F z_g^2 \tau_s}{\eta T_A C_s \Delta \rho_{rms}^2 (\sigma_s/\sigma_t)} . \quad (2.45)$$

Multiplying the energy required for a single star given in Equation (2.44) by the number of required guide stars  $N_{gs}$  (Equation (2.14)) gives the total required laser pulse energy  $E_T$ :

$$E_T = \frac{12.57 F h c D^2 h_t^2}{\eta T_A^2 \lambda_L C_s \sigma_s r_o^2}. \quad (2.46)$$

For an optimum wavefront sensor design the subaperture size  $d$  will be given by  $d_o$  in Equation (2.22), and the required photon flux density  $F$  will be given by  $F_{min}$  in Equation (2.23). Substituting  $F_{min}$  into Equations (2.45) and (2.46) gives

$$E_T = \frac{1.78 \times 10^{-3} \eta_c^2 h c D^2 h_t^2}{r_o^4 (\Delta\phi/\lambda)^{22/5} \eta T_A^2 \lambda_L C_s \sigma_s}, \quad (2.47)$$

$$\Delta t = \frac{2.84 \times 10^{-4} \eta_c^2 z_g^2 \tau_s}{r_o^2 (\Delta\phi/\lambda)^{22/5} \eta T_A C_s \Delta\rho_{rms}^2 (\sigma_s/\sigma_t)}. \quad (2.48)$$

Equations (2.47) and (2.48) express the required pulse energy  $E_T$  and pulse length  $\Delta t$  to achieve a specified level of phase error across the aperture ( $\Delta\phi$ ). Note that  $E_T$  is inversely proportional to  $r_o^4$ . As in the case of Rayleigh guide stars, this dependence highlights the importance of choosing an observatory site with good seeing in order to minimize the required laser pulse energy. Also note that the expressions for  $E_T$  given by Equation (2.33) for the Rayleigh guide star and Equation (2.47) for the Na guide star are similar in form except for the additional factor of  $r_o^2$  in the denominator of Equation (2.47). This additional factor (of  $r_o^2$ ) causes the pulse energy requirement for the Na guide star approach to be much more sensitive to changes in seeing conditions ( $r_o$ ) than the Rayleigh guide star approach. The expression for  $E_T$  for Rayleigh guide stars lacks the additional factor



of  $r_0^2$  in the denominator because the width of the scattering region  $\Delta z$  is inversely proportional to  $r_0^2$ . As  $r_0$  decreases, the column abundance of air molecules within the illuminated area increases for the Rayleigh guide star approach, whereas for the Na guide star approach the column abundance of Na atoms is constant, since the entire thickness of the layer is used.

It is important to note that  $\sigma_s$  is a function of  $\tau_s$  and the width of the laser line shape. The functional dependence on the laser line width is evident from the expression for  $\sigma_s$  given in Equation (2.42). By plotting  $\sigma_s$  as a function of laser line width, Welsh and Gardner<sup>7</sup> show that the line width can be chosen to maximize  $\sigma_s$ , thereby minimizing  $E_T$  and  $\Delta t$ . Figure 2.23 is a plot of  $\sigma_s$  as a function of the FWHM laser line width for the Na layer characteristics described in Table 2.3. A line width of  $\sim 600$  MHz FWHM is optimum for  $\tau_s/\tau_n$  ranging from 0.5 to 2.0. For a fixed line width,  $\tau_s$  is chosen to obtain the most desirable combination of pulse energy and pulse length. A large value of  $\tau_s$  (i.e., negligible saturation) decreases the required pulse energy  $E_T$ , but requires a long pulse length  $\Delta t$ . A small value of  $\tau_s$  (i.e., significant saturation) decreases the required pulse length, but requires a large pulse energy. Welsh and Gardner<sup>7</sup> find that a value of  $\tau_s = 2\tau_n$  is a reasonable choice, since it nearly achieves the minimum possible pulse energy while at the same time requiring a relatively small pulse length. For a laser line width of 600 MHz FWHM and  $\tau_s = 2\tau_n$ ,  $\sigma_s$  is equal to  $5.1 \times 10^{-16} \text{ m}^2$ .

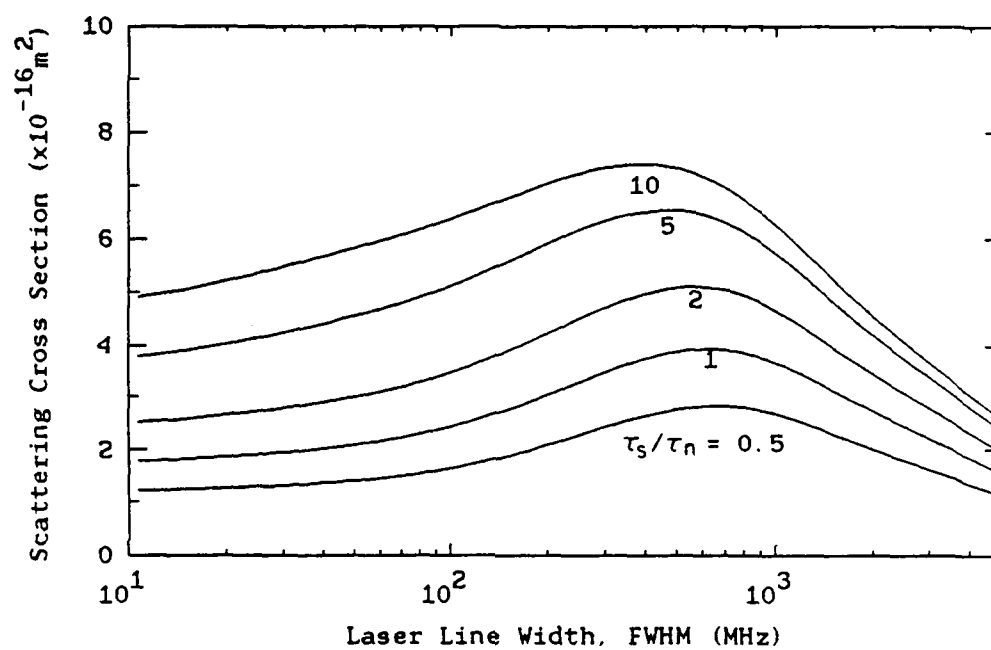


Figure 2.23. Scattering cross section  $\sigma_s$  versus laser line width. Curves are shown for  $\tau_s/\tau_n$  ranging from 0.5 to 10.

Table 2.3

Assumptions for the Na Laser Guide Star  
Pulse Energy Calculations

---

**ATMOSPHERE:**

Width of Doppler distribution $n(\omega_d)$ , FWHM	1.07 GHz
Natural decay time of Na, $\tau_n$	16 ns
Scattering cross section, $\sigma_t$	$8.27 \times 10^{-16} \text{ m}^2$
Scattering cross section, $\sigma_s$	$5.10 \times 10^{-16} \text{ m}^2$
Atmospheric transmission, $T_A$	0.85
Turbulence layer height, $h_t$	10 km
Na column abundance, $C_s$	$5 \times 10^{13} \text{ m}^{-2}$
Nominal Na layer height, $z_g + z_t$	92 km
Telescope entrance plane altitude, $z_t$	2 km

**LASER AND RECEIVER SYSTEM:**

Observation wavelength, $\lambda$	500 nm
Laser wavelength, $\lambda_L$	589 nm
Laser linewidth, FWHM	600 MHz
Laser pulse repetition rate	100 Hz
Laser rms beamwidth, $\Delta\rho_{rms}$	$z_g(0.431\lambda/r_o)$
Overall optical efficiency, $\eta$	7.5 %
Centroid detector efficiency factor, $\eta_c$	1.35

We are now able to compute the required pulse energy and pulse length as a function of  $\Delta\phi$ . Figures 2.24 and 2.25 are plots of  $E_T$  versus  $\Delta\phi$  and  $\Delta t$  versus  $\Delta\phi$  for a telescope diameter  $D = 2\text{m}$  and  $r_o = 10, 20, \text{ and } 30\text{ cm}$ . Figure 2.26 is a plot of  $E_T$  versus  $D$  for  $\Delta\phi = \lambda/17.5$ . Consider, for example, the following parameter values:  $\Delta\phi = \lambda/17.5$ ,  $D = 2\text{m}$  and  $r_o = 20\text{ cm}$ . For these conditions the total required pulse energy  $E_T$  is 58 mJ/cycle and the required pulse length  $\Delta t$  is 54  $\mu\text{s}$ . According to Equation (2.14) this energy is sent to a single guide star. If the atmospheric sampling rate is 100 Hz, the total system power required is 6 W.

The required pulse energy increases for observation directions away from zenith. Using the geometrical correction factors discussed in Chapter 4 and by Welsh and Gardner,<sup>7</sup> the factor change in the required pulse energy is given by

$$\frac{E_T(\theta)}{E_T(0)} = \exp\left[-2\sigma_d\left(1 - \frac{1}{\cos\theta}\right)\right] \frac{\sigma_s(0)}{\sigma_s(\theta)} \frac{1}{(\cos\theta)^{17/5}}, \quad (2.49)$$

where  $\theta$  is the zenith angle and  $E_T(\theta)$  is the required pulse energy as a function of zenith angle. The scattering cross section  $\sigma_s(\theta)$  is given by Equation (2.42) with  $\tau_s$  replaced with

$$\tau_s(\theta) = \frac{2 \Delta t \pi \Delta\rho_o^2 h c}{E \lambda_L T_A(\theta) \sigma_t (\cos\theta)^2}, \quad (2.50)$$

where  $\Delta\rho_o$  is the zenith value of the rms beam width of the laser.

Equation (2.49) is derived assuming the angular width of the guide star

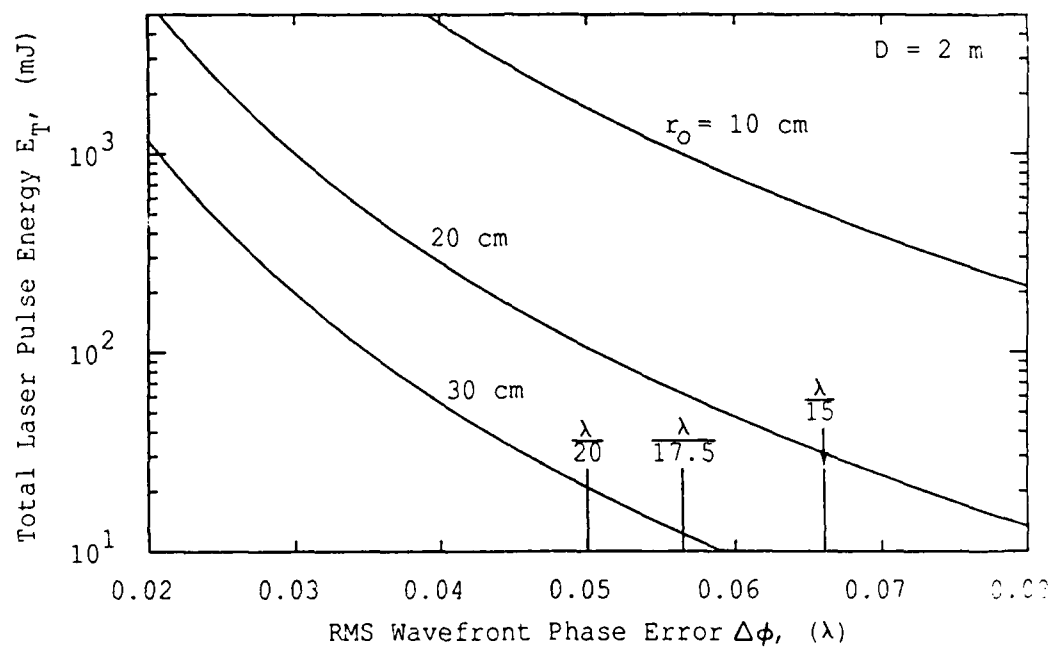


Figure 2.24. Total Na laser pulse energy requirements versus residual RMS phase error over the aperture. Curves are shown for  $r_0 = 10$  cm, 20 cm and 30 cm. The aperture diameter is assumed to be 2 m.

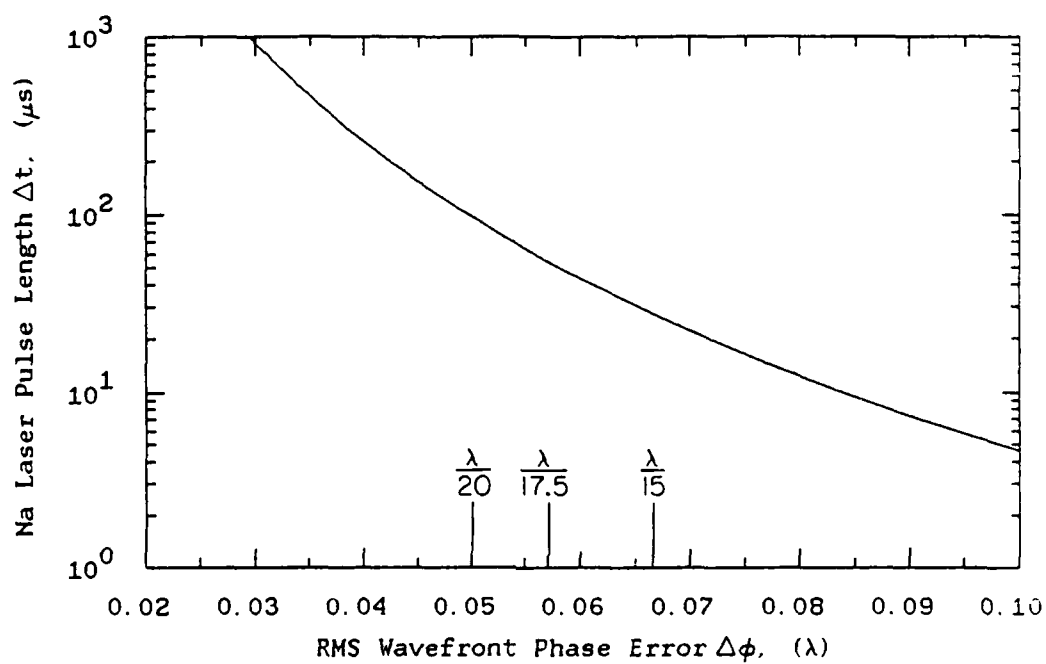


Figure 2.25. Na laser pulse length requirements versus residual RMS phase error over the aperture.

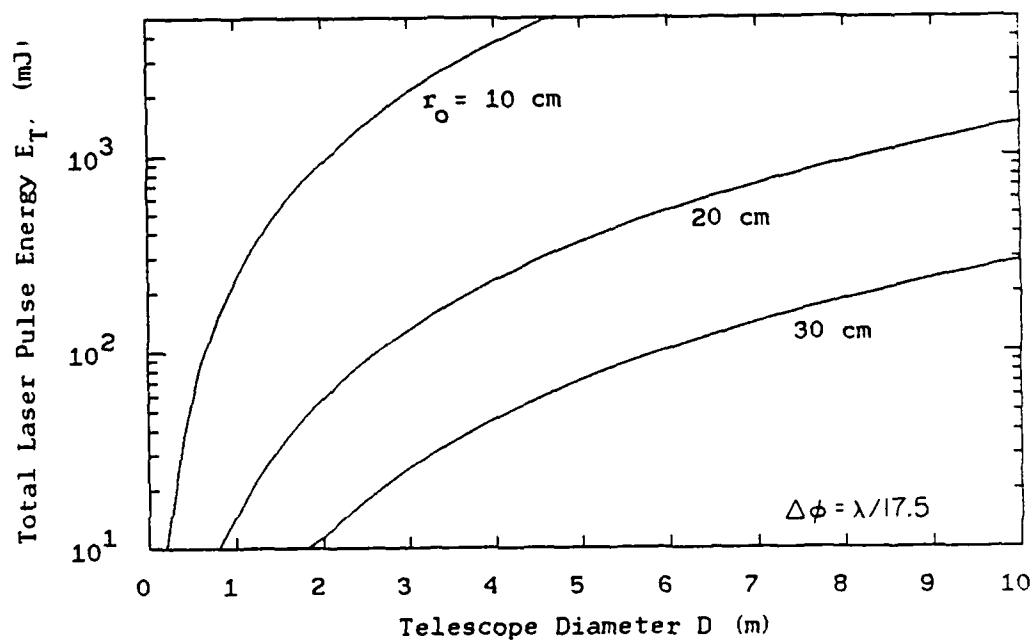


Figure 2.26. Total Na laser pulse energy requirements versus telescope diameter. The value of residual RMS phase error over the aperture is assumed to be  $\lambda/17.5$  and  $r_0$  ranges from 10 cm to 30 cm.

is held constant as the observation direction is pointed away from zenith. The factor increase in required pulse energy is plotted versus zenith angle in Figure 2.27 for the laser and atmospheric parameters given in Table 2.3. For a zenith angle out to  $30^\circ$  the factor increase in  $E_p$  is 1.52. At this angle the required pulse energy increases to 89 mJ/cycle, which corresponds to a laser power of 9 W at 100 pps.

At the present time the primary stumbling block to building a Na guide star system is the lack of an adequate laser. Because Na  $D_2$  lasers have not been widely used in science or industry, there is limited experience with high-power versions that might meet the laser guide star requirements. At present, the three most common Na  $D_2$  lasers are 1) flashlamp, 2) Nd:YAG laser, or 3) excimer laser pumped systems with a liquid organic dye solution in the lasing cavity. If the energy density in the lasing cavity exceeds a certain limit, the beam divergence properties deteriorate. Janes<sup>42</sup> at Avco Research Laboratory, working under contract to MIT Lincoln Laboratory, recently reported a novel solution to the beam divergence problem. A pump laser beam is optically scanned across an extended dye cell, and each laser pulse is produced in a separate region of the cavity. This laser appears to meet all specifications for producing laser guide stars. A second solution is currently under development by Jeys at Lincoln Laboratory.<sup>43</sup> A pair of Nd:YAG lasers with excellent beam divergence properties are frequency mixed in a crystal to produce the Na  $D_2$  light directly. This laser also promises to meet all the specifications for producing laser guide stars.



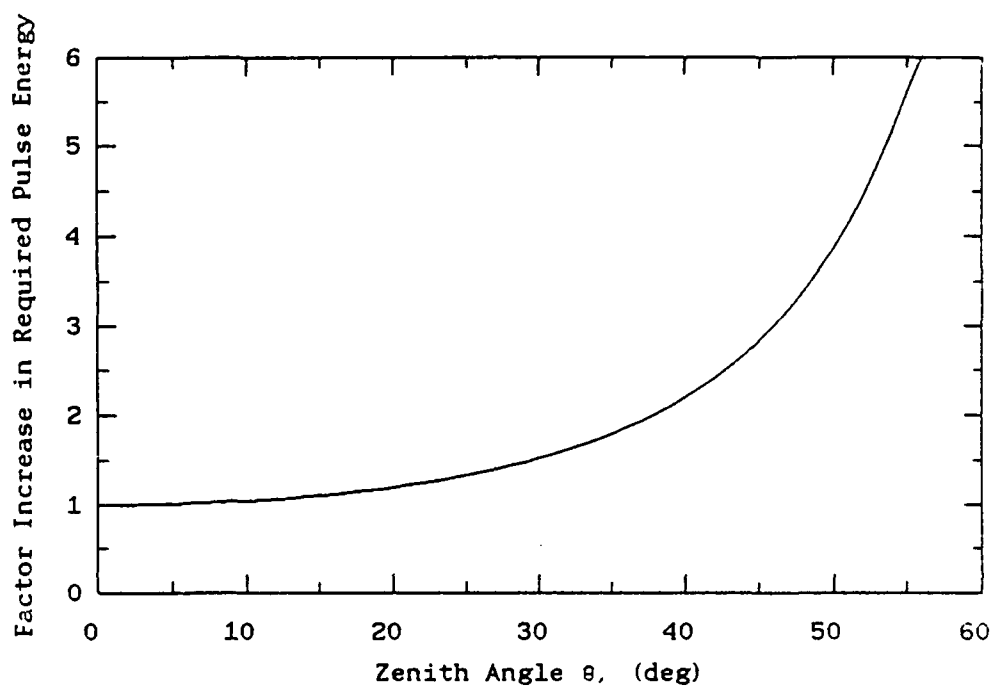


Figure 2.27. Factor increase of the Na laser pulse energy requirements versus zenith angle.

## 2.6 Design Summaries for Rayleigh and Na Guide Star Systems

In this section we present the key design parameters for 2 and 4 m diameter adaptive telescope systems. The imaging performance is specified by the rms wavefront phase variation across the telescope aperture,  $\Delta\phi$ . Assume, for the simplified analysis of Section 2.3, the desired value of  $\Delta\phi$  is  $\lambda/17.5$ . The wavefront sensor is assumed to be a Hartmann sensor with subapertures of diameter  $d_o$  given by Equation (2.22). The deformable mirror is assumed to be of monolithic design with an actuator spacing equal to  $d_o$ . Assuming  $r_o = 20$  cm, Tables 2.4 and 2.5 list the optimum design parameters for both the 2 and 4 m apertures for the Rayleigh and Na guide star approaches, respectively. From Equation (2.22) the optimum sensor spacing  $d_o$  is 13.8 cm and from Equation (2.23) the minimum photon flux requirement is 1907 photons/m<sup>2</sup>/cycle time. Figure 2.7 specifies the number of subapertures  $N_{s,a}$  required to sample the entire telescope pupil. Approximately 210 subapertures are required for the 2 meter aperture, and approximately 840 subapertures are required for the 4 meter aperture. For observation angles away from zenith  $r_o$  decreases as  $(\cos\theta)^{3/5}$  (see Equation (2.5)). Figures 2.28 and 2.29 show how the optimum subaperture size  $d_o$  and the required number of subapertures  $N_{s,a}$  vary as a function of zenith angle. For observation angles out to 30°, the optimum sensor diameter decreases to  $d_o = 12.7$  cm. The number of subapertures required increases to ~ 248 for the 2 m aperture and ~ 990 for the 4 m aperture.

**Table 2.4**  
**Rayleigh Laser Guide Star Design Requirements**  
**for 2 and 4 m Adaptive Telescopes\***

<b>Zenith Design Parameters:</b>	<u>2 m aperture</u>	<u>4 m aperture</u>
Number of guide stars, $N_{gs}$	~69	~278
Subaperture size, $d$	13.8 cm	13.8 cm
Number of subapertures, $N_{sA}$	210	840
Laser pulse energy, $E_T$	330 mJ	1.3 J
Laser power @ 100 pps	33 w	130 w
 <b>Design Parameters for Observation Angles out to 30 °:</b>		
Number of guide stars, $N_{gs}$	~82	~330
Subaperture size, $d$	12.7 cm	12.7 cm
Number of subapertures, $N_{sA}$	248	990
Laser pulse energy, $E_T$	620 mJ	2.5 J
Laser power @ 100 pps	62 w	250 w

\* Derived for  $r_o = 20$  cm,  $\Delta\phi = \lambda/17.5$  and the parameters listed in Table 2.3.

Table 2.5

Na Laser Guide Star Design Requirements  
for 2 and 4 m Adaptive Telescopes\*

<b>Zenith Design Parameters:</b>	<u>2 m aperture</u>	<u>4 m aperture</u>
Number of guide stars, $N_{gs}$	~1	~5
Subaperture size, $d$	13.8 cm	13.8 cm
Number of subapertures, $N_{SA}$	210	840
Laser pulse energy, $E_T$	58 mJ	235 mJ
Laser pulse length, $\Delta t$	54 $\mu s$	54 $\mu s$
Laser power @ 100 pps	6 w	24 w
 <b>Design Parameters for Observation Angles out to 30 °:</b>		
Number of guide stars,	~1	~6
Subaperture size, $d$	12.7 cm	12.7 cm
Number of subapertures, $N_{SA}$	248	990
Laser pulse energy, $E_T$	89 mJ	355 mJ
Laser pulse length, $\Delta t$	54 $\mu s$	54 $\mu s$
Laser power @ 100 pps	9 w	36 w

\* Derived for  $r_o = 20$  cm,  $\Delta\phi = \lambda/17.5$  and the parameters listed in Table 2.4.

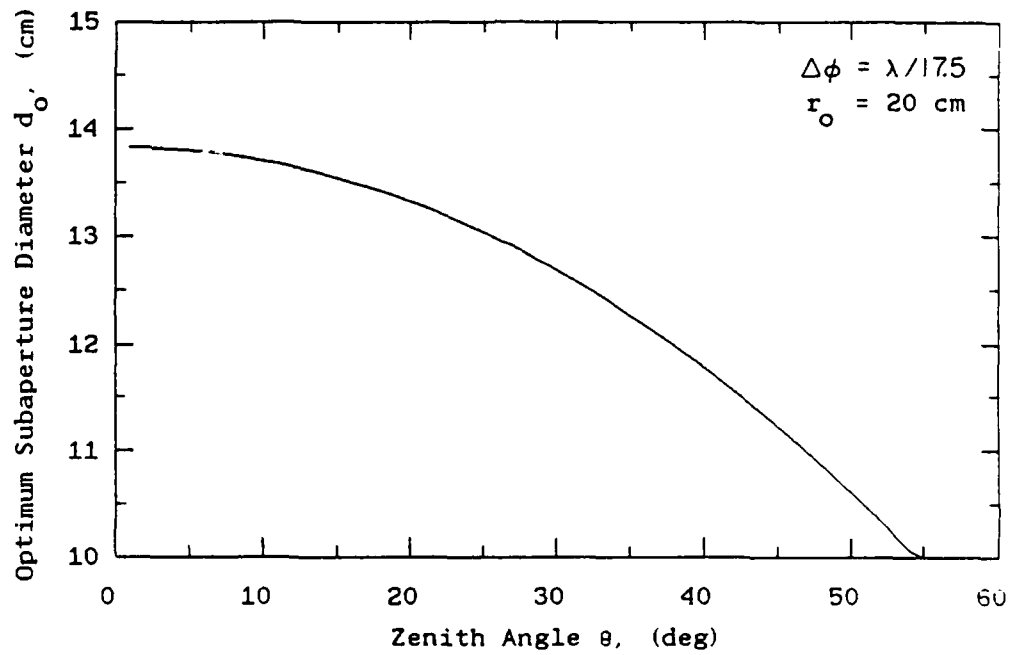


Figure 2.28. Optimum subaperture diameter versus zenith angle for the adaptive telescope designs summarized in Tables 2.4 and 2.5.

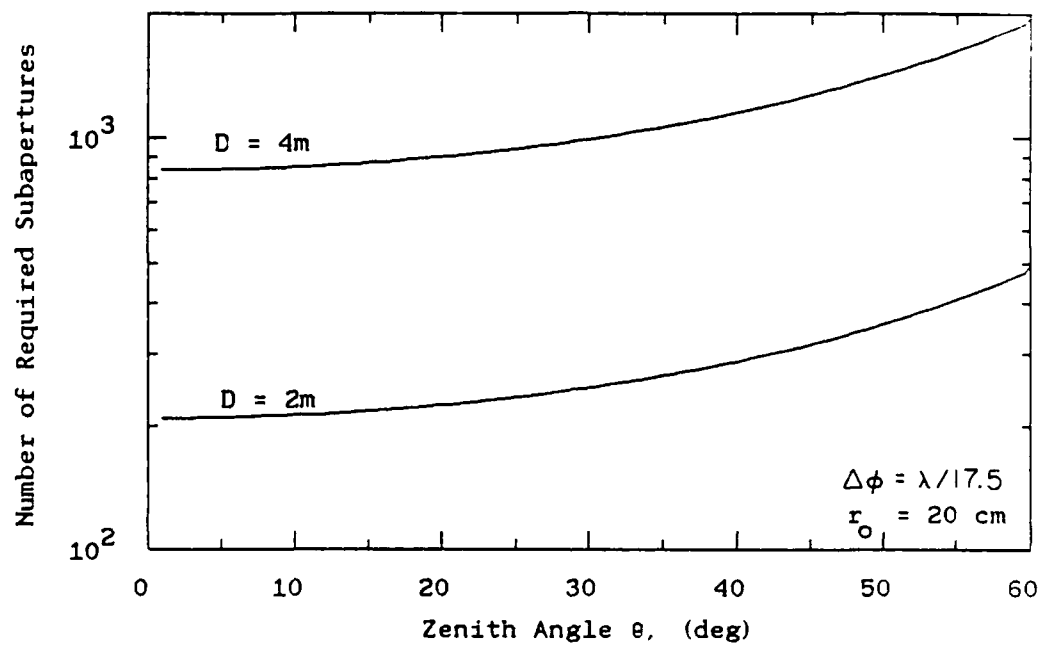


Figure 2.29. Required number of subapertures versus zenith angle for the adaptive telescope designs summarized in Tables 2.4 and 2.5.

For the Rayleigh guide star approach and the atmospheric and laser parameters listed in Table 2.2, the required laser pulse energy  $E_T$  at zenith is 330 mJ for the 2 m aperture and 1.3 J for the 4 m aperture. At a sampling rate of 100 Hz, the required laser output power is respectively, 33 and 130 W. The number of guide stars required is ~69 for the 2 m telescope and ~278 for the 4 m telescope. Figure 2.17 indicates how the required laser pulse energy  $E_T$  varies as a function of zenith angle  $\theta$ . For observation angles out to  $30^\circ$ ,  $E_T$  must be increased by a factor of 1.88. At this angle the required pulse energy is 620 mJ and 2.5 J/cycle for the 2 and 4 meter apertures, respectively. These pulse energies correspond to laser output powers of 62 and 250 W at 100 pps. Table 2.4 summarizes the design parameters.

For the Na guide star approach and the atmospheric and laser parameters listed in Table 2.3, the required laser pulse energy  $E_T$  at zenith is 58 mJ for the 2 m aperture and 235 mJ for the 4 m aperture. In order to minimize the effects of saturation for these pulse energies, the laser's pulse length  $\Delta t$  must be at least 54  $\mu s$ . At a sampling rate of 100 Hz, the required laser power is 6 W for the 2 m aperture and 24 W for the 4 m aperture. The number of guide stars required is ~ 1 for the 2 m telescope and ~ 5 for the 4 m telescope. Figure 2.27 indicates how the required laser pulse energy  $E_T$  varies as a function of zenith angle. For observation angles out to  $30^\circ$ ,  $E_T$  must be increased by a factor of 1.52. At this angle the required pulse energy is 89 and 355 mJ/cycle for the 2 and 4 meter apertures,

respectively. These pulse energies correspond to laser output powers of 9 and 36 W at 100 pps. Table 2.5 summarizes the design parameters.

For the wavefront sensor and mirror configuration analyzed in Figure 2.8 these parameters yield nearly diffraction limited imaging. Table 2.1 indicates that the rms value of the phase error will be  $\sim \lambda/11.1$  and the Strehl ratio  $\sim 0.73$ . The resolution of the telescopes will be 1.09 times the resolution for diffraction limited imaging. For an observation wavelength of  $0.5 \mu\text{m}$ , the angular resolution would be  $\sim 0.069$  and  $\sim 0.034$  arcsec for the 2 and 4 meter apertures, respectively. Note that these resolutions are measured from the 1D PSFs shown in Figure 2.11.

## 2.7 Optical Interferometric Imaging

Although laser-guided adaptive telescopes will be capable of achieving excellent resolution using conventional imaging techniques, the greatest advances in angular resolution will result when adaptive telescopes are used as the detector elements of an optical interferometer. The interferometric techniques developed for radio telescopes are now capable of achieving milli-arc-second resolution. Current practice in radio astronomy is to use arrays of interferometers to measure the magnitude of discrete Fourier components of the brightness distribution across the source. Data processing techniques can then be used to synthesize the source image. Radio synthesis telescope techniques have been under development since the mid 1940s and brought to their highest pitch in the Very Large Array (VLA).<sup>44</sup> It



has been suggested that these same techniques, combined with recent advances in image processing<sup>45,46</sup> and electro-optics technology, can be used to develop optical analogs of the VLA.<sup>47-49</sup> Townes and his colleagues<sup>50,51</sup> have already made significant progress in developing the heterodyne interferometry technique at infrared wavelengths.

Optical synthesis telescopes will employ heterodyne detection at several widely spaced telescopes and digital correlation techniques to compute the Fourier components of the source brightness distribution. Heterodyne detection at optical wavelengths for astronomical applications has usually been considered ineffective by virtue of the very narrow bandwidths ( $\sim 1$  GHz). Astronomical signals are typically very weak, and small bandwidths can be a serious handicap for all but the brightest sources. The interferometer signal levels are also severely limited by turbulence, because for heterodyne detection, the effective telescope diameter can be no larger than  $r_0$ . The wavefront tilt which reduces the resolution of large telescopes also reduces the detection efficiency of the heterodyne interferometer. Several years ago Swenson, Gardner and Bates<sup>47,48</sup> suggested that the effective optical bandwidth of the interferometer could be increased substantially by electronically multiplexing many parallel optical channels with the aid of large-scale-integration techniques. If laser-guided adaptive telescopes are also used to compensate for turbulence, the heterodyne detection efficiency of the interferometer will be improved substantially. In fact, the correlator signal-to-noise ratio (SNR) will be increased by the factor  $(D/r_0)^2$  where  $D$  is

the telescope diameter. For  $r_0 = 20$  cm, the SNR improvement is 20 dB for a 2 m aperture and 34 dB for a 10 m aperture. Based upon the calculations reported by Swenson and his colleagues, for  $D = 2$  m it should be possible to achieve excellent SNR performance at visible wavelengths for sources of visual magnitude 10 or less with reasonable integration times ( $\sim 10^3$  s) and optical bandwidths ( $\sim 10^{12}$  Hz). Since the interferometer baseline can be 100 to 1000 m, the potential resolution of the optical heterodyne interferometer would be  $10^{-3} - 10^{-4}$  arc-second compared to approximately  $10^{-1}$  arc-second for a single 2 m diameter adaptive telescope.

## 2.8 Summary

Ground-based adaptive telescopes using laser guide stars can produce images that are nearly diffraction limited. We have addressed the major design issues for such a system and have presented the expected imaging performance. A 2 m laser-guided telescope, using a single laser that can be either bought off the shelf or built with today's technology, can achieve imaging performance levels nearly matching those of the Hubble Space Telescope (HST). The laser power requirement for the Rayleigh and Na guide star approaches is on the order of 33 and 6 W, respectively, for seeing conditions of  $r_0 = 20$  cm and zenith viewing. For either approach, near diffraction limited imaging is achieved with a Strehl ratio of  $\sim 0.73$  and an angular resolution of approximately 0.07 arcsec at  $\lambda = 0.5 \mu\text{m}$  (2.09 times that of diffraction limited imaging).

One of the more important design issues is determining the required laser power. The viability of building laser-guided telescopes depends on the ability of the designer to minimize the laser power requirements in order to achieve power levels within range of today's laser technology. The main factors affecting the power requirements include the expected imaging performance as specified by  $\Delta\phi$ , the subaperture diameter  $d$ , the Fried seeing cell diameter  $r_0$ , and the isoplanatic angle. The dependence of total laser power on  $r_0$  given in Equations (2.33) and (2.47) serves to reinforce the importance of choosing a site with extremely good seeing conditions (i.e.,  $r_0 \geq 15$  to 20 cm) in order to achieve reasonable laser power requirements. Figures 2.15 and 2.24 illustrate the large increases in the pulse energy requirements for the case of  $r_0$  decreasing from 20 cm to 10 cm. Other factors affecting the required laser power include the height of the guide stars for the Rayleigh guide star approach and saturation effects for the Na guide star approach. We show that the height of Rayleigh guide stars can be chosen to minimize the laser pulse energy requirements. For Na guide stars we show that the combination of laser pulse energy, pulse length and line width can be chosen to minimize the effects of saturation.

Even for laser powers considerably less than those given in Tables 2.4 and 2.5, the expected resolution of the adaptive telescope is still on the order of that for diffraction limited imaging. For flux levels as low as 1/7 the flux produced by the lasers specified in Tables 2.4 and 2.5, the expected resolution of the telescope degrades to only

~1.47 times that of diffraction limited imaging. In the case of low guide star flux levels for the 2 m telescope, the angular resolution is still expected to be 0.09 arcsec at  $\lambda = 0.5 \mu\text{m}$ . However, the Strehl ratio decreases to a value well below 0.6. The combination of good resolution and a poor Strehl ratio indicates the system will produce images with a core FWHM comparable to the telescope's theoretical resolution along with a broader halo of light surrounding the core. As the laser power decreases, a larger and larger percentage of the light from the image core is transferred to the surrounding halo, thereby decreasing the Strehl ratio.

### 3. PERFORMANCE ANALYSIS OF ADAPTIVE OPTICS SYSTEMS USING LASER GUIDE STARS AND SLOPE SENSORS

#### 3.1 Introduction

It is well known that the resolution of large ground-based telescopes is limited by random wavefront aberrations caused by atmospheric turbulence. Real time wavefront reconstruction systems, commonly called adaptive optics systems, have been shown to improve the image resolution of these telescopes.<sup>1</sup> However, the question of how well these systems perform under less than ideal operating conditions has been the subject of much ongoing research and discussion. These "less than ideal conditions" can basically be summarized as the inability to build perfect wavefront sensors and wavefront correction devices. The accuracy of wavefront sensors is limited by photon noise and by the finite number of sampling points over the wavefront surface. For example, wavefront aberrations having characteristic spatial frequencies greater than the sensor's spatial sampling frequency go undetected. Wavefront correction devices are also less than ideal. The ability of a correction device to cancel wavefront aberrations is limited by the finite degrees of freedom in the device's response. This limited response will prevent it from correcting higher order wavefront aberrations. The response time of a wavefront correction system also limits performance. Since wavefront aberrations evolve in time, a delay between wavefront sensing and wavefront correction will result in less than optimal wavefront reconstruction.

The performance of wavefront correction systems has been treated extensively in the literature. These performance measures have generally fallen into two categories. In the first, performance is measured in terms of the mean square (MS) residual error between the phase of the reconstructed wavefront and the actual wavefront.<sup>33, 52-62</sup> In the second, performance is measured in terms of the spatial frequency response of the phase corrected optical system.<sup>63-66</sup> This frequency response is commonly called the optical transfer function (OTF). Of the recent works on this subject, Wallner's<sup>52</sup> analysis is most complete in the sense that all the elements of the wavefront correction system are included. Wallner analyzes the performance of a wavefront correction system in terms of the MS residual phase error across the aperture. He includes in his analysis realistic wavefront sensor and wavefront corrector models, and a control law connecting the two.

Much of the past work has dealt with only parts of the overall system configuration. Several papers have addressed how to use a set of noisy, single point phase difference measurements to reconstruct the wavefront phase at a set of grid points in the aperture.<sup>54-59</sup> In general, these studies have not included the effect of finite sensor subaperture areas, nor the effect of a realistic wavefront correcting device. Performance is generally measured in terms of the residual phase error at the grid points. The effects of the interpolation between the grid points, inherent in any real wavefront corrector, are not addressed. Additionally, the derivation of the minimum MS fit of

the reconstructed wavefront to the actual wavefront at the grid points makes no use of the phase statistics of the actual wavefront.

Other papers have addressed the performance limitations of wavefront correctors.<sup>62-66</sup> In these papers the effects of wavefront sensing are ignored and only the performance of the corrector is considered. Gaffard and Boyer,<sup>63</sup> for example, analyze the performance of continuous deformable mirrors and optimize their design in terms of actuator spacing and influence radius.

Most of the previous work has not included the effect of a time delay between wavefront sensing and wavefront correction. Only Hudgin<sup>33</sup> considers this delay in his study of optimal wavefront estimation. He computes the residual phase error in the aperture, for some given time delay between wavefront sensing and wavefront correction. As in the previously mentioned work, the error is computed at a set of grid points.

In this work we analyze the performance of a complete wavefront correction system in terms of the optical transfer function. The basic wavefront correction system under consideration consists of an aperture, a wavefront slope sensor, a wavefront correcting device and a control law. We concentrate on phase correcting systems, and assume that turbulence induced amplitude effects are negligible. The wavefront correcting device is a deformable mirror with a finite number of actuators. The wavefront sensor samples the aperture plane over a

specified number of subapertures. The wavefront phase slope is measured within each of these subapertures. The measured slopes are used by a control law to position the deformable mirror. A time delay is specified between wavefront sensing and positioning of the mirror.

The advantage of using the OTF as a performance measure lies in the wealth of information that is contained in and can be derived from it. The OTF clearly illustrates the response of the optical system to the whole range of spatial frequencies. High spatial frequencies are of particular interest, since it is in this region that the magnitude of the OTF indicates the ultimate resolution of the system. In addition to the OTF, the point spread function (PSF) is computed. The PSF is the image plane intensity distribution that would result from imaging a point source and is easily computed from the OTF. This intensity distribution is a useful performance measure, since the resolution of the optical system can be determined directly from the width of the distribution's main lobe. We also compute the Strehl ratio, which is obtained from the PSF by comparing the peak of the main lobe of the intensity distribution to that of a perfect unaberrated system.

In Section 3.2 the basic assumptions and definitions characterizing the wavefront sensor, deformable mirror, measurement noise, and control law are introduced. In Section 3.3 we summarize Wallner's<sup>52</sup> derivations for the MS residual phase error between the reconstructed wavefront and actual wavefront. In Section 3.4 the OTF



is formulated in terms of the MS residual phase error found in Section 3.3. The statistical descriptions of the wavefront phase and sensor noise are introduced in Sections 3.5 and 3.6. These statistical descriptions are in turn incorporated in the results of Sections 3.2 and 3.3. Finally, in Section 3.7, we present computational results for two wavefront reconstruction systems based on a Hartmann wavefront sensor and continuously deformable mirrors. As discussed in Chapter 2, these results are particularly important in the design of laser-guided adaptive telescopes used for imaging in astronomy.

### 3.2 Definitions and Assumptions

The following system definitions and assumptions closely follow those of Wallner.<sup>52</sup> Consider a wavefront correction system consisting of an aperture, a deformable mirror, a wavefront sensor and a control law. The deformable mirror and aperture pupil plane are optically conjugated. The mirror surface is controlled by a finite number of actuators which can affect zonal or modal surface deformations. The plane of the wavefront sensor and the pupil plane are also optically conjugated. The aperture is segmented into subapertures, and the wavefront sensor measures the average wavefront slope within each. The control law uses the measured wavefront slope information to position the actuators of the deformable mirror.

The aperture of the optical system is described by the weighting function  $W_A(\underline{x})$ , where  $\underline{x}$  is a two-dimensional vector in the pupil plane.  $W_A(\underline{x})$  is given by

$$W_A(\underline{x}) = \begin{cases} k & \text{points within the aperture} \\ 0 & \text{points outside the aperture} \end{cases} \quad (3.1)$$

where  $k$  is defined such that

$$\int d^2\underline{x} W_A(\underline{x}) = 1, \quad (3.2)$$

and  $\int d^2\underline{x}$  indicates integration over the entire aperture plane.

The phase of the incoming wave at  $\underline{x}$  and at time  $t$  is designated  $\psi(\underline{x}, t)$  (rad). The phase  $\psi(\underline{x}, t)$  is random process in time and in space. It is convenient to define a zero mean phase  $\phi(\underline{x}, t)$  (rad) which is related to  $\psi(\underline{x}, t)$  by

$$\phi(\underline{x}, t) = \psi(\underline{x}, t) - \int d^2\underline{x}' W_A(\underline{x}') \psi(\underline{x}', t). \quad (3.3)$$

The output of the  $n$ th sensor is a noisy measurement of the average slope of  $\phi(\underline{x}, t)$  over a subaperture defined by  $W_n(\underline{x})$ :

$$s_n(t) = \int d^2\underline{x} W_n(\underline{x}) [\nabla \phi(\underline{x}, t) \cdot \underline{d}_n] + \alpha_n(t), \quad (3.4)$$

where

$s_n(t)$  = slope signal from the nth sensor at time  $t$  (rad/m),

$W_n(\underline{x})$  = weighting function for the nth sensor ( $m^{-2}$ ),

$\nabla\phi(\underline{x}, t)$  = spatial gradient of  $\phi$ ,

$\underline{d}_n$  = unit vector in the direction of the sensitivity of the nth sensor,

$\alpha_n(t)$  = slope measurement error for the nth sensor at time  $t$  (rad/m).

The weighting function  $W_n(\underline{x})$  is defined in a manner similar to that of  $W_A(\underline{x})$ . The slope signal can be rewritten by integrating the first term of Equation (3.4) by parts:

$$s_n(t) = - \int d^2\underline{x} [\nabla W_n(\underline{x}) \cdot \underline{d}_n] \phi(\underline{x}, t) + \alpha_n(t). \quad (3.5)$$

For notational simplicity in the development to follow we designate  $\nabla W_n(\underline{x}) \cdot \underline{d}_n$  with  $W_n^s(\underline{x})$  where the superscript indicates the slope of  $W_n(\underline{x})$  in the direction of the sensitivity of the nth slope sensor. The measurement error  $\alpha_n(t)$  is attributed to photon noise in the slope detection process and is assumed independent of  $\phi(\underline{x}, t)$ .

The control law generates a command for each actuator of the deformable mirror based on the slope measurements. Using a linear control law we define the actuator drive signal  $c_j(t)$

$$c_j(t) = \sum_n M_{jn} s_n(t), \quad (3.6)$$

where  $c_j(t)$  is the command sent to the  $j$ th actuator and  $M_{jn}$  is the weighting of the  $n$ th sensor signal in the  $j$ th actuator command.

Finally we define the reconstructed wavefront  $\hat{\phi}(\underline{x}, t)$  as

$$\hat{\phi}(\underline{x}, t) = \sum_j c_j(t) r_j(\underline{x}), \quad (3.7)$$

where  $r_j(\underline{x})$  is the response of the mirror to a unit command at the  $j$ th actuator.

### 3.3 Mean-Square Residual Phase Error

The following development summarizes the derivations and analytical results obtained by Wallner<sup>52</sup> and is included for completeness. We generalize Wallner's results by including the effect of a time delay between wavefront sensing and the wavefront correction. This delay will be inherent in any wavefront correction system.

Since the deformable mirror is located in a conjugate plane of the pupil, we can analyze the system as if the corrected wavefront passes through the pupil plane. As a consequence, we can write the residual phase error in the aperture plane as

$$\begin{aligned}
\Delta\phi(\underline{x}, t, \tau) &= \hat{\phi}(\underline{x}, t-\tau) - \phi(\underline{x}, t) \\
&= \sum_j r_j(\underline{x}) \sum_n M_{jn} s_n(t-\tau) - \phi(\underline{x}, t), \tag{3.8}
\end{aligned}$$

where  $\tau$  is the delay between wavefront sensing and wavefront correction. Note that, as defined in Equation (3.8),  $\Delta\phi$  has units of radians. For the results in Section 3.7 the phase error is presented in units of waves ( $m$ ). Rather than define a separate notation, we use the symbol  $\Delta\phi$  to designate the error for both cases. The units of  $\Delta\phi$  should be obvious in each case. The mean-square residual error is given by

$$\begin{aligned}
\langle \Delta\phi^2(\underline{x}, t, \tau) \rangle &= \\
&\sum_j \sum_{j'} \sum_n \sum_{n'} r_j(\underline{x}) r_{j'}(\underline{x}) M_{jn} M_{j'n'} \langle s_n(t-\tau) s_{n'}(t-\tau) \rangle \\
&- 2 \sum_j \sum_n r_j(\underline{x}) M_{jn} \langle s_n(t-\tau) \phi(\underline{x}, t) \rangle + \langle \phi^2(\underline{x}, t) \rangle, \tag{3.9}
\end{aligned}$$

where  $\langle f \rangle$  is the ensemble average of  $f$ . We assume that  $\phi(\underline{x}, t)$  and  $s_n(t)$  are wide sense stationary random processes in time. This assumption allows us to write Equation (3.9) as solely a function of the time delay  $\tau$ . Averaging  $\langle \Delta\phi^2(\underline{x}, \tau) \rangle$  over the aperture  $W_A(\underline{x})$  gives the average MS residual error

$$\langle \Delta \phi(\tau)^2 \rangle = \int d^2 \underline{x} W_A(\underline{x}) \langle \Delta \phi^2(\underline{x}, \tau) \rangle. \quad (3.10)$$

Substituting Equation (3.9) into Equation (3.10) we obtain

$$\begin{aligned} \langle \Delta \phi(\tau)^2 \rangle = & \sum_j \sum_{j'} \sum_n \sum_{n'} M_{jn} M_{j'n'} S_{nn'} R_{jj'} \\ & - 2 \sum_j \sum_n M_{jn} A_{jn}(\tau) \\ & + \langle \Delta \phi_0^2 \rangle, \end{aligned} \quad (3.11)$$

where  $S_{nn'}$ ,  $R_{jj'}$ , and  $A_{jn}(\tau)$  are defined by

$$\begin{aligned} S_{nn'} &= \langle s_n(t) s_{n'}(t) \rangle \\ &= \int d^2 \underline{x}' \int d^2 \underline{x}'' W_n^s(\underline{x}') W_{n'}^s(\underline{x}'') \langle \phi(\underline{x}', t) \phi(\underline{x}'', t) \rangle \\ &\quad + \langle \alpha_n(t) \alpha_{n'}(t) \rangle, \end{aligned} \quad (3.12)$$

$$R_{jj'} = \int d^2 \underline{x} W_A(\underline{x}) r_j(\underline{x}) r_{j'}(\underline{x}), \quad (3.13)$$

$$\begin{aligned} A_{jn}(\tau) &= \int d^2 \underline{x} W_A(\underline{x}) r_j(\underline{x}) \langle s_n(t-\tau) \phi(\underline{x}, t) \rangle \\ &= - \int d^2 \underline{x} \int d^2 \underline{x}' W_A(\underline{x}) r_j(\underline{x}) W_n^s(\underline{x}') \langle \phi(\underline{x}, t) \phi(\underline{x}', t-\tau) \rangle, \end{aligned} \quad (3.14)$$

and the average mean-square uncorrected error  $\langle \Delta \phi_o^2 \rangle$  is defined as

$$\langle \Delta \phi_o^2 \rangle = \int d^2 \underline{x} W_A(\underline{x}) \langle \phi^2(\underline{x}, t) \rangle. \quad (3.15)$$

Note that, due to the stationarity of  $\phi(\underline{x}, t)$  and  $\alpha_n(t)$ , the time dependence  $t$  does not appear on the left-hand side of Equations (3.12), (3.14) and (3.15).

The mean-square residual phase error given by Equation (3.11) is valid for an arbitrary control matrix  $M_{jn}$ . A control matrix giving the minimum MS residual error is obtained by differentiating Equation (3.11) with respect to  $M_{jn}$  and equating the result to zero. Wallner<sup>52</sup> gives the minimizing control matrix  $M_{jn}^*$  as

$$M_{jn}^*(\tau) = R_{jj}^{-1} A_{j'n'}(\tau) S_{n'n}^{-1}, \quad (3.16)$$

where we have used standard matrix multiplication notation to denote the summations. Wallner states the general conditions for the existence of  $R_{jj}^{-1}$  and  $S_{n'n}^{-1}$ . Substituting this control matrix back into Equation (3.11) results in the minimum MS residual phase error:

$$\langle \Delta \phi(\tau)^2 \rangle_{\min} = \langle \Delta \phi_o^2 \rangle - R_{jj}^{-1} A_{j'n'}(\tau) S_{n'n}^{-1} A_{jn}(\tau). \quad (3.17)$$

### 3.4 Optical Transfer Function

We now consider the OTF for the phase corrected wavefront optical system. We start by defining the OTF in terms of the complex amplitude field  $E(\underline{x})$  in the aperture of an optical system. Assume  $E(\underline{x})$  is

produced by a far field point source. It is well known that the OTF can be written as the convolution of  $E(\underline{x})$  with its complex conjugate  $E^*(\underline{x})$ <sup>67</sup>:

$$H(\underline{\rho}) = \frac{\int d^2\underline{x} W_A(\underline{x}) E(\underline{x}) W_A^*(\underline{x}-\underline{\rho}) E^*(\underline{x}-\underline{\rho})}{\int d^2\underline{x} |W_A(\underline{x}) E(\underline{x})|^2}, \quad (3.18)$$

where  $H(\underline{\rho})$  is the OTF, and  $\underline{\rho}$  and  $\underline{x}$  are two-dimensional vectors in the aperture pupil plane. Note that spatial frequency, designated  $\nu$  (cycles/meter), is related to the positional vector  $\underline{\rho}$  by  $\nu = |\underline{\rho}|/\lambda f_D$ , where  $f_D$  is the focal length of the aperture lens. Writing  $E(\underline{x})$  as a product of a magnitude and a phase term we can rewrite Equation (3.18) giving

$$H(\underline{\rho}) = \frac{\int d^2\underline{x} |W_A(\underline{x}) E(\underline{x})| |W_A^*(\underline{x}-\underline{\rho}) E^*(\underline{x}-\underline{\rho})| \exp\{j[\xi(\underline{x}) - \xi(\underline{x}-\underline{\rho})]\}}{\int d^2\underline{x} |W_A(\underline{x}) E(\underline{x})|^2}, \quad (3.19)$$

where  $\xi(\underline{x})$  is the phase of  $E(\underline{x})$ . Applying Equation (3.19) to the wavefront correction system defined in Section 3.2, we find that  $\xi(\underline{x})$  corresponds to the residual phase error  $\Delta\phi(\underline{x}, t, \tau)$  defined in Equation (3.8). If the aperture of the optical system is in the near field region of the turbulence we may ignore the effects of amplitude perturbations and equate  $|E(\underline{x})|$  to 1. This near field criterion is satisfied if the distance between the aperture pupil plane and the turbulence region is less than  $D^2/\lambda\pi$  where  $D$  is the diameter of the



aperture and  $\lambda$  is the optical wavelength.<sup>12</sup> Equating  $\xi(\underline{x})$  to  $\Delta\phi(\underline{x}, t, \tau)$ , and  $|E(\underline{x})|$  to 1, and rewriting Equation (3.19), we obtain the OTF for the phase corrected optical system:

$$H(\underline{\rho}) = \frac{\int d^2\underline{x} W_A(\underline{x}) W_A^*(\underline{x}-\underline{\rho}) \exp \left[ j \left( \Delta\phi(\underline{x}, t, \tau) - \Delta\phi(\underline{x}-\underline{\rho}, t, \tau) \right) \right]}{\int d^2\underline{x} |W_A(\underline{x})|^2}. \quad (3.20)$$

Since  $\Delta\phi(\underline{x}, t, \tau)$  is a random process in time and space, further progress is impossible unless a statistical approach is taken. We continue by defining an ensemble average OTF,  $\langle H(\underline{\rho}) \rangle$ :

$$\langle H(\underline{\rho}) \rangle = \frac{\int d^2\underline{x} W_A(\underline{x}) W_A^*(\underline{x}-\underline{\rho}) \langle \exp \left[ j \left( \Delta\phi(\underline{x}, t, \tau) - \Delta\phi(\underline{x}-\underline{\rho}, t, \tau) \right) \right] \rangle}{\int d^2\underline{x} |W_A(\underline{x})|^2}. \quad (3.21)$$

At this point the standard approach is to assume that  $\Delta\phi(\underline{x}, t, \tau)$  is a Gaussian, zero mean, random process.<sup>18</sup> This assumption allows us to write

$$\langle H(\underline{\rho}) \rangle = \frac{\int d^2\underline{x} W_A(\underline{x}) W_A^*(\underline{x}-\underline{\rho}) \exp \left[ -\frac{1}{2} \langle \left( \Delta\phi(\underline{x}, t, \tau) - \Delta\phi(\underline{x}-\underline{\rho}, t, \tau) \right)^2 \rangle \right]}{\int d^2\underline{x} |W_A(\underline{x})|^2}. \quad (3.22)$$

Using the expression for  $\langle \Delta \phi^2(\underline{x}, t, \tau) \rangle$  in Equation (3.9), Equation (3.22) is expanded into the following form:

$$\begin{aligned} \langle H(\underline{\rho}) \rangle = & \frac{\exp\left(\frac{-\langle (\phi(\underline{x}, t) - \phi(\underline{x} - \underline{\rho}, t))^2 \rangle}{2}\right)}{\int d^2 \underline{x} |W_A(\underline{x})|^2} \int d^2 \underline{x} W_A(\underline{x}) W_A^*(\underline{x} - \underline{\rho}) \\ & \times \left[ \exp\left(-\frac{1}{2} \sum_j \sum_i [r_j(\underline{x}) - r_j(\underline{x} - \underline{\rho})][r_i(\underline{x}) - r_i(\underline{x} - \underline{\rho})] C_{ji}\right. \right. \\ & \left. \left. + \sum_j [r_j(\underline{x}) - r_j(\underline{x} - \underline{\rho})] \langle c_j(t - \tau) [\phi(\underline{x}, t) - \phi(\underline{x} - \underline{\rho}, t)] \rangle \right) \right] \quad (3.23) \end{aligned}$$

where

$$\begin{aligned} C_{ji} &= \langle c_j(t) c_i(t) \rangle \\ &= \sum_n \sum_m M_{jn} M_{im} S_{nm}, \quad (3.24) \end{aligned}$$

Gaffard and Boyer<sup>63</sup> obtained a result nearly identical to Equation (3.23) in their study of the performance characteristics of continuous deformable mirrors. Like the approach taken here, they analyzed performance in terms of the OTF. They concentrated their efforts on the optimization of the mirror design, and as such, did not include the effects of a wavefront sensor in their analysis. The difference between Gaffard and Boyer's expressions for the OTF and the expression given in Equation (3.23) is in the definition of the term  $c_j(t)$  ( $h_j$  in

Gafford and Boyer). In both results this term is the drive signal sent to the  $j$ th actuator. Here  $c_j(t)$  is derived from the measured wavefront slope information. In Gafford and Boyer's analysis  $c_j(t)$  is derived from complete knowledge of the phase of the aberrated wavefront (i.e., they assume a perfect wavefront sensor).

### 3.5 Wavefront Phase Statistics

Equations (3.17) and (3.23) are the main results of the previous two sections. To evaluate Equations (3.17) and (3.23) the correlation  $\langle \phi(\underline{x}, t) \phi(\underline{x}', t - \tau) \rangle$  must be computed. Both  $S_{nn}$  and  $A_{jn}(\tau)$  depend on this phase correlation. Wallner<sup>52</sup> derives an expression for the phase correlation as a function of the spatial phase structure function. We make use of the slightly more general spatio-temporal phase structure function defined as

$$D(\underline{x}, \underline{x}', \tau) = \langle [\psi(\underline{x}, t) - \psi(\underline{x}', t - \tau)]^2 \rangle. \quad (3.25)$$

Finding  $\langle \phi(\underline{x}, t) \phi(\underline{x}', t - \tau) \rangle$  in terms of Equation (3.25) is a straightforward application of the derivation performed by Wallner. We do not repeat the derivation here, but simply rewrite the expressions that depend on  $\langle \phi(\underline{x}, t) \phi(\underline{x}', t - \tau) \rangle$  in terms of Equation (3.25). These expressions include  $S_{nn}$ ,  $A_{jn}(\tau)$  and  $\langle H(\underline{\rho}) \rangle$ . First consider  $S_{nn}$  and  $A_{jn}(\tau)$ :

$$S_{nn} = -\frac{1}{2} \int d^2 \underline{x}' \int d^2 \underline{x}'' W_n^s(\underline{x}') W_n^s(\underline{x}'') D(\underline{x}', \underline{x}'', 0) + \langle \alpha_n(t) \alpha_n(t) \rangle, \quad (3.26)$$

$$A_{jn}(\tau) = - \int d^2\underline{x} \int d^2\underline{x}' W_A(\underline{x}) r_j(\underline{x}) W_n^s(\underline{x}') \times [-\frac{1}{2}D(\underline{x}, \underline{x}', \tau) + g(\underline{x}', \tau)] \quad (3.27)$$

where

$$g(\underline{x}, \tau) = \frac{1}{2} \int d^2\underline{x}' W_A(\underline{x}') D(\underline{x}, \underline{x}', \tau). \quad (3.28)$$

The expression for  $A_{jn}$  given by Wallner (Equation (28) of Ref. 52) contains a sign error and does not include the second term given in the right-hand side of Equation (3.27) above. This second term will integrate to zero if the spatial average of the actuator response  $r_j(\underline{x})$  is zero. Finally, rewriting  $\langle H(\underline{\rho}) \rangle$  as a function of Equation (3.25) gives

$$\begin{aligned} \langle H(\underline{\rho}) \rangle = & \frac{\exp\left(\frac{-D(\underline{x}, \underline{x}-\underline{\rho}, 0)}{2}\right)}{\int d^2\underline{x} |W_A(\underline{x})|^2} \int d^2\underline{x} W_A(\underline{x}) W_A^*(\underline{x}-\underline{\rho}) \\ & \times \left[ \exp\left(-\frac{1}{2} \sum_j \sum_i [r_j(\underline{x}) - r_j(\underline{x}-\underline{\rho})][r_i(\underline{x}) - r_i(\underline{x}-\underline{\rho})] C_{ji}\right. \right. \\ & \left. \left. + \sum_j [r_j(\underline{x}) - r_j(\underline{x}-\underline{\rho})] \langle c_j(t-\tau) [\phi(\underline{x}, t) - \phi(\underline{x}-\underline{\rho}, t)] \rangle \right) \right] \quad (3.29) \end{aligned}$$

where

$$\begin{aligned} \langle c_j(t-\tau) [\phi(\underline{x}, t) - \phi(\underline{x}-\underline{p}, t)] \rangle = \\ \frac{1}{2} \sum_n M_{jn} \int d^2 \underline{x}' W_n^2(\underline{x}') [D(\underline{x}, \underline{x}', \tau) - D(\underline{x}-\underline{p}, \underline{x}', \tau)] . \end{aligned} \quad (3.30)$$

### 3.6 Slope Measurement Noise

The slope measurement noise is modeled with a random slope error signal  $\alpha_n(t)$ . This error signal is attributed to photon noise in the slope detection process. We assume that slope measurements on non-overlapping subapertures and orthogonal slope measurements on coincident subapertures are uncorrelated. We also assume the slope noise is white in the sense that  $\alpha_n(t)$  and  $\alpha_n(\tau)$  are uncorrelated for  $t \neq \tau$ . This is easily justified by modeling the photon noise as Poisson and assuming sequential slope measurements in time are derived from nonoverlapping time intervals. Combining these assumptions results in a noise correlation function given by

$$\langle \alpha_n(t) \alpha_{n'}(\tau) \rangle = \sigma_n^2 k_{nn'}(t-\tau), \quad (3.31)$$

where

$\sigma_n^2$  = mean-square slope error ( $\text{rad}^2 \text{ m}^{-2}$ ),

$k_{nn'}(t-\tau) = \cos\theta \delta(t-\tau) \delta_{nn'}$ ,

$\theta$  = the angle between the direction of sensitivity of the  $n$ th and  $n'$ th sensors,

$\delta(t-\tau)$  = Dirac delta function,

$\delta_{nn'} = \begin{cases} 1 & \text{nth and n'th subapertures coincide} \\ 0 & \text{otherwise.} \end{cases}$

The magnitude of  $\sigma_n^2$  depends on the type and configuration of slope sensors used in the wavefront sensor. In the numerical example of the following section we find  $\sigma_n^2$  for the Hartmann wavefront sensor.

### 3.7 Computational Results for Continuous Mirrors

We apply the analytical results derived in Sections 3.3 and 3.4 to two wavefront correction systems. Both systems employ a Hartmann wavefront sensor and use continuous deformable mirrors. The difference between the two systems is in the response function of the deformable mirror. For the first system, the mirror response function is modeled with a Gaussian deformation. For the second, the response function is characteristic of a membrane mirror. We compute the performance of these two wavefront correction systems in terms of the average mean-square residual error across the aperture (Equation (3.17)) and the OTF (Equation (3.29)). In contrast to the motivation for the computational results presented in Chapter 2, here we are primarily interested in demonstrating the effects of slope measurement noise in the wavefront sensor, time delay between wavefront sensing and correction, and finite sensor/actuator spacing. As a result, the parameter used to describe the wavefront sensor and deformable mirror are chosen more for convenience than to match those parameters that might be used in an actual design.

### Mirror Descriptions.

The mirror for system 1 is a continuous mirror with a Gaussian actuator response proportional to

$$r_j(x,y) \propto \exp \left( \frac{-(x-x_j)^2 - (y-y_j)^2}{d_a^2} \right) \quad (3.32)$$

where  $x$  and  $y$  specify a point in the plane of the mirror,  $x_j$  and  $y_j$  specify the actuator location, and  $d_a$  is the influence radius. The Gaussian response is often used to model piezoelectric deformable mirrors.

The mirror for system 2 is a membrane mirror. The response function for this type of mirror must satisfy Poisson's equation:<sup>68</sup>

$$\nabla^2 r_j(x,y) = -P_j(x,y)/T \quad (3.33)$$

where  $P_j(x,y)$  is the pressure distribution on the membrane mirror surface caused by the  $j$ th actuator, and  $T$  is the surface tension (force/distance) of the membrane. Equation (3.33) has been solved for a circular membrane centered at the origin<sup>69</sup> (see Figure 3.1). For a membrane of radius  $\alpha$ , the solution is

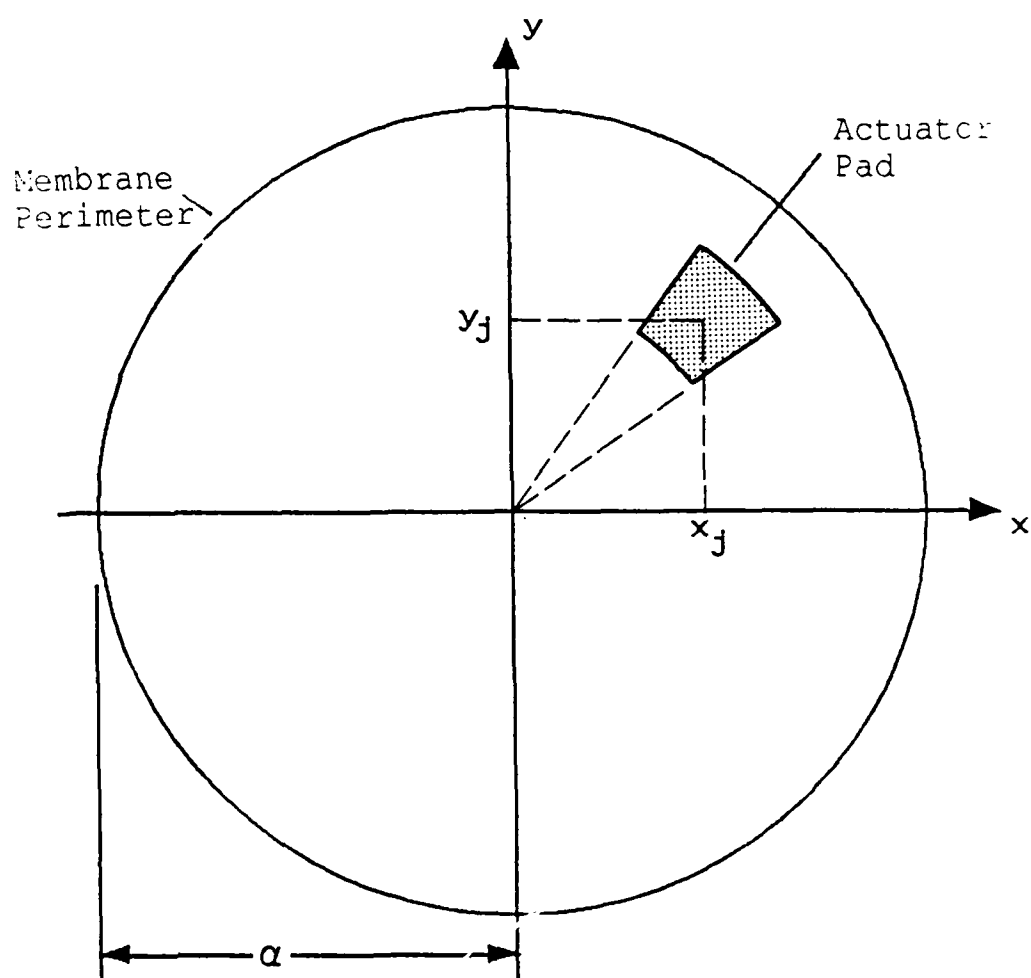


Figure 3.1. Membrane mirror and actuator pad configuration.



$$\begin{aligned}
 r_j(\alpha\rho, \phi) &= \frac{\alpha^2}{2\pi T} \int_0^{2\pi} d\phi' \\
 &\times \left\{ \int_0^\rho \rho' d\rho' \left\{ \ln(1/\rho) - \sum_{n=1}^{\infty} \frac{1}{n} [(\rho\rho')^n - (\rho'/\rho)^n] \right. \right. \\
 &\quad \left. \times \cos n(\phi' - \phi) \right\} P_j(\rho', \phi') \\
 &+ \int_\rho^1 \rho' d\rho' \left\{ \ln(1/\rho') - \sum_{n=1}^{\infty} \frac{1}{n} [(\rho\rho')^n - (\rho/\rho')^n] \right. \\
 &\quad \left. \times \cos n(\phi' - \phi) \right\} P_j(\rho', \phi') \Bigg\}, \tag{3.34}
 \end{aligned}$$

where  $(\rho, \phi)$  are the polar coordinates in the plane of the membrane. The radial coordinate  $\rho$  is normalized by the radius  $\alpha$ , and  $(x, y)$  is related to  $(\rho, \phi)$  by  $x = \alpha\rho\cos\phi$  and  $y = \alpha\rho\sin\phi$ . For our computations we assume the pressure distribution  $P_j(\rho', \phi')$  is constant over the actuator pad. The boundaries of each actuator pad are defined by lines of constant  $\rho$  and  $\phi$  in a fashion similar to the actuator model used by Claflin and Bareket.<sup>68</sup> Figure 3.1 illustrates the membrane geometry and the shape of an actuator pad. The solution of Equation (3.34) for this pressure distribution is given in detail by Claflin and Bareket and will not be repeated here. Figure 3.2 illustrates a typical mirror response for a series of actuator locations positioned on the x-axis. For the following results the centers of the actuator pads are located

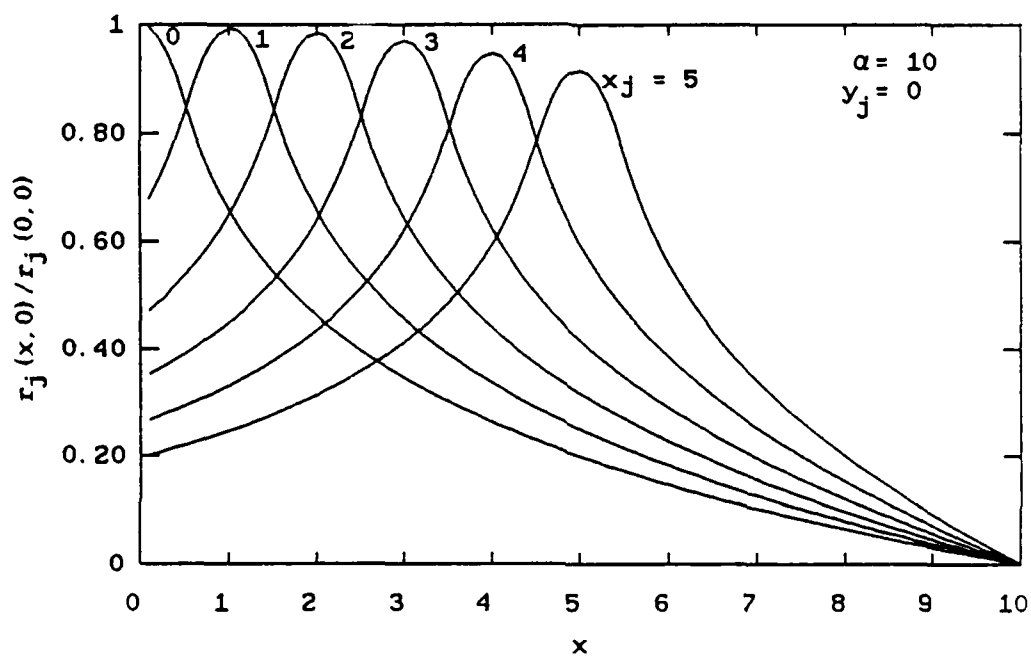


Figure 3.2. Membrane actuator response for actuators positioned along the  $x$  axis. The center of the membrane is at  $x = 0$  and the edge is at  $x = 10$ .

on a rectangular grid as shown in Figure 3.3. The area of each pad is adjusted to match the area of a  $d \times d$  subaperture. This model is not completely realistic because of the possibility of overlap and gaps between adjacent actuator pads. For modeling purposes, though, the computational results should not be significantly affected by the inaccuracies.

### Slope Sensor Description.

The model of the wavefront sensor is derived from the basic characteristics of the Hartmann sensor. Figure 3.3 illustrates the geometry of the sensor. This geometry was also treated by Wallner.<sup>52</sup> A square aperture of dimension  $d$  is divided into equal size subapertures of dimension  $d$ . In each subaperture the slope is sensed in both the  $x$  and  $y$  directions. The size of the aperture  $d$  is stated in terms of the number of subapertures on a side.

The accuracy of each slope detector is related to the magnitude of the slope measurement noise  $\sigma_n$ . To compute  $\sigma_n$  we must consider the Hartmann sensor in more detail. Note that the derivation to follow is slightly different from the tilt measurement error derived in Chapter 2. In this case we are interested in square subapertures and the error in one direction ( $x$  or  $y$  direction). Consider the single Hartmann sensor shown in Figure 3.4. The subaperture slope is measured by sensing the position of the diffraction limited spot in the focal plane of the lens. If the focal plane detector measures the position of the spot within some rms accuracy  $\Delta x$  (m), the corresponding slope

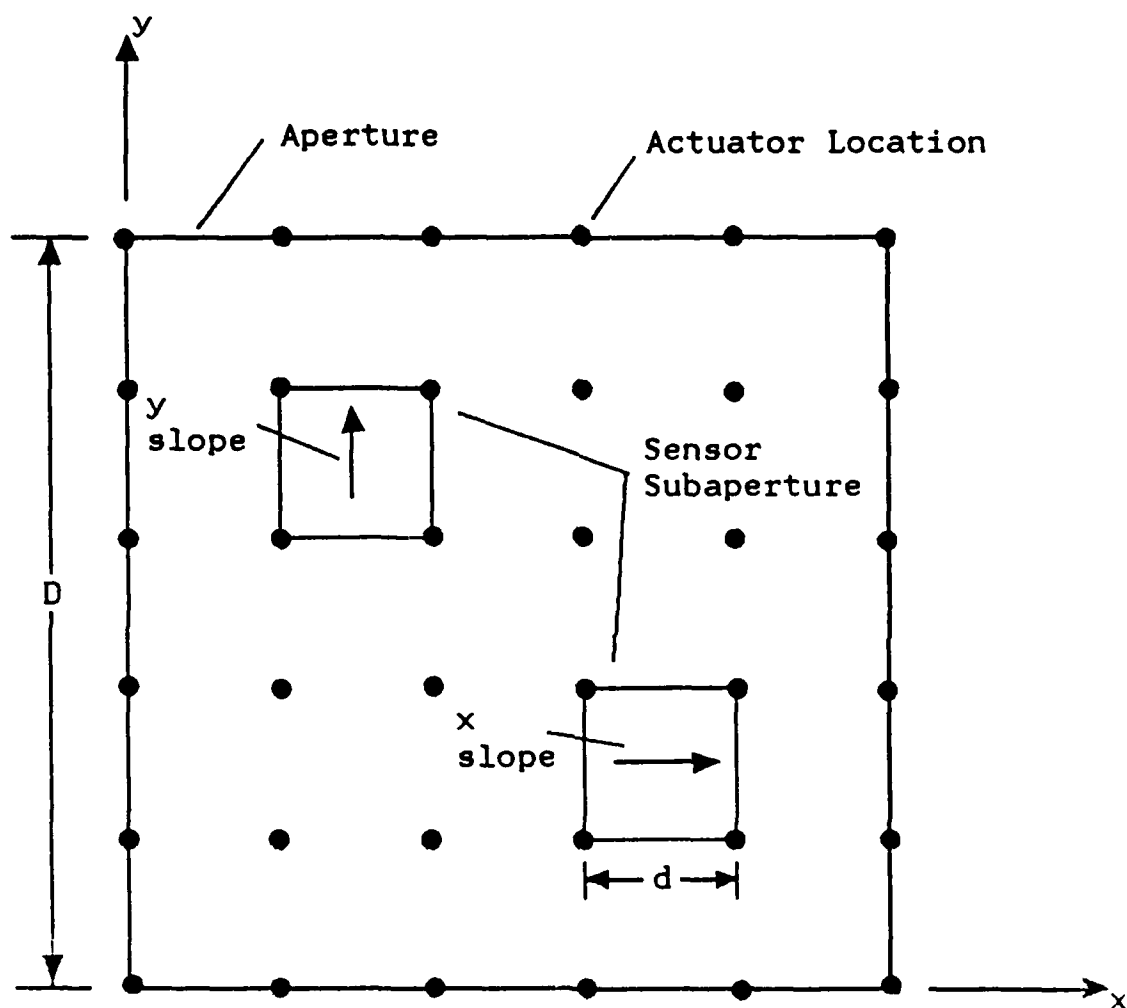


Figure 3.3. Wavefront sensor configuration.

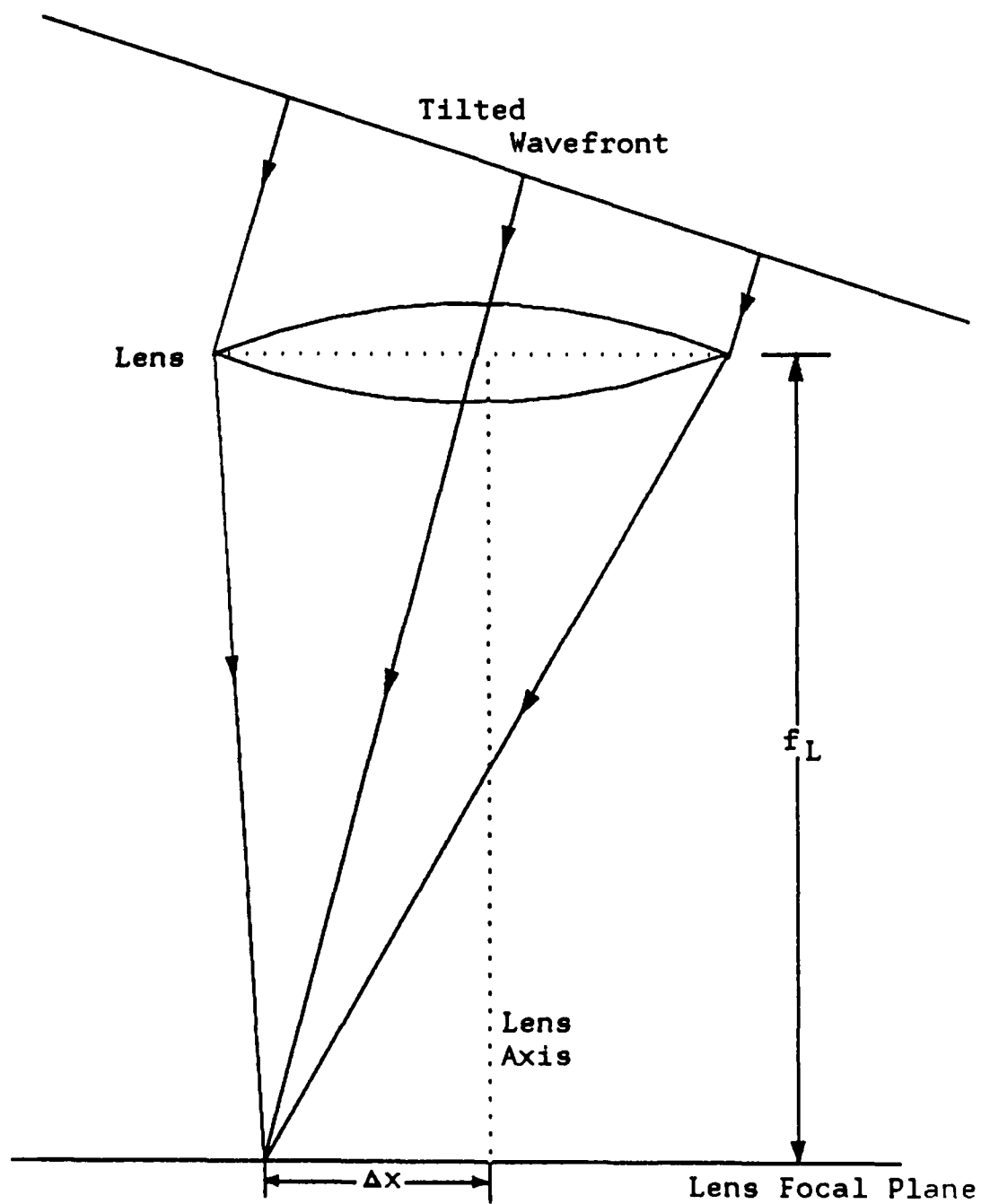


Figure 3.4. Single Hartmann tilt sensor.

measurement accuracy (rad/m) is

$$\sigma_n = \frac{2\pi\Delta x}{\lambda f_d} \quad (3.35)$$

where  $f_d$  is the focal length of the subaperture lens and  $\lambda$  is the wavelength of the detected light. The focal plane detector is typically an array of photon counting detectors (a CCD array for example). It is common to express the positional accuracy of this type of detector by

$$\Delta x = \frac{\eta_c \sigma_I}{\sqrt{N}} \quad (3.36)$$

where  $\eta_c$  is a parameter accounting for imperfections of the detector array (i.e., the effects of finite size array elements and dead space between array elements),  $\sigma_I$  (m) is the rms width of the spot on the detector array surface and  $N$  is the total subaperture photon count. Note that  $\eta_c \geq 1$  and that  $\eta_c = 1$  only in the ideal case of infinitely small detector elements with no dead space between elements. The spot size  $\sigma_I$  is determined by the lens size  $d$  or the Fried seeing cell size  $r_0$ . To compute  $\sigma_I$  we model the focal plane spot with a Gaussian intensity distribution. The Gaussian distribution is matched to the  $e^{-1}$  points of the diffraction limited intensity distribution from the subaperture. The Gaussian distribution is a reasonable approximation, since random perturbations of the wavefront caused by the atmosphere will tend to produce a Gaussian-shaped spot.<sup>16</sup> If  $d > r_0$  the Gaussian distribution is matched to a diffraction limited spot from a circular

subaperture of diameter  $r_o$ . If  $d < r_o$  the Gaussian distribution is matched to a diffraction limited spot from a square subaperture of side  $d$ . The rms spot size  $\sigma_r$  is given by

$$\sigma_r = \begin{cases} \frac{1.22\lambda f_d}{2\sqrt{2} r_o} & d > r_o \\ \frac{1.05\lambda f_d}{2\sqrt{2} d} & d \leq r_o \end{cases} \quad (3.37)$$

Substituting Equations (3.36) and (3.37) into Equation (3.35) gives

$$\sigma_n = \begin{cases} \frac{0.86\pi\eta_c}{\sqrt{N} r_o} & d > r_o \\ \frac{0.74\pi\eta_c}{\sqrt{N} d} & d \leq r_o \end{cases} \quad (3.38)$$

In the following computations we assume  $\eta_c=1.5$ . This value is typical of the minimum achievable for currently available CCD detector arrays used in conjunction with an image intensifier.<sup>14,15</sup>

#### Phase Structure Function.

Finally, we must assume the form of the phase structure function defined in Equation (3.18). For a "frozen," locally isotropic random turbulence field we can write<sup>70</sup>

$$\begin{aligned} D(\underline{x}, \underline{x}', \tau) &= D(\underline{x}, \underline{x}' + \underline{v}\tau) \\ &= D(\underline{x} - \underline{x}' - \underline{v}\tau) \end{aligned} \quad (3.39)$$

where  $\underline{v}$  is a velocity vector describing the speed and direction of the turbulence region relative to the optical system. Implicit in Equation (3.39) is the assumption that the whole turbulence region is moving with the same velocity  $\underline{v}$ . If we further assume, for computational simplicity, that the turbulence layers are confined to a relatively narrow vertical region in the atmosphere, and that the turbulence is described by Kolmogorov statistics, we can approximate the phase structure function with<sup>10</sup>

$$D(\underline{x}, \underline{x}', \tau) = 6.88 \left( \frac{|\underline{x} - \underline{x}' - \underline{v}\tau|}{r_o} \right)^{5/3}. \quad (3.40)$$

#### Computational Results.

1) Average RMS Residual Phase Error,  $\langle \Delta\phi^2(\tau) \rangle^{1/2}$ : We now are able to compute the average MS residual phase error  $\langle \Delta\phi^2(\tau) \rangle^{1/2}$  given in Equation (3.17). We start by assuming that the delay time  $\tau$  is zero and examine the effects of sensor noise, and aperture and subaperture size. We also assume, throughout the rest of this section, that the actuator centers are located at the corners of the sensors (see Figure 3.3). This arrangement is nearly optimal for the case in which  $d \sim r_o$ .<sup>63</sup> First consider variations in aperture size  $D$ . Figures 3.5a and 3.5b illustrate plots of  $\langle \Delta\phi^2(0) \rangle^{1/2}$  versus  $N$  photons/subaperture for both wavefront correction systems. The aperture size ranges from  $D = 2d$  to  $7d$  (corresponding to apertures having 9 to 64 actuators). The subaperture size  $d$  is held constant at a value of  $r_o$ . Both plots show the decreasing trend in residual phase error as  $N$  increases. Recall that the measurement noise power  $\sigma_n^2$  is inversely proportional to  $N$ . As



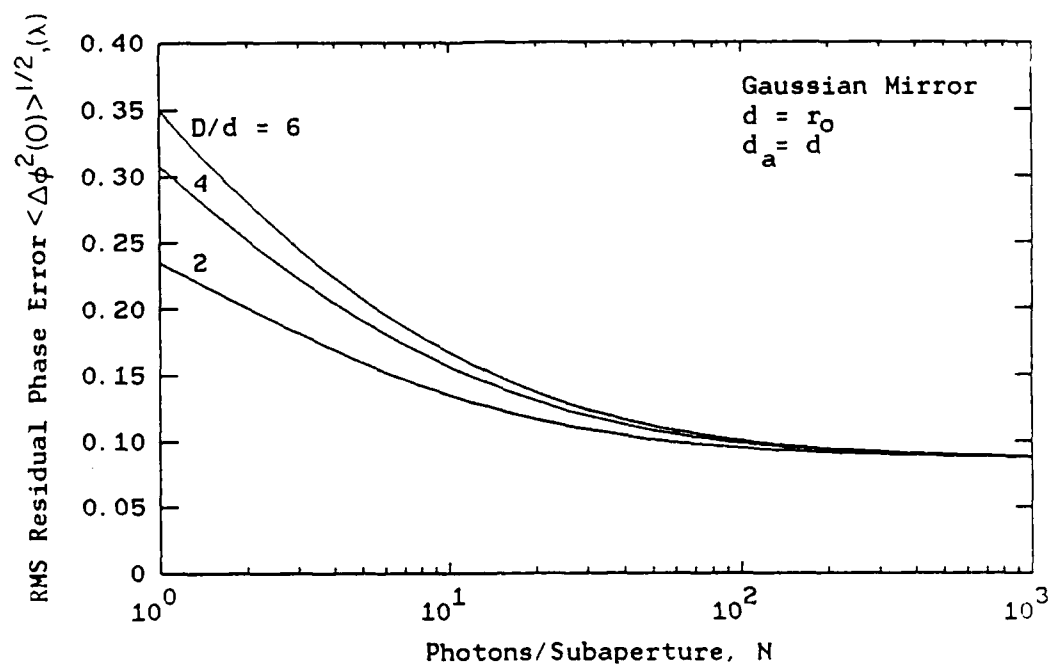


Figure 3.5a. Average RMS residual phase error versus photocounts/subaperture for the Gaussian mirror response function. The aperture size ranges from  $D=6d$  to  $2d$ . The other parameters are constant:  $d=r_0$  and  $\tau=0$ .

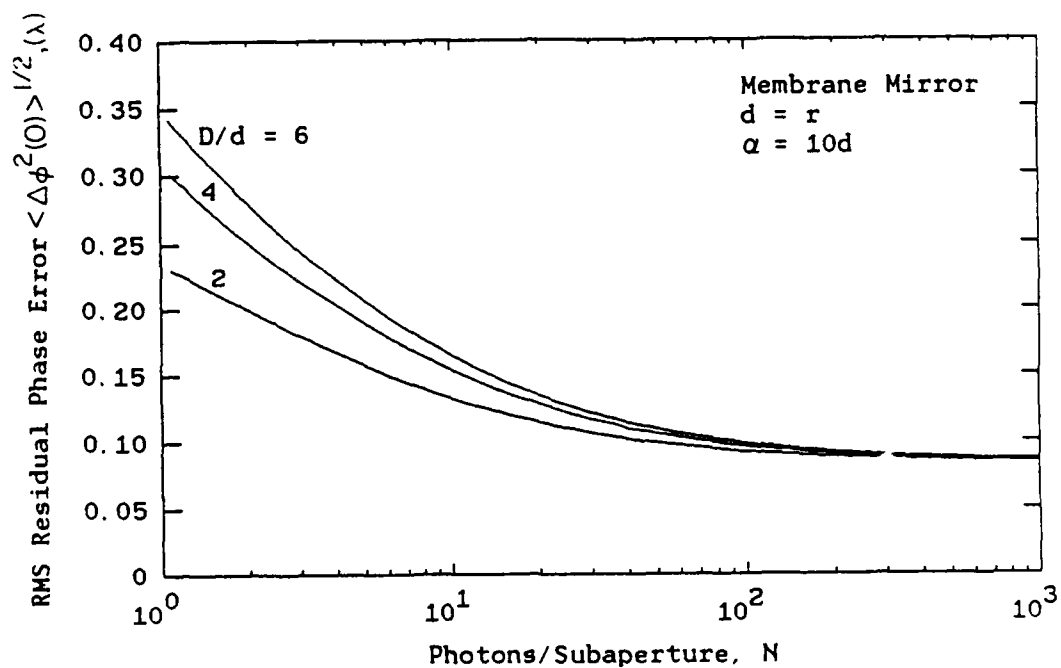


Figure 3.5b. Average RMS residual phase error versus photocounts/subaperture for the membrane mirror response function. The aperture size ranges from  $D=6d$  to  $2d$ . The other parameters are constant:  $d=r_0$  and  $\tau=0$ .

$N$  increases the effects of the slope measurement noise become negligible, and the errors introduced by the finite actuator and sensor spacing establish the minimum possible phase error. This minimum is approximately 0.55 radians (or equivalently  $0.087 \lambda$ ). These results show, as expected, that as the measurement noise becomes negligible ( $N \geq 100$ ) the phase error is approximately the same, regardless of aperture size.

Now consider variations in subaperture size  $d$ . Figures 3.6a and 3.6b illustrate plots of  $\langle \Delta \phi^2(0) \rangle^h$  versus photons/subaperture  $N$  for subaperture sizes ranging from  $d = 0.5r_0$  to  $1.5r_0$ . In this case, the aperture size  $D$  is held constant at a value of  $4d$ . These figures show that the residual phase error approaches increasingly lower minimums as the size of the subaperture  $d$  is decreased. This lower limit is determined by the sensor size  $d$ , and is proportional to  $(d/r_0)^{5/3}$ . Obviously, improved performance can be obtained by decreasing the subaperture size relative to the seeing cell size  $r_0$ . This improvement, though, is gained at the expense of increased system complexity due to the increased number of subapertures for a given aperture.

The effects of a time delay between wavefront sensing and wavefront correction are studied by choosing a magnitude for the non-dimensional quantity  $|\underline{v}| \tau / r_0 = v \tau / r_0$ , where  $\underline{v}$  is the velocity of the turbulence layers and  $\tau$  is the time delay between wavefront sensing and reconstruction. For illustration purposes we assume  $\underline{v}$  is in a

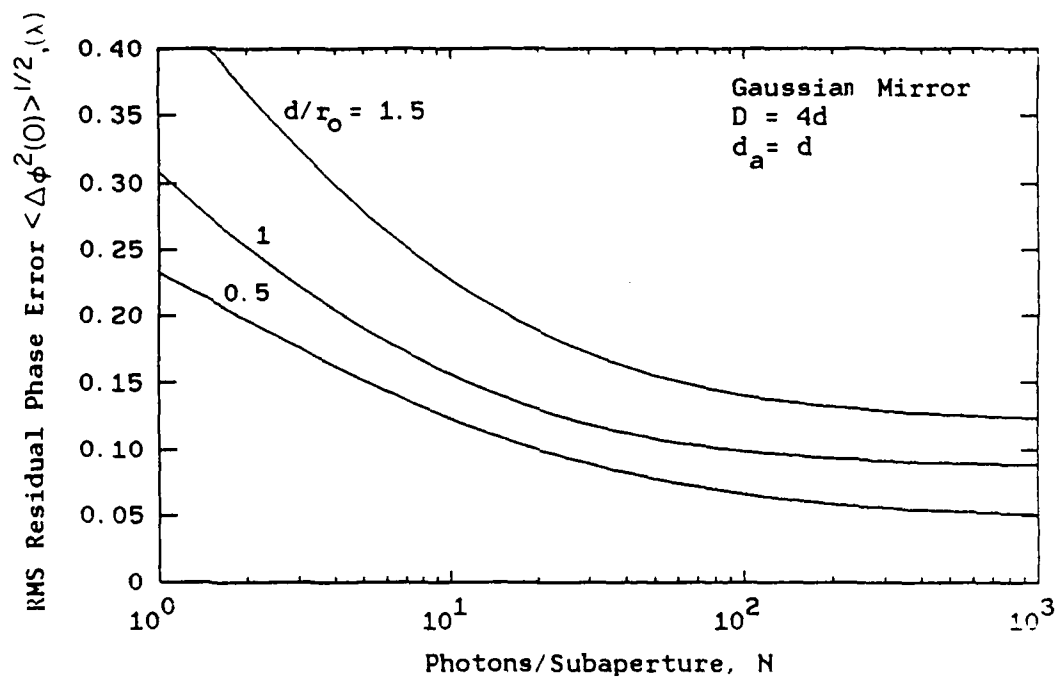


Figure 3.6a. Average RMS residual phase error versus photocounts/subaperture for the Gaussian mirror response function. The subaperture size ranges from  $d = 1.5r_0$  to  $0.5r_0$ . The other parameters are constant:  $D = 4d$  and  $\tau = 0$ .

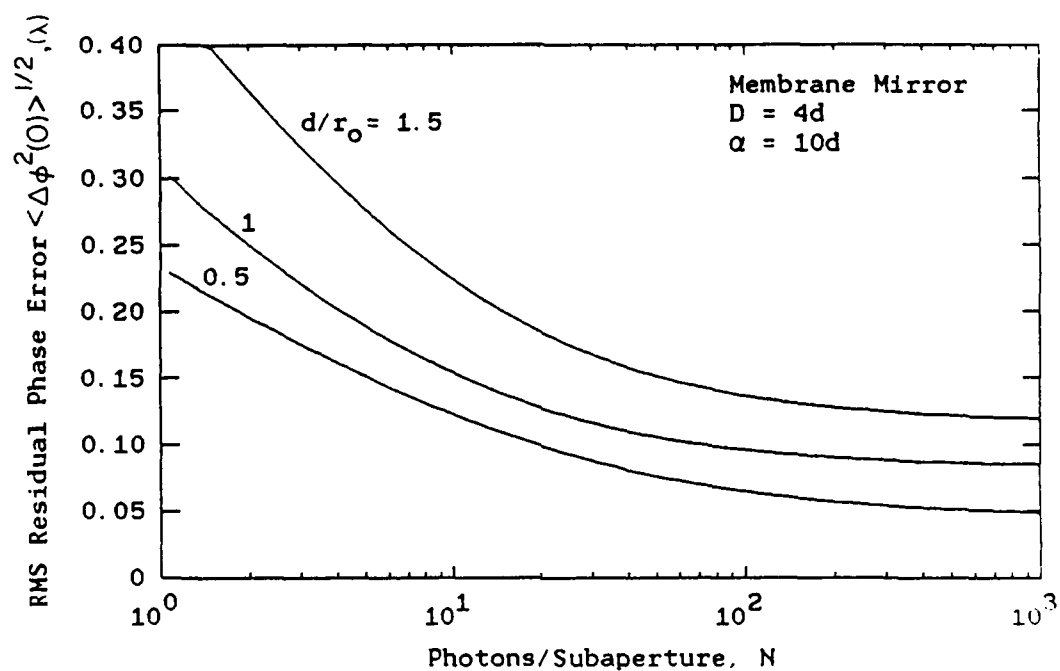


Figure 3.6b. Average RMS residual phase error versus photocounts/subaperture for the membrane mirror response function. The subaperture size ranges from  $d = 1.5r_0$  to  $0.5r_0$ . The other parameters are constant:  $D = 4d$  and  $\tau = 0$ .

direction perpendicular to an edge of the aperture (see Figure 3.3). Figure 3.7 illustrates a plot of  $\langle \Delta \phi^2(\tau) \rangle^{1/2}$  versus photons/subaperture  $N$  for  $v\tau/r_0$  ranging from 0 to 2.5. The aperture size  $D$  and subaperture size  $d$  are held constant at values of  $4d$  and  $r_0$ , respectively. Not until  $v\tau/r_0$  becomes greater than  $\sim 0.5$  do we see a significant degradation in imaging performance. This value of  $v\tau/r_0$  corresponds to the point at which the turbulence has moved a significant fraction (i.e.,  $1/2$ ) of a seeing cell diameter  $r_0$ . Assume, for example,  $v = 50$   $r_0/s$ , which corresponds to a wind speed of 10 m/s for  $r_0 = 20$  cm. For this speed, time delays on the order of 10 ms or less between wavefront sensing and reconstruction result in minimal degradation of imaging performance.

2) Average Optical Transfer Function,  $\langle H(\rho) \rangle$ : We now compute average OTF  $\langle H(\rho) \rangle$  given by Equation (3.29). In addition to the average OTF, we also consider the average PSF and the Strehl ratio. The PSF is related to the OTF by the two-dimensional inverse Fourier transform:<sup>6,7</sup>

$$\langle s(u/\lambda f_D, v/\lambda f_D) \rangle = \frac{F_2^{-1}(\langle H(x, y) \rangle)}{(\lambda f_D)^2} \quad (3.41)$$

where  $s(u/\lambda f_D, v/\lambda f_D)$  is the PSF of the optical system,  $(u, v)$  are Cartesian coordinates in the image plane of the aperture,  $(x, y)$  are Cartesian coordinates in the pupil plane, and the operator  $F_2^{-1}$  is the two-dimensional inverse Fourier transform. In an effort to reduce the amount of computation time required, the one-dimensional PSF is

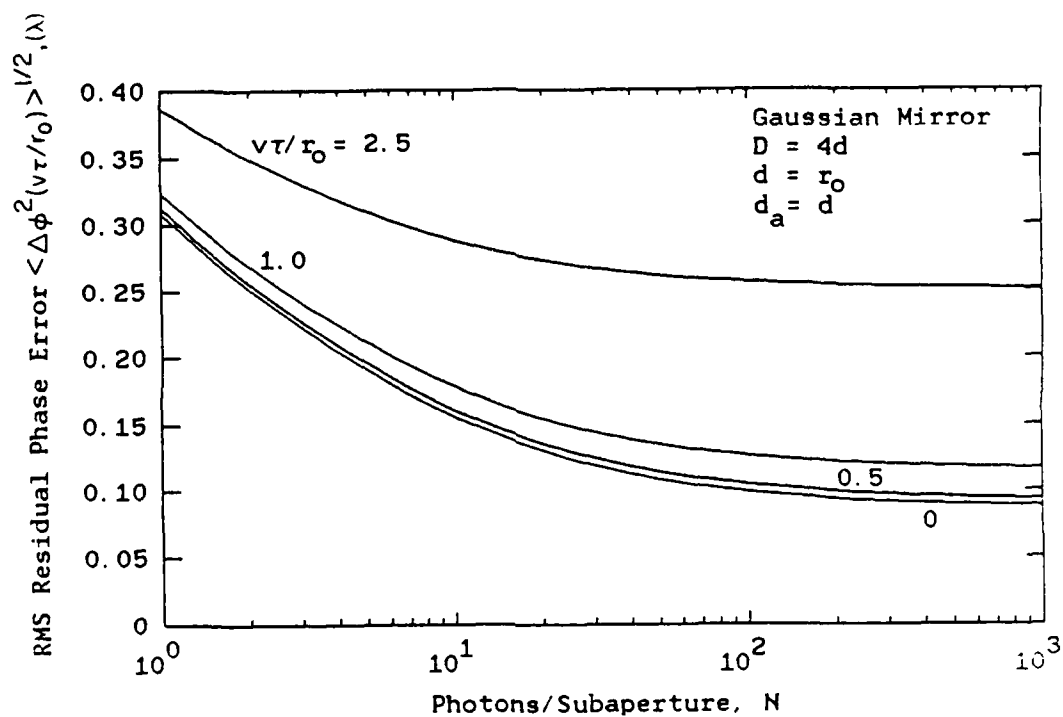


Figure 3.7. Average RMS residual phase error versus subaperture photon count. The dimensionless quantity  $v\tau/r_0$  ranges from 0 to 2.5. The other parameters are constant:  $D=4L$ , and  $L=r_0$ .

calculated instead. The one-dimensional PSF is related to the two-dimensional PSF by

$$\begin{aligned}
 \langle s(u/\lambda f_d) \rangle &= \int dv \langle s(u/\lambda f_d, v/\lambda f_d) \rangle \\
 &= \int dx \frac{\langle H(x, 0) \rangle}{\lambda f_d} \exp \left[ j 2 \pi x \left( \frac{u}{\lambda f_d} \right) \right] \\
 &= \frac{F_1^{-1}(\langle H(x, 0) \rangle)}{\lambda f_d}
 \end{aligned} \tag{3.42}$$

where the operator  $F_1^{-1}$  is the one-dimensional inverse Fourier transform.

Rather than consider all the aperture sizes addressed in 1) above, we consider only the size  $D = 4d$  in the subsequent results. The results of the computations are presented as plots of the magnitude of the OTF versus  $|\underline{\rho}|/D = \rho/D$ . Recall that spatial frequency  $v$  (cycles/meter) is related to  $\rho$  by  $v = \rho/\lambda f_d$  where  $f_d$  is the focal length of the aperture lens. In all cases, the vector  $\underline{\rho}$  is assumed in the  $x$  or  $y$  directions giving  $\langle H(\underline{\rho}) \rangle = \langle H(x, 0) \rangle$ , or equivalently  $\langle H(\underline{\rho}) \rangle = \langle H(0, y) \rangle$ .

We begin by assuming the time delay  $\tau$  is zero and examine the effects of sensor noise and subaperture spacing. First consider the effects of sensor noise. Figures 3.8a and 3.8b illustrate OTF curves for the two wavefront correction systems. Each curve corresponds to



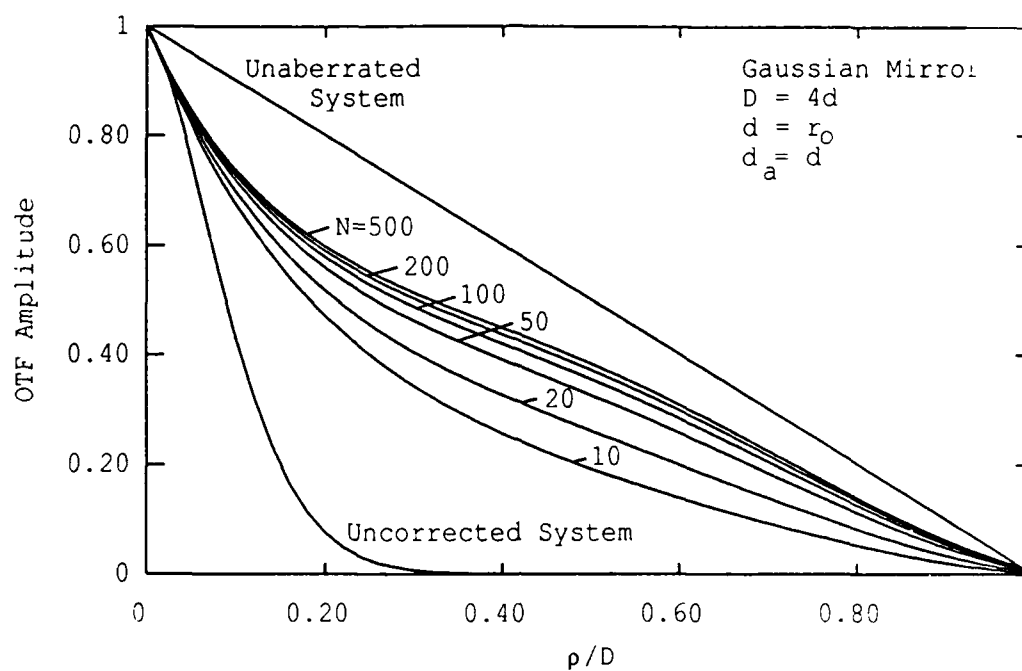


Figure 3.8a. OTF for the system using the Gaussian mirror response function. The photocounts/subaperture ranges from 10 to 500. The other parameters are constant:  $D=4d$ ,  $d=r_0$ ,  $\tau=0$ .

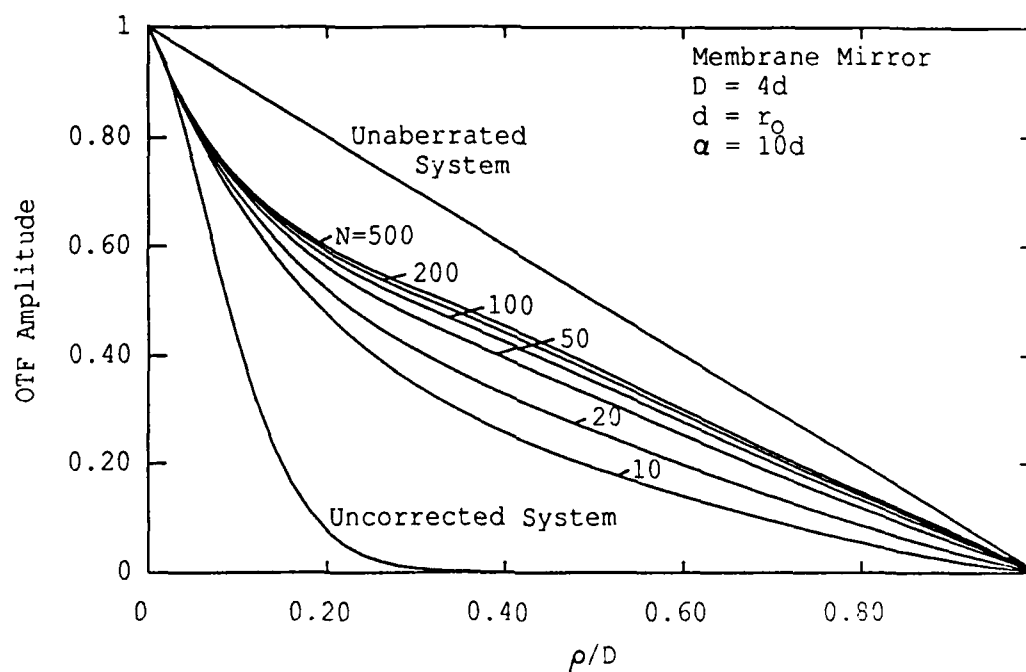


Figure 3.8b. OTF for the system using the membrane mirror response function. The photocounts/subaperture ranges from 10 to 500. The other parameters are constant:  $D=4d$ ,  $d=r_0$ ,  $\tau=0$ .

photocount/subaperture levels ranging from  $N = 10$  to 500. The uppermost curve in both figures is the OTF of the perfect unaberrated system. The bottom-most curve is the OTF for the aberrated system, assuming no wavefront correction. Even for a count as low as  $N=10$  the OTF for the partially corrected aperture demonstrates considerable improvement over that of no correction. As the photon count increases, the frequency responses show steady improvement until converging to an upper limit. This same convergence was also seen in Figures 3.5 and 3.6 for the residual phase error. For our particular sensor and mirror configurations the improvement in the OTF beyond 100 to 200 counts per subaperture is marginal. Figures 3.9a and 3.9b illustrate the corresponding one-dimensional PSFs for the OTFs illustrated in Figure 3.8. The amplitude of the PSF is plotted versus the dimensionless quantity  $uD/\lambda f_D$ , where  $u$  is the image plane coordinate. The PSF for both the unaberrated system and the aberrated system with no wavefront correction are shown. The interesting thing to notice from these curves is that the resolution (i.e., width of the PSF main lobe) does not significantly degrade from that of the unaberrated system for decreasing photon flux levels. The Strehl ratio, on the other hand, shows considerable degradation in performance as sensing accuracy decreases. The Strehl ratio is plotted in Figure 3.10 versus  $N$ . Recall the Strehl ratio compares the peak of the intensity of the PSF to that of an unaberrated system, and is an indication of how well the peak intensity can be discerned from the surrounding intensity distribution. The ratio drops from a value of nearly 0.8 for 500 photocounts/subaperture to  $\sim 0.54$  for 10 photocounts/subaperture.

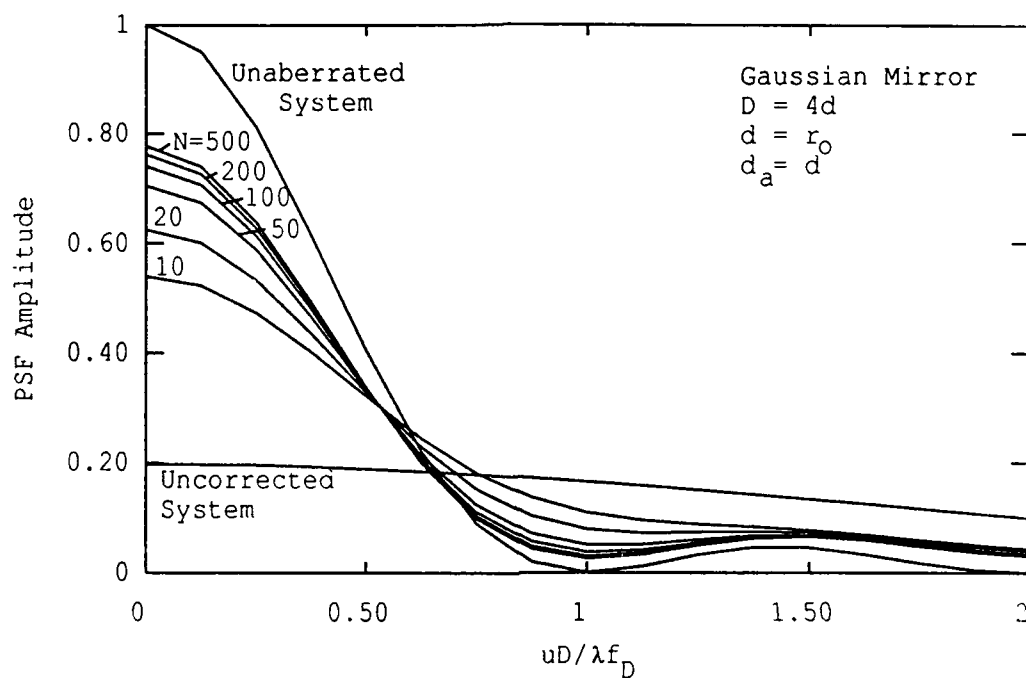


Figure 3.9a. PSF for the system using the Gaussian mirror response function. The photocounts/subaperture ranges from 10 to 500. The other parameters are constant:  $D=4d$ ,  $d=r_0$ ,  $\tau=0$ .

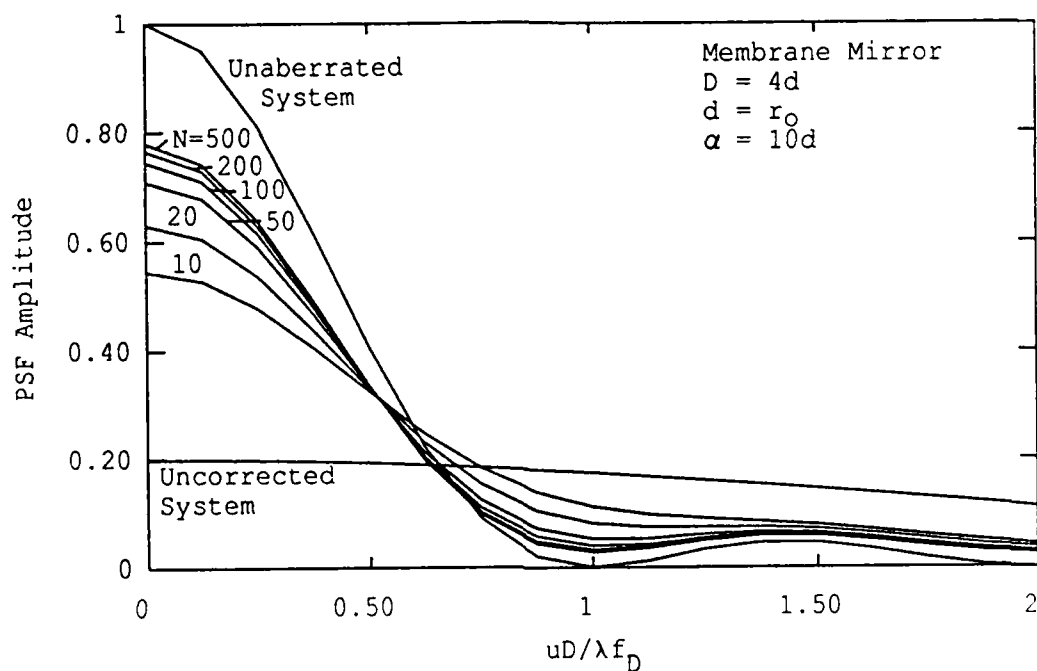


Figure 3.9b. PSF for the system using the membrane mirror response function. The photocounts/subaperture ranges from 10 to 500. The other parameters are constant:  $D=4d$ ,  $d=r_0$ ,  $\tau=0$ .

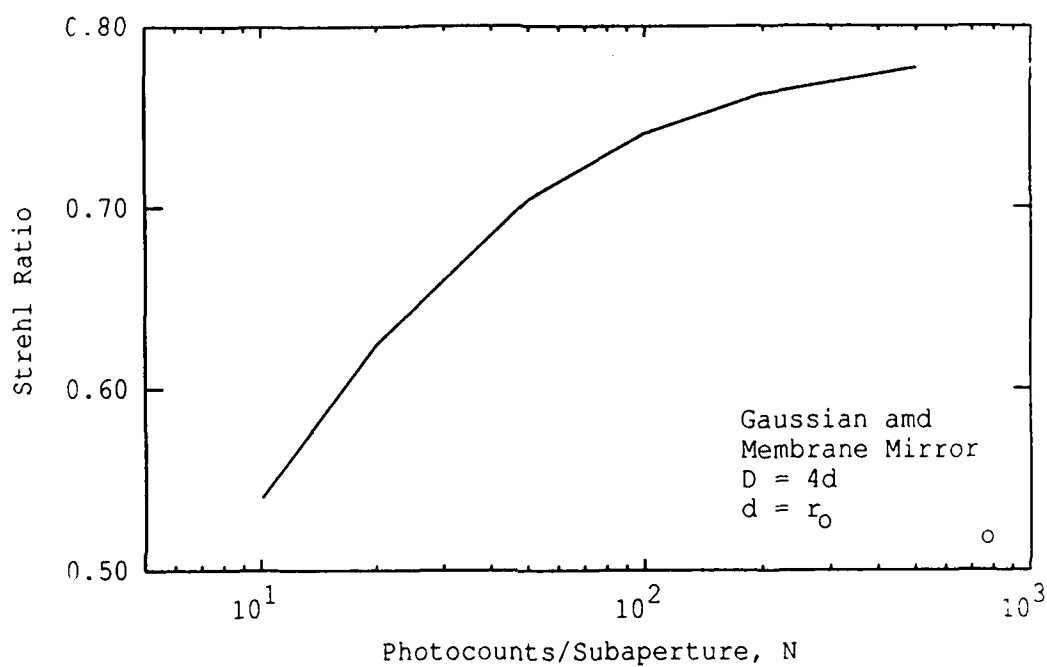


Figure 3.10. Strehl ratio versus photocounts/subaperture for either the Gaussian or membrane mirror response functions. The other parameters are constant:  $D=4d$ ,  $d=r_0$ ,  $\tau=0$ .

It is interesting to note from the data shown in Figures 3.8 and 3.9 that both correction systems perform nearly identically. This was also seen for the residual phase error shown in Figures 3.5 and 3.6. This similarity in performance is not surprising, considering the similarity of the two mirror response functions  $r_j(\underline{x})$  in the region near the center of the actuator. The response functions differ considerably in regions away from the actuator center, but the contribution to the overall shape of the mirror from these distant points is small compared to that of the center. Since the two mirrors perform nearly identically, only the Gaussian mirror response is considered in the subsequent computations.

We now consider the effect of varying subaperture size. Figures 3.11 and 3.12 illustrate the OTF and PSF for subaperture sizes ranging from  $d = 0.5r_0$  to  $1.5r_0$ . The photocount/subaperture level  $N$  is held constant at a value of 500 (resulting in insignificant slope measurement noise). These results illustrate the advantage of sampling the aperture with smaller and smaller subapertures. The peak magnitude of the PSF improves considerably as the subaperture size is decreased. Again, the interesting thing to notice from these curves is that resolution (width of the PSF main lobe) does not significantly degrade from that of an unaberrated system for increasing subaperture size. The FWHM of the PSF main lobe is approximately the same for each value of  $d$ . This result was also found by Smithson et al.<sup>71, 72</sup> in a performance simulation of a 19-element segmented mirror. They found no significant loss in resolution (as measured by the FWHM of the PSF) as

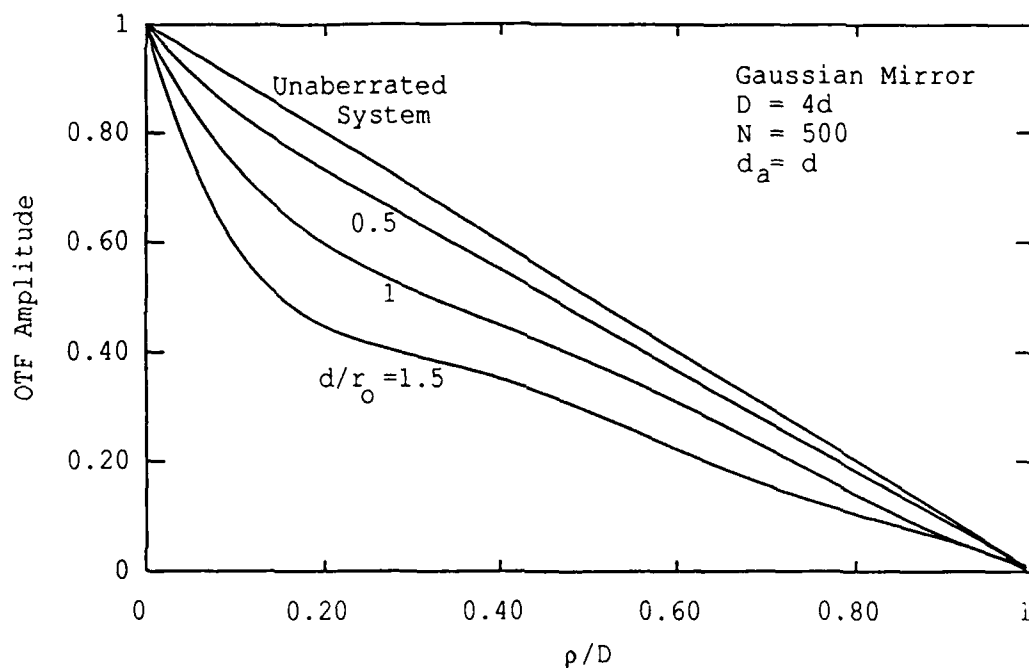


Figure 3.11. OTF for the system using the Gaussian mirror response function. The subaperture size ranges from  $d = 1.5r_0$  to  $0.5r_0$ . The other parameters are constant:  $D = 4d$ ,  $\tau = 0$ ,  $N = 500$ .



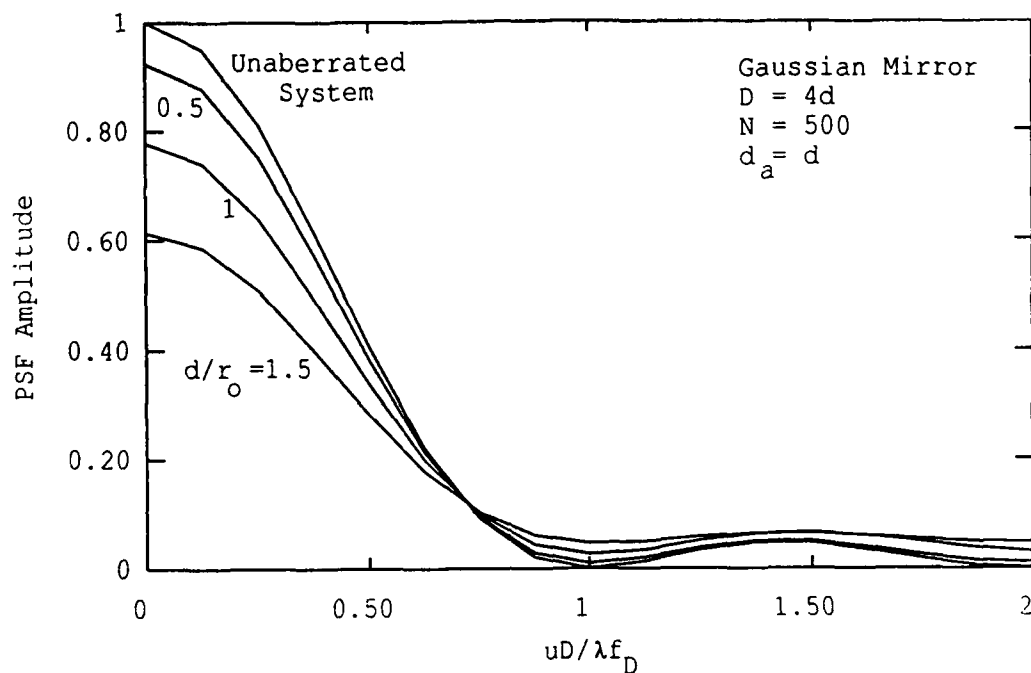


Figure 3.12. PSF for the system using the Gaussian mirror response function. The subaperture size ranges from  $d = 1.5r_0$  to  $0.5r_0$ . The other parameters are constant:  $D = 4d$ ,  $\tau = 0$ ,  $N = 500$ .

the subaperture size was increased from approximately  $r_0$  to  $6r_0$ . They did find, though, that the Strehl ratio degrades rapidly as the subaperture size is increased. We also find this true as illustrated by Figure 3.13. The Strehl ratio drops from a value of approximately 0.9 for  $d/r_0 = 0.5$  to a value of approximately 0.6 for  $d/r_0 = 1.5$ .

The effect of a nonzero time delay  $\tau$  on the average OTF is not considered. Since the time domain fluctuations of the wavefront phase are caused by the velocity of the turbulence layers, we find that  $\langle H(\underline{\rho}) \rangle$  depends on the direction of  $\underline{v}$  and  $\underline{\rho}$ . For example, if  $\underline{\rho}$  is in the x-direction,  $\langle H(\underline{\rho}) \rangle$  and  $\langle H(-\underline{\rho}) \rangle$  are not equal for any  $\underline{v}$  having a nonzero x-component. The OTF is spatially invariant with respect to  $\underline{v}$ , and the meaning of  $\langle H(\underline{\rho}) \rangle$  becomes impossible to interpret.

### 3.8 Summary

We have derived an expression for the average optical transfer function of an adaptive optics system using slope sensors. The adaptive optics system consists of an aperture, a wavefront slope sensor, a deformable mirror, and a linear control law. The nonideal characteristics typical of these components are incorporated in the analysis by realistically modeling the slope sensors, the deformable mirror and the photon noise in the wavefront sensor.

A problem not addressed in this analysis is the effects of anisoplanatism, which limits the FOV over which the wavefront compensations are effective, thereby limiting the effective FOV

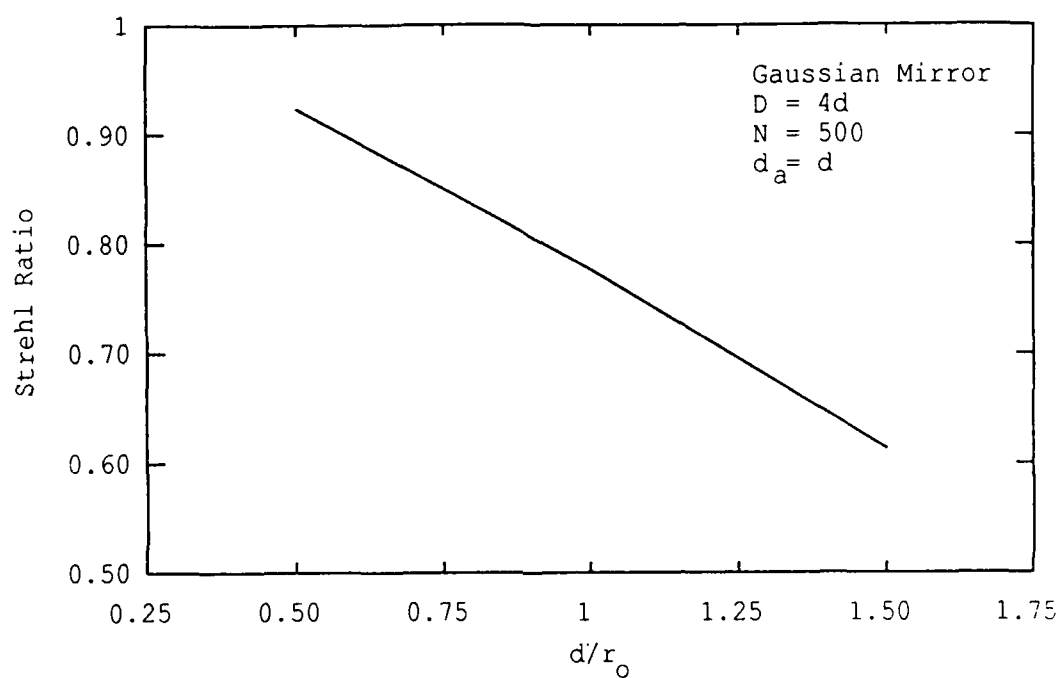


Figure 3.13. Strehl ratio versus  $d/r_0$  for the Gaussian response function. The other parameters are constant:  $D=4d$ ,  $\tau=0$ ,  $N=500$ .

of the adaptive telescope. The impact of anisoplanatism on the design of laser-guided telescopes is addressed in Chapter 5.

#### 4. NONLINEAR RESONANT ABSORPTION EFFECTS ON THE DESIGN OF RESONANCE FLUORESCENCE LIDARS AND LASER GUIDE STARS

##### 4.1 Introduction

Many areas of research rely on pulsed laser systems to excite the resonant frequency of selected atoms in a medium. Examples include resonant fluorescence lidars which are used to study the upper atmosphere metal layers<sup>32,36-40,73,74</sup> and laser guide star techniques for use in adaptive imaging in astronomy. For both of these applications the laser beam is tuned to the resonant frequency of the atoms, giving rise to resonant absorption and fluorescence. In certain situations these systems may experience a significant reduction in the backscattered signal due to saturation effects. Saturation arises when the energy density within the scattering medium is large enough to significantly alter the population densities of the atomic states. In terms of a simple two-state system, a large energy density can significantly reduce the number of lower state atoms while increasing the number of excited state atoms. These altered state populations lead to nonlinear absorption of the laser energy, which results in an increased rate of stimulated emission and a reduced rate of fluorescence. The combined effect is a reduction in the backscattered energy. Laser guide star systems are particularly vulnerable to saturation effects because of the large energy densities required to create a sufficiently bright guide star. The guide star must be small enough to approximate a point source, while at the same time bright enough to provide adequate signal-to-noise ratios in the wavefront sensor. For both lidar and guide star applications, choosing the laser

parameters to minimize saturation becomes an important consideration in the system design.

Saturation effects for pulsed lasers have been quantified by Megie,<sup>73</sup> Cardinal<sup>75</sup> and Measures.<sup>76,77</sup> These authors limited their analyses to scattering media characterized by homogeneous broadening of the atom's absorption line, or equivalently, applications employing broad line width lasers. They also restricted their attention to uniformly illuminated media. We build on this previous work by quantifying saturation effects for an inhomogeneously broadened absorption line and an arbitrary laser beam cross section. Doppler broadening of the absorption line is an important example of inhomogeneous broadening. This type of broadening dominates homogeneous broadening for many media, including the mesospheric metal layers. The importance of allowing for inhomogeneous broadening will become evident for narrow line width lasers. The effects of an arbitrary laser pulse shape and laser line profile are also included in the analysis.

In Section 4.2 we introduce the rate equation describing the upper state atomic density for a medium illuminated by a laser pulse. The solution of the equation is used to quantify the effect of saturation on a pulsed laser system in terms of the reduction in fluorescence backscatter. The section concludes by evaluating the reduction in backscattered flux for three specific combinations of laser pulse shape and beam cross section. In Section 4.3 these results are used to

illustrate the effect on saturation for changing values of the laser pulse length, pulse energy, beamwidth, and line width. Finally, in Section 4.4, laser design examples are presented for both lidar and laser guide star applications.

#### 4.2 Population State Rate Equation and Specific Solutions

We begin our analysis by defining a simple two-state model for the atomic transitions associated with absorption and fluorescence. An atom in the lower energy state is excited to the upper state by absorbing a photon, and an atom in the upper state deexcites to the lower state by either spontaneous or stimulated emission. Use of this model implies that the effects of collisionally induced transitions are negligible. This is a reasonable assumption if the mean time between collisions is relatively long compared to the natural decay time of the atoms. In particular, the model is an excellent representation of the atomic transitions for the mesospheric Na layer where the mean time between collisions is approximately 10  $\mu$ s compared to a natural decay time of 16 ns.

We next consider the laser and scattering medium. The geometric relationship between the two is shown in Figure 4.1. A laser beam passes through a thin layer of the medium. The thickness of the layer is  $\Delta z$  and the density is assumed constant. The scattered energy due to fluorescence is detected by a receiver a distance  $z$  from the layer.

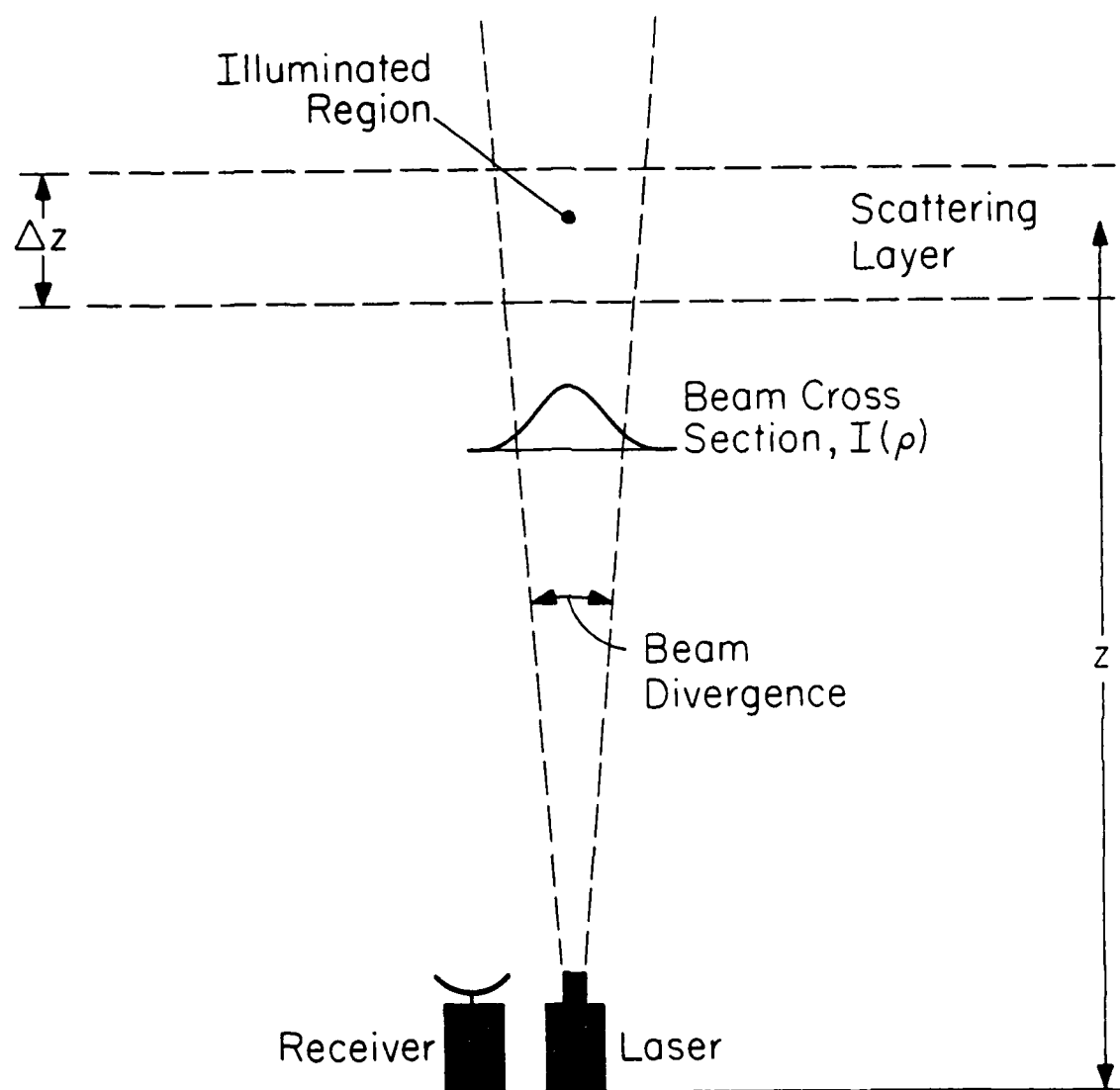


Figure 4.1. Geometry between the laser, receiver, and scattering layer.



The laser pulse is described in time ( $t$ ), space ( $\underline{\rho}$ ), and angular frequency ( $\omega$ ) by  $p(t, \underline{\rho}, \omega)$  ( $\text{m}^{-2} \text{rad}^{-1}$ ). The pulse  $p(t, \underline{\rho}, \omega)$  is the photon flux density per unit time and per unit angular frequency. The magnitude of the two-dimensional vector  $\underline{\rho}$  is the radial distance from the laser beam center in the plane perpendicular to the beam axis. The energy absorbed and scattered by each atom is characterized by the absorption cross section  $\sigma$  ( $\text{m}^2$ ). The cross section  $\sigma$  is a function of angular frequency and essentially represents the cross-sectional area that the atom presents to the incident beam for scattering.

Megie<sup>73</sup> gives the rate equation for the density of upper state atoms. Here, this rate equation is generalized to include the effects of inhomogeneous broadening and an arbitrary beam cross section. The distribution of upper state atoms  $n_u$  for an arbitrary temporal pulse shape, beam cross section and line profile is given by

$$\begin{aligned} \frac{\partial n_u(t, \underline{\rho}, \omega_d)}{\partial t} = & \frac{-n_u(t, \underline{\rho}, \omega_d)}{\tau_n} \\ & + \left( n(\omega_d) - n_u(t, \underline{\rho}, \omega_d) \right) T_a \int_{-\infty}^{\infty} \sigma(\omega' - \omega_d) p(t, \underline{\rho}, \omega') d\omega' \\ & - n_u(t, \underline{\rho}, \omega_d) \propto T_a \int_{-\infty}^{\infty} \sigma(\omega' - \omega_d) p(t, \underline{\rho}, \omega') d\omega', \end{aligned} \quad (4.1)$$

where

$t$  = time (s),

$\underline{\rho}$  = two-dimensional vector describing the radial position relative to the laser beam axis,

$\omega_d$  = Doppler angular frequency shift associated with a given atom (rad/s),

$n_u(t, \underline{\rho}, \omega_d)$  = density of excited state atoms per unit Doppler angular frequency shift ( $\text{m}^{-3} \text{rad}^{-1} \text{s}$ ),

$n(\omega_d)$  = total density of atoms per unit Doppler angular frequency shift ( $\text{m}^{-3} \text{rad}^{-1} \text{s}$ ),

$\tau_n$  = natural lifetime of an excited state atom (s),

$T_a$  = atmospheric transmission associated with the one-way path from the laser to the scattering layer,

$\alpha = g_1/g_2$ , the ratio of the degeneracies for the lower and upper states,  $g_1$  and  $g_2$ , respectively,

$\sigma(\omega)$  = absorption cross section ( $\text{m}^2$ ).

The distributions  $n(\omega_d)$ , and  $p(t, \underline{\rho}, \omega)$  satisfy

$$\int_{-\infty}^{\infty} n(\omega_d) d\omega_d = n_o, \quad (4.2)$$

and

$$\int_{-\infty}^{\infty} dt \int_{-\infty}^{\infty} \int_{-\infty}^{\infty} d^2 \underline{\rho} \int_{-\infty}^{\infty} d\omega p(t, \underline{\rho}, \omega) = N_L, \quad (4.3)$$

where  $n_0$  is the total atomic density of scatters ( $\text{m}^{-3}$ ) and  $N_L$  is the total number of photons emitted by the laser per pulse. The terms on the right-hand side of Equation (4.1) can be attributed to the rate of atomic transitions due to emission or absorption. In particular, the first and third terms describe the rate of decrease of the upper state density due to spontaneous and stimulated emission, respectively. The second term is the rate of increase of the upper state density due to absorption.

The effects of both homogeneous and inhomogeneous broadening of the absorption line are included in Equation (4.1). The absorption cross section  $\sigma(\omega)$  describes the effect of homogeneous broadening, whereas the atomic density  $n(\omega_d)$  describes the effect of inhomogeneous broadening. Homogeneous broadening results from the finite lifetimes of the excited state atoms. Inhomogeneous broadening, in this case, is assumed to be due to the thermal motions of the atoms. This motion gives rise to the Doppler distribution  $n(\omega_d)$ , which relates the distribution of radial speeds of the atoms to a distribution in Doppler frequency shifts. The effect of Doppler broadening is included in the analysis by writing Equation (4.1) as a function of Doppler angular frequency  $\omega_d$ .

When the laser pulse can be modeled as separable in time, space, and frequency, a solution to Equation (4.1) is easily obtained. This model is reasonable for many lasers (excluding very short pulse, narrow

line width lasers) and is an often used simplification. Assuming  $p(t, \underline{\rho}, \omega)$  is separable, we can write

$$p(t, \underline{\rho}, \omega) = N_L(t) I(\underline{\rho}) g(\omega), \quad (4.4)$$

where

$N_L(t)$  = total number of photons emitted per unit time ( $s^{-1}$ ),

$I(\underline{\rho})$  = distribution of the photon flux per unit area ( $m^{-2}$ ),

$g(\omega)$  = distribution of the photon flux per unit frequency  
( $rad^{-1}s$ ),

and the following relationships hold:

$$\int_{-\infty}^{\infty} N_L(t) dt = N_L, \quad (4.5)$$

$$\int_{-\infty}^{\infty} \int_{-\infty}^{\infty} I(\underline{\rho}) d^2 \underline{\rho} = 1, \quad (4.6)$$

$$\int_{-\infty}^{\infty} g(\omega) d\omega = 1. \quad (4.7)$$

Throughout the remaining sections the functions  $N_L(t)$ ,  $I(\underline{\rho})$  and  $g(\omega)$  will be referred to as the laser temporal pulse shape, beam cross section, and line profiles, respectively.

The separation of  $p(t, \underline{\rho}, \omega)$  allows Equation (4.1) to be simplified by defining an effective absorption cross section  $\sigma_{eff}(\omega_d)$

$$\sigma_{eff}(\omega_d) = \int_{-\infty}^{\infty} \sigma(\omega - \omega_d) g(\omega) d\omega, \quad (4.8)$$

where  $\sigma_{eff}(\omega_d)$  is simply the absorption cross section for those atoms experiencing a Doppler frequency shift  $\omega_d$  weighted by the laser energy at the corresponding frequency. Substituting Equation (4.8) into Equation (4.1), a compact form of the rate equation is obtained:

$$\begin{aligned} \frac{\partial n_u(t, \underline{p}, \omega_d)}{\partial t} = & -n_u(t, \underline{p}, \omega_d) \left( \frac{1}{\tau_n} + (1+\alpha) \sigma_{eff}(\omega_d) T_a I(\underline{p}) N_L(t) \right) \\ & + n(\omega_d) \sigma_{eff}(\omega_d) T_a I(\underline{p}) N_L(t). \end{aligned} \quad (4.9)$$

The general solution to Equation (4.9) for zero initial conditions is

$$\begin{aligned} n_u(t, \underline{p}, \omega_d) = & \int_0^t \exp \left[ - \int_{\tau}^t \left( \frac{1}{\tau_n} + (1+\alpha) \sigma_{eff}(\omega_d) T_a I(\underline{p}) N_L(\gamma) \right) d\gamma \right] \\ & n(\omega_d) \sigma_{eff}(\omega_d) T_a I(\underline{p}) N_L(\tau) d\tau, \end{aligned} \quad (4.10)$$

where the laser temporal pulse  $N_L(t)$  is assumed zero for  $t < 0$ .

Ultimately, we want to relate the solution in Equation (4.10) to the reduction in backscattered energy for a lidar configuration such as that shown in Figure 4.1. This reduction is quantified by calculating the ratio of the actual detected counts per pulse  $N_R$  to the detected counts per pulse for no saturation  $N_{R0}$ . The counts  $N_R$  and  $N_{R0}$  are

given by<sup>73</sup>

$$N_R = \frac{\eta A_r T_a \Delta z}{4\pi z^2} \int_{-\infty}^{\infty} d\omega_d \int_{-\infty}^{\infty} \int_{-\infty}^{\infty} d^2 \underline{\rho} \int_{-\infty}^{\infty} dt \frac{n_u(t, \underline{\rho}, \omega_d)}{\tau_n}, \quad (4.11)$$

and

$$N_{Ro} = \frac{\eta A_r T_a^2 \Delta z n_o \sigma_t N_L}{4\pi z^2}, \quad (4.12)$$

where

$A_r$  = the receiving aperture area ( $m^2$ ),

$\eta$  = the efficiency of the receiver,

$\Delta z$  = the thickness of the scattering layer (m),

$z$  = the distance between the scattering layer and the receiver  
(m),

$\sigma_t$  = the total effective absorption cross section of the atoms  
( $m^2$ ).

The total effective cross section  $\sigma_t$  introduced in Equation (4.12) is related to  $\sigma_{eff}(\omega_d)$  by

$$\sigma_t = \int_{-\infty}^{\infty} \frac{n(\omega_d)}{n_o} \sigma_{eff}(\omega_d) d\omega_d. \quad (4.13)$$

In writing Equations (4.11) and (4.12) we have assumed that the spontaneous emission is isotropic. Any anisotropic effects in the

scattering are included in the calculation of the absorption cross section  $\sigma(\omega)$ . Substituting Equation (4.10) into Equation (4.11) gives

$$N_R = \frac{\Delta t_{rms}}{\tau_n} \int_{-\infty}^{\infty} d\omega_d \int_{-\infty}^{\infty} \int_{-\infty}^{\infty} d^2 \underline{\rho} \int_0^{\infty} dt \int_0^{\tau} d\tau \exp \left[ \frac{\Delta t_{rms}}{\tau_n} (\tau - t) \right. \\ \left. + \frac{(1+\alpha) \sigma_{eff}(\omega_d) T_a N_L \hat{I}(\underline{\rho})}{\Delta \rho_{rms}^2} \int_t^{\tau} \hat{N}_L(\gamma) d\gamma \right] \\ N_{Ro}(\omega_d) \hat{I}(\underline{\rho}) \hat{N}_L(\tau), \quad (4.14)$$

where  $I(\underline{\rho})$ ,  $N_L(t)$  and  $g(\omega)$  have been expressed in terms of the dimensionless equivalents  $\hat{I}(\underline{\rho}')$ ,  $\hat{N}_L(t')$  and  $\hat{g}(\omega')$ :

$$\hat{I}(\underline{\rho}') = \Delta \rho_{rms}^2 I(\underline{\rho}' \Delta \rho_{rms}), \quad (4.15)$$

$$\hat{N}_L(t') = \frac{\Delta t_{rms} N_L(t' \Delta t_{rms})}{N_L}, \quad (4.16)$$

$$\hat{g}(\omega') = \Delta \omega_{rms} g(\omega' \Delta \omega_{rms}). \quad (4.17)$$

The arguments  $\underline{\rho}'$ ,  $t'$  and  $\omega'$  are dimensionless, and the parameters  $\Delta t_{rms}$ ,  $\Delta \rho_{rms}$  and  $\Delta \omega_{rms}$  are the rms pulse length, rms beam radius and rms line width, respectively. The distribution  $N_{Ro}(\omega_d)$  in Equation (4.14) is the unsaturated count as a function of Doppler frequency  $\omega_d$

$$N_{Ro}(\omega_d) = \frac{\eta A_r T_a^2 \Delta z n(\omega_d) \sigma_{eff}(\omega_d) N_L}{4\pi z^2}. \quad (4.18)$$

At this point it is useful to define the average photon flux density  $I_s$  and the saturation time  $\tau_s$

$$I_s = \frac{N_L T_a}{\pi \Delta \rho_{rms}^2}, \quad (4.19)$$

$$\tau_s = \frac{2\sqrt{12} \Delta t_{rms} \pi \Delta \rho_{rms}^2}{N_L T_a \sigma_t}. \quad (4.20)$$

The saturation time  $\tau_s$  was first defined by Megie<sup>73</sup> and is a measure of the characteristic time of stimulated emission. The ratio  $\tau_s/\tau_n$  indicates the level of saturation within the layer. A large ratio implies that the natural decay time is much faster than the characteristic time of stimulated emission. In this case, the rate of stimulated emission is much smaller than the rate of natural decay, which results in negligible saturation effects. On the other hand, a small ratio implies the rate of stimulated emission is much larger than the rate of natural decay, which results in significant saturation effects. Incorporating  $\tau_s$  and  $I_s$  into Equation (4.14) and taking the ratio  $N_R/N_{R0}$  give

$$\begin{aligned} \frac{N_R}{N_{R0}} = & \int_{-\infty}^{\infty} d\omega_d \int_{-\infty}^{\infty} \int_{-\infty}^{\infty} d^2 \underline{\rho} \int_0^{\infty} dt \int_0^t d\tau \frac{\tau_s I_s n(\omega_d) \sigma_{eff}(\omega_d)}{2\sqrt{12} \tau_n n_0} \\ & \exp \left[ \frac{\tau_s \sigma_t I_s}{2\sqrt{12} \tau_n} (\tau - t) + (1 + \alpha) \pi \sigma_{eff}(\omega_d) I_s \hat{I}(\underline{\rho}) \int_t^{\tau} \hat{N}_L(\gamma) d\gamma \right] \\ & \hat{N}_L(\tau) \hat{I}(\underline{\rho}). \end{aligned} \quad (4.21)$$



Equation (4.21) is the main result of this section. It describes the effect of saturation on a pulsed laser system for an arbitrary pulse shape  $\hat{N}_L(t)$ , beam cross section  $\hat{I}(\underline{\rho})$  and spectral line profile  $\hat{g}(\omega)$  (recall  $\sigma_{eff}(\omega_d)$  is a function of  $\hat{g}(\omega)$ ). The ratio  $N_R/N_{R0}$  is equivalent to the ratio  $\sigma_s/\sigma_t$ , where  $\sigma_s$  was introduced in Chapter 2 to designate the generalized scattering cross section in the case of non-negligible saturation. If the functional forms of  $\hat{I}(\underline{\rho})$ ,  $\hat{N}_L(t)$  and  $\hat{g}(\omega)$  are known, Equation (4.21) becomes a function of only  $\tau_s$ ,  $I_s$  and  $\Delta\omega_{rms}$  ( $\sigma_{eff}(\omega_d)$  is also a function of  $\Delta\omega_{rms}$ ). As will be seen later, the dependence of Equation (4.21) on  $I_s$  becomes negligible for  $\Delta t_{rms} \gg \tau_n$ . In this case, the two remaining parameters,  $\tau_s$  and  $\Delta\omega_{rms}$ , completely determine the effect of pulse length, pulse energy, beamwidth and line width on saturation. To illustrate this dependence, Equation (4.21) is evaluated for three specific combinations of beam cross section and pulse shape.

#### CASE 1. Uniform Beam Cross Section and Rectangular Pulse Shape.

For this case  $N_L(t)$  is given by a rectangular pulse and  $I(\underline{\rho})$  is given by a uniform beam cross section

$$N_L(t) = \begin{cases} \frac{N_L}{\Delta t} & 0 < t < \Delta t \\ 0 & \text{elsewhere,} \end{cases} \quad (4.22)$$

$$I(\underline{\rho}) = \begin{cases} \frac{1}{\pi \Delta \rho^2} & 0 < |\underline{\rho}| < \Delta \rho \\ 0 & \text{elsewhere,} \end{cases} \quad (4.23)$$

where  $\Delta t$  is the length of the pulse and  $\Delta \rho$  is the radius of the beam. The rms length of the rectangular pulse is  $\Delta t_{\text{rms}} = \Delta t/\sqrt{12}$ . For our purpose we define the rms radius of the beam  $\Delta \rho_{\text{rms}}$  as the second moment of the distribution that results from integrating  $I(\underline{\rho})$  over one dimension of the plane defined by  $\underline{\rho}$ . The rms radius of the uniform beam cross section is  $\Delta \rho_{\text{rms}} = \Delta \rho/2$ . Substituting Equation (4.22) into Equation (4.16) and Equation (4.23) into Equation (4.15) gives the dimensionless functions

$$\hat{N}_L(t') = \begin{cases} \frac{1}{\sqrt{12}} & 0 < t' < \sqrt{12} \\ 0 & \text{elsewhere,} \end{cases} \quad (4.24)$$

and

$$\hat{I}(\underline{\rho}') = \begin{cases} \frac{1}{4\pi} & 0 < |\underline{\rho}'| < 2 \\ 0 & \text{elsewhere.} \end{cases} \quad (4.25)$$

Substituting Equations (4.24) and (4.25) into Equation (4.21) and performing the integration over  $\tau$ ,  $t$  and the plane defined by  $\underline{\rho}$  gives

$$\begin{aligned}
\frac{N_R}{N_{R0}} = \frac{1}{\sigma_t} & \int_{-\infty}^{\infty} \frac{n(\omega_d) \sigma_{eff}(\omega_d)}{n_o \left( 1 + \frac{\tau_n (1+\alpha) \sigma_{eff}(\omega_d)}{2\tau_s \sigma_t} \right)} \\
& \left[ 1 - \frac{1+\alpha}{\frac{\tau_s \sigma_t I_s}{\tau_n} \left( \frac{\tau_s \sigma_t}{\tau_n \sigma_{eff}(\omega_d)} + \frac{1+\alpha}{2} \right)} \right] \\
& \left\{ \exp \left( \frac{-\sigma_{eff}(\omega_d) I_s \left( \frac{\tau_s \sigma_t}{\tau_n \sigma_{eff}(\omega_d)} + \frac{1+\alpha}{2} \right)}{2} \right) - 1 \right\} d\omega_d. \quad (4.26)
\end{aligned}$$

If the pulse length  $\Delta t$  is much greater than the natural decay time  $\tau_n$ , it can be shown that  $\tau_s \sigma_t I_s / \tau_n \gg 1$  and Equation (4.26) is closely approximated by

$$\frac{N_R}{N_{R0}} = \frac{1}{\sigma_t} \int_{-\infty}^{\infty} \frac{n(\omega_d) \sigma_{eff}(\omega_d)}{n_o \left( 1 + \frac{\tau_n (1+\alpha) \sigma_{eff}(\omega_d)}{2\tau_s \sigma_t} \right)} d\omega_d. \quad (4.27)$$

## CASE 2. Gaussian Beam and Rectangular Temporal Pulse Shape.

In this case, the rectangular laser pulse shape  $N_L(t)$  is again given by Equation (4.22), and  $I(\rho)$  is given by a Gaussian beam cross section

$$I(\underline{\rho}) = \frac{1}{2\pi\Delta\rho_{rms}^2} \exp\left(\frac{-\rho^2}{2\Delta\rho_{rms}^2}\right), \quad (4.28)$$

where  $\Delta\rho_{rms}$  is the rms radius of the beam and  $\rho = |\underline{\rho}|$ . Substituting  $I(\underline{\rho})$  into Equation (4.15) gives the dimensionless function

$$\hat{I}(\underline{\rho}') = \frac{1}{2\pi} \exp\left(\frac{-\rho'^2}{2}\right). \quad (4.29)$$

Substituting the dimensionless functions for  $\hat{I}(\underline{\rho}')$  and  $\hat{N}_L(t')$  given in Equations (4.29) and (4.24) into Equation (4.21), and performing the integration over  $\tau$  and  $t$ , we obtain

$$\begin{aligned} \frac{N_R}{N_{Ro}} = \frac{1}{\sigma_t} & \int_{-\infty}^{\infty} d\omega_d \int_0^{\infty} \rho d\rho \frac{n(\omega_d) \sigma_{eff}(\omega_d) \exp(-\rho^2/2)}{n_o \left( 1 + \frac{\tau_n (1+\alpha) \sigma_{eff}(\omega_d) \exp(-\rho^2/2)}{\tau_s \sigma_t} \right)} \\ & \left[ 1 - \frac{2(1+\alpha)\exp(-\rho^2/2)}{\frac{\tau_s \sigma_t I_s}{\tau_n} \left( \frac{\tau_s \sigma_t}{\tau_n \sigma_{eff}(\omega_d)} + (1+\alpha)\exp(-\rho^2/2) \right)} \right. \\ & \left. \left\{ \exp\left(-\sigma_{eff}(\omega_d) I_s \left( \frac{\tau_s \sigma_t}{2\tau_n \sigma_{eff}(\omega_d)} + \frac{1+\alpha}{2} \exp(-\rho^2/2) \right)\right) - 1 \right\} \right]. \quad (4.30) \end{aligned}$$

If  $\Delta t$  is much greater than the natural decay time  $\tau_n$  then again

$\tau_s \sigma_t I_s / \tau_n \gg 1$  and the second term of Equation (4.30) can be neglected.

In this case

$$\frac{N_R}{N_{Ro}} = \frac{1}{\sigma_t} \int_{-\infty}^{\infty} d\omega_d \int_0^{\infty} \rho d\rho \frac{n(\omega_d) \sigma_{eff}(\omega_d) \exp(-\rho^2/2)}{n_o \left( 1 + \frac{\tau_n (1+\alpha) \sigma_{eff}(\omega_d) \exp(-\rho^2/2)}{\tau_s \sigma_t} \right)}. \quad (4.31)$$

Performing the integration over  $\rho$  gives the final form of the ratio

$$N_R / N_{Ro}$$

$$\frac{N_R}{N_{Ro}} = \frac{1}{\sigma_t} \int_{-\infty}^{\infty} \frac{\tau_s \sigma_t n(\omega_d)}{2\tau_n n_o} \ln \left( \frac{(1+\alpha)\tau_n \sigma_{eff}(\omega_d)}{\tau_s \sigma_t} + 1 \right) d\omega_d. \quad (4.32)$$

### CASE 3. Gaussian Section and Realistic Temporal Pulse Shape.

In this case the Gaussian beam cross section  $I(\rho)$  is again given by Equation (4.28), and the laser pulse  $N_L(t)$  is given by the more realistic pulse shape

$$N_L(t) = \frac{N_L}{t_r^2} t \exp(-t^2/2t_r^2), \quad (4.33)$$

where  $t_r$  is the risetime of the pulse. The rms length of the pulse is

$\Delta t_{rms} = t_r (2-\pi/2)^{1/2}$ . Equation (4.33) is plotted in Figure 4.2.

Substituting Equation (4.33) into Equation (4.16) gives the dimensionless function

$$\hat{N}_L(t') = (2-\pi/2) t' \exp(-t'^2(1-\pi/4)). \quad (4.34)$$

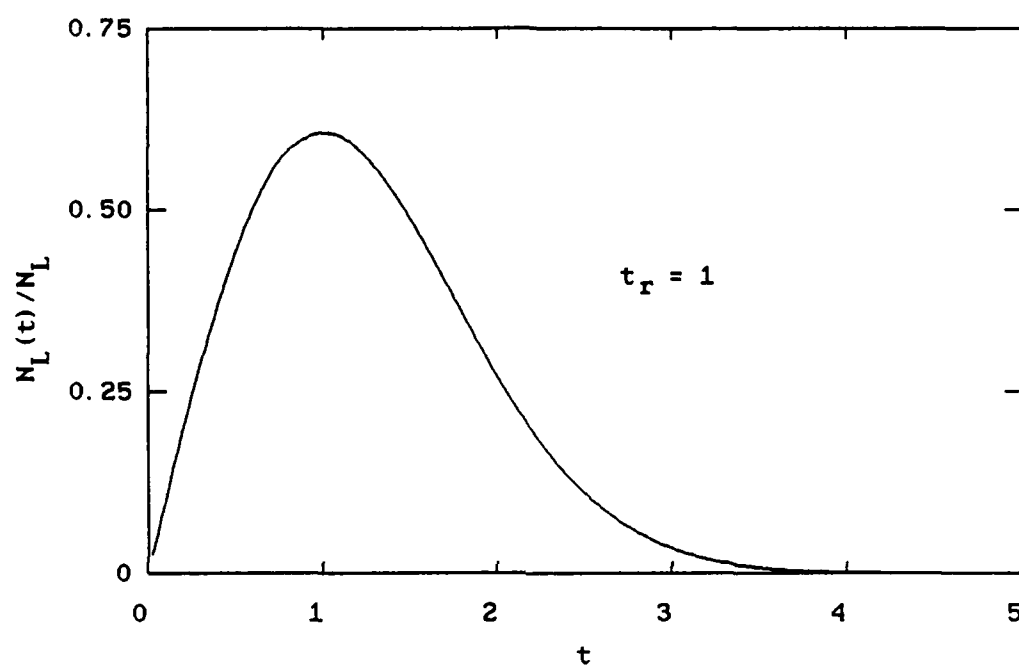


Figure 4.2. Realistic pulse shape,  $t_r = 1$ .

Substituting  $\hat{N}_L(t')$  and  $\hat{I}(\underline{\rho}')$  given in Equations (4.34) and (4.29) into Equation (4.21) and performing the integration over the plane defined by  $\underline{\rho}$  gives

$$\frac{N_R}{N_{Ro}} = \frac{1}{\sigma_t} \int_{-\infty}^{\infty} \frac{\tau_s \sigma_t n(\omega_d) f(\tau_s/\tau_n, I_s, \omega_d)}{n_o \tau_n} d\omega_d, \quad (4.35)$$

where

$$f(\tau_s/\tau_n, I_s, \omega_d) = \frac{(1-\pi/4)}{\sqrt{12}} \int_0^{\infty} dt \int_0^t d\tau \exp\left\{ \frac{\tau_s \sigma_t I_s}{2\sqrt{12}\tau_n} (\tau-t) \right\} \\ \left\{ \frac{\exp\left[ \frac{(1+\alpha)}{2} \sigma_{eff}(\omega_d) I_s \left( \exp(-t^2(1-\pi/4)) - \exp(-\tau^2(1-\pi/4)) \right) \right] - 1}{\exp(-t^2(1-\pi/4)) - \exp(-\tau^2(1-\pi/4))} \right\} \\ \tau \exp(-\tau^2(1-\pi/4)). \quad (4.36)$$

This result, as in the previous cases, is independent of  $I_s$  for  $\Delta t \gg \tau_n$ . The analytical results of Cases 1, 2 and 3 are summarized in Table 4.1.

#### 4.3 Interpretation and Comparison of Results

Unfortunately, the results summarized in Table 4.1 are not easily interpreted in terms of the laser pulse length, pulse energy, beamwidth and line width. To illustrate the influence of these parameters on

TABLE 4.1

Saturation Effects ( $N_R/N_{R0}$ ) for the Laser Beam Cross Sections and Pulse Shapes Assumed in Cases 1, 2 and 3

Case 1: Uniform Beam Cross Section and Rectangular Pulse Shape.\*

$$\frac{N_R}{N_{R0}} = \frac{1}{\sigma_t} \int_{-\infty}^{\infty} \frac{n(\omega_d) \sigma_{eff}(\omega_d)}{n_0 \left( 1 + \frac{\tau_n (1+\alpha) \sigma_{eff}(\omega_d)}{2\tau_s \sigma_t} \right)} d\omega_d$$

Case 2: Gaussian Beam Cross Section and Rectangular Pulse Shape.\*

$$\frac{N_R}{N_{R0}} = \frac{1}{\sigma_t} \int_{-\infty}^{\infty} \frac{\tau_s \sigma_t n(\omega_d)}{2\tau_n n_0} \ln \left( \frac{(1+\alpha)\tau_n \sigma_{eff}(\omega_d)}{\tau_s \sigma_t} + 1 \right) d\omega_d$$

Case 3: Gaussian Beam Cross Section and Realistic Pulse Shape.

$$\frac{N_R}{N_{R0}} = \frac{1}{\sigma_t} \int_{-\infty}^{\infty} \frac{\tau_s \sigma_t n(\omega_d) f(\tau_s/\tau_n, I_s, \omega_d)}{n_0 \tau_n} d\omega_d$$

where

$$f(\tau_s/\tau_n, I_s, \omega_d) = \frac{(1-\pi/4)}{\sqrt{12}} \int_0^{\infty} dt \int_0^t d\tau \exp \left\{ \frac{\tau_s \sigma_t I_s}{2\sqrt{12}\tau_n} (\tau-t) \right\}$$

$$\left\{ \frac{\exp \left[ \frac{(1+\alpha)}{2} \sigma_{eff}(\omega_d) I_s \left( \exp(-t^2(1-\pi/4)) - \exp(-\tau^2(1-\pi/4)) \right) \right] - 1}{\exp(-t^2(1-\pi/4)) - \exp(-\tau^2(1-\pi/4))} \right\}$$

$$\tau \exp(-\tau^2(1-\pi/4))$$

\* Valid only for  $\Delta t \gg \tau_n$



saturation, the results in Table 4.1 are evaluated for two limiting circumstances: a very broad laser line width and a very narrow laser line width. To perform these computations, the form of  $\sigma(\omega)$  and  $n(\omega_d)$  must also be known. For simplicity and illustration purposes the absorption cross section  $\sigma(\omega)$  is assumed to be given by a single Lorentzian profile

$$\sigma(\omega) = \frac{\sigma_o (\Delta\omega/2)^2}{(\omega_o - \omega)^2 + (\Delta\omega/2)^2}, \quad (4.37)$$

where  $\Delta\omega$  is the FWHM of the spectrum,  $\sigma_o$  is the peak cross section, and  $\omega_o$  is the center frequency. The distribution of atoms in Doppler frequency  $n(\omega_d)$  is assumed to be given by a Gaussian profile which is characteristic of thermal broadening. We write

$$n(\omega_d) = \frac{n_o 2(\ln 2)^{1/2}}{\sqrt{\pi} \Delta\omega_d} \exp \left\{ - \left( \frac{2(\ln 2)^{1/2} \omega_d}{\Delta\omega_d} \right)^2 \right\} \quad (4.38)$$

where  $\Delta\omega_d$  is the FWHM of the distribution. Doppler broadening is assumed to dominate natural broadening, implying  $\Delta\omega_d \gg \Delta\omega$ . Recall  $\sigma(\omega)$  is the result of homogeneous broadening (namely the finite decay time of the atoms) and inhomogeneous broadening is characterized by  $n(\omega_d)$ .

First consider the situation in which the laser line width is large compared to  $\Delta\omega_d$ . It follows that  $g(\omega)$  will be approximately constant over the frequency range of the absorption spectrum  $\sigma(\omega)$ . The effective cross section  $\sigma_{eff}(\omega_d)$  reduces to

$$\begin{aligned}\sigma_{eff} &\approx g(\omega_o) \int_{-\infty}^{\infty} \sigma(\omega - \omega_d) d\omega \\ &= \frac{g(\omega_o) \sigma_o \Delta\omega \pi}{2},\end{aligned}\quad (4.39)$$

where  $\omega_o$  is the center frequency of  $\sigma(\omega)$ . Substituting Equation (4.39) into Equations (4.27) and (4.32) and noting from Equation (4.13) that  $\sigma_t = \sigma_{eff}$ , gives the following results for Cases 1 and 2 (assuming the degeneracies  $g_1$  and  $g_2$  are equal)

**Case 1:**

$$\frac{N_R}{N_{Ro}} = \frac{\tau_s}{\tau_n} \left( 1 + \frac{\tau_s}{\tau_n} \right)^{-1} \quad (\text{Broad laser line width}) \quad (4.40)$$

**Case 2:**

$$\frac{N_R}{N_{Ro}} = \frac{\tau_s}{2\tau_n} \ln \left( 1 + \frac{2\tau_s}{\tau_n} \right) \quad (\text{Broad laser line width}) \quad (4.41)$$

Equations (4.40) and (4.41) are plotted in Figure 4.3 versus the ratio  $\tau_s/\tau_n$ . The Case 3 results given by Equation (4.35) were computed numerically and are also plotted in Figure 4.3.

Now consider a narrow line width laser of frequency  $\omega_o$  (i.e.,  $g(\omega) = \delta(\omega - \omega_o)$ ). By substituting  $g(\omega) = \delta(\omega - \omega_o)$  into Equation (4.8) we obtain

$$\sigma_{eff}(\omega_d) = \sigma(\omega_o - \omega_d). \quad (4.42)$$

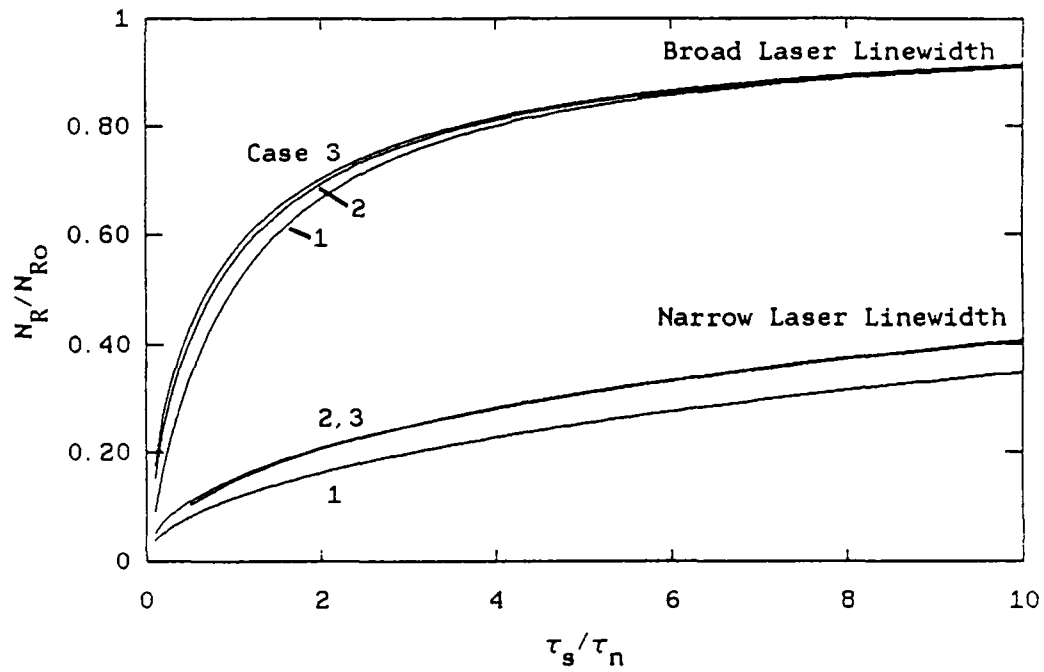


Figure 4.3. Saturation effects for broad and narrow laser line widths:  $N_R/N_{R0}$  versus  $t_s/t_n$  for Cases 1, 2 and 3.

The corresponding results for Cases 1 and 2 are

Case 1:

$$\frac{N_R}{N_{R0}} = \left\{ \frac{\tau_s \Delta\omega (\pi \ln 2)^{1/2}}{\tau_n \Delta\omega_d} \left( 1 + \frac{\tau_s \Delta\omega (\pi \ln 2)^{1/2}}{\tau_n \Delta\omega_d} \right)^{-1} \right\}^{1/2} \quad (4.43)$$

Case 2:

$$\frac{N_R}{N_{R0}} = \frac{\tau_s \Delta\omega (\pi \ln 2)^{1/2}}{\tau_n \Delta\omega_d} \left( \sqrt{1 + \frac{2\tau_n \Delta\omega_d}{\tau_s \Delta\omega (\pi \ln 2)^{1/2}}} - 1 \right) \quad (4.44)$$

Equations (4.43) and (4.44) are plotted versus the ratio  $\tau_s/\tau_n$  in Figure 4.3. The Case 3 results are also plotted in Figure 4.3.

The six curves plotted in Figure 4.3 illustrate the effects of saturation on  $N_R/N_{R0}$  as a function of the ratio  $\tau_s/\tau_n$ . Recall from the definition given in Equation (4.20) that  $\tau_s$  is proportional to pulse length and beamwidth, and inversely proportional to pulse energy. These curves show that saturation effects decrease (i.e.,  $N_R/N_{R0}$  increases) for one or more of the following actions: increasing pulse length, increasing beamwidth, or decreasing pulse energy. The gross effects of laser line width are also demonstrated in Figure 4.3. For a given value of  $\tau_s/\tau_n$ , the effects of saturation are obviously worse for a narrow line width than for a broad line width. This fact is explained by realizing that the total energy of the laser is absorbed by only a fraction of the Doppler shifted atoms for a very narrow laser line width. The saturation effects derived here for the broad line

width are equivalent to the results of Megie<sup>73</sup> and Measures.<sup>77</sup> This equivalence is due to the fact that all the atoms at a point in the laser beam see the same laser energy density. Whether the absorption line is homogeneously or inhomogeneously broadened makes no difference. As a result, the form of the equations describing saturation are the same. For the narrow line width situation, however, the saturation effects derived here are different from those of Megie and Measures. In this case, inhomogeneous broadening results in a situation in which the atoms at a point in the beam do not all experience the same laser energy density. In particular, for the preceding narrow line width example, only those atoms with a zero Doppler shift see the full energy of the laser, and as a consequence, the functional form of the narrow line width equations differs considerably from those of Megie and Measures.

#### 4.4 Design of Pulsed Lidar Systems

The results of the previous section show that saturation effects are determined by the choice of laser pulse length, pulse energy, beamwidth and line width. In the following section we illustrate, by example, how these results affect the design of pulsed lidar systems. In general, lidar systems such as those described in References 32, 36-40, 73 and 74 are designed to achieve a specified range resolution and signal-to-noise ratio. Range resolution is related to laser pulse length  $\Delta t$  by  $\Delta r = c\Delta t/2$  where  $\Delta r$  is the range resolution, and  $c$  is the speed of light. Decreasing  $\Delta t$ , while maintaining a fixed pulse energy, improves range resolution but may result in a significantly reduced

signal level due to saturation effects. The expected signal-to-noise ratio, on the other hand, is affected primarily by the pulse energy. For negligible saturation, the backscattered signal level increases linearly with pulse energy. At the onset of saturation, however, the backscattered signal increases at a lesser rate, reducing the signal from that expected for negligible saturation. The signal-to-noise level is also affected by the laser beam divergence. The ratio of signal-to-background noise is maximized by matching the field-of-view (FOV) of the receiving telescope to the divergence of the laser beam. For the case of negligible saturation, decreasing the beam divergence and receiver FOV together reduces the background noise while maintaining the signal level. However, as the beam divergence is decreased, the onset of saturation will reduce the signal level, and thus reducing the signal-to-noise ratio. The choice of laser line width also affects the backscattered signal by determining the efficiency with which the atoms absorb the incident laser energy. In the case of inhomogeneous broadening, the laser line width also determines the percentage of atoms within an illuminated volume that can resonantly absorb the laser energy. A narrow line width implies that only a fraction of the atoms in the volume can absorb the energy. This situation, as shown in Section 4.3, has a lower threshold of saturation, possibly resulting in a significantly reduced backscattered signal from that expected for negligible saturation.

In the following design examples we consider three sodium (Na) lidar systems: a daytime lidar system used to measure the mesospheric

Na layer's vertical density profile, a mesopause temperature measurement system based on Na lidar, and a pulsed lidar system for the creation of laser guide stars in the mesospheric Na layer for use in adaptive imaging in astronomy.

### 1) Daytime Mesospheric Na Lidar System

The mesospheric Na layer was discovered in the late 20's and has been explored extensively since the late 1960's with lidar techniques. Meteoric ablation is believed to be the dominant source of the layer. The vertical density characteristics of the layer have received considerable attention in recent years. Much of the past and current experimental research of the density characteristics has been conducted using monostatic lidar systems.<sup>32, 36-40, 73</sup> These lidar systems measure the vertical structure of the layer by transmitting a short laser pulse and recording the return flux as a function of time. These profiles are calibrated and scaled to provide measurements of the Na layer density as a function of altitude. Figure 2.20 is a typical Na layer density profile showing a meteor trail measured with the CEDAR lidar system.<sup>39</sup> Daytime measurements of the Na layer's vertical density pose special problems to the lidar designer. Foremost of these problems is the large background noise associated with the bright daytime sky. To achieve an acceptable signal-to-noise level, the FOV of the receiving system must be matched to the laser beam divergence and the beam divergence itself should be as small as possible. Unfortunately, the beneficial effects of decreasing the beam divergence are limited by the onset of saturation. Since saturation effects tend to limit both the

range resolution and the expected signal-to-noise level, it is reasonable to require negligible saturation. This condition implies that the ratio  $N_R/N_{R0}$  must be nearly unity, and this in turn imposes limits on the combinations of pulse energy, pulse length, beamwidth, and line width. To illustrate these limitations we consider the CEDAR lidar system operated by the University of Illinois at the Urbana, Illinois field site.<sup>39</sup> This system is presently being operated as a nighttime system, but is also being modified for daytime use. The major system specifications of the CEDAR lidar are listed in Table 4.2. For daytime use, beam expanding optics will be added to decrease the outgoing beam divergence. We are interested in the minimum allowed beam divergence for negligible saturation. We also wish to know how this minimum varies for changes in either the pulse energy or pulse length.

The minimum beam divergence (or equivalently minimum beam width) is found by computing  $N_R/N_{R0}$  given in Equation (4.21), versus rms beam width  $\Delta\rho_{rms}$  (recall  $\tau_s$  and  $I_s$  are functions of  $\Delta\rho_{rms}$ ). The minimum allowed beam width is specified as the point in which  $N_R/N_{R0}$  falls below some threshold (0.9 for example). For computational simplicity we approximate the beam cross section  $\hat{I}(\rho)$  by a rectangular profile and the pulse shape  $\hat{N}_L(t)$  by a rectangular waveform. These approximations allow us to use the Case 1 results of Section 4.3, Equation (4.26). We have found that it is the values of the rms beam width and pulse length that are most significant in the computation. Computations using the more realistic beam cross section and pulse shape models in Cases 2 and



**TABLE 4.2**  
**CEDAR Lidar Specifications<sup>39</sup>**

---

**LASER:**

Wavelength	589 nm
Line Width	1.4 pm (1.2 GHz)
Pulse Energy	25 mJ (typ)
Pulse Rate	200 pps (typ)
Pulse Length	25 ns
Beam Divergence	1 mrad

**RECEIVING SYSTEM:**

Telescope Area	1.17 m <sup>2</sup>
Field-of-View	3 mrad
Optical Bandwidth	20 Å FWHM
Range Resolution	75 m

3 of Section 4.3 have given results essentially identical to the Case 1 results for equivalent rms parameter values. Note that the simplified result in Equation (4.27) may not be used in this case since the pulse length of the CEDAR lidar is on the order of  $\tau_n$ . We model the fine structure of Na's absorption cross section  $\sigma(\omega)$  with the weighted sum of six Lorentzian profiles. Each profile corresponds to one of the six atomic transitions within the Na  $D_2$  line.<sup>2</sup> The cross section  $\sigma(\omega)$  is plotted in Figure 2.21. The Doppler distribution  $n(\omega_d)$  is assumed Gaussian with a FWHM of 1070 MHz. This width is the expected value for the Na layer at an altitude of 95 km and a temperature of 200° K. The Doppler broadened absorption spectrum is also plotted in Figure 2.21. The natural decay time  $\tau_n$  of Na is assumed to be 16 ns. We also assume that  $N_R/N_{R0}$  must be greater than 0.9 for negligible saturation. Combining these assumptions and the laser wavelength and line width specified in Table 4.2 with Equation (4.26) results in the design curves shown in Figure 4.4. These curves were obtained by setting Equation (4.26) equal to 0.9 and solving for the beam width for various combinations of pulse energy and pulse length.

The general trends in the curves are as expected from the discussion in Section 4.3. Increasing the pulse length or decreasing pulse energy lowers the minimum allowed beam divergence. Obviously, lasers with very short pulse lengths and large pulse energies are limited the most by the minimum allowed beam divergence. In terms of the use of these curves for design, operation in the region above and

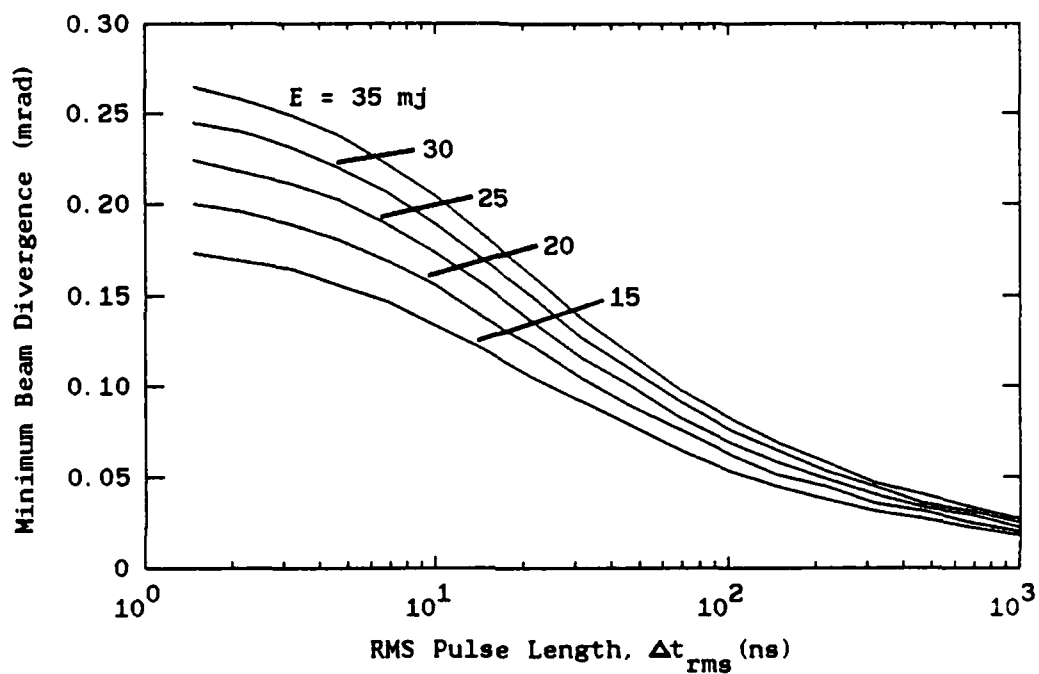


Figure 4.4. Minimum allowed beam divergence versus rms pulse length for the CEDAR lidar system (daytime configuration).

to the right of a curve ( $N_R/N_{R0} > 0.9$ ) will insure negligible saturation effects for the listed pulse energy. For the CEDAR lidar system with a rms pulse length of 7.2 ns (pulse length of 25 ns) and a pulse energy of 25 mj we find that the beam divergence can be no smaller than 0.18 mrad.

## 2) Na Temperature Lidar System

High resolution temperature profiles near the mesopause can be obtained by active probing of the Doppler broadened hyperfine structure of the Na  $D_2$  resonance line.<sup>36,74</sup> The ratio of the absorption cross section at one of the peaks to the minimum between the peaks is a very sensitive indicator of temperature (see Figure 2.21). This ratio can be measured by alternatively tuning a narrowband lidar between the peak and the minimum of the resonance line.<sup>36</sup> A narrowband lidar is required because of the bandwidth resolution needed to accurately probe the fine structure of the resonance line. We observed in Section 4.3 that for a given pulse energy, pulse length, and beam divergence, saturation effects can be significantly worse for a narrowband laser than for a wideband laser. To illustrate the effects of saturation on the design process, we again consider the CEDAR lidar specifications in Table 4.2 and investigate modifications to the system for a temperature measurement system. As in Example 1, we are interested in daytime as well as nighttime operation. Basically, the same design considerations and assumptions as in Example 1 are valid for this problem. The primary difference between the two systems is the line width of the laser. In this case the laser line width is reduced to 0.13 pm so that

the fine structure of the Na absorption line can be probed.<sup>74</sup>

Performing the same computations as in Example 1, but for the narrow line width, we obtain the design curves shown in Figure 4.5.

These results are similar in form to those of the previous example, but differ in magnitude. This difference can be attributed to the difference in line width between the two examples. As before, operation in the region above and to the right of a curve ( $N_R/N_{R0} > 0.9$ ) will insure negligible saturation effects for the listed pulse energy. For the CEDAR lidar system with an rms pulse length of 7.2 ns (pulse length of 25 ns) and a pulse energy of 25 mj we find that the beam divergence can be no smaller than 0.5 mrad. This minimum divergence is ~2.5 times greater than that allowed for the wide line width laser in the previous example.

### 3) Laser Guide Stars in the Mesospheric Na Layer: Off Zenith Effects

A potentially important application of pulsed Na lidars is the creation of bright artificial guide stars in the mesospheric Na layer for adaptive imaging applications in astronomy. The basic design equations giving the required Na laser parameters are derived in Chapter 2 (see Equations (2.47)-(2.49)). These equations include the effects of saturation by incorporating the generalized scattering cross section  $\sigma_s$ . Here  $\sigma_s$  is related to the ratio  $N_R/N_{R0}$  by the simple relationship

$$\sigma_s = \sigma_t \frac{N_R}{N_{R0}}, \quad (4.45)$$

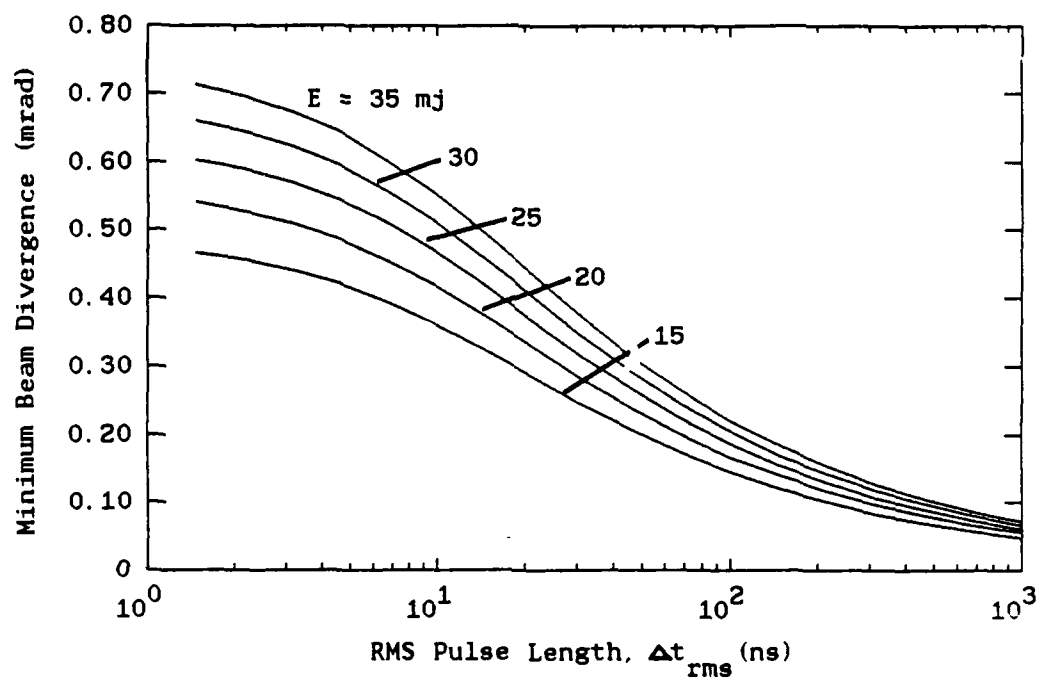


Figure 4.5. Minimum allowed beam divergence versus rms pulse length for the narrow line width (0.13 pm) CEDAR lidar system (atmospheric temperature measurement configuration).

where the ratio  $N_R/N_{R0}$  is given by Equation (4.21). Recall that  $\sigma_t$  is the scattering cross section for negligible saturation. Since the laser-guided telescope must work for a range of zenith angles, the effects of scanning the guide stars away from zenith must also be considered. This is done by first finding the laser requirements for a zenith pointing guide star and then computing the percentage change in pulse energy required for the largest zenith angle of interest. This percentage change is given by Equation (2.49) of Chapter 2. Here we discuss the factors that lead to Equation (2.49).

The geometry for the off zenith effects is shown in Figure 4.6. The effects of pointing the laser off zenith are manifested through several geometrical correction factors. These factors must be incorporated into the expression for the required laser pulse energy  $E_r$  given by Equation (2.47). The rms beam radius at the scattering layer for an arbitrary zenith angle is

$$\Delta\rho_{rms} = \frac{\Delta\rho_0}{\cos\theta}, \quad (4.46)$$

where  $\Delta\rho_0$  is the rms beam radius at zenith. At angles away from zenith the atmospheric transmission will decrease due to the increased path length through the lower atmosphere. The transmission at zenith is written

$$T_s(\theta=0) = \exp(-\sigma_d), \quad (4.47)$$

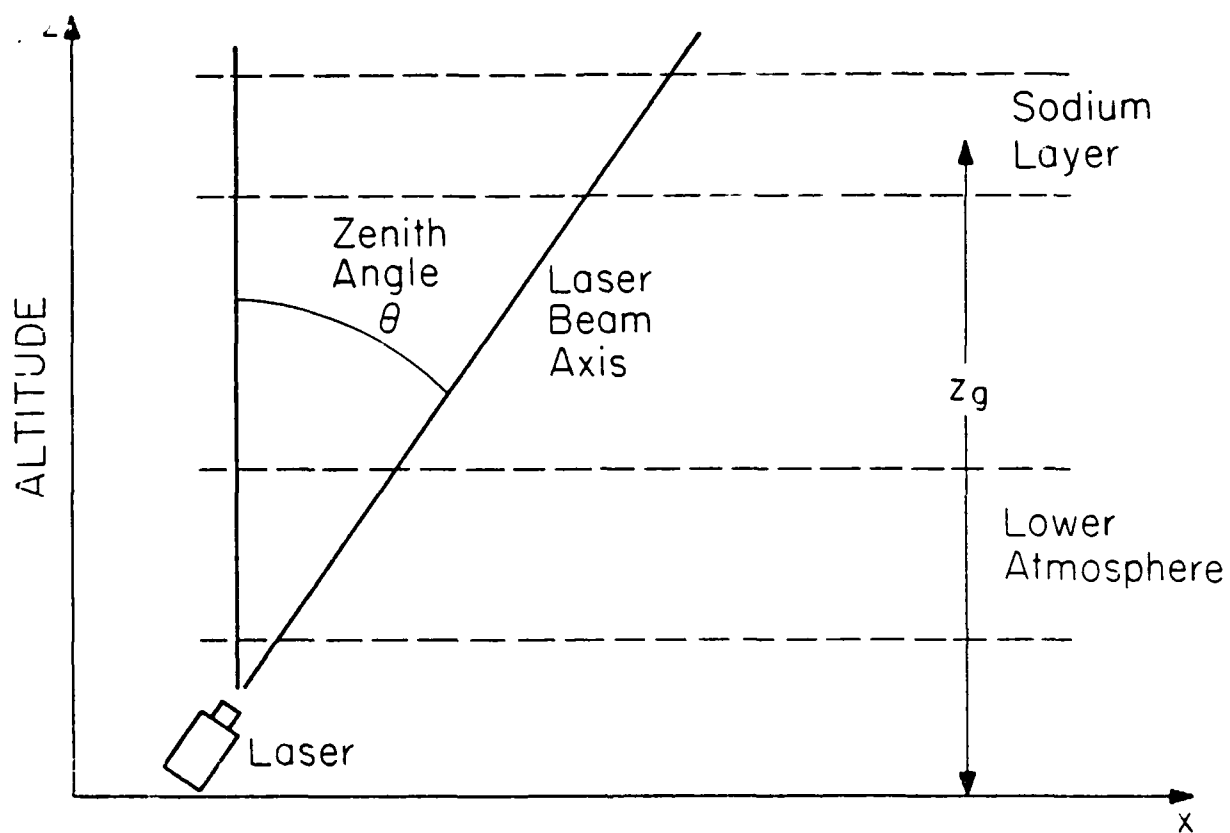


Figure 4.6. Off zenith geometry.



where  $\sigma_d$  is the optical depth of the lower atmosphere. For angles away from zenith the optical depth must be increased to account for the increased path length to the layer giving

$$T_a(\theta) = \exp(-\sigma_d / \cos\theta). \quad (4.48)$$

The distance from the telescope to the turbulence layer  $h_t$  increases with zenith angle. It is easy to see from Figure 4.6 that  $h_t$  varies as

$$h_t(\theta) = \frac{h_t}{\cos\theta}. \quad (4.49)$$

At zenith the column abundance will simply be the vertical column abundance of the layer. The column abundance for an arbitrary angle is

$$C_s(\theta) = C_s / \cos\theta. \quad (4.50)$$

The seeing cell diameter  $r_o$  also varies with zenith angle (see Equation (2.5))

$$r_o(\theta) = r_o (\cos\theta)^{3/5}. \quad (4.51)$$

Incorporating Equations (4.46)-(4.51) into Equation (2.47) we find

$$E_T(\theta) = \frac{1.78 \times 10^{-3} \eta_c^2 h c D^2 h_t^2}{r_o^4 (\Delta\phi/\lambda)^{22/5} \eta T_A^2(\theta) \lambda_L C_s \sigma_s(\theta) (\cos\theta)^{17/5}}, \quad (4.52)$$

where  $E_T(\theta)$  is the required pulse energy as a function of zenith angle. The scattering cross section  $\sigma_s(\theta)$  is given by Equation (4.45) where  $\tau_s$ , used in the evaluation of  $N_R/N_{R_0}$ , is replaced with

$$\tau_s(\theta) = \frac{2 \Delta t \pi \Delta \rho_o^2 h c}{E \lambda_L T_A(\theta) \sigma_t (\cos\theta)^2}. \quad (4.53)$$

Finally, the ratio  $E_T(\theta)/E_T(0)$  is found to be

$$\frac{E_T(\theta)}{E_T(0)} = \exp \left[ -2\sigma_d \left( 1 - \frac{1}{\cos\theta} \right) \right] \frac{\sigma_s(0)}{\sigma_s(\theta)} \frac{1}{(\cos\theta)^{17/5}}, \quad (4.54)$$

which is the same as that given in Chapter 2, Equation (2.49).

#### 4.5 Summary

Nonlinear resonance absorption (saturation) effects for pulsed laser systems have been quantified in terms of the laser's pulse energy, pulse length, beamwidth and line width. Saturation effects arise when the atomic population densities in the scattering medium are altered by large laser energy densities within the layer. These large energy densities can reduce the number of lower state atoms giving rise to significantly reduced backscattered signal levels. The fundamental parameters describing the saturation effects are the saturation time  $\tau_s$  and the laser line width  $\Delta\omega_{rms}$ . The ratio  $\tau_s/\tau_n$  is a measure of the level of saturation and is proportional to pulse length and beamwidth and inversely proportional to pulse energy. The choice of  $\tau_s/\tau_n$  involves tradeoffs of these laser parameters. The line width, on the other hand, can be chosen to minimize laser power requirements. For negligible saturation, a narrow line width at the peak of the absorption spectrum of the atoms is optimum. For appreciable saturation, the optimal line width is on the order of the width of the Doppler broadened absorption spectrum.

## 5. EFFECTS OF TURBULENCE INDUCED ANISOPLANATISM ON THE IMAGING PERFORMANCE OF ADAPTIVE ASTRONOMICAL TELESCOPES USING LASER GUIDE STARS

### 5.1 Introduction

The performance of adaptive optics systems has been studied extensively during the last 15 years, and several fundamental limitations preventing ideal imaging performance have been identified. One of these limitations is anisoplanatism. An adaptive optical system consists of two fundamental components: the wavefront sensor and wavefront correction device. The wavefront sensor measures the turbulence induced phase perturbations across the aperture of the optical system, and this information is in turn used to drive the wavefront correction device. The perturbations are detected by measuring the shape of a wavefront from a reference source. The reference source may coincide with or be adjacent to the object being imaged. In the case of an adaptive telescope used for astronomical imaging, the reference source is typically a bright, natural star (guide star) adjacent to the celestial object of interest or, as suggested more recently, a laser guide star created in the upper atmosphere. Regardless of the application, anisoplanatism degrades the imaging performance of the adaptive optics system for nonzero separations between the object and reference sources. The effects of anisoplanatism arise because of the distribution of the turbulence along the optical path. An angular separation between the reference source and the object results in two optical paths traversing different regions in the turbulence. The turbulence effects in one path are only partially correlated with the turbulence effects in the other path.

This partial correlation degrades the accuracy of the wavefront compensation in the adaptive optics system. In the case of astronomical imaging, effective wavefront compensation is limited to an angular region surrounding the position of the guide star. This angular region is quantified by the isoplanatic angle. For astronomical imaging using laser guide stars, anisoplanatism has an additional impact on imaging performance due to the relatively low altitude of the guide stars. The spherical wavefront from the guide star in combination with the effects of anisoplanatism increasingly degrade the wavefront compensation for points farther and farther away from the center of the aperture (i.e., those points not directly in line with the guide star and object). The degradation is caused by the increasing difference between the incidence angles of the laser guide star and object wavefronts. For large telescopes, multiple laser guide stars are required to sample the entire aperture.<sup>3</sup> These astronomical applications highlight the importance of being able to quantify anisoplanatic effects on the performance of an adaptive imaging system.

The effects of anisoplanatism on adaptive optics systems have been treated extensively in the literature.<sup>26-30,35,78</sup> These past studies characterize the effects of anisoplanatism by calculating how the optical transfer function (OTF) of an adaptive optics system changes as a function of the angular separation between the reference and the object sources. The previous analyses depend ultimately on the ability to calculate the wavefront phase correlation between the two

propagation directions. Inherent in the past analyses is the assumption that the adaptive optics system is capable of perfectly measuring and reconstructing the perturbations of the reference wavefront. The nonideal characteristics of the wavefront sensor and wavefront correction device are not included. The accuracy and spatial frequency response in any real wavefront sensor is limited by photon noise and by the finite number of sampling areas over the wavefront surface. For example, wavefront aberrations having characteristic spatial frequencies greater than the sensor's spatial sampling frequency, go undetected. Wavefront correction devices, such as deformable mirrors, are also less than ideal. The ability of a deformable mirror to cancel wavefront aberrations is limited by the finite degrees of freedom in the device's response. This limited response will prevent it from correcting higher order wavefront aberrations. Another limitation of the previous analyses is that, in effect, only the measured perturbations of the reference wavefront are used to compensate for the perturbations of the object wavefront. No attempt is made to use the statistical correlation between the object and reference wavefronts in the wavefront compensation process.

We present an analysis technique for characterizing the effects of anisoplanatism on adaptive optics systems using slope sensors. The technique is developed in a very general sense, allowing for an arbitrary geometry between the reference source, the imaged object and the aperture of the optical system. Imaging performance is quantified by two measures: the residual mean-square phase error over the

aperture and the OTF. The wavefront correction system consists of an aperture, a wavefront slope sensor, a wavefront correcting device and a control law. We concentrate on phase correcting systems, and assume that turbulence induced amplitude effects are negligible. The wavefront correcting device is a deformable mirror with a finite number of actuators. The wavefront sensor samples the aperture plane over a specified number of subapertures. Each subaperture sensor makes a noisy measurement of the phase slope of the reference wavefront. The control law uses the slope measurements in addition to the phase correlations between the reference and object wavefronts to calculate the actuator control signals for the deformable mirror. The control signals are adjusted to minimize the mean-square difference between the reconstructed wavefront and the object wavefront.

In Section 5.2 a general framework is introduced to describe the geometry between the reference source, the imaged object and the aperture of the optical system. Section 5.3 introduces the basic assumptions and definitions characterizing the adaptive optics system. These assumptions encompass the wavefront sensor, deformable mirror, and control law and are similar to the assumptions of Chapter 3. In Section 5.4 we calculate the mean-square residual phase error between the reconstructed wavefront and object wavefront. In Section 5.5 the OTF is formulated in terms of the results found in Section 5.4. Sections 5.4 and 5.5 are brief, since the basic analysis approach has been treated in Chapter 3 and in References 6 and 52. In Section 5.6 the statistical correlations of the reference and object wavefront

phases are derived in terms of the generalized phase structure function, which is then introduced in Section 5.7. Finally, in Section 5.8, we present computational results showing how anisoplanatism affects the design and performance of the laser-guided telescopes discussed in Chapter 2. The computational results indicate how many guide stars are required for a given telescope size and how imaging performance degrades as the observation direction is separated in angle from that of the laser guide stars.

## 5.2 Geometry

A critical component of the analysis presented in Sections 5.4-5.6 is the statistical correlation between the wavefront phase at two arbitrary points in the aperture. The two points are associated with two optical paths through the turbulence. The paths may originate from two separate sources, as in the case of an adaptive telescope using a guide star, or may originate from a common source, as in the case of a system using the object itself for the reference wavefront. In either case, to calculate the phase correlations, we must characterize the transverse distance between the two paths as a function of position along the paths.

Consider two point sources within the field of view (FOV) of an optical system. The wavefronts from both sources pass through a turbulence region in the atmosphere. Figure 5.1 illustrates the

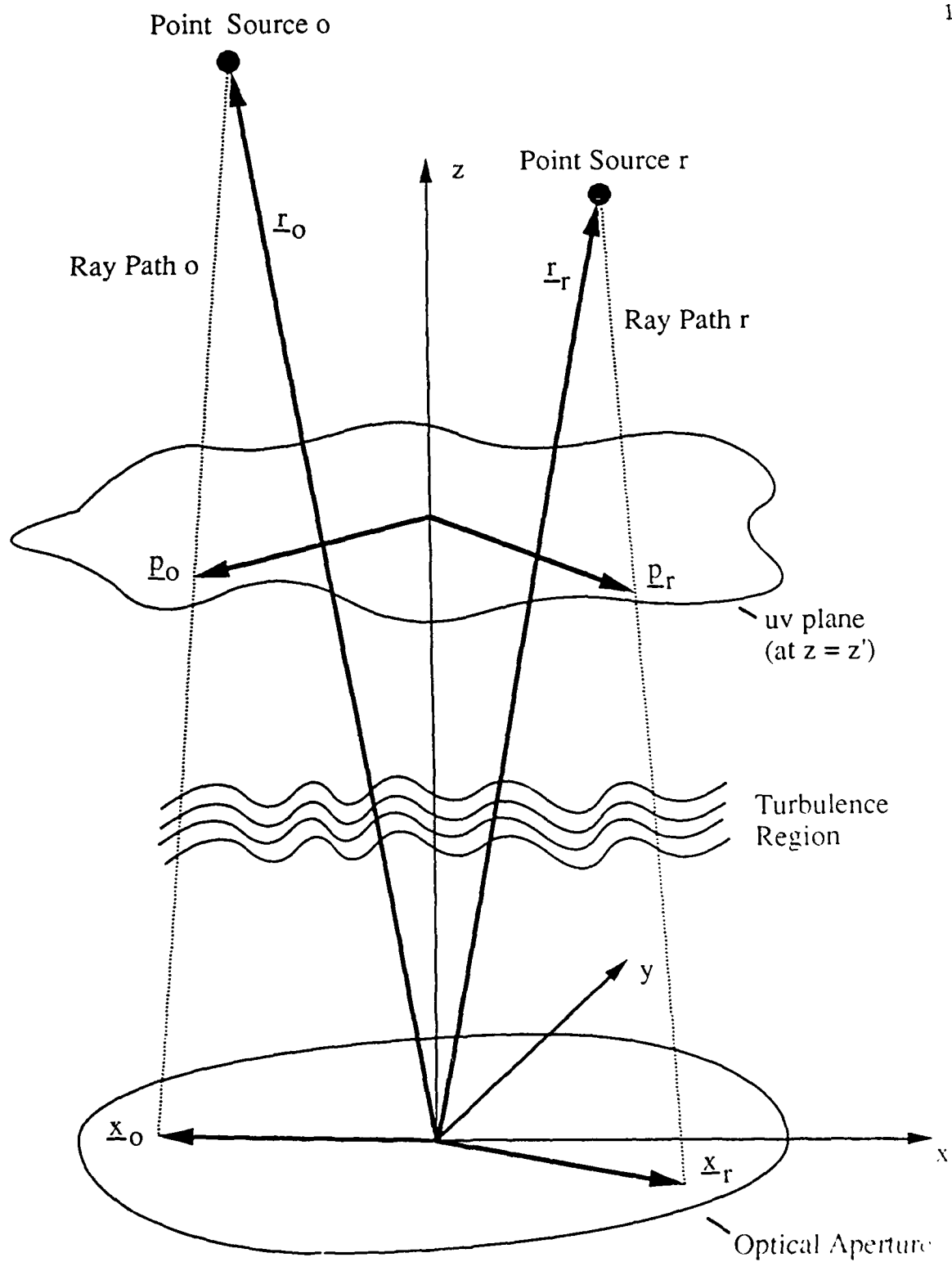


Figure 5.1. Geometry between point sources and optical aperture.



geometry between the point sources and the aperture of the optical system. Assume the two sources are located at the vector positions  $\underline{r}_o$  and  $\underline{r}_r$ . The z-components of the vectors  $\underline{r}_o$  and  $\underline{r}_r$  are designated  $z_o$  and  $z_r$ , respectively. Let the vectors  $\underline{x}_o$  and  $\underline{x}_r$  describe the points of incidence in the aperture plane (xy plane) for waves traveling from the two sources. The subscripts "o" and "r" are arbitrary, but are later related to the object and reference wavefront sources. The uv plane is defined to be parallel to the image plane and located on the z-axis at  $z = z'$ . The vectors  $\underline{p}_o$  and  $\underline{p}_r$  lie in the uv plane and describe the points of intersection between the plane and the optical paths from the sources o and r. The vector  $\underline{p}_o$  is given by

$$\underline{p}_o = \underline{x}_o + \left( \frac{z'}{z_o} \right) \left( [(\underline{r}_o - \underline{x}_o) \cdot \hat{x}] \hat{x} + [(\underline{r}_o - \underline{x}_o) \cdot \hat{y}] \hat{y} \right), \quad (5.1)$$

where  $\hat{x}$  and  $\hat{y}$  are unit vectors in the x and y directions. The vector  $\underline{p}_r$  is given by Equation (5.1) with the subscript "o" replaced with "r." Of particular interest is the distance between the intersection points  $\underline{p}_o$  and  $\underline{p}_r$  as a function of the position of the uv plane on the z-axis. Let the vector  $\Delta \underline{p}_{or}$  be defined by

$$\Delta \underline{p}_{or} = \underline{p}_o - \underline{p}_r. \quad (5.2)$$

Substituting Equation (5.1) into Equation (5.2) gives

$$\begin{aligned}
\Delta p_{or}(\underline{x}_o, \underline{x}_r, z') &= \underline{x}_o - \underline{x}_r \\
&+ z' \left( \frac{[(\underline{r}_o - \underline{x}_o) \cdot \underline{\hat{x}}]}{z_o} - \frac{[(\underline{r}_r - \underline{x}_r) \cdot \underline{\hat{x}}]}{z_r} \right) \underline{\hat{x}} \\
&+ z' \left( \frac{[(\underline{r}_o - \underline{x}_o) \cdot \underline{\hat{y}}]}{z_o} - \frac{[(\underline{r}_r - \underline{x}_r) \cdot \underline{\hat{y}}]}{z_r} \right) \underline{\hat{y}}.
\end{aligned} \tag{5.3}$$

Equation (5.3) is applicable for any reference-object-aperture geometry. In the case of astronomical imaging using laser guide stars, the source of the reference wavefront is a laser guide star, and the source of the object wavefront is a celestial object. The guide star is modeled with a point source located on the telescope axis (z-axis) with a height corresponding to that of the guide star. The wavefront from the celestial object is assumed to be a plane wave and is modeled with a far field point source located at a zenith angle  $\theta$ . By letting the subscript "g" designate the optical path from the guide star and the subscript "o" designate the optical path from the celestial object, we find that Equation (5.3) simplifies to

$$\begin{aligned}
\Delta p_{og}(\underline{x}_o, \underline{x}_g, z') &= \underline{x}_o - \underline{x}_g \left( 1 - \left( \frac{z'}{z_g} \right) \right) \\
&+ z' (\tan \theta_x \underline{\hat{x}} + \tan \theta_y \underline{\hat{y}}),
\end{aligned} \tag{5.4}$$

where  $\theta_x$  and  $\theta_y$  are angular offsets in the x and y directions and are related to the zenith angle  $\theta$  by

$$\theta = \tan^{-1} \left[ \tan^2 \theta_x + \tan^2 \theta_y \right]^{1/2}. \tag{5.5}$$

If  $\theta \ll 1$ , Equation (5.4) is well approximated by

$$\Delta p_{o_g}(\underline{x}_o, \underline{x}_g, z') \approx \underline{x}_o - \underline{x}_g \left( 1 - \frac{z'}{z_g} \right) + z' (\theta_x \hat{x} + \theta_y \hat{y}). \quad (5.6)$$

The geometry of two optical paths emanating from a single source is also of interest. In this case the two points in the aperture are designated  $\underline{x}$  and  $\underline{x}'$  and the source positional vectors satisfy  $\underline{r}_o = \underline{r}_r$ . For the laser guide star geometry described above we find that

$$\Delta p_{g_g}(\underline{x}, \underline{x}', z') = (\underline{x} - \underline{x}') \left( 1 - \frac{z'}{z_g} \right), \quad (5.7)$$

and

$$\Delta p_{o_o}(\underline{x}, \underline{x}', z') = \underline{x} - \underline{x}'. \quad (5.8)$$

### 5.3 Adaptive Optics System Definitions and Assumptions

The following system definitions and assumptions closely follow those of Chapter 3 and References 52 and 6. Here the definitions and assumptions are generalized from those given previously to account for the possibility of separate reference and object wavefronts sources. Consider a wavefront correction system consisting of an aperture, a deformable mirror, a wavefront sensor and a control law. The deformable mirror and aperture pupil plane are optically conjugated. The mirror surface is controlled by a finite number of actuators which can effect zonal or modal surface deformations. The wavefront sensor

and the pupil plane are also optically conjugated. The aperture is segmented into subapertures, and the wavefront sensor measures the average phase slope of the reference wavefront within each. The control law uses the measured wavefront slopes in addition to the phase correlations between the reference and object wavefronts to position the actuators of the deformable mirror.

The aperture of the optical system is described by the weighting function  $W_A(\underline{x})$  where  $\underline{x}$  is a vector in the pupil plane. It is convenient to normalize  $W_A(\underline{x})$  such that

$$\int d^2\underline{x} W_A(\underline{x}) = 1, \quad (5.9)$$

where  $\int d^2\underline{x}$  indicates integration over the entire aperture plane.

The phase perturbation of the object wavefront at a point  $\underline{x}$  in the aperture plane is designated  $\psi_o(\underline{x})$  (rad). The phase perturbation of the reference wavefront is designated  $\psi_r(\underline{x})$  (rad). The geometry between the object and reference sources is arbitrary at this point and is not specified until we consider the laser guide star geometry in Section 5.7. Since any uniform phase perturbation over the aperture does not affect optical performance, it is convenient to define zero mean phase perturbations  $\phi_o(\underline{x})$  and  $\phi_r(\underline{x})$  which are related to  $\psi_o(\underline{x})$  and  $\psi_r(\underline{x})$  by

$$\phi_{o,r}(\underline{x}) = \psi_{o,r}(\underline{x}) - \int d^2\underline{x}' W_A(\underline{x}') \psi_{o,r}(\underline{x}'). \quad (5.10)$$

The output of the  $n$ th wavefront sensor is a noisy measurement of the average slope of  $\phi_r(\underline{x})$  over a subaperture defined by  $W_n(\underline{x})$ :

$$s_n = \int d^2\underline{x} W_n(\underline{x}) [\nabla\phi_r(\underline{x}) \cdot \underline{d}_n] + \alpha_n, \quad (5.11)$$

where

$s_n$  = slope signal from the  $n$ th sensor (rad/m),

$W_n(\underline{x})$  = weighting function for the  $n$ th sensor ( $m^{-2}$ ),

$\nabla\phi_r(\underline{x})$  = spatial gradient of  $\phi_r$ ,

$\underline{d}_n$  = unit vector in the direction of the sensitivity of the  $n$ th sensor,

$\alpha_n$  = slope measurement error for the  $n$ th sensor (rad/m).

The weighting function  $W_n(\underline{x})$  is defined in a manner similar to that of  $W_A(\underline{x})$ . Welsh and Gardner<sup>6</sup> show that  $s_n$  can be rewritten as

$$s_n = - \int d^2\underline{x} [\nabla W_n(\underline{x}) \cdot \underline{d}_n] \phi_r(\underline{x}) + \alpha_n. \quad (5.12)$$

For notational simplicity we let  $W_n^s(\underline{x})$  designate  $\nabla W_n(\underline{x}) \cdot \underline{d}_n$ , where the superscript "s" indicates the slope of  $W_n(\underline{x})$  in the direction of the sensitivity of the  $n$ th slope sensor. The measurement error  $\alpha_n$  is attributed to photon noise in the slope measurement and is assumed independent of the wavefront phases  $\phi_r(\underline{x})$  and  $\phi_o(\underline{x})$ .

The control law generates a command for each actuator of the deformable mirror based on the slope measurements. Using a linear control law we define the actuator drive signal  $c_j$

$$c_j = \sum_n M_{jn} s_n, \quad (5.13)$$

where  $c_j$  is the command sent to the  $j$ th actuator and  $M_{jn}$  is the weighting of the  $n$ th sensor signal in the  $j$ th actuator command.

Finally we define the reconstructed wavefront  $\hat{\phi}(\underline{x})$  as

$$\hat{\phi}(\underline{x}) = \sum_j c_j r_j(\underline{x}), \quad (5.14)$$

where  $r_j(\underline{x})$  is the response of the mirror to a unit command at the  $j$ th actuator.

#### 5.4 Mean-Square Residual Phase Error over the Corrected Aperture

Since the deformable mirror is located in a conjugate plane of the pupil, we can analyze the system as if the corrected wavefront passes through the pupil plane. As a consequence, we can write the residual phase error between the estimated wavefront phase  $\hat{\phi}$  and the object wavefront phase  $\phi_o$  as

$$\begin{aligned}
\Delta\phi(\underline{x}) &= \hat{\phi}(\underline{x}) - \phi_o(\underline{x}) \\
&= \sum_j r_j(\underline{x}) \sum_n M_{jn} s_n - \phi_o(\underline{x}) .
\end{aligned} \tag{5.15}$$

Note that, as defined in Equation (5.15),  $\Delta\phi$  has units of radians. For the results in Section 5.8 the phase error is presented in units of waves ( $m$ ). Rather than define a separate notation, we use the symbol  $\Delta\phi$  to designate the error for both cases. The units of  $\Delta\phi$  should be obvious in each case.

We are interested in calculating the average mean-square residual error defined by

$$\langle \Delta\phi^2 \rangle = \int d^2\underline{x} W_A(\underline{x}) \langle \Delta\phi^2(\underline{x}) \rangle , \tag{5.16}$$

where the operator  $\langle \rangle$  designates an ensemble average. Substituting Equation (5.15) into Equation (5.16) gives<sup>6,52</sup>

$$\begin{aligned}
\langle \Delta\phi^2 \rangle &= \sum_j \sum_{j'} \sum_n \sum_{n'} M_{jn} M_{j'n'} S_{nn'} R_{jj'} \\
&\quad - 2 \sum_j \sum_n M_{jn} A_{jn} + \langle \Delta\phi_o^2 \rangle ,
\end{aligned} \tag{5.17}$$

where  $S_{nn'}$ ,  $R_{jj'}$ , and  $A_{jn}$  are given by

$$\begin{aligned}
S_{nn'} &= \langle s_n s_{n'} \rangle \\
&= \int d^2 \underline{x}' \int d^2 \underline{x}'' W_n^s(\underline{x}') W_n^s(\underline{x}'') \langle \phi_r(\underline{x}') \phi_r(\underline{x}'') \rangle \\
&\quad + \langle \alpha_n \alpha_{n'} \rangle,
\end{aligned} \tag{5.18}$$

$$R_{jj'} = \int d^2 \underline{x} W_A(\underline{x}) r_j(\underline{x}) r_{j'}(\underline{x}), \tag{5.19}$$

$$\begin{aligned}
A_{jn} &= \int d^2 \underline{x} W_A(\underline{x}) r_j(\underline{x}) \langle s_n \phi_o(\underline{x}) \rangle \\
&= - \int d^2 \underline{x} \int d^2 \underline{x}' W_A(\underline{x}) r_j(\underline{x}) W_n^s(\underline{x}') \langle \phi_o(\underline{x}) \phi_r(\underline{x}') \rangle,
\end{aligned} \tag{5.20}$$

and the average mean-square uncorrected error  $\langle \Delta \phi_o^2 \rangle$  is

$$\langle \Delta \phi_o^2 \rangle = \int d^2 \underline{x} W_A(\underline{x}) \langle \phi_o^2(\underline{x}) \rangle. \tag{5.21}$$

The terms  $S_{nn'}$  and  $A_{jn}$  given in Equations (5.18) and (5.20) are nearly identical to the terms derived in Chapter 3 and by Wallner,<sup>52</sup> and Welsh and Gardner.<sup>6</sup> The subtle, but important, difference between the terms shown above and those derived earlier is the generalization of the expressions to include the effects of separate reference and object wavefronts. The previous analyses only consider the possibility of a single wavefront source. The additional generality in Equations (5.18) and (5.20) allows us to investigate the effects of anisoplanatism on the performance of the adaptive optics system.



The mean-square residual phase error given by Equation (5.17) is valid for an arbitrary control matrix  $M_{jn}$ . A control matrix giving the minimum mean-square residual error is obtained by differentiating Equation (5.17) with respect to  $M_{jn}$  and equating the result to zero. Wallner<sup>52</sup> gives the minimizing control matrix  $M_{jn}^*$  as

$$M_{jn}^*(\tau) = R_{jj'}^{-1} A_{j'n'} S_{n'n}^{-1}, \quad (5.22)$$

where we have used standard matrix multiplication notation to denote the summations. Wallner states the general conditions for the existence of  $R_{jj'}^{-1}$  and  $S_{n'n}^{-1}$ . Substituting this control matrix back into (5.18) results in the minimum mean-square residual phase error:

$$\langle \Delta \phi^2 \rangle_{\min} = \langle \Delta \phi_o^2 \rangle - R_{jj'}^{-1} A_{j'n'} S_{n'n}^{-1} A_{jn}. \quad (5.23)$$

### 5.5 Optical Transfer Function

The OTF is defined in terms of the complex amplitude field  $E(\underline{x})$  in the aperture of the optical system. Assume  $E(\underline{x})$  is produced by a far field point source. It is well known that the OTF can be written as the convolution of  $E(\underline{x})$  with its complex conjugate  $E^*(\underline{x})$ :<sup>67</sup>

$$H(\underline{\rho}) = \frac{\int d^2 \underline{x} W_A(\underline{x}) E(\underline{x}) W_A^*(\underline{x}-\underline{\rho}) E^*(\underline{x}-\underline{\rho})}{\int d^2 \underline{x} |W_A(\underline{x}) E(\underline{x})|^2}, \quad (5.24)$$

where  $H(\underline{\rho})$  is the OTF, and  $\underline{\rho}$  and  $\underline{x}$  are two-dimensional vectors in the aperture pupil plane. Spatial frequency is related to the positional vector  $\underline{\rho}$  by  $v = |\underline{\rho}|/\lambda f_p$ , where  $v$  is spatial frequency (cycles/m) and  $f_p$  is the focal length of the aperture lens. Using the results given in the previous section and the derivation introduced by Welsh and Gardner<sup>6</sup> (see Chapter 3, Equations (3.18)-(3.24)), we can show that the ensemble average OTF of the phase corrected aperture,  $\langle H(\underline{\rho}) \rangle$ , is

$$\begin{aligned} \langle H(\underline{\rho}) \rangle = & \frac{\exp\left(\frac{-\langle (\phi_o(\underline{x}) - \phi_o(\underline{x} - \underline{\rho}))^2 \rangle}{2}\right)}{\int d^2\underline{x} |W_A(\underline{x})|^2} \int d^2\underline{x} W_A(\underline{x}) W_A^*(\underline{x} - \underline{\rho}) \\ & \times \left[ \exp\left(-\frac{1}{2} \sum_j \sum_i [r_j(\underline{x}) - r_j(\underline{x} - \underline{\rho})][r_i(\underline{x}) - r_i(\underline{x} - \underline{\rho})] C_{ji}\right. \right. \\ & \left. \left. + \sum_j [r_j(\underline{x}) - r_j(\underline{x} - \underline{\rho})] \langle c_j [\phi_o(\underline{x}) - \phi_o(\underline{x} - \underline{\rho})] \rangle \right) \right] \quad (5.25) \end{aligned}$$

where

$$\begin{aligned} C_{ji} &= \langle c_j c_i \rangle \\ &= \sum_n \sum_m M_{jn} M_{im} S_{nm}, \quad (5.26) \end{aligned}$$

and

$$\begin{aligned} \langle c_j [\phi_o(\underline{x}) - \phi_o(\underline{x}-\underline{p})] \rangle = \\ - \sum_n M_{jn} \int d^2 \underline{x}' W_n^s(\underline{x}') \left( \langle \phi_r(\underline{x}') \phi_o(\underline{x}) \rangle - \langle \phi_r(\underline{x}') \phi_o(\underline{x}-\underline{p}) \rangle \right). \end{aligned} \quad (5.27)$$

Just as in the case of  $\langle \Delta \phi^2 \rangle$ , the expressions given in Equations (5.25)-(5.27) are nearly identical to the expressions derived in Chapter 3 and by Welsh and Gardner.<sup>6</sup> The difference is in the generalization of the equations to include the effects of separate reference and object wavefronts.

### 5.6 Wavefront Phase Statistics

Equations (5.23) and (5.25) are the main results of the previous two sections. To evaluate these equations the phase correlations  $\langle \phi_r(\underline{x}) \phi_r(\underline{x}') \rangle$ ,  $\langle \phi_o(\underline{x}) \phi_r(\underline{x}') \rangle$  and  $\langle \phi_o(\underline{x}) \phi_o(\underline{x}') \rangle$  must be computed. These correlations can be written as a function of the generalized phase structure function  $D_{or}(\underline{x}, \underline{x}')$ . The structure function  $D_{or}(\underline{x}, \underline{x}')$  is defined by

$$D_{or}(\underline{x}, \underline{x}') = \langle [\psi_o(\underline{x}) - \psi_r(\underline{x}')]^2 \rangle, \quad (5.28)$$

where the vectors  $\underline{x}$  and  $\underline{x}'$  are positional vectors in the aperture plane of the optical system. Calculating the phase correlations in terms of Equation (5.28) is a straightforward application of the derivation introduced by Wallner.<sup>52</sup> We do not repeat the derivation here, but simply state the result:

$$\langle \phi_o(\underline{x}) \phi_r(\underline{x}') \rangle = -\frac{1}{2} D_{or}(\underline{x}, \underline{x}') + g_{or}(\underline{x}) + g_{ro}(\underline{x}') - f, \quad (5.29)$$

where

$$g_{or}(\underline{x}) = \frac{1}{2} \int d^2 \underline{x}'' W_A(\underline{x}'') D_{or}(\underline{x}, \underline{x}''), \quad (5.30)$$

and

$$f = \frac{1}{2} \int d\underline{x}'' \int d\underline{x}''' W_A(\underline{x}'') W_A(\underline{x}''') D_{or}(\underline{x}'', \underline{x}'''). \quad (5.31)$$

Substituting Equation (5.29) into the expressions for  $S_{nn'}$  and  $A_{jn}$  given by Equations (5.18) and (5.20) results in

$$\begin{aligned} S_{nn'} = & -\frac{1}{2} \int d^2 \underline{x}' \int d^2 \underline{x}'' W_n^s(\underline{x}') W_n^s(\underline{x}'') D_{rr}(\underline{x}', \underline{x}'') \\ & + \langle \alpha_n \alpha_{n'} \rangle, \end{aligned} \quad (5.32)$$

and

$$\begin{aligned} A_{jn} = & - \int d^2 \underline{x} \int d^2 \underline{x}' W_A(\underline{x}) r_j(\underline{x}) W_n^s(\underline{x}') \\ & \times [-\frac{1}{2} D_{or}(\underline{x}, \underline{x}') + g_{ro}(\underline{x}')], \end{aligned} \quad (5.33)$$

where it is assumed that  $\int d^2 \underline{x} W_n^s(\underline{x}) = 0$ . Also substituting Equation (5.29) into the expression for  $\langle H(\underline{\rho}) \rangle$  given by Equation (5.25) results in

$$\begin{aligned}
\langle H(\underline{p}) \rangle = & \frac{\exp\left(\frac{-D_{oo}(\underline{x}, \underline{x}-\underline{p})}{2}\right)}{\int d^2\underline{x} |W_A(\underline{x})|^2} \int d^2\underline{x} W_A(\underline{x}) W_A^*(\underline{x}-\underline{p}) \\
& \times \left[ \exp\left(-\frac{1}{2} \sum_j \sum_i [r_j(\underline{x}) - r_j(\underline{x}-\underline{p})][r_i(\underline{x}) - r_i(\underline{x}-\underline{p})] C_{ji}\right. \right. \\
& \left. \left. + \sum_j [r_j(\underline{x}) - r_j(\underline{x}-\underline{p})] \langle c_j [\phi_o(\underline{x}) - \phi_o(\underline{x}-\underline{p})] \rangle \right) \right], \quad (5.34)
\end{aligned}$$

where

$$\begin{aligned}
\langle c_j [\phi_o(\underline{x}) - \phi_o(\underline{x}-\underline{p})] \rangle = \\
\frac{1}{2} \sum_n M_{jn} \int d^2\underline{x}' W_n^s(\underline{x}') [D_{or}(\underline{x}, \underline{x}') - D_{or}(\underline{x}-\underline{p}, \underline{x}')]. \quad (5.35)
\end{aligned}$$

### 5.7 Phase Structure Function

For homogeneous isotropic turbulence with a Kolomogorov spectral density, Lutomirski and Buser<sup>79</sup> show that the phase structure function  $D_{or}$  is given by

$$D_{or}(\underline{x}, \underline{x}') = 2.91 k^2 \int_0^{z_{min}} C_n^2(z') |\Delta \underline{p}_{or}(\underline{x}, \underline{x}', z')|^{5/3} dz' \quad (5.36)$$

where  $C_n$  ( $m^{-2/3}$ ) is the structure constant of the refractive index fluctuations and  $z_{min}$  is the minimum of the  $z$  components of the source's positional vectors  $\underline{r}_o$  and  $\underline{r}_r$ . Lutomirski and Buser<sup>79</sup> obtain the expression in Equation (5.36) by assuming that the magnitudes of the vectors  $\underline{x}$ ,  $\underline{x}'$ ,  $\underline{p}_o$  and  $\underline{p}_r$  are much smaller than  $z_o$  and  $z_r$ . Also, in

the case of separate wavefront sources, Equation (5.36) is valid only if the turbulence effects are negligible for  $z > z_{\min}$  (i.e.,  $C_n(z) = 0$  for  $z > z_{\min}$ ). In the case of astronomical imaging, the first restriction is satisfied for  $\theta z_h \ll 1$  and  $D \ll z_h$  where  $\theta$  is the angular offset from the telescope axis of the direction of interest and  $z_h$  is the maximum height of the turbulence. The second restriction is satisfied if the guide star height  $z_g (=z_r)$  is greater than  $z_h$ . Rewriting Equation (5.36) in terms of the Fried seeing cell diameter  $r_o$  gives

$$D_{or}(\underline{x}, \underline{x}') = \frac{6.88 \int_0^{z_{\min}} C_n^2(z') |\Delta p_{or}(\underline{x}, \underline{x}', z')|^{5/3} dz'}{r_o^{5/3} \int_0^{z_{\min}} C_n^2(z') dz'} \quad (5.37)$$

where we have used the following definition of  $r_o$ :<sup>28</sup>

$$r_o = \left[ \frac{2.91}{6.88} k^2 \int_0^{z_{\min}} C_n^2(z) dz \right]^{-3/5} \quad (5.38)$$

In the computational results of the following section we consider the laser guide star geometry discussed in Section 5.2. In this case the subscript "r" (reference source) is replaced with "g" (guide star) in the equations of Sections 5.3-5.6. The expressions for  $\Delta p_{og}$ ,  $\Delta p_{gg}$  and  $\Delta p_{oo}$  given by Equations (5.6)-(5.8) are substituted into Equation (5.37) to obtain

$$D_{og}(\underline{x}, \underline{x}') = \frac{6.88}{r_o^{5/3} \int_0^{z_{min}} C_n^2(z') dz'}$$

$$\times \int_0^{z_{min}} C_n^2(z') \left| \underline{x} - \underline{x}' \left( 1 - \left( \frac{z'}{z_g} \right) \right) + z' (\theta_x \hat{x} + \theta_y \hat{y}) \right|^{5/3} dz', \quad (5.39)$$

$$D_{gg}(\underline{x}, \underline{x}') = \frac{6.88 |\underline{x} - \underline{x}'|^{5/3} \int_0^{z_{min}} C_n^2(z') \left( 1 - \frac{z'}{z_g} \right)^{5/3} dz'}{r_o^{5/3} \int_0^{z_{min}} C_n^2(z') dz'}, \quad (5.40)$$

and

$$D_{oo}(\underline{x}, \underline{x}') = 6.88 \frac{|\underline{x} - \underline{x}'|^{5/3}}{r_o^{5/3}}. \quad (5.41)$$

Note that Equations (5.40) and (5.41) are commonly referred to in the literature as the spherical and plane wave phase structure functions, respectively.

## 5.8 Computational Results

One of the key design parameters that ultimately determines the laser power requirements for a laser-guided adaptive telescope is the number of guide stars required to fully sample the telescope aperture.<sup>5</sup> Due to the small size of the isoplanatic angle at visible wavelengths, multiple guide stars are required to correct a large telescope aperture. This was first pointed out by Foy and Labeyrie.<sup>3</sup> Thompson

and Gardner<sup>31</sup> and Gardner et al.<sup>5</sup> calculate the required number of guide stars by specifying that each point in the aperture of the telescope must lie within the isoplanatic angle of a guide star. Figure 2.4 illustrates a diagram of the isoplanatic angle superimposed on a cross section of the telescope aperture. The points in the aperture that lie within the isoplanatic angle are encircled by an area of diameter  $D_{IP}$  where  $D_{IP}$  is given by<sup>31</sup>

$$D_{IP} = 2 z_g \theta_{IP}, \quad (5.42)$$

$z_g$  is the height of the guide star above the telescope entrance plane, and  $\theta_{IP}$  is the isoplanatic angle. For aperture diameters  $D > D_{IP}$ , Gardner et al.<sup>5</sup> calculate that the approximate number of guide stars ( $N_{gs}$ ) required is

$$N_{gs} \approx \frac{D^2}{D_{IP}^2} = \frac{D^2}{4 z_g^2 \theta_{IP}^2}. \quad (5.43)$$

The value of  $\theta_{IP}$  substituted into Equation (5.43) depends on the definition used and the desired imaging performance. Gardner et al., rather arbitrarily, chose a definition given by Fried:<sup>28</sup>

$$\theta_{IP} = \frac{r_o}{(6.88)^{5/3}} \left[ \frac{\int_0^h \left[ 1 - \frac{\xi}{h} \right]^{5/3} C_n^2(\xi) d\xi}{\int_0^h C_n^2(\xi) \xi^{5/3} d\xi} \right]^{3/5}. \quad (5.44)$$

Modeling the atmosphere with a single turbulent layer at an altitude  $h_t$  and using Equation (5.44) they find that



$$\theta_{IP} \approx \frac{r_o}{3h_t}. \quad (5.45)$$

In this case  $N_{gs}$  is given by

$$N_{gs} \approx 2.25 \frac{D^2 h_t^2}{z_g^2 r_o^2}. \quad (5.46)$$

Fried's definition of  $\theta_{IP}$  is based on the assumptions that the object and reference wavefronts are plane waves and the adaptive optics system is capable of perfect wavefront compensation for the case of coincident object and reference sources. For these assumptions Fried finds that when the angular separation between the object and reference wavefront is  $\theta_{IP}$ , the Strehl ratio of the adaptive optics system degrades to a value of  $\sim 0.4$  for aperture sizes larger than  $r_o$ .

The calculation method used to obtain Equation (5.46) does not take into account the nonideal characteristics of the wavefront sensor and deformable mirror, nor the effects of photon noise on the wavefront measurements. Additionally, the approach fails to take into account the spherical nature of the wavefront from the laser guide star. In the first half of this section we present computational results that indicate how many guide stars are required for a given aperture size and guide star height. We also show how imaging performance varies as a function of the number and height of the guide stars. In addition to the requirement of multiple guide stars, the effects of anisoplanatism also limit the FOV of the adaptive telescope. In the last part of this

section we quantify the degradation in imaging performance as a function of angular separation between the laser guide star and observation direction. These results also indicate the maximum FOV of the laser-guided telescope.

### Performance Measures

The performance measures used in the following results include the residual phase error across the aperture, the Strehl ratio, the ensemble average OTF, and the ensemble average point spread function (PSF). The residual phase error  $\langle \Delta\phi^2 \rangle$  and the OTF  $\langle H(\underline{\rho}) \rangle$  are given by Equations (5.23) and (5.34). The Strehl ratio is a general indication of how well the peak intensity of the image due to a point source can be discerned from the surrounding intensity distribution. For  $\langle \Delta\phi^2 \rangle^{\frac{1}{2}} < 2\pi/10$  radians the Strehl ratio  $S$  can be approximated by<sup>1</sup>

$$S(\langle \Delta\phi^2 \rangle) \approx \exp(-\langle \Delta\phi^2 \rangle). \quad (5.47)$$

The ensemble average PSF  $\langle s \rangle$  is related to  $\langle H \rangle$  by the two-dimensional inverse Fourier transform:<sup>6,7</sup>

$$\langle s(\underline{\gamma}/\lambda f_d) \rangle = \frac{F_2^{-1}(\langle H(\underline{\rho}) \rangle)}{(\lambda f_d)^2} \quad (5.48)$$

where  $s$  is the unaveraged PSF,  $\underline{\gamma}$  and  $\underline{\rho}$  are vectors in the image and pupil planes respectively, and the operator  $F_2^{-1}$  is the two-dimensional inverse Fourier transform. As in Chapter 3, the computational requirements are reduced by calculating the one-dimensional (1D) PSF instead. The 1D PSF is related to the 2D PSF by

$$\begin{aligned}
\langle s(u/\lambda f_d) \rangle &= \int dv \langle s(u/\lambda f_d, v/\lambda f_d) \rangle \\
&= \int dx \frac{\langle H(x, 0) \rangle}{\lambda f_d} \exp \left[ j 2 \pi x \left( \frac{u}{\lambda f_d} \right) \right] \\
&= \frac{F_1^{-1}(\langle H(x, 0) \rangle)}{\lambda f_d},
\end{aligned} \tag{5.49}$$

where  $(u, v)$  and  $(x, y)$  are Cartesian coordinates in the image and pupil planes respectively, and the operator  $F_1^{-1}$  is the 1D inverse Fourier transform.

#### Description of Deformable Mirror and Wavefront Sensor

The mirror is assumed to be of monolithic design with an actuator spacing equal to  $d$ . Figure 5.2 illustrates the actuator geometry. The actuator response  $r_j(\underline{x})$  is assumed Gaussian:

$$r_j(x, y) \propto \exp \left( \frac{-(x-x_j)^2 - (y-y_j)^2}{d_a^2} \right), \tag{5.50}$$

where  $x$  and  $y$  specify a point in the plane of the mirror,  $x_j$  and  $y_j$  specify the actuator location, and  $d_a$  is the influence radius. The Gaussian response is often used to model piezoelectric or membrane deformable mirrors.<sup>6</sup>

The model of the wavefront sensor is derived from the basic characteristics of the Hartmann sensor. Figure 5.2 illustrates the

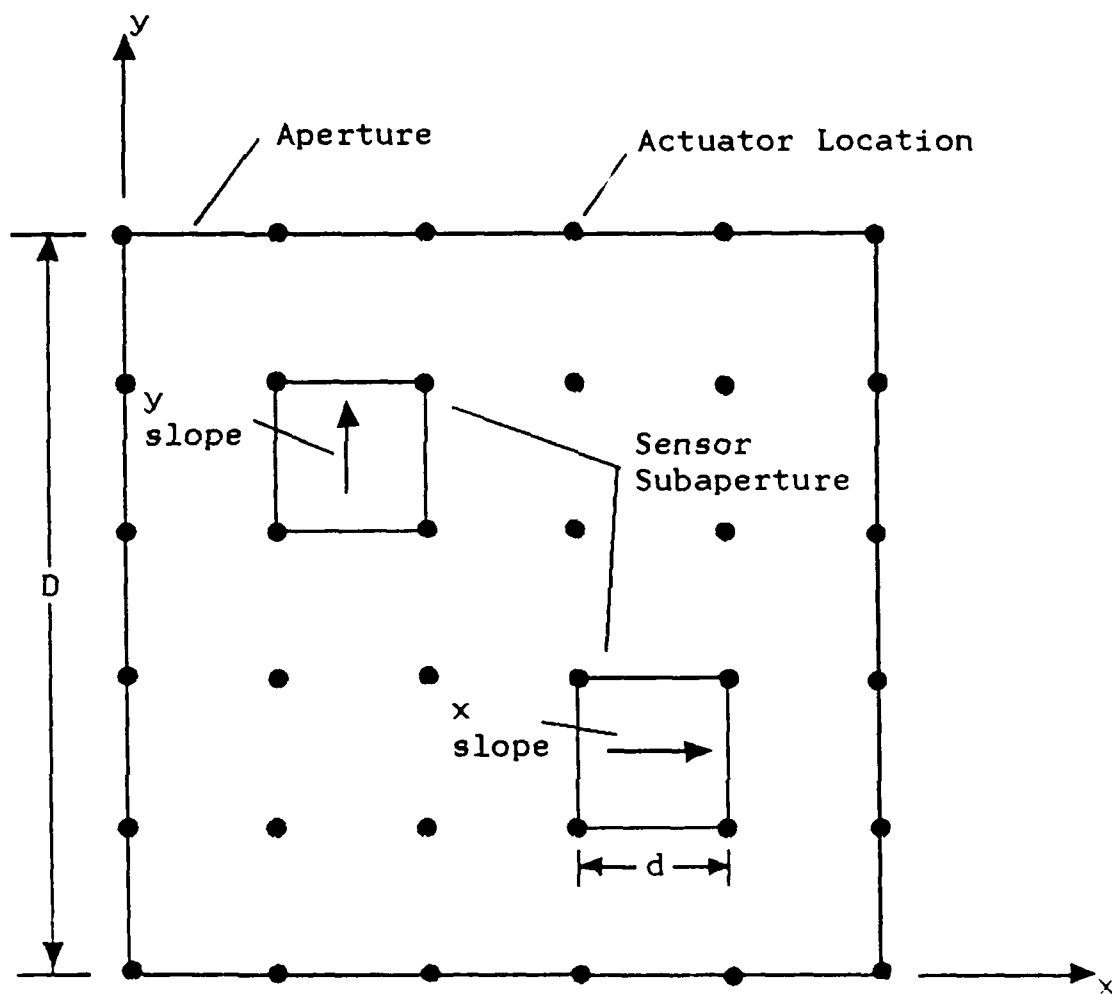


Figure 5.2. Wave front sensor and mirror actuator configuration.

geometry of the sensor. A square aperture of dimension  $D$  is divided into equal size subapertures of dimension  $d$ . In each subaperture the slope is sensed in both the  $x$  and  $y$  directions.

The following model for the second-order statistics of the slope measurement noise  $\alpha_n$  is presented in Chapter 3 and by Welsh and Gardner:<sup>6</sup>

$$\langle \alpha_n \alpha_{n'} \rangle = \sigma_n^2 k_{nn'}, \quad (5.51)$$

where

$$\sigma_n^2 = \text{mean square slope error (rad}^2 \text{ m}^{-2}\text{)},$$

$$k_{nn'} = \cos \psi \delta_{nn'},$$

$\psi$  = the angle between the direction of sensitivity of the  $n$ th and  $n'$ th sensors,

$$\delta_{nn'} = \begin{cases} 1 & \text{nth and } n'\text{th subapertures coincide} \\ 0 & \text{otherwise.} \end{cases}$$

The magnitude of  $\sigma_n^2$  depends on the type and configuration of the slope sensors used in the wavefront sensor. Consider the single Hartmann sensor shown in Figure 3.4. The subaperture slope is measured by sensing the position of the diffraction limited spot in the focal plane of the lens. The spot centroid is sensed with an array of photon counting devices such as a CCD detector array. In Chapter 3 we showed that  $\sigma_n$  can be written

$$\sigma_n = \begin{cases} \frac{0.86\pi\eta}{\sqrt{N} r_o} & d > r_o \\ \frac{0.74\pi\eta}{\sqrt{N} d} & d \leq r_o \end{cases} \quad (5.52)$$

where  $\eta$  is a parameter accounting for imperfections of the detector array (i.e., the effects of finite size array elements and dead space between array elements), and  $N$  is the total subaperture photon count. Note that  $\eta \geq 1$  and that  $\eta = 1$  only in the ideal case of infinitely small detector elements with no dead space between elements. In the following computations we assume  $\eta=1.35$ . This value is typical of the minimum achievable for currently available intensified CCD detector arrays.<sup>14,15</sup>

#### Turbulence Model, $C_n$

Two models are used to characterize how the turbulence is distributed in the lower atmosphere. In the first model the turbulence is confined to a single layer at an altitude  $h_t$ . The structure constant  $C_n^2$  is given by

$$C_n^2(z) = C_n^2 \delta(z-h_t), \quad (5.53)$$

where  $\delta(z)$  is a Dirac-delta function. This model was chosen for two reasons. First, the use of Equation (5.53) simplifies the expression for the phase structure function  $D_{\phi r}$  given in Equation (5.37). The simplification results in one less integral to evaluate and greatly reduces the amount of computation required to calculate  $\langle \Delta \phi^2 \rangle$  and  $\langle H(\rho) \rangle$ . Secondly, in the past analyses, the atmosphere is frequently

modeled with a single turbulent layer. For comparison purposes, this model matches that assumed by Gardner et al.<sup>5</sup> for their calculation of the required number of guide stars.

In the second model, the turbulence is distributed continuously from ground level to an altitude of ~ 20 km. The structure constant  $C_n^2$  is assumed to be given by the Hufnagel model<sup>80</sup>

$$C_n^2(z) = A \left[ 2.2 \times 10^{-23} z^{10} e^{-z} + 10^{-16} e^{-z/1.5} \right], \quad (5.54)$$

where A is an arbitrary scaling constant. Figure 5.3 is a plot of  $C_n^2$  normalized by its integrated area. The Hufnagel model is included because it represents a more realistic model of the atmosphere than the single layer model.

## Results

1) Number of Guide Stars Required for a Laser-guided Adaptive Telescope: The required number of guide stars is computed by first studying the imaging performance of an adaptive optics system for the case of a single laser guide star on the axis of the aperture. The results are then extended to multiple guide stars. For a fixed aperture size, the altitude of the guide star  $z_g$  is varied, and the change in imaging performance is computed. The object wavefront is modeled with a far field point source on the axis of the aperture (i.e., at a zenith angle  $\theta = 0$ ). To indicate that the calculations are

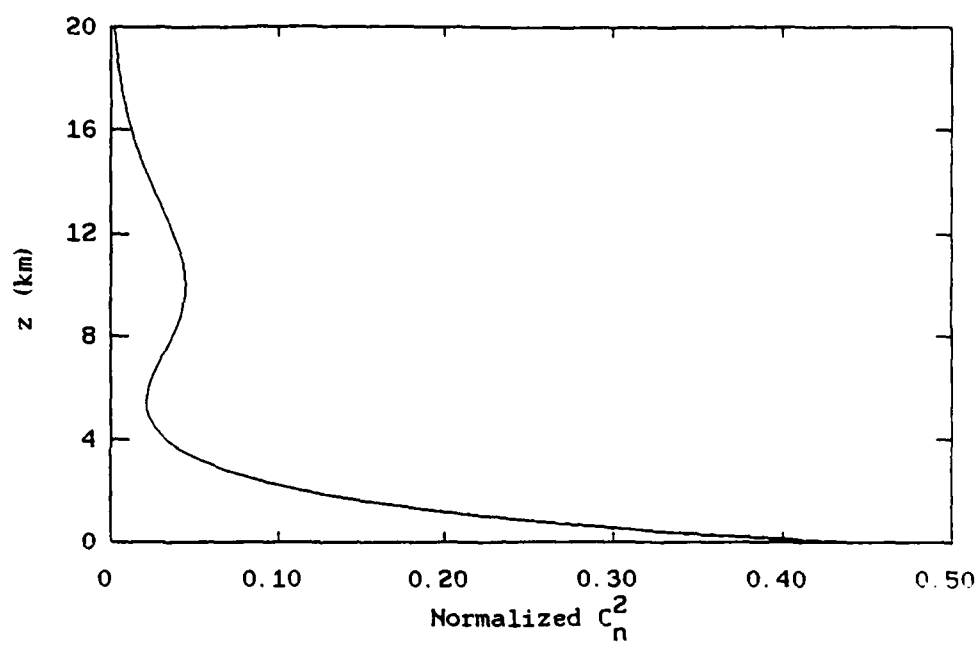


Figure 5.3. Normalized plot of  $C_n^2$  versus altitude.



for a single guide star we let  $D_1$  designate the dimension of the aperture. The results are computed for relatively small apertures (i.e., apertures with 4 to 36 subapertures) in order to minimize the computation requirements. The small aperture calculations are generalized for larger apertures by using a simple scaling relationship.

The results indicate, as expected, that as the altitude of the guide star decreases the imaging performance degrades in a continuous manner. The mean-square wavefront phase error  $\langle \Delta\phi^2 \rangle$  asymptotically approaches a minimum as the distance between the aperture and guide star goes to infinity. The value of  $\langle \Delta\phi^2 \rangle$  is dependent on the height of the guide star, the size of the aperture, the subaperture/actuator spacing, and the photon noise level in the wavefront sensor. For a fixed subaperture/actuator spacing and a fixed photon noise level, the dependence of  $\langle \Delta\phi^2 \rangle$  on the two remaining parameters,  $z_g$  and  $D_1$ , is reduced to a dependence on the ratio  $D_1/z_g$ . This dependence verifies the applicability of the scaling relationship discussed above. For example, the computed results for a given aperture size are valid for a larger aperture as long as the ratio  $D_1/z_g$ , the subaperture/actuator spacing, and photon noise level are all equal for the two apertures. In the following results both the subaperture/actuator spacing and the photon noise level are fixed, and only the effects of varying  $D_1/z_g$  are examined. The effects of varying the subaperture/actuator spacing and the noise level have been investigated in Chapter 3 and in Reference 6.

For the two turbulence models, Figures 5.4 and 5.5 show the residual rms phase error  $\langle \Delta\phi^2 \rangle^{1/2}$  as a function of  $D_1/D_0$ , where  $D_0$  is defined to be

$$D_0 = \frac{z_g r_0}{h_t}. \quad (5.55)$$

The ratio  $D_1/D_0$  is simply the ratio of an aperture of diameter  $D_1$  to an aperture of diameter  $D_0$ , where  $D_0$  can be interpreted as a measure of the largest telescope diameter requiring only one guide star. From Equations (5.42) and (5.45) we see that  $D_0 = 3D_{IP}/2$ , where  $D_{IP}$  is interpreted by Gardner et al.<sup>5</sup> as the largest telescope diameter requiring a single guide star. In the case of the Hufnagel model,  $h_t$  is equated (somewhat arbitrarily) to the altitude of the upper peak of the  $C_n^2$  distribution (see Figure 5.3). The upper peak occurs at an altitude of  $\sim 10$  km. The parameter  $h_t$  for the Hufnagel model is defined in this way to make the data in Figures 5.4 and 5.5 comparable for the specific case in which  $h_t = 10$  km for the single layer model.

The results were computed for a photon flux level of  $76 \text{ counts}/r_0^2$  and a subaperture/actuator spacing of  $d = 0.69r_0$ . These parameter values were chosen to match the values used in the telescope design examples presented in Chapter 2 and by Gardner et al.<sup>5</sup> The results show that as  $D_1/D_0$  decreases, the rms phase error decreases asymptotically to a minimum value of  $\sim 0.09 \lambda$ . This minimum error is the limiting value caused by the slope measurement noise and the finite subaperture/actuator spacing. Results are shown for aperture

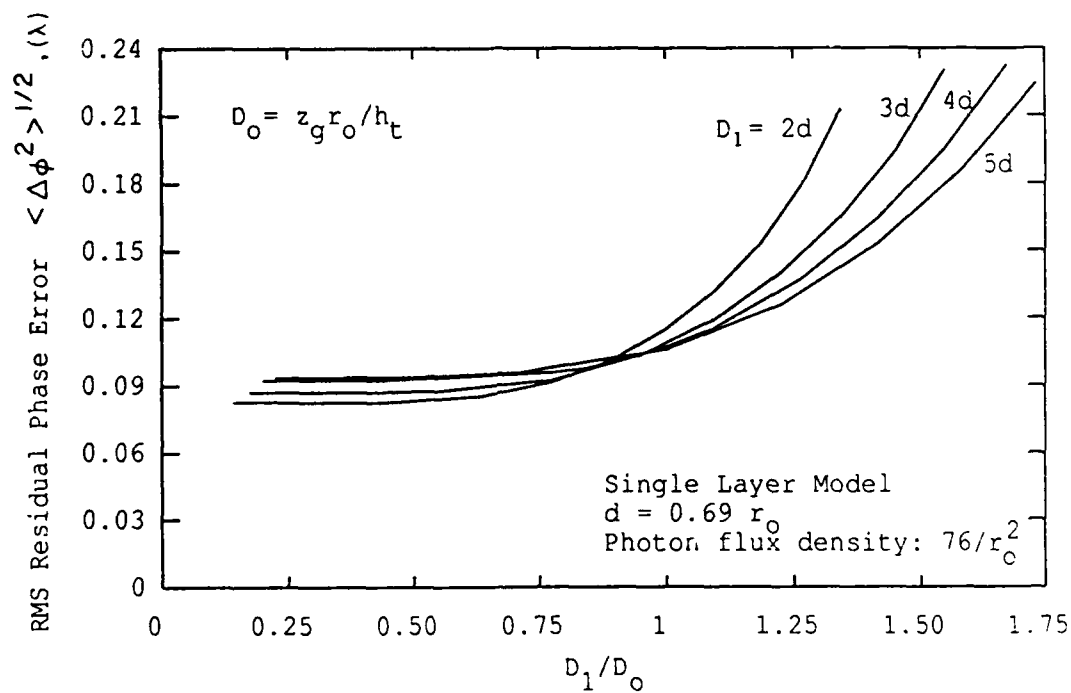


Figure 5.4. Residual RMS phase error over the aperture versus  $D_1/D_0$  for the single layer turbulence model. Curves are shown for aperture dimensions ranging from  $D_1 = 2d$  to  $5d$ .

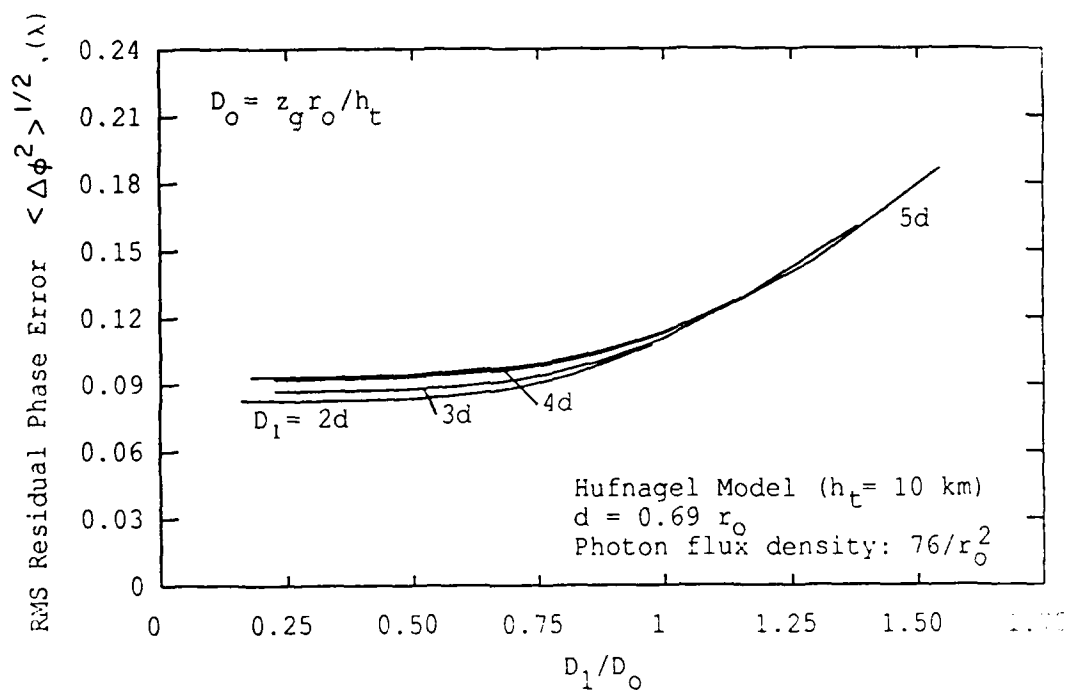


Figure 5.5. Residual RMS phase error over the aperture versus  $D_1/D_0$  for the Hufnagel turbulence model. Curves are shown for aperture dimensions ranging from  $D_1 = 2d$  to  $5d$ .

dimensions ranging from  $D_1 = 2d$  to  $5d$ . These various aperture sizes were investigated to verify the general applicability of the scaling relationship discussed above. The curves in each plot show a convergence to a single locus of points as the aperture dimension increases. The convergence verifies the applicability of the scaling relationship for large telescopes (i.e., those having more than  $\sim 5$  subapertures across the aperture). The slight differences between the curves are due in part to edge effects. As the size of the aperture increases the edge effects play less and less of a role in the total phase error, and the curves converge to a single locus of points. Photon noise in the wavefront sensor also contributes to the slight differences between the curves. Welsh and Gardner<sup>6</sup> show that the photon flux level must be greater than 100 to 200 photons/ $r_0^2$  before the phase error becomes completely independent of aperture diameter. Notice that the results for the Hufnagel model, shown in Figure 5.5, do not extend to large values of  $D_1/D_0$  as they do in Figure 5.4. This limitation is an artifact of setting  $h_t = 10$  km for the Hufnagel model and requiring the height of the guide star  $z_g$  to be greater than the highest turbulence (in our case we assume that  $C_n \sim 0$  for  $z > 20$  km). The largest values of  $D_1/D_0$  plotted in Figure 5.5 represent the points in which the height of the guide star is 20 km. This limitation is not encountered for the data in Figure 5.4, since  $h_t$  is not fixed as it is in the case of the Hufnagel model.

In addition to  $\langle \Delta\phi^2 \rangle$ , the variation of the Strehl ratio as a function of  $D_1/D_0$  is also computed using Equation (5.47). Figure 5.6

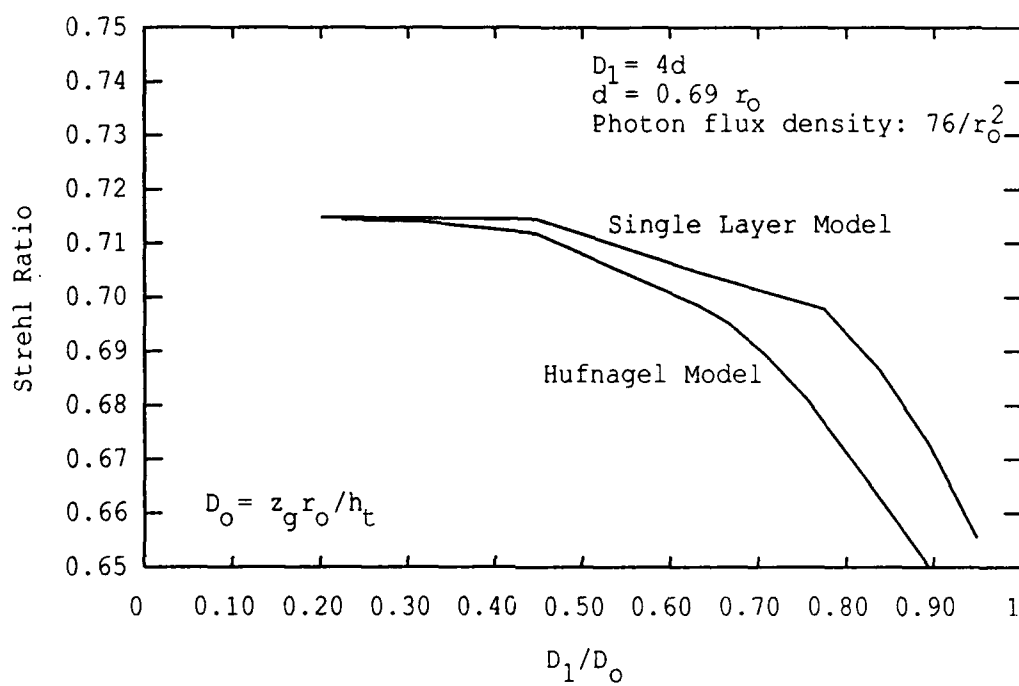


Figure 5.6. Strehl ratio versus  $D_1/D_0$  for both turbulence models.

is a plot of the Strehl ratio calculated from the data in Figures 5.4 and 5.5 for the case of  $D_1 = 4d$ . The curves for the other aperture sizes are similar to that shown. Notice that the Strehl ratio starts to significantly degrade as  $D_1/D_0$  becomes larger than  $\sim 2/3$ . Interestingly, this point corresponds to the case in which  $D_1/D_{IP} = 1$ . Recall that  $D_{IP}$  is derived from Fried's definition of the isoplanatic angle.

In order to calculate the number of guide stars required for a given telescope, the desired imaging performance of the telescope must be specified by choosing the maximum allowed phase error  $\langle \Delta\phi^2 \rangle_{\max}$  (or equivalently the minimum allowed Strehl ratio  $S_{\min}$  from Figure 5.6). Choosing  $\langle \Delta\phi^2 \rangle_{\max}$  from Figures 5.4 or 5.5 corresponds to specifying a maximum allowed value of  $D_1/D_0 = (D_1/D_0)_{\max}$ . The aperture dimension  $D_1$  must satisfy

$$D_1 \leq D_0 (D_1/D_0)_{\max} = \frac{z_g r_o}{h_t} \left( \frac{D_1}{D_0} \right)_{\max} \quad (5.56)$$

in order to achieve a phase error less than  $\langle \Delta\phi^2 \rangle_{\max}$ . To maintain a phase error of  $\langle \Delta\phi^2 \rangle_{\max}$  over an aperture dimension  $D > D_1$ , an additional guide star is required for each subaperture area of dimension  $D_1$ . The total number of guide stars required then becomes

$$N_{gs} = \frac{D^2}{D_1^2} = \frac{D^2}{D_0^2 (D_1/D_0)_{\max}^2} = \frac{D^2 h_t^2}{r_o^2 z_g^2 (D_1/D_0)_{\max}^2} \quad (5.57)$$

where  $D_1$  is assumed to satisfy the equality in Equation (5.56).

Comparing Equation (5.57) to the expression found by Gardner et al.<sup>5</sup> in Equation (5.46) reveals that the two are equivalent if  $1/(D_1/D_0)_{\max}^2 = 2.25$  (i.e.,  $(D_1/D_0)_{\max} = 2/3$ ). Gardner et al. derived this value of  $(D_1/D_0)_{\max}$  from the definition of  $\theta_{IP}$  given by Fried.<sup>28</sup> In the approach presented here,  $(D_1/D_0)_{\max}$  is related directly to the maximum allowed phase error across the telescope aperture. Figures 5.4 and 5.5 indicate that  $(D_1/D_0)_{\max}$  can be increased from 2/3 without significantly increasing  $\langle \Delta\phi^2 \rangle_{\max}$ . For example, if the phase error is allowed to be as large as  $\sim 0.11 \lambda$  (or equivalently the Strehl ratio as small as 0.62) then  $(D_1/D_0)_{\max}$  can be as large as unity. In this case, the required number of guide stars decreases by a factor of 2.25 from that calculated by Gardner et al. Equivalently, the value of the isoplanatic angle  $\theta_{IP}$  increases from Fried's value of  $r_0/3h_t$  to  $r_0/2h_t$ . The factor decrease in the number of required guide stars translates directly into an equivalent factor decrease in the required laser power for the laser-guided adaptive telescope. For a 2-meter diameter telescope, Gardner et al. calculate that the required laser powers for Rayleigh and Na guide stars are 75 W and 13 W, respectively. With these power levels and a subaperture/actuator spacing of  $0.69r_0$ , the rms phase error across the aperture would be  $\sim 0.09\lambda = \lambda/11$ , which corresponds to a Strehl ratio of 0.73. If the number of guide stars is decreased by a factor of 2.25, then the power requirements are reduced to 33 W and 6 W for Rayleigh and Na guide stars, respectively. The number of Na guide stars required decreases from 3 to 1, and the number of Rayleigh guide stars decreases from 156 to 70. Note that the



required number of guide stars must be an integer. The penalty paid, though, is a loss in imaging performance. The rms phase error across the aperture increases from a value of  $\sim 0.09\lambda \approx \lambda/11$  to  $\sim 0.11\lambda \approx \lambda/9$ .

Recall that the comparison between Figures 5.4 and 5.5 is valid for the case in which  $h_c = 10$  km for the single layer model. The close similarity between the data in Figures 5.4 and 5.5 indicates that the turbulence effects of the smoothly varying Hufnagel model are well characterized by a single layer of turbulence at an altitude of 10 km. This conclusion is very important since it implies that it is possible to characterize the effects of an arbitrary  $C_n^2$  profile with a simpler, single layer model.

The OTF  $\langle H(\underline{\rho}) \rangle$  of the laser-guided telescope is also computed as a function of  $D_1/D_0$ . The expression for  $\langle H(\underline{\rho}) \rangle$  given by Equation (5.34) is evaluated for both turbulence models. Rather than consider all the aperture sizes addressed above we consider only the aperture dimension  $D_1 = 4d$  in the subsequent results. The results of the computations are presented as plots of the magnitude of the OTF versus  $|\underline{\rho}|/D_1 = \rho/D_1$ . Recall that spatial frequency  $\nu$  (cycles/meter) is related to  $\rho$  by  $\nu = \rho/\lambda f_D$  where  $f_D$  is the focal length of the aperture lens. In all cases, the vector  $\underline{\rho}$  is assumed in the  $x$  or  $y$  directions giving  $\langle H(\underline{\rho}) \rangle = \langle H(x,0) \rangle$ , or equivalently  $\langle H(\underline{\rho}) \rangle = \langle H(0,y) \rangle$ .

Figures 5.7 and 5.8 illustrate the OTF of the corrected aperture for the two turbulence models. The OTF is calculated for  $D_1/D_0$  ranging

from 0.2 to 2.0,  $D_1 = 4d$ ,  $d = 0.69r_0$ , and a photon flux level of 76 photons/ $r_0^2$ . The uppermost curve in both figures is the OTF of the perfect unaberrated system. The bottom-most curve is the OTF for the aberrated system assuming no wavefront correction. As  $D_1/D_0$  decreases, the frequency responses show steady improvement until converging to an upper limit. This same convergence was also seen in Figures 5.4 and 5.5 for the residual phase error  $\langle \Delta\phi^2 \rangle$ . In Figures 5.4 and 5.5 we saw that  $D_1/D_0$  could be as large as unity before significantly degrading imaging performance. This same behavior is illustrated in Figures 5.7 and 5.8. The degradation in the response of the OTF is relatively insignificant until  $D_1/D_0$  becomes larger than 1. Just as in Figures 5.4 and 5.5, there is very little difference between the results of Figures 5.7 and 5.8. Again, this points to the feasibility of modeling the continuously distributed  $C_n$  profile with a single layer of turbulence at an appropriate altitude.

Figures 5.9 and 5.10 illustrate the corresponding one-dimensional PSFs for the OTFs illustrated in Figures 5.7 and 5.8. The amplitude of the PSF is plotted versus the dimensionless quantity  $uD_1/\lambda f_p$ , where  $u$  is the image plane coordinate. The 1D PSFs for both the unaberrated system and the aberrated system with no wavefront correction are shown. The interesting feature to notice from these curves is that angular resolution (i.e., FWHM of the PSF main lobe) does not rapidly

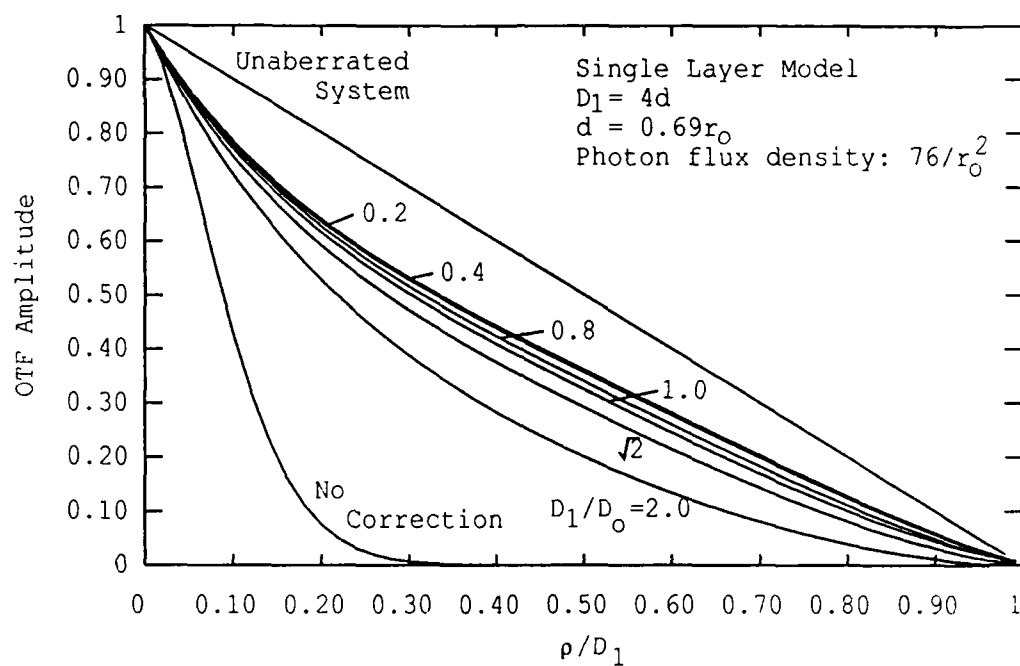


Figure 5.7. OTF of the phase corrected aperture for  $D_1/D_0$  ranging from 0.2 to 2.0 and the single layer turbulence model.

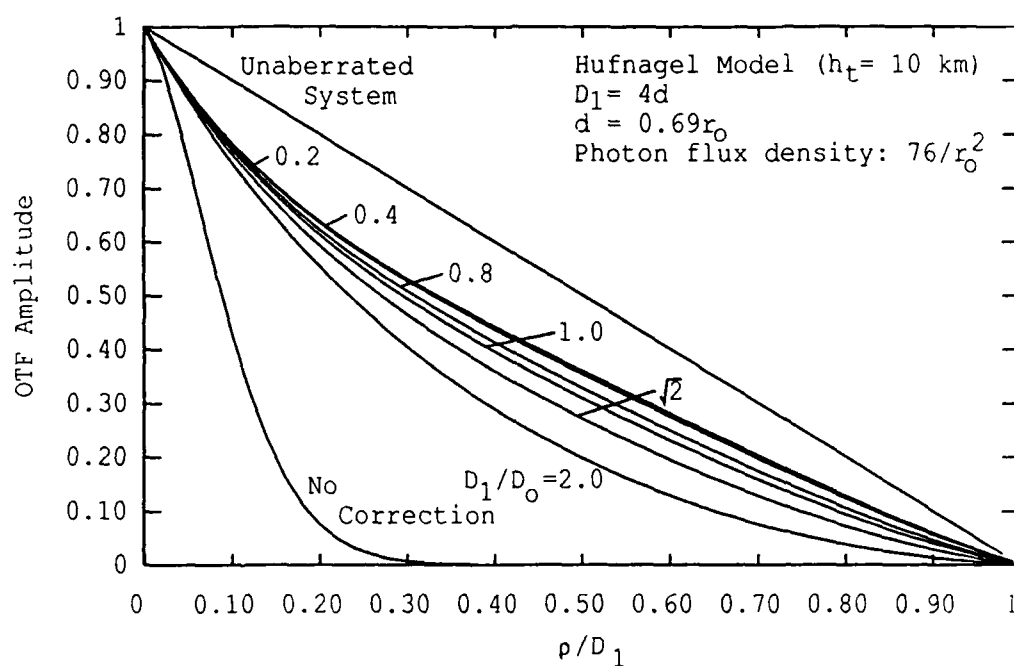


Figure 5.8. OTF of the phase corrected aperture for  $D_1/D_0$  ranging from 0.2 to 2.0 and the Hufnagel turbulence model.

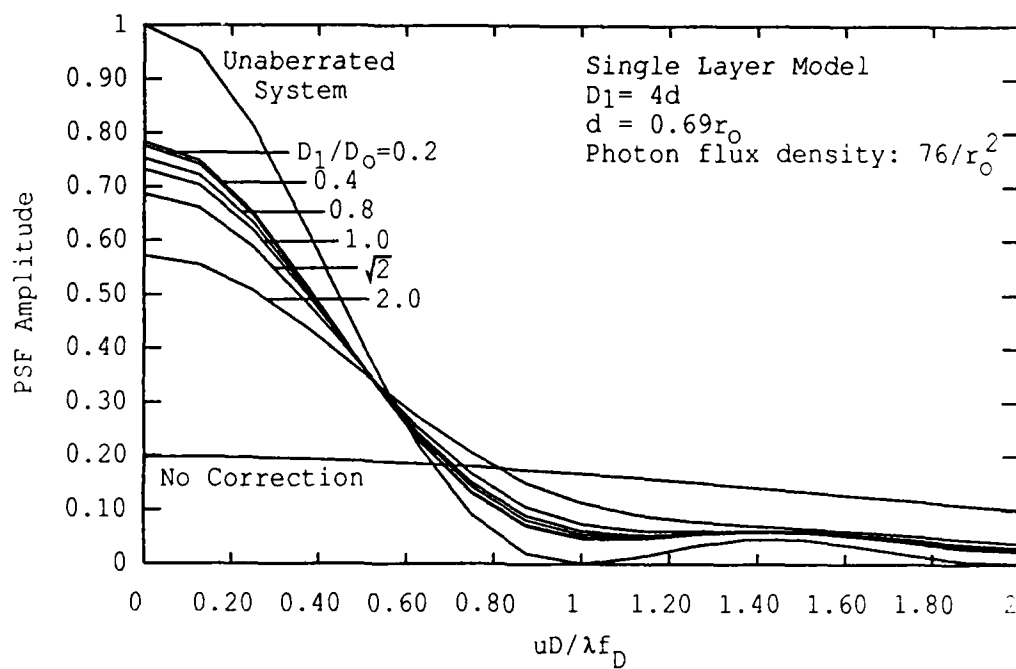


Figure 5.9. PSF of the phase corrected aperture for  $D_1/D_0$  ranging from 0.2 to 2.0 and the single layer turbulence model.

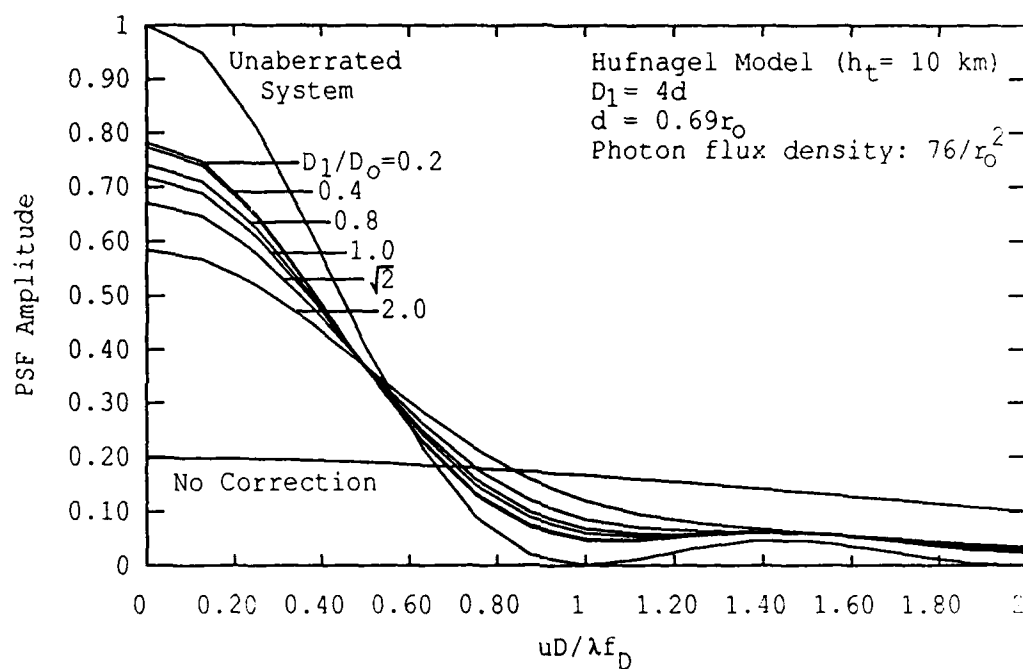


Figure 5.10. PSF of the phase corrected aperture for  $D_1/D_0$  ranging from 0.2 to 2.0 and the Hufnagel turbulence model.

degrade from that of the unaberrated system for increasing values of  $D_1/D_0$ . Figure 5.11 illustrates a plot of FWHM angular resolution as a function of  $D_1/D_0$ . The angular resolution is normalized by the FWHM resolution of the unaberrated system, which is  $0.88\lambda/D$  (calculated from the unaberrated 1D PSF in Figures 5.9 or 5.10). Only one curve is shown, since the results are nearly identical for both turbulence models. Figure 5.11 indicates that for  $D_1/D_0$  as large as  $\sqrt{2}$ , the FWHM angular resolution is only 1.2 times that of diffraction limited imaging. This resolution represents a modest increase from the limiting value of  $\sim 1.07$  times diffraction limited imaging at  $D_1/D_0 = 0.0$ . For  $D_1/D_0 = \sqrt{2}$ , the number of guide stars required decreases by a factor of 4.5 from that given by Gardner et al., with an equivalent decrease in the laser power requirements. Even though the angular resolution is only modestly degraded, the value of  $\langle \Delta\phi^2 \rangle$  increases to  $\sim 0.13\lambda \approx \lambda/7.7$ , resulting in a significant decrease of the Strehl ratio.

2) FOV of the Laser-guided Telescope: In addition to the degradation in imaging performance caused by the finite altitude of the guide star, imaging performance also degrades as the angular separation between object and guide stars increases. The degradation in imaging performance is computed as a function of the angular offset between the object source and the guide stars. In order to reduce the computational requirements we considered only the single layer turbulence model in the subsequent results. The OTF is not considered for this problem since  $\langle H(\underline{\rho}) \rangle$  does not satisfy the condition  $\langle H(\underline{\rho}) \rangle = \langle H(-\underline{\rho}) \rangle$  for any nonzero  $\theta$ . In this case the OTF is undefined.<sup>67</sup>

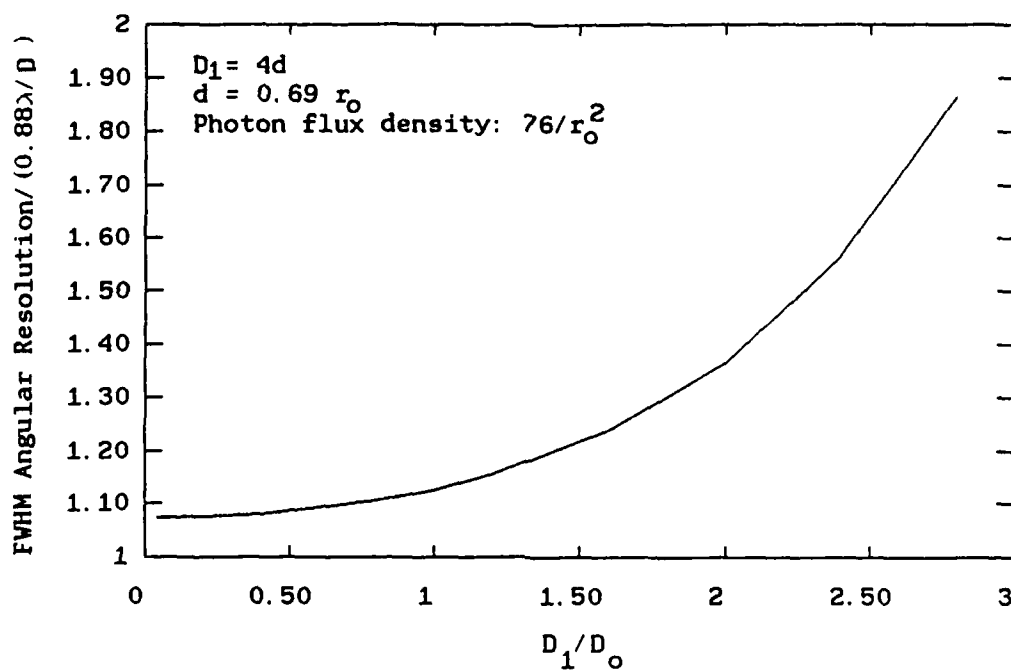


Figure 5.11. Normalized angular resolution of the phase corrected aperture versus  $D_1/D_0$ . The normalizing resolution is  $0.88\lambda/D$  and is computed from the unaberrated PSF in Figure 5.10.



Figure 5.12 is a plot of the rms phase error  $\langle \Delta\phi^2 \rangle^{1/2}$  versus  $\theta_x/\theta_o$  (or equivalently  $\theta_y/\theta_o$ ), where  $\theta_o$  is the proportional to the isoplanatic angle given by Equation (5.45):

$$\theta_o = \frac{r_o}{h_t}. \quad (5.58)$$

Recall  $\theta_x$  is the angular offset in the x-direction between the object and the telescope axis. Curves are shown for  $D_1/D_o$  ranging from 0.0 to 2.0. The other parameters have fixed values of  $D_1 = 4d$ ,  $d = 0.69r_o$  and a photon flux density of 76 photons/ $r_o^2$ . Computational results for other aperture sizes indicate that the results shown in Figure 5.12 are generally applicable for all aperture sizes.

The FOV of the adaptive telescope is quantified by specifying the maximum allowed increase in phase error as the observation angle is increased from zero. Figure 5.13 is a plot of the change in phase error,  $\Delta\epsilon$ , as a function of  $\theta_x/\theta_o$ . Let the maximum allowed increase in  $\langle \Delta\phi^2 \rangle^{1/2}$  be designated  $\Delta\epsilon_{\max}$ . Specifying a value of  $\Delta\epsilon_{\max}$  corresponds to specifying a maximum allowed value of  $\theta_x/\theta_o = (\theta_x/\theta_o)_{\max}$ . The maximum radial FOV of the telescope then becomes

$$\theta_{\text{fov}} = \theta_o \left( \frac{\theta_x}{\theta_o} \right)_{\max} = \frac{r_o}{h_t} \left( \frac{\theta_x}{\theta_o} \right)_{\max}. \quad (5.59)$$

If, for example, the phase error is allow to increase by  $\Delta\epsilon_{\max} = 0.03\lambda$  over the FOV of the telescope, then  $(\theta_x/\theta_o)_{\max}$  is approximately one for

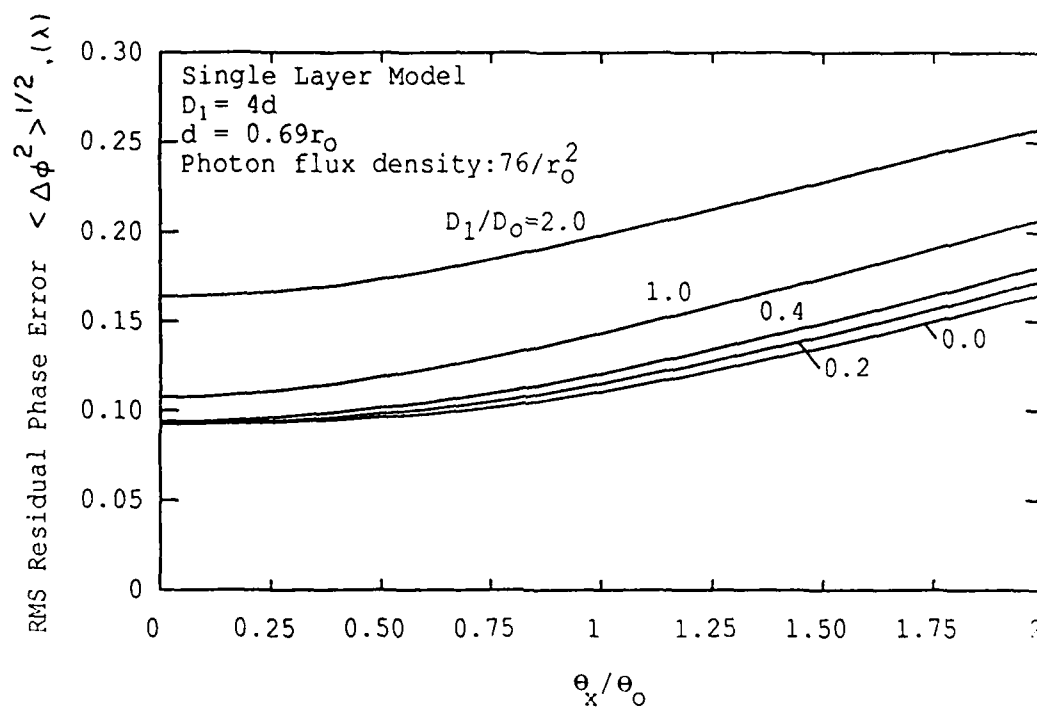


Figure 5.12. Residual rms phase error versus  $\theta_x/\theta_0$  for  $D_1/D_0$  ranging from 0.0 to 2.0.  $\theta_x$  is the angular offset in the x direction between the object and axis of the telescope.

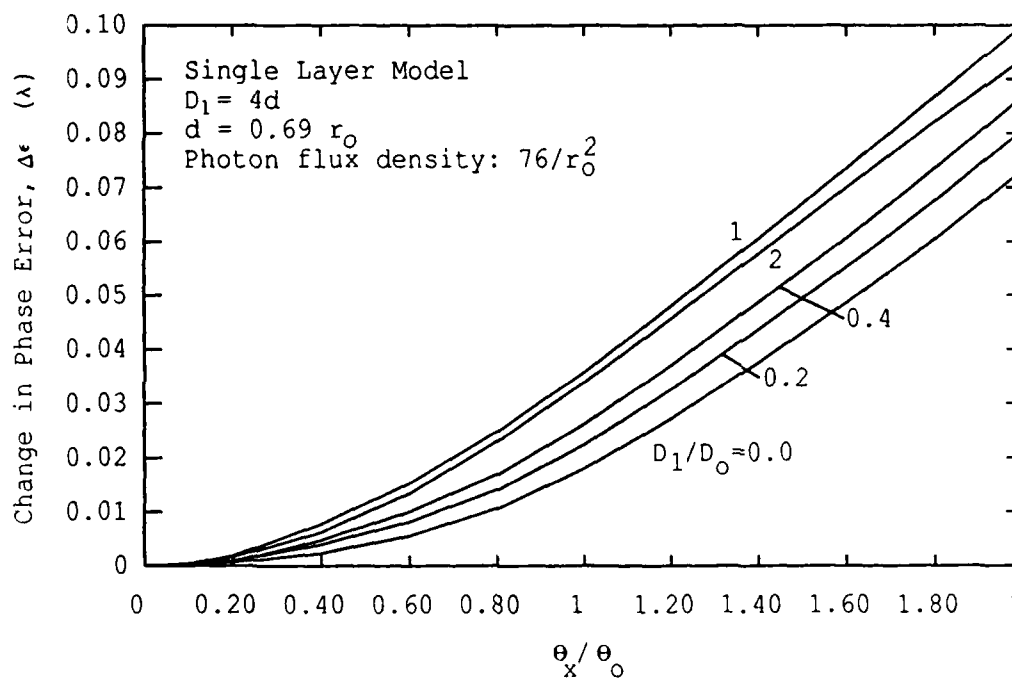


Figure 5.13. Change in the residual rms phase error  $\Delta\epsilon$  versus  $\theta_x/\theta_o$  for  $D_1/D_o$  ranging from 0.0 to 2.0.  $\theta_x$  is the angular offset in the x direction between the object and axis of the telescope.

$D_1/D_0 = 1$ . In this case the radial FOV is  $\theta_0$ . For the specific case of  $r_0 = 20$  cm and  $h_t = 10$  km, the radial FOV becomes 20  $\mu$ rad ( $\sim 4$  arcsec). These values of  $r_0$  and  $h_t$  correspond to those assumed by Gardner et al.<sup>5</sup>

Consider a constant value of  $\theta_x/\theta_0$ . From Figure 5.13 we see that  $\Delta\epsilon$  increases with  $D_1/D_0$  and then decreases as  $D_1/D_0$  becomes greater than 2. This trend may be unexpected at first glance. Figure 5.12 shows that as  $D_1/D_0$  increases, the wavefront phase error increases. At some point the phase error attributed to the effects of increasing  $D_1/D_0$  begins to dominate the phase error attributed to  $\theta_x > 0$ . As a result, the increase in the phase error,  $\Delta\epsilon$ , decreases as  $D_1/D_0$  increases beyond approximately two. Finally note that the curves for  $D_1/D_0 = 0$  in Figures 5.12 and 5.13 are applicable for the case of astronomical imaging using natural guide stars (i.e., the wavefront from the guide star is a plane wave).

## 5.9 Summary

We have presented an analysis technique for characterizing the effects of anisoplanatism on adaptive optics systems using slope sensors. The technique is developed in a very general sense allowing for an arbitrary geometry between the reference source, the imaged object and the aperture of the optical system. The adaptive optics system consists of an aperture, a wavefront slope sensor, a deformable mirror, and a linear control law. The nonideal characteristics typical of these components are incorporated into the analysis by realistically

modeling the slope sensors, the deformable mirror and the photon noise in the wavefront sensor.

The effects of anisoplanatism on the design of laser-guided telescopes are investigated. In particular, the issue of determining the required number of laser guide stars for a given telescope diameter is addressed. Numerical results are also presented, indicating the maximum FOV of the adaptive telescope. The results show explicitly how the imaging performance of the adaptive telescope varies with the number and height of the guide stars, and with the angular separation between direction of the object and guide star wavefronts. Two fundamental parameters result from the computations. The first parameter,  $D_0$ , is a measure of the diameter of the largest telescope requiring a single guide star. The diameter  $D_0$  is related to the height of the guide star  $z_g$ , the Fried seeing cell diameter  $r_0$  and the height of the turbulence layer  $h_t$  by the simple relationship  $D_0 = z_g r_0 / h_t$ . The second parameter,  $\theta_0$ , is a measure of the radial FOV of the adaptive telescope and is given by  $\theta_0 = r_0 / h_t$ . The numerical results indicate that the number of guide stars can be decreased from that first derived by Gardner et al.<sup>5</sup> without significantly decreasing imaging performance.

## 6. THE BISTATIC IMAGING LIDAR TECHNIQUE FOR UPPER ATMOSPHERIC STUDIES

### 6.1 Introduction

The structural characteristics of the mesospheric sodium (Na) layer have received considerable attention in recent years. The impetus for much of the current Na layer measurements is the study of the mesopause dynamics. Knowledge of the Na layer dynamics has proven to be particularly useful for studying the influence of gravity waves and tides on the structure of the mesosphere. Much of the past and current experimental research on the mesospheric Na layer has been conducted using monostatic lidar systems.<sup>32,37,73,74</sup> Bistatic lidar techniques have also been proposed for upper atmospheric studies.<sup>81</sup> These lidar systems measure the vertical structure of the layer by transmitting a short laser pulse and recording the return flux as a function of time. These profiles are calibrated and scaled to provide measurements of the Na layer density as a function of altitude. The vertical resolution of a monostatic system is proportional to  $c\Delta t/2$ , where  $\Delta t$  is the pulse length and  $c$  is the speed of light. An alternate approach is to use a bistatic lidar configuration, consisting of a long pulse or cw laser and an imaging system. The laser illuminates the Na layer while the imaging system records the spot created by the resonant Na scattering. In contrast to the time domain approach this approach measures the density characteristics of the layer by a direct spatial measurement. One advantage of this approach is the use of relatively simple transmitting and receiving equipment. The laser transmitter can be a cw or long pulse laser and the receiver can be a simple narrowband

telescope with a one-dimensional detector array. In contrast, the time domain approach requires a short pulse laser and a wide bandwidth, time gated receiver. Another advantage of the imaging technique is the possibility of improved spatial resolution. In the following sections we demonstrate that vertical resolution on the order of 10 meters is feasible.

In Section 6.2 we discuss the configuration of the bistatic imaging lidar and derive the fundamental equations describing the image data as a function of the layer density profile and laser beam cross section. These results are discussed in Section 6.3 in terms of familiar linear systems concepts. The limits imposed on the system resolution by atmospheric turbulence and shot noise are discussed in Section 6.4. Finally, in Section 6.5, experimental data are presented.

## 6.2 Analysis

Figure 6.1 illustrates the configuration of the bistatic imaging lidar. The telescope and laser are separated by a distance  $d$ . The laser is pointed in the vertical ( $z$ ) direction and the telescope is pointed at the center of the spot created by the resonant scattering. The imaged laser spot will be elliptical in shape due to the separation between the telescope and laser. A zenith angle ( $\phi$ ) profile through the recorded image contains information about the sodium layer's vertical structure, while an azimuth angle ( $\alpha$ ) profile contains information about the laser beam cross section. From the geometry

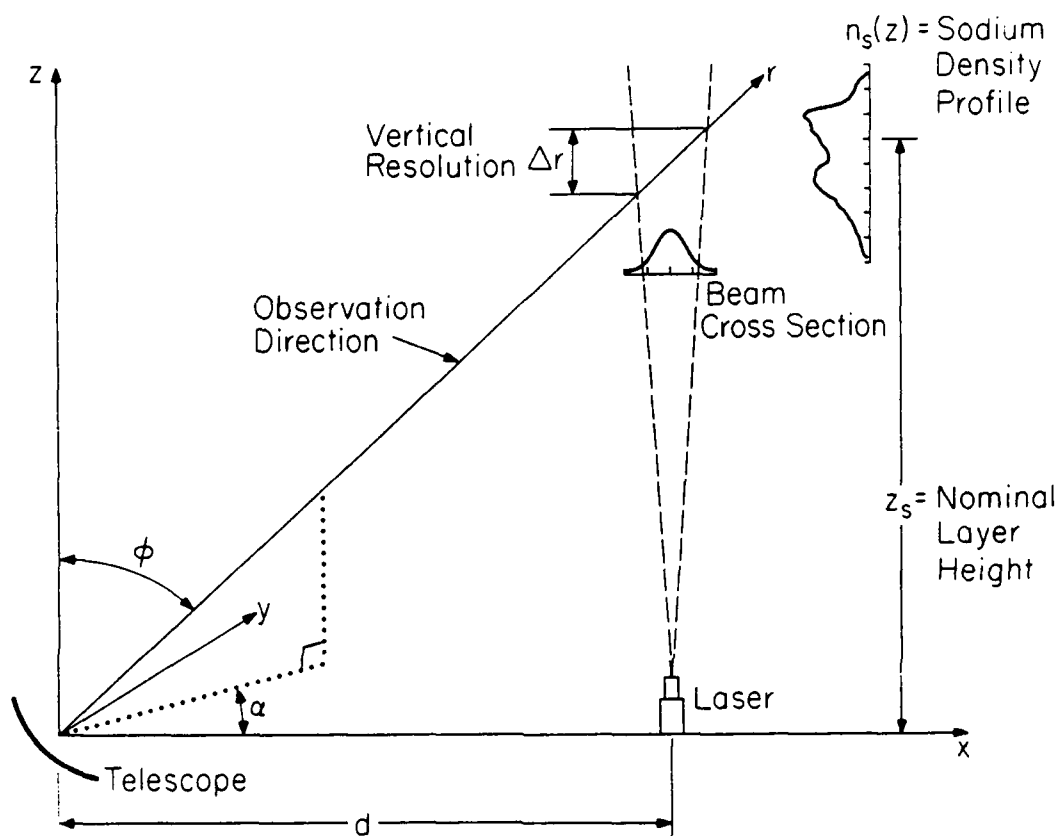


Figure 6.1. Imaging lidar configuration.



illustrated in Figure 6.1 we see intuitively how vertical resolution  $\Delta r$  is affected by laser beamwidth and separation distance  $d$ . The resolution can be improved by decreasing the laser beamwidth or increasing the separation  $d$ . Exactly how much the resolution is improved by these two actions is quantified in the following analysis.

The theoretical system performance is found by starting with an expression describing the measured image data as a function of the layer density profile and the laser beam cross section. This expression is derived by applying the lidar equation<sup>3,2</sup> to the geometry illustrated in Figure 6.1. To facilitate the analysis, we first assume the angular extent of the laser spot is very small. For the nominal altitude of the Na layer (90 km) and a reasonable beam divergence this assumption is justified.

Applying the lidar equation to the geometry illustrated in Figure 6.1, we can write the photon flux distribution  $\gamma$  at the telescope detector as a function of observation angles  $\phi$  and  $\alpha$  as

$$\gamma(\phi, \alpha) = \frac{\eta A_r T_i T_l \lambda P \sigma_t}{4 \pi h c} \times \int_0^{\infty} \frac{I(r \sin \phi \cos \alpha - d, r \sin \phi \sin \alpha) n_s(r \cos \phi) r^2 \sin \phi}{r^2} dr + \gamma_b \quad (6.1)$$

where

$\phi$  = zenith angle,

$\alpha$  = azimuth angle,

$r$  = radial distance from the imaging system in the  
observation direction (m),

$n_s(z)$  = sodium density as a function of altitude  $z$  ( $\text{m}^{-3}$ ),

$I(x,y)$  = laser beam cross section at the nominal sodium layer  
height ( $\text{m}^{-2}$ ),

$\eta$  = overall imaging system efficiency,

$T_i$  = atmospheric transmittance for the imaging system,

$T_l$  = atmospheric transmittance for the laser,

$\lambda$  = optical wavelength (m),

$P$  = laser power (W),

$A_r$  = telescope aperture ( $\text{m}^2$ ),

$\sigma_t$  = effective backscatter cross section ( $\text{m}^2$ ),

$h$  = Planck's constant ( $6.63 \times 10^{-34}$  J s),

$c$  = velocity of light ( $3 \times 10^8$  m/s),

$\gamma_b$  = flux due to background and detector dark counts ( $\text{s}^{-1}$ ).

Also note that the laser beam cross section  $I(x,y)$  satisfies the following relationship:

$$\int_{-\infty}^{\infty} \int_{-\infty}^{\infty} I(x,y) \, dx \, dy = 1. \quad (6.2)$$

Equation (6.1) describes the total flux intensity for a particular observation direction  $(\phi, \alpha)$ . In deriving Equation (6.1) we have

assumed that the altitude dependent absorption losses within the Na layer are negligible. At this point we can estimate the constant noise term  $\gamma_b$  and subtract it from the total flux giving the "signal" flux  $\gamma_s$ . The flux  $\gamma_b$  can be estimated by measuring the flux levels when the laser is turned off. For the remainder of this section we base our analysis on this signal flux  $\gamma_s(\phi)$ . If the layer density does not change for small variations in azimuth ( $\alpha$ ), the only information contained in the azimuthal data is the shape of the laser beam cross section. Since we are primarily interested in the vertical structure of the layer, Equation (6.1) can be simplified by integrating over  $\alpha$ . Assuming the laser beam cross section  $I(x,y)$  is separable, and using the small angle approximations for  $\cos\alpha$  and  $\sin\alpha$ , the integration over  $\alpha$  gives

$$\gamma_s(\phi) = \frac{\eta A_r T_i T_l \lambda P \sigma_t}{4 \pi h c} \times \int_0^{\infty} \frac{I(r \sin\phi - d) n_s(r \cos\phi)}{r} dr \quad (6.3)$$

where  $I(x)$  describes the laser beam cross section in one dimension. The integration along the observation path  $r$  can be converted to an integration along the vertical path  $z'$  by making the change of variables:  $z' = r \cos\phi$ . Carrying out this change of variables we obtain

$$\gamma_s(\phi) = \frac{\eta A_r T_i T_l \lambda P \sigma_t}{4 \pi h c} \times \int_0^\infty \frac{I(z' \tan \phi - d) n_s(z')}{z'} dz'. \quad (6.4)$$

The flux distribution  $\gamma_s$  can be written as a corresponding distribution in altitude by relating the observation angle  $\phi$  to the altitude  $z$  by the geometric relationship  $\tan \phi = d/z$  (see Figure 6.1). We transform the flux distribution  $\gamma_s(\phi)$  to the flux distribution  $\xi_s(z)$  using

$$\frac{d\phi}{dz} = - \frac{(\sin \phi)^2}{d} = \frac{d}{d^2 + z^2} \quad (6.5)$$

and the constraint  $\xi_s(z)dz = \gamma_s(\phi)d\phi$ . This transformation yields

$$\xi_s(z) = \frac{\eta A_r T_i T_l \lambda P \sigma_t d}{4 \pi h c (d^2 + z^2)} \times \int_0^\infty \frac{I\left(\frac{z' - z}{z/d}\right) n_s(z')}{z'} dz'. \quad (6.6)$$

Equation (6.6) is approximated by replacing the factor  $1/z'$  in the integrand with  $1/z$ . This is a reasonable approximation if the width of the kernel  $I(z'd/z)$  is small compared to the magnitude of  $z$ . The rms width of  $I(z'd/z)$  is equal to  $\sigma_1 z/d$  where  $\sigma_1$  is the rms width of the laser beam cross section. This rms width is small compared to  $z$  when  $\sigma_1/d \ll 1$ . We further simplify Equation (6.6) by replacing the quotient  $d/z$  in the argument of the kernel  $I(z'd/z)$  with the constant

$d/z_s$ , where  $z_s$  is the nominal centroid height of the layer. This approximation is a reasonable one since the width of  $I(z'd/z)$  will vary by roughly 10 percent for the typical altitude range of interest ( $z = 80$  to  $100$  km). Making the described replacements results in the following convolutional form:

$$\xi_s(z) = \frac{\eta A_r T_i T_l \lambda P \sigma_t d}{4 \pi h c (d^2 + z^2) z_s} \int_0^\infty I\left(\frac{z' - z}{z_s/d}\right) n_s(z') dz'. \quad (6.7)$$

### 6.3 Discussion

The convolution in Equation (6.7) can be interpreted using familiar concepts of linear system theory. The flux distribution  $\xi_s(z)$  may be regarded as the output of a linear filter with input  $n_s(z)$  and impulse response  $I(zd/z_s)$ . To obtain the most accurate representation of  $n_s(z)$  from  $\xi_s(z)$ , the spatial bandwidth of  $I(zd/z_s)$  should be at least as large as the spatial bandwidth of  $n_s(z)$ . In other words, the width of  $I(zd/z_s)$  must be small compared to the smallest structure in  $n_s(z)$ . If this condition is satisfied, the estimate of the density profile  $n_s(z)$  is given by  $K\xi_s(z)$ , where  $K$  is simply a normalizing constant.

Since the width of  $I(zd/z_s)$  determines the vertical resolution of the imaging lidar, we would like to equate some measure of this width to the system resolution  $\Delta r$ . In many cases  $I(x)$  will be well

approximated by a Gaussian beam cross section. The Gaussian beam cross section is completely described by its rms width, and we use this width as a measure of system resolution  $\Delta r$ . We can easily show that the rms width of  $I(zd/z_s)$  is

$$\Delta r = \frac{\sigma_1 z_s}{d} \quad (6.8)$$

where  $\sigma_1$  is the rms width of the laser beam cross section. Two approaches to improve resolution are evident from Equation (6.8). The first is simply decreasing the width of the laser beam. The second is increasing the separation  $d$  between the laser and telescope. Figures 6.2 and 6.3 show how the resolution given in Equation (6.8) varies with separation distance  $d$  and rms beamwidth  $\sigma_1$  (or equivalently, beam divergence). For example, to achieve a resolution on the order of 100 meters with  $d = 1000$  meters and  $z_s = 90$  km, we must have an rms beam width of 1.11 meters which corresponds to a FWHM beam divergence of roughly  $50 \mu\text{rad}$ .

In addition to the detailed structure of the layer, the gross characteristics of the layer, such as centroid height and the rms width, are also of interest. Using the altitude profile  $\xi_s(z)$  in Equation (6.7) we compute the profile's centroid height and rms width. This computation reveals the centroid height of the image profile  $\xi_s(z)$  is equal to the centroid height of density profile  $n_s(z)$ . In a similar manner, computing the rms width  $\sigma_i$  of the image profile  $\xi_s(z)$  we find

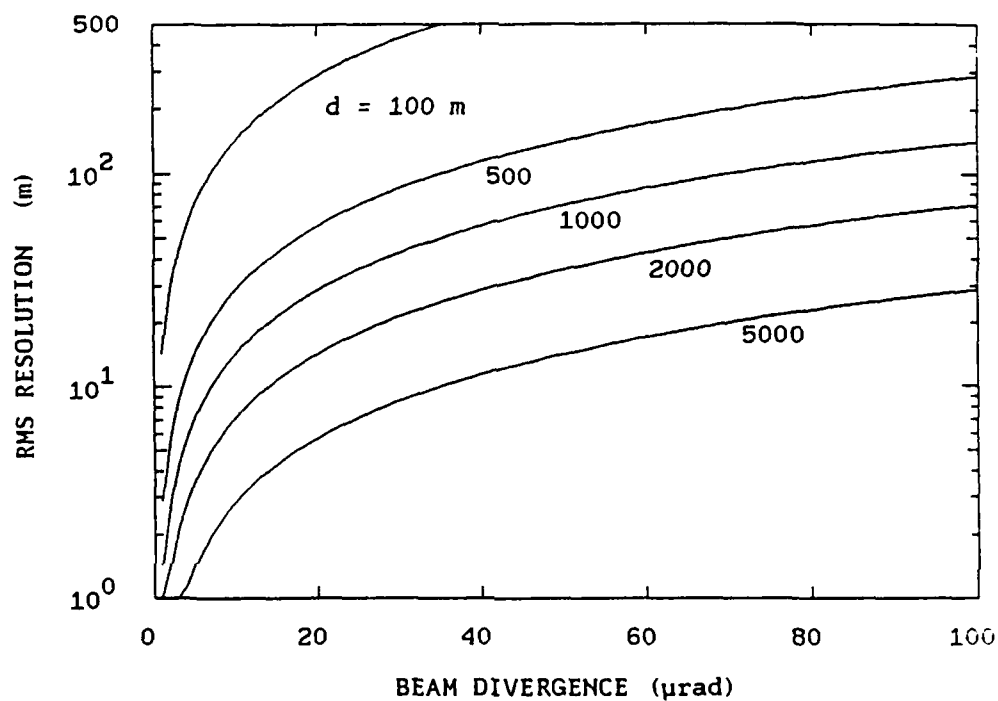


Figure 6.2. Vertical resolution of the imaging lidar versus laser beam divergence for several values of the separation distance  $d$ .

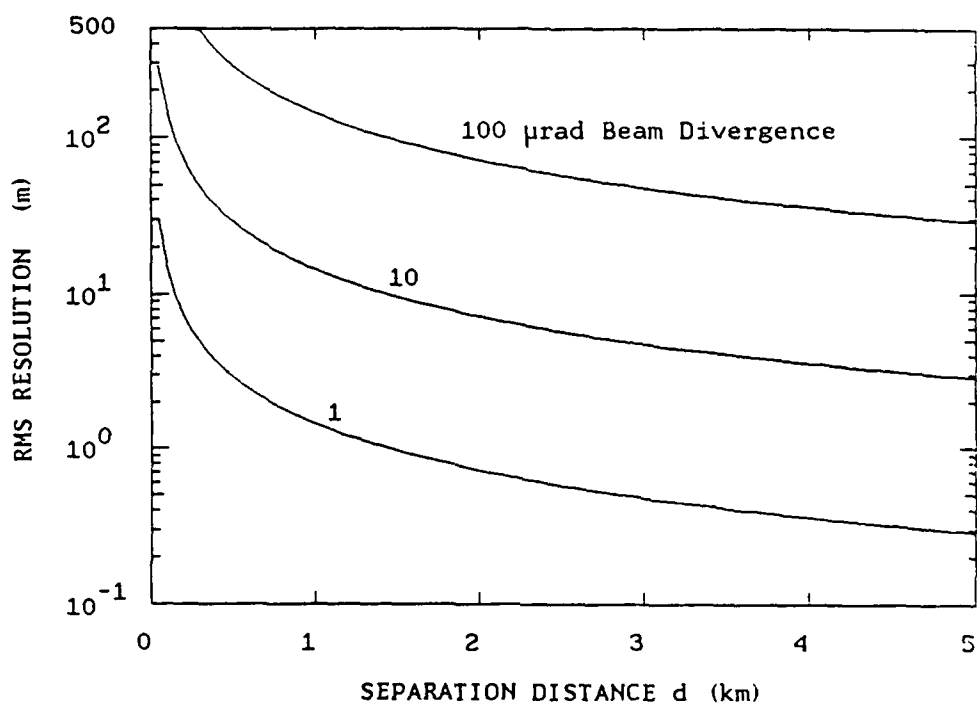


Figure 6.3. Vertical resolution of the imaging lidar versus separation distance  $d$  for several values of the laser beam divergences.



$$\sigma_i = \left[ \left( \frac{\sigma_1 z_s}{d} \right)^2 + \sigma_s^2 \right]^{1/2}$$

$$= (\Delta r^2 + \sigma_s^2)^{1/2} \quad (6.9)$$

where  $\sigma_s$  is the true rms width of the Na layer. If  $\Delta r \ll \sigma_s$  the measured rms width  $\sigma_i$  will closely approximate the true rms width  $\sigma_s$ .

For cases in which the vertical resolution  $\Delta r$  is larger than the smallest spatial structure of  $n_s(z)$ , then a simple scaling of the image data will not give an accurate representation of  $n_s(z)$ . To obtain a more accurate representation we could mathematically invert Equation (6.7) by performing a deconvolution. This approach is less desirable because of the inherent problems encountered when attempting to recover high frequency information from shot noise contaminated data. Shot noise effects arise because of the random nature of photon arrival times at the telescope receiver. In practice the telescope receiver cannot determine the instantaneous flux  $\xi_s(z)$  given in Equation (6.7). Instead, the receiver counts photons over an integration time  $\tau$  and estimates  $\xi_s(z)$ . The deconvolution process is very sensitive to the shot noise inherent in this estimation process.<sup>82</sup> As a result, small perturbations in the estimated values of  $\xi_s(z)$  due to shot noise will cause large perturbations in the deconvolution result.

#### 6.4 Factors Affecting Resolution

For a given separation  $d$ , Equation (6.8) implies vertical resolution is limited only by the size of the laser spot. If the

optics of the laser system are large enough, atmospheric turbulence will ultimately limit the minimum spot size. Once this minimum size is reached, resolution can be improved only by increasing  $d$ . Atmospheric turbulence limits the minimum spot size to a full width angular diameter of  $2.44\lambda/r_0$  where  $r_0$  is the atmospheric seeing cell diameter. The seeing cell diameter  $r_0$  was first introduced by Fried,<sup>10</sup> and it represents the diameter of the largest aperture achieving diffraction limited performance in the presence of atmospheric turbulence. Also note that  $r_0$  is wavelength dependent, varying as  $\lambda^{6/5}$ . Calculating the smallest possible rms beamwidth in the presence of atmospheric turbulence we obtain

$$\sigma_{1_0} = z_s \left( \frac{2.44 \lambda}{4\sqrt{2} r_0} \right). \quad (6.10)$$

Substituting Equation (6.10) into Equation (6.8) gives the following lower bound on  $\Delta r$

$$\Delta r > \frac{0.43 \lambda z_s^2}{r_0 d}. \quad (6.11)$$

The right-hand side of the inequality Equation (6.11) is plotted versus  $r_0$  in Figure 6.4 for a range of separation distances  $d$ . In this plot we have assumed  $z_s = 90$  km and  $\lambda = 589$  nm. Consider, for example, a desired resolution of 100 m. For an offset distance of 1000 m, the seeing cell diameter  $r_0$  must be greater than 2 cm (poor seeing conditions). On the other hand, for a resolution of 10 meters, the seeing cell diameter  $r_0$  must be greater than 20 cm (excellent seeing

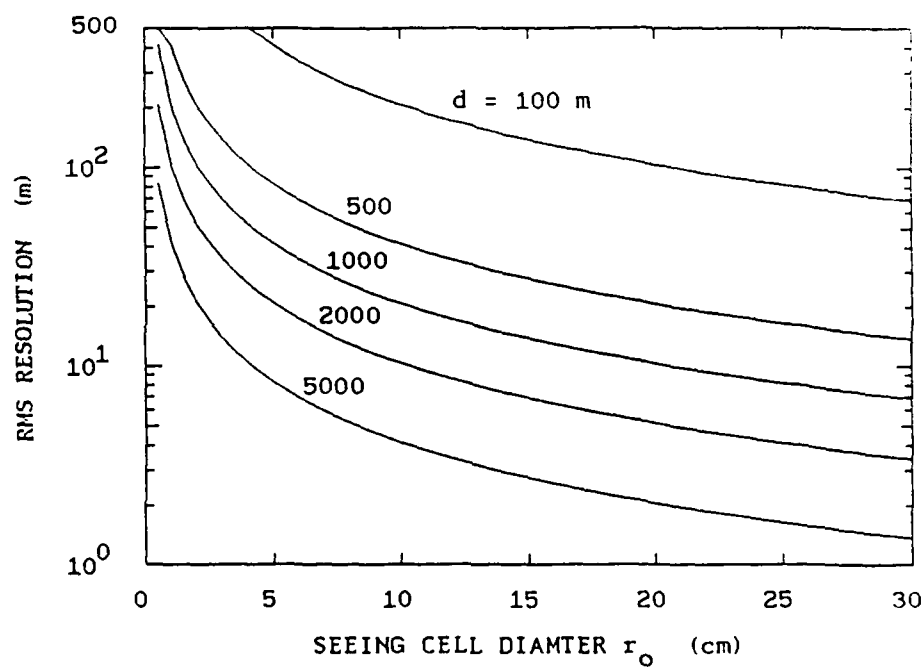


Figure 6.4. Minimum vertical resolution versus the atmospheric cell size  $r_0$  for several values of the separation distance  $d$ .

conditions). Values of  $r_0$  greater than 20 to 30 cm can be achieved only at the best observatory sites.

Up to this point resolution has been discussed in terms of the smallest vertical cell size the system is able to resolve. We can also speak of resolution in terms of the system's ability to observe the vertical structure of mesospheric gravity waves. If the imaging system has an adequate vertical resolution in the sense discussed above (i.e.,  $\Delta r \leq 100$  m), then the system's ability to measure short-wavelength gravity waves is ultimately limited by shot noise. Gardner and Voelz<sup>37</sup> found that to detect vertical wavelengths as short as 1 km, the shot noise levels in the power spectrum of a typical image profile  $\xi_s(z)$  must be on the order of -50 dB or equivalently the number of signal counts/profile must be on the order of  $10^5$ . The total expected signal count per profile is obtained by integrating Equation (6.7) over  $z$  giving

$$N_s = \frac{\eta A_r T_i T_l \lambda P \sigma_t C_s \tau}{4 \pi h c (d^2 + z^2)}, \quad (6.12)$$

where  $\tau$  is the exposure time and  $C_s$  is the sodium layer column abundance. Consider, for example, the nominal atmospheric and lidar system parameter values listed in Table 6.1. The listed atmospheric parameter values are typical of those expected for a low altitude site like Urbana, Illinois.<sup>37</sup> The receiver efficiency  $\eta$  is representative of currently available telescope and detector equipment. Substituting these nominal values into Equation (6.12) and imposing a maximum shot

TABLE 6.1  
Atmospheric and Imaging System Parameters

---

Atmospheric Parameters:	$T_i = T_1 = 0.3$
	$C_s = 5 \times 10^{13} \text{ m}^{-2}$
	$z_s = 90 \text{ km}$
	$\sigma_t = 9 \times 10^{-16} \text{ m}^2$
	(FWHM laser linewidth < 0.5pm)
Imaging System Parameters:	$\lambda = 589 \text{ nm}$
	$\eta = 0.075$
	$d = 1000 \text{ m}$

noise level of -50 dB (i.e.,  $N_g > 10^5$ ) gives

$$P A_r \tau \geq 10. \quad (6.13)$$

If, for example, the product  $PA_r$  is  $0.1 \text{ w m}^2$  (i.e., a 1 m diameter receiving aperture and a 130 mw laser) the integration time  $\tau$  must be greater than 100 s. A system with these characteristics will be able to observe gravity waves having wavelengths as short as 1 km.

### 6.5 Experimental Data

Initial tests of the imaging lidar were conducted in January of 1987 at the University of Hawaii's Mauna Kea Observatory. The laser spots were generated by the University of Illinois monostatic lidar system and imaged by the University of Hawaii 2.2 meter telescope.<sup>4</sup> The horizontal separation between the laser and telescope was 117 m. Figures 6.5 and 6.6 illustrate contour plots of two imaged laser spots. The images in Figures 6.5 and 6.6 were taken on Jan. 20 and 21, respectively. The spot dimensions were approximately  $0.87 \text{ mrad} \times 1.4 \text{ mrad}$  FW at  $e^{-2}$ . The thin horizontal contours in the images were caused by stars drifting through the telescope FOV during the 8 minute exposures. Consider integrated photocount profiles of the imaged spot. These integrated profiles are obtained by first summing the data over the axis perpendicular to the profile axis and then plotting the resulting one-dimensional data. A profile through the narrow axis of the spot corresponds to the azimuth ( $\alpha$ ) direction and is a measure of the laser beam cross section. A profile through the broad axis of the

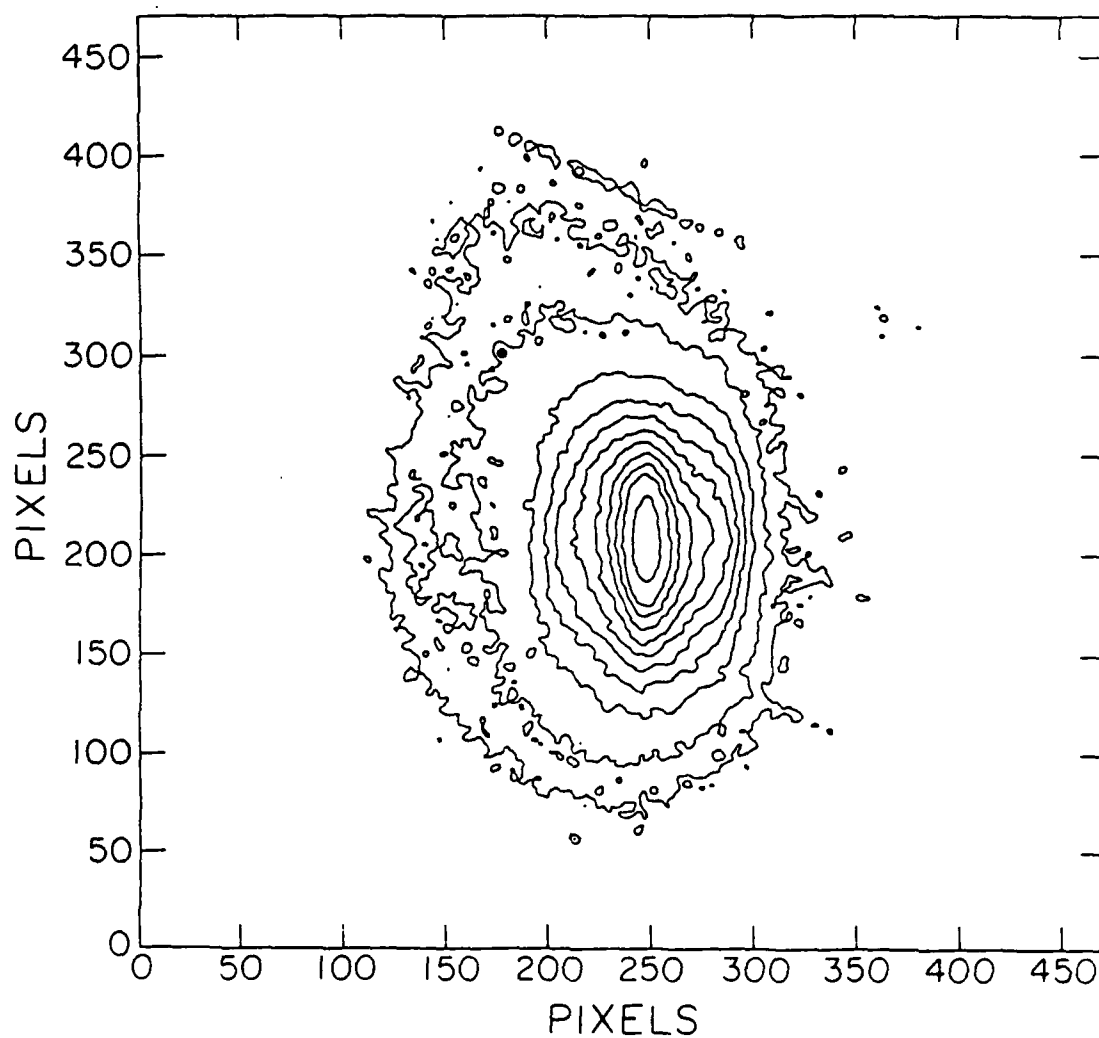


Figure 6.5. Photocount contour plot of the laser spot image taken on January 20. The contours are 350, 400, 500, 600, 700, 800, 900, 1000, 1100, 1200 and 1400 counts per pixel. The pixel size is  $3.4 \mu\text{rad}$ .

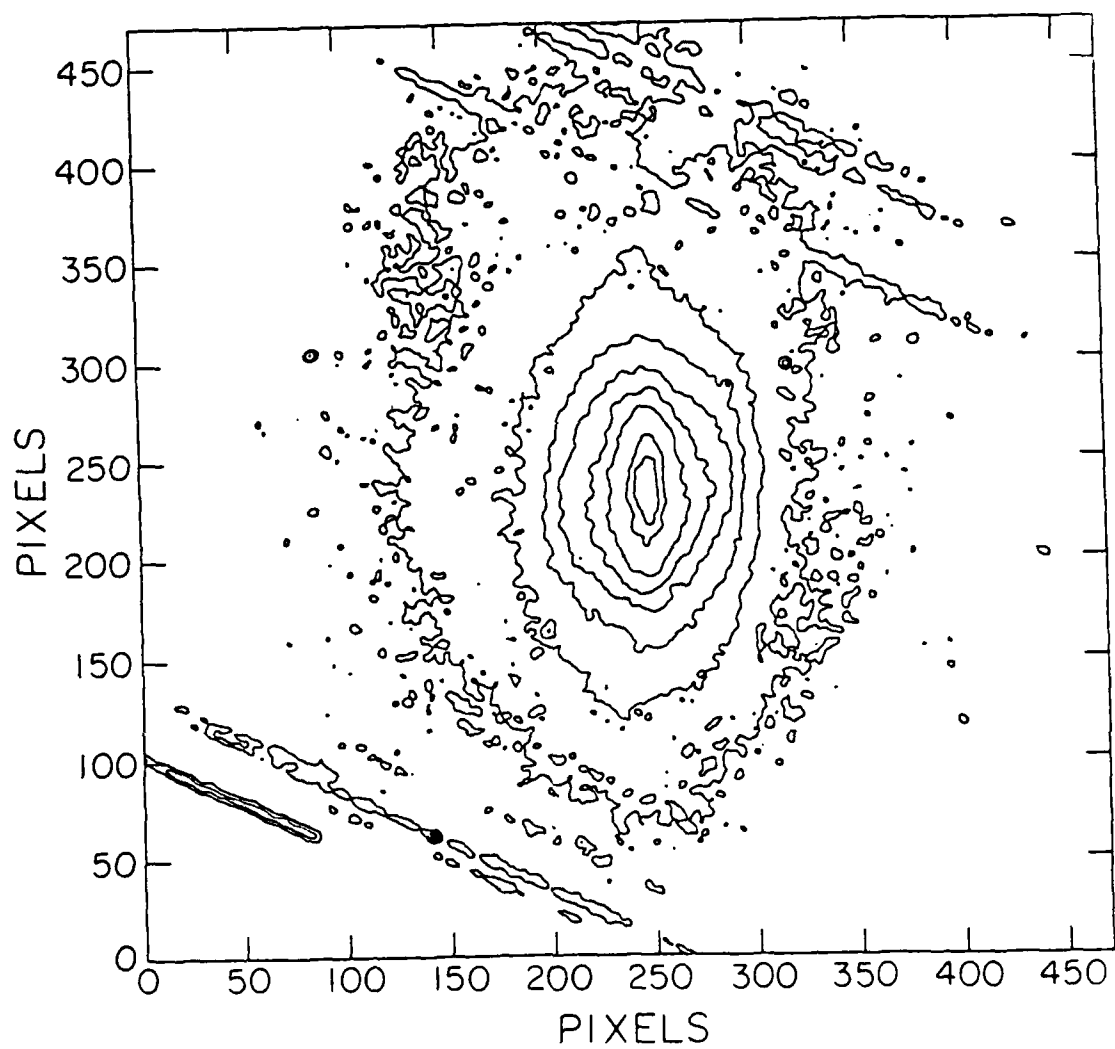


Figure 6.6. Photocount contour plot of the laser spot image taken on January 21. The contours are 150, 200, 300, 400, 500, 600, 800 and 900 counts per pixel. The pixel size is 3.4  $\mu$ rad.



spot corresponds to the zenith ( $\phi$ ) direction and is a measure of the Na density profile. Figures 6.7 and 6.8 illustrate these narrow and broad axis profiles for the image shown in Figure 6.5. The profile in Figure 6.7 is equivalent to integrating Equation (6.1) over  $\phi$  and plotting versus  $\alpha$ . The profile in Figure 6.8 is equivalent to integrating Equation (6.1) over  $\alpha$  and plotting versus  $\phi$ . Computing the rms beamwidth from the narrow axis profile gives  $\sigma_1 = 20.5$  m. Substituting  $\sigma_1$ ,  $d = 117$  m, and  $z_s = 95$  km into Equation (6.8) gives an rms vertical resolution of 16.6 km for the imaging lidar. Figures 6.9 and 6.10 illustrate Na density profiles obtained by performing a simple scaling of the image profiles. Also shown are Na density profiles derived from simultaneous monostatic lidar data. In contrast to the relatively poor resolution of the image data, the monostatic lidar data had a vertical resolution of 150 meters. Comparing the image data to the monostatic data reveals the large amount of smearing and loss of spatial detail resulting from the poor resolution of the experimental configuration. The poor resolution was caused primarily by the small separation (117m) between the laser and telescope.

The centroid height and rms width of the Na density profiles were also computed and compared. The centroid heights computed from the image profiles were 105 km and 100 km on the 20th and 21st, respectively. The centroid heights computed from the monostatic lidar data were 94.8 km and 93.8 km. The difference in these results is due partly to the uncertainty in the pointing angle of the telescope and partly to the varying width of the kernel  $I(z'D/z)$  in Equation (6).

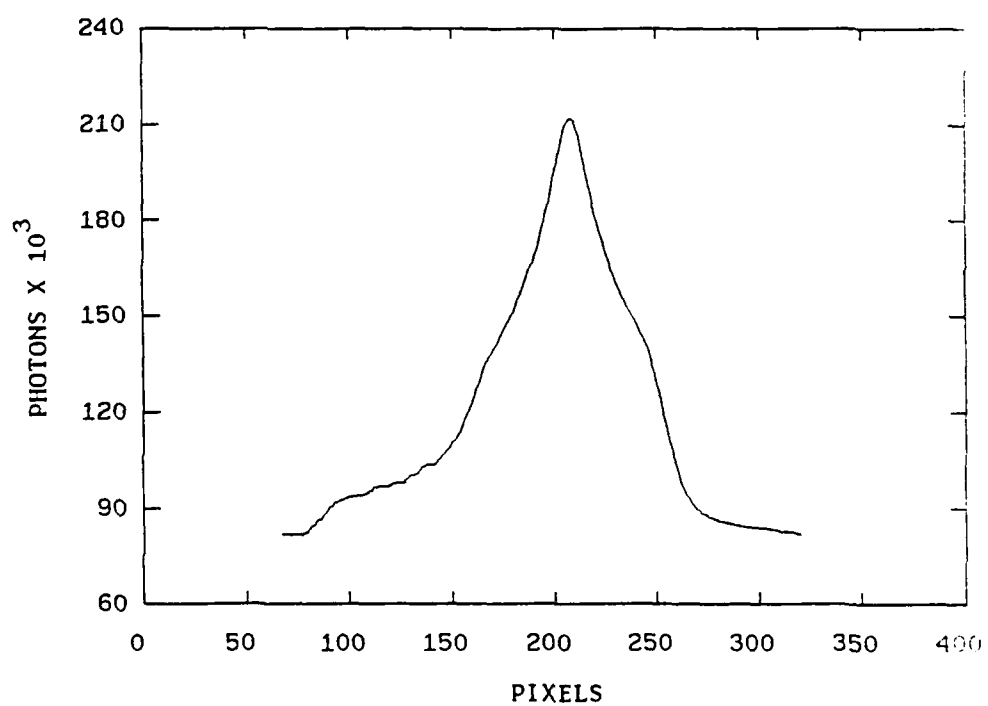


Figure 6.7. Integrated azimuth ( $\alpha$ ) angle profile through the image in Figure 6.5.

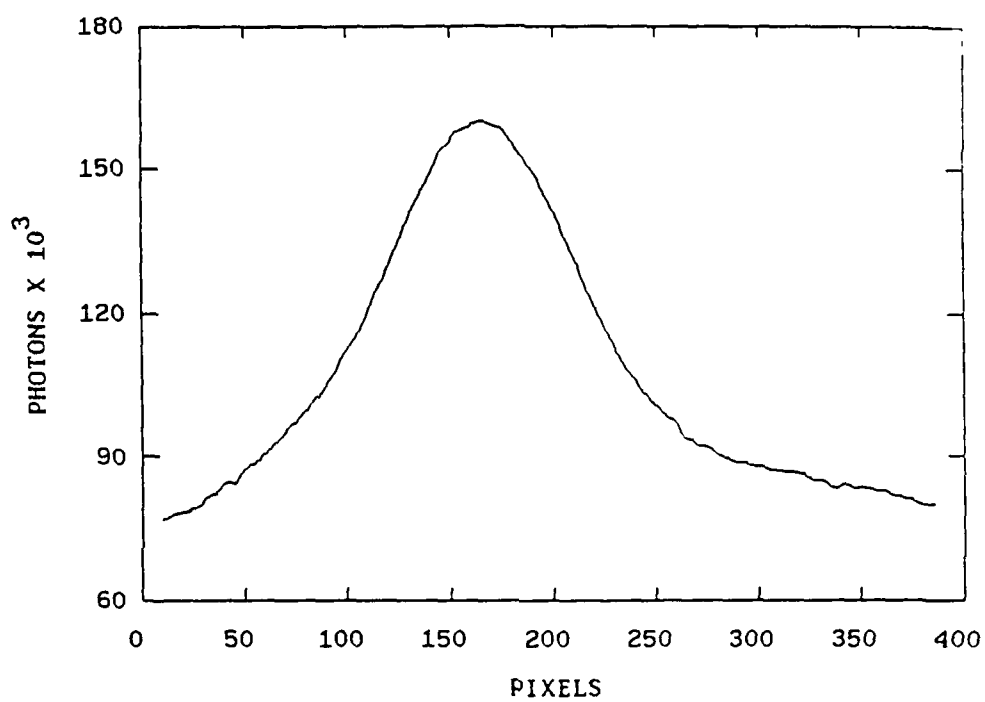


Figure 6.8. Integrated zenith ( $\phi$ ) angle profile through the image in Figure 6.5.

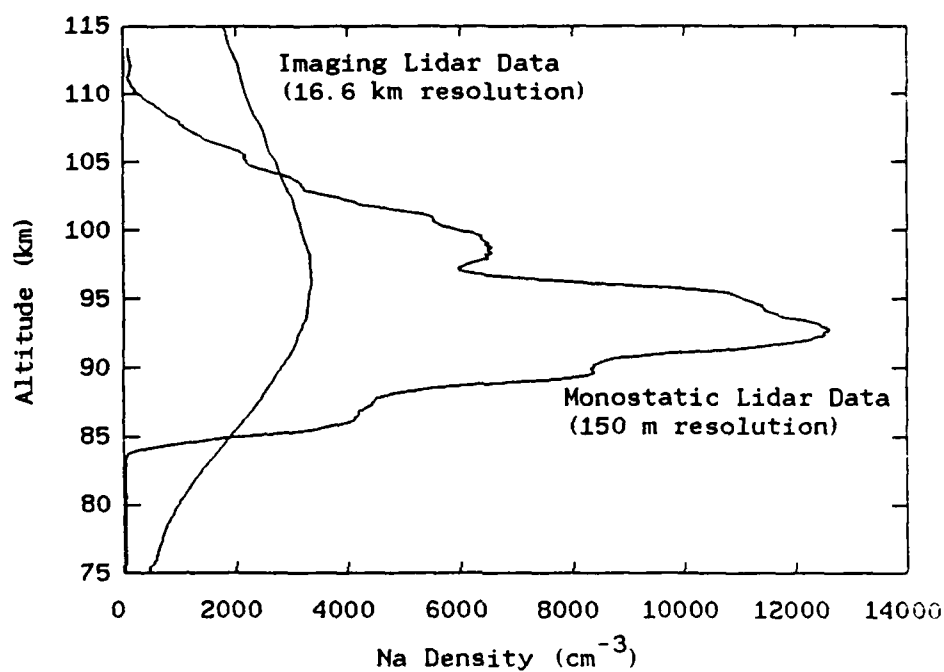


Figure 6.9. Na density profiles computed from the azimuthally integrated data shown in Figure 6.5 and from simultaneous monostatic lidar data. The imaging lidar had a vertical resolution of 16.6 km, while the monostatic lidar had a resolution of 150 m.

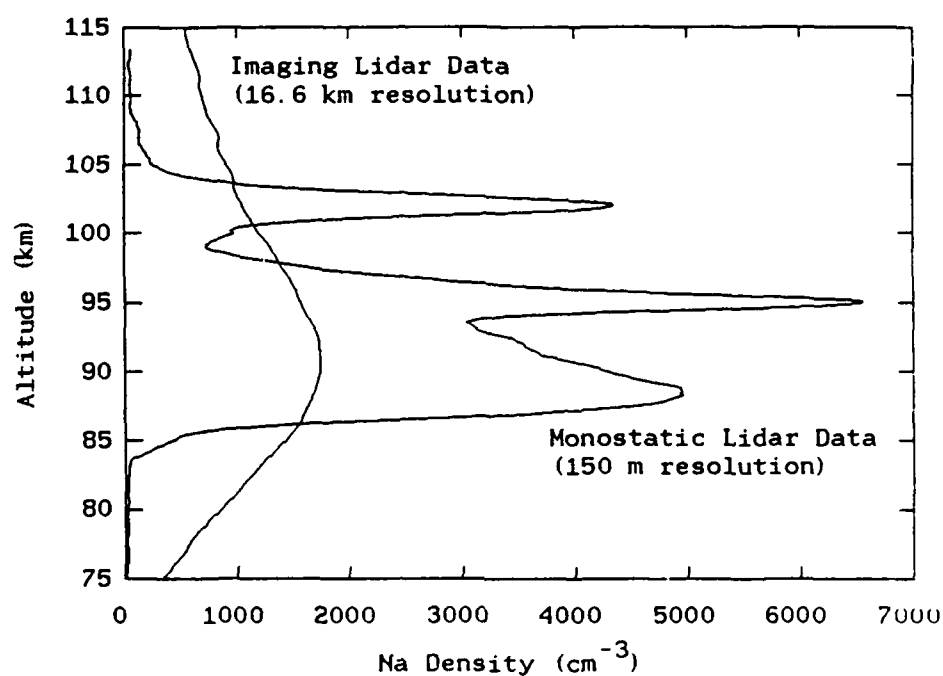


Figure 6.10. Na density profiles computed from the azimuthally integrated data shown in Figure 6.6 and from simultaneous monostatic lidar data. The imaging lidar had a vertical resolution of 16.6 km, while the monostatic lidar had a resolution of 150 m.

The width of the kernel increases with increasing altitude  $z$ . Normally this effect would be negligible for high resolution systems ( $\Delta r \ll \sigma_s$ ), but in this case the resolution is comparable to the total width of the layer. Since the width of the kernel is so large, the small percentage increases in the width with increasing altitude have the effect of shifting the observed centroid higher in altitude. A similar effect was noted for the rms width calculations. The rms widths  $\sigma_1$  of the image profiles were 18.1 km and 18.5 km on the 20th and 21st, respectively. Substituting these values into Equation (6.9) and solving for the rms width of the layer  $\sigma_s$ , resulted in values of 7.21 km and 8.17 km. In contrast, the rms widths  $\sigma_s$  computed from the monostatic lidar data were 5.35 km and 5.28 km.

The scaled photocount profiles gave a very poor estimate of  $n_s(z)$  for our particular configuration of the imaging lidar. This conclusion is immediately obvious from Figures 6.9 and 6.10. We alternately considered inverting Equation (6.7) by performing a deconvolution. Since the solution obtained by a deconvolution is very sensitive to shot noise, we first quantified the shot noise level over the spatial frequency range of interest. Figures 6.11 and 6.12 illustrate comparisons of the power spectra of the imaging and monostatic lidar data. The image data were obviously shot noise limited for spatial frequencies greater than  $0.1 \text{ km}^{-1}$  (i.e., for spatial structures having characteristic dimensions less than 10 km). The image data shot noise level was approximately -65 dB. This level matched the expected shot noise level computed from the total signal photocount  $N_s$ . The

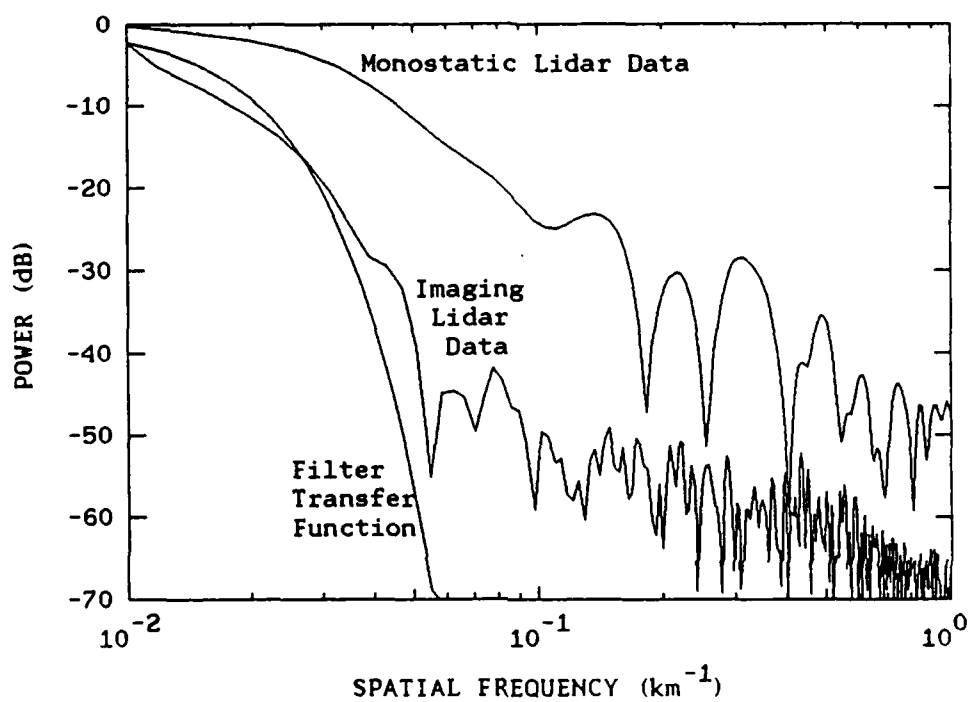


Figure 6.11. Power spectra of the Na density profiles in Figure 6.9.

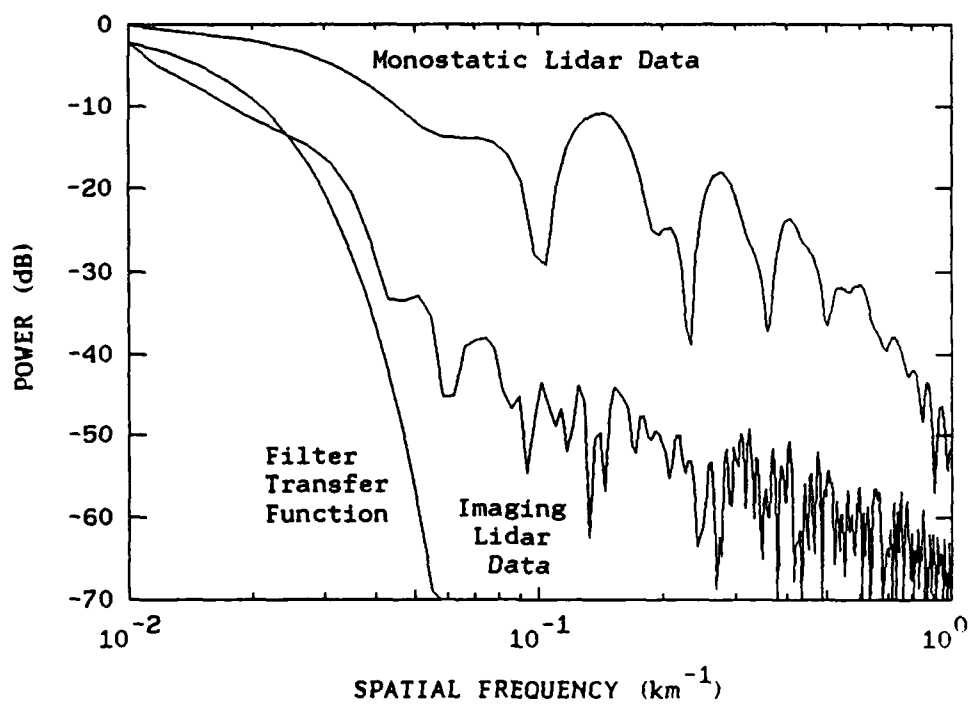


Figure 6.12. Power spectra of the Na density profiles in Figure 6.10.



photocount  $N_s$  was equal to  $5.01 \times 10^6$  and  $3.06 \times 10^6$  on the 20th and 21st, respectively. Comparing the spectra of the image data to the monostatic data reveals that the frequency components greater than  $0.1 \text{ km}^{-1}$  were suppressed by at least 30 dB. This high frequency suppression was a result of the narrow frequency response of the kernel  $I(zd/z_s)$ . The theoretical frequency response of  $I(zd/z_s)$  is also illustrated in Figures 6.11 and 6.12. This response was derived assuming a Gaussian laser beam cross section with an rms width of  $\sigma_1 = 20.5 \text{ m}$ . From these results we concluded that a deconvolution would be infeasible.

Before concluding this section, we comment briefly on the calibration procedure employed for our experiments. In this type of measurement the measured flux levels must be calibrated to determine the absolute magnitude of the density profiles. The imaging system was partially calibrated by measuring the flux levels from a natural star. This calibration procedure eliminated the unknowns associated with the telescope and atmospheric transmission but did not eliminate the unknowns in the laser. The laser characteristics must be known precisely for complete calibration of the flux levels. For our particular configuration the laser power was not known precisely, thus preventing an absolute calibration of the measured density profiles. As a result, the density profiles computed from the image data were normalized to the column abundance computed from the monostatic data.

## 6.6 Summary

We have shown theoretically that bistatic imaging lidar can achieve or exceed the vertical resolution of pulsed monostatic lidar systems without the use of wideband pulsed lasers and time gated receivers. The simplicity of the imaging lidar's transmitting and receiving equipment, in contrast to that of pulsed lidar systems, is the main advantage of the bistatic imaging technique. In terms of analysis, the operation of the imaging lidar is easily expressed in terms of linear systems. The image profiles can be interpreted as the output of a filter having the Na density as the input and an impulse response which is related to the laser beam cross section and imaging geometry. From this linear systems interpretation we found vertical resolution was proportional to the laser beam width and inversely proportional to the separation between the laser and telescope.

The vertical resolution of the imaging lidar is ultimately limited by atmospheric turbulence effects. Atmospheric turbulence limits the size of the focused laser spot in the Na layer. Once this limit is reached, resolution can be improved only by increasing the laser and telescope separation. For a site with poor seeing conditions ( $r_0 = 2$  cm) and laser-telescope separation of 1000 meters, the best possible resolution is approximately 100 m. If this same site has excellent seeing conditions ( $r_0 = 20$  cm), 10 meter resolution is possible.

Resolution can also be thought of in terms of the smallest observable vertical wavelength of mesospheric gravity waves. Shot

noise effects ultimately limits the system's ability to detect short wavelength waves. To detect wavelengths as short as 1 km the shot noise level must be down by at least 50 dB (i.e.,  $N_s > 10^5$ ). The laser power, receiver aperture, and integration time are the main system parameters we can choose to set the shot noise level. For typical atmospheric conditions (see Table 6.1) and  $PA_r = 0.1 \text{ W m}^2$ , integration times greater than 100 s are required to observe vertical wavelengths as short as 1 km.

The experiments described in Section 6.5 were conducted primarily to test the feasibility of creating laser guide stars for adaptive imaging in astronomy.<sup>4</sup> The imaging lidar concept was developed after these experiments. Unfortunately, the experimental configuration resulted in such a poor resolution ( $\Delta r = 16.6 \text{ km}$ ) that the measured data failed to demonstrate the imaging lidar's full capability. The experimental data did show, however, the feasibility of creating and imaging a laser spot on the mesospheric sodium layer for use in the bistatic imaging technique.

## 7. CONCLUSIONS

### 7.1 Conclusions

Ground-based adaptive telescopes using laser guide stars can produce images that are nearly diffraction limited. The major design issues have been addressed and the expected imaging performance predicted. The optimum design of a laser-guided telescope depends on the ability to predict the imaging performance of the telescope as a function of all of the factors which degrade imaging performance. These factors include photon noise in the wavefront sensor, finite sensor/actuator spacing, finite response time of the deformable mirror and control system, and anisoplanatism. A new performance analysis has been presented which takes into account these factors and includes realistic models of the physical characteristics of the wavefront sensor and deformable mirrors. The results of the performance analysis are used to specify design requirements for the wavefront sensor, deformable mirror, and laser. For laser guide stars created in the mesospheric Na layer, the effects of nonlinear absorption (saturation) must be well understood to specify the characteristics of the laser. A new analysis of resonance backscattering from pulse lasers is presented. This analysis is crucial for choosing the optimum combination of laser characteristics for the laser guide star application.

Combining the results of these two analyses into a specific design indicates that a two-meter laser-guided telescope, using a single laser

that can be either bought off the shelf or built with today's technology, can achieve imaging performance levels nearly matching that of the Hubble Space Telescope (HST). The laser power requirements for the Rayleigh and Na guide star approaches are on the order of 33 and 6 W, respectively, for seeing conditions of  $r_0 = 20$  cm and zenith viewing. For either approach, near diffraction limited imaging is achieved with a Strehl ratio of  $\sim 0.73$  and an angular resolution of approximately 0.07 arcsec at  $\lambda = 0.5 \mu\text{m}$  (2.09 times that of diffraction limited imaging). The FOV of the telescope is approximately 8 arcsec.

The bistatic imaging lidar has been shown to achieve or exceed the vertical resolution of pulsed monostatic lidar systems without the use of wideband pulsed lasers and time gated receivers. The simplicity of the imaging lidar's transmitting and receiving equipment, in contrast to the more complex transmitting and receiving equipment of pulsed lidar systems, is the main advantage of the bistatic imaging technique. The vertical resolution of the imaging lidar is ultimately limited by atmospheric turbulence effects. For a site with poor seeing conditions ( $r_0 = 2$  cm) and laser-telescope separation of 1000 m, the best possible resolution is approximately 100 m. If this same site has excellent seeing conditions ( $r_0 = 20$  cm), 10 m resolution is possible. Resolution can also be thought of in terms of the smallest observable vertical wavelength of mesospheric gravity waves. Shot noise effects ultimately limited the system's ability to detect short wavelength waves. To detect wavelengths as short as 1 km, the shot noise level must be down by at least 50 dB (i.e.,  $N_s > 10^5$ ). The laser power,

receiver aperture, and integration time are the main system parameters we can choose to set the shot noise level. For typical atmospheric conditions (see Table 6.1) and  $PA_r = 0.1 \text{ w m}^2$ , integration times greater than 100 s are required to observe vertical wavelengths as short as 1 km.

## REFERENCES

1. J. W. Hardy, "Active optics: a new technology for the control of light," Proc. IEEE, vol. 66, pp. 651-697, 1978.
2. J. M. Beckers, F. J. Roddier, P. R. Eisenhardt, L. E. Goad, and K-L Shu, "National Optical Astronomy Observatories (NOAO) Infrared Adaptive Optics Program I: general description," Proc. SPIE, vol. 628, p. 290, 1986.
3. R. Foy and A. Labeyrie, "Feasibility of adaptive telescope with laser probe," Astron. Astrophys., vol. 152, pp. 129-131, 1985.
4. L. A. Thompson and C. S. Gardner, "Experiments on laser guide stars at mauna kea observatory for adaptive imaging in astronomy," Nature, vol. 328, pp. 229-231, 1987.
5. C. S. Gardner, B. M. Welsh, and L. A. Thompson, "Design and performance analysis of adaptive optical telescopes using laser guide stars," submitted for publication to Proc. IEEE, June 1989.
6. B. M. Welsh and C. S. Gardner, "Performance analysis of adaptive optics systems using laser guide stars and slope sensors," accepted for publication in J. Opt. Soc. Am., July 1989.
7. B. M. Welsh and C. S. Gardner, "Nonlinear resonant absorption effects on the design of resonance fluorescence lidars and laser guide stars," accepted for publication in Appl. Opt., July 1989.
8. B. M. Welsh and C. S. Gardner, "Effects of turbulence induced anisoplanatism on the imaging performance of adaptive astronomical telescopes using laser guide stars," submitted for publication to J. Opt. Soc. Am., July 1989.
9. B. M. Welsh and C. S. Gardner, "Bistatic imaging lidar technique for upper atmospheric studies," Appl. Opt., vol. 28, pp. 82-88, 1989.
10. D. L. Fried, "Optical resolution through a randomly inhomogeneous medium for very long and very short exposures," J. Opt. Soc. Am., vol. 56, pp. 1372-1379, 1966.
11. L. A. Thompson and H. R. Ryerson, "An active mirror image stabilizing instrument system (ISIS) for use on Mauna Kea," Proc. SPIE, vol. 755, pp. 560-568, 1984.
12. A. T. Young, "Seeing: Its cause and cure," Astrophys. J., vol. 189, pp. 587-604, 1974.

13. L. A. Thompson and C. S. Gardner, "Laser guide stars for adaptive optical telescopes," in Instrumentation for Ground-Based Optical Astronomy, L. B. Robinson, Ed. New York, NY: Springer-Verlag, 1988.
14. T. J. Kane, B. M. Welsh, C. S. Gardner, and L. A. Thompson, "Wave front detector optimization for laser guided adaptive telescopes," Proc. SPIE, vol. 1114, in press, 1989.
15. T. J. Kane and C. S. Gardner, "Optimal design of an adaptive optic wavefront sensor," EOSL Report 89-002, Department of Electrical and Computer Engineering, University of Illinois, Urbana, Illinois, 1989.
16. K. A. Winick, "Cramer-Rao lower bounds on the performance of charge-coupled-device optical position estimators," J. Opt. Soc. Am. A, vol. 3, pp. 1809-1814, 1986.
17. D. L. Fried, "Limiting resolution looking down through the atmosphere," J. Opt. Soc. Am., vol. 56, pp. 1380-1384, 1966.
18. J. W. Goodman, Statistical Optics New York, NY: John Wiley and Sons, 1985.
19. F. Roddier, "The effects of atmospheric turbulence in optical astronomy," in Progress in Optics XIX, E. Wolf, Ed. Amsterdam: North-Holland, 1981, pp. 283-377.
20. H. T. Yura, "An elementary derivation of phase fluctuations of an optical wave in the atmosphere," Proc. SPIE, vol. 75, pp. 9-15, 1976.
21. C. E. Coulman, "Fundamentals and applied aspects of astronomical 'Seeing,'" in Annual Review of Astronomy and Astrophysics Vol 23, G. Burbidge, D. Layzer, and J. G. Phillips, Ed. Annual Reviews Inc., 1985, pp. 19-57.
22. D. J. Land, "Effects of atmospheric turbulence on imaging in theory and experiment," Proc. SPIE, vol. 147, pp. 80-90, 1978.
23. R. S. Lawrence, "A review of the optical effects of the clear turbulent atmosphere," Proc. SPIE, vol. 75, pp. 2-8, 1976.
24. V. N. Mahajan and B. K. C. Lum, "Imaging through atmospheric turbulence with annular pupils," Appl. Opt., vol. 20, pp. 3233-3237, 1981.
25. D. L. Fried, "Statistics of a geometric representation of wave front distortion," J. Opt. Soc. Am., vol. 55, pp. 1427-1435, 1965.



26. D. Korff, G. Dryden, and R. P. Leavitt, "Isoplanicity: The translation invariance of the atmospheric Green's function," J. Opt. Soc. Am., vol. 65, pp. 1321-1330, 1975.
27. D. L. Fried, "Varieties of isoplanatism," Proc. SPIE, vol. 75, pp. 20-29, 1976.
28. D. L. Fried, "Anisoplanatism in adaptive optics," J. Opt. Soc. Am., vol. 72, pp. 52-61, 1982.
29. G. C. Valley, "Isoplanatic degradation of tilt correction and short-term imaging systems," Appl. Opt., vol. 19, pp. 574-577, 1980.
30. F. Roddier and C. Roddier, "National Optical Astronomy Observatories (NOAO) Infrared Adaptive Optics Program II: modeling atmospheric effects in adaptive optics systems for astronomical telescopes," Proc. SPIE, vol. 628, pp. 298-304, 1986.
31. L. A. Thompson and C. S. Gardner, "Excimer laser guide star technique for adaptive imaging in astronomy," Proc. SPIE, vol. 1114, in press, 1989.
32. C. S. Gardner, D. G. Voelz, C. F. Sechrist, and A. C. Segal, "Lidar studies of the nighttime sodium layer over Urbana, Illinois: 1. seasonal and nocturnal variations," J. Geophys. Res., vol. 91, pp. 13659-13673, 1986.
33. R. H. Hudgin, "Optimal wave front estimation," J. Opt. Soc. Am., vol. 67, pp. 378-382, 1977.
34. D. P. Greenwood and D. L. Fried, "Power spectra requirements for wave-front-compensative systems," J. Opt. Soc. Am., vol. 66, pp. 193-206, 1976.
35. G. A. Tyler, "Turbulence-induced adaptive-optics performance degradation: evaluation in the time domain," J. Opt. Soc. Am. A, vol. 1, pp. 251-262, 1984.
36. C. S. Gardner, "Sodium resonance fluorescence lidar applications in atmospheric science and astronomy," Proc. IEEE, vol. 77, pp. 408-418, 1989.
37. C. S. Gardner and D. G. Voelz, "Lidar studies of the nighttime sodium layer over Urbana, Illinois: 2. Gravity waves," J. Geophys. Res., vol. 92, pp. 4673-4694, 1987.
38. K. H. Kwon, C. S. Gardner, D. C. Senft, F. L. Roesler and J. Harlander, "Daytime lidar measurements of the tidal winds in the mesospheric sodium layer at Urbana, Illinois," J. Geophys. Res., vol. 92, pp. 8781-8786, 1987.

39. T. J. Beatty, R. E. Bills, K. H. Kwon, and C. S. Gardner, "Cedar lidar observations of sporadic Na layers at Urbana, Illinois," Geophys. Res. Lett., vol. 15, pp. 1137-1140, 1988
40. C. S. Gardner, D. C. Senft and K. H. Kwon, "Lidar observations of substantial sodium depletion in the summertime Arctic mesosphere," Nature, vol. 332, pp. 142-144, 1988.
41. B. M. Welsh, C. S. Gardner, and L. A. Thompson, "Effects of nonlinear resonant absorption on sodium laser guide stars," Proc. SPIE, vol. 1114, in press, 1989.
42. S. Janes, "A long-pulse duration, good-beam-quality, supersonically 'scanned'-beam dye laser," presented at Lasers '87, Lake Tahoe, December 1987.
43. T. H. Jeys, "Sum frequency mixing of two tunable Nd:YAG lasers for sodium fluorescence LIDAR measurements," presented at the Workshop on Lasers and Optical Remote Sensing, Cape Cod, MA, September 28 - October 1, 1987.
44. P. J. Napier, A. R. Thompson and R. D. Ekers, "The Very Large Array: design and performance of a modern synthesis radio telescope," Proc. IEEE, vol. 71, pp. 1295-1320, 1983.
45. R. H. T. Bates, "Astronomical speckle imaging," Phys. Rep., vol. 90, pp. 203-297, 1982.
46. J. R. Fienup, "Phase retrieval algorithms: A comparison," Appl. Opt., vol. 21, pp. 2758-2769, 1982.
47. G. W. Swenson, Jr., C. S. Gardner and R. H. T. Bates, "Optical synthesis telescopes," Proc. SPIE, vol. 643, pp. 129-140, 1986.
48. G. W. Swenson, Jr., C. S. Gardner and R. H. T. Bates, "On prospects for an extremely large optical/infrared array telescope," Proc. SPIE, vol. 628, pp. 277-280, 1986.
49. G. W. Swenson, Jr., "Radio-Astronomy precedent for optical interferometer imaging," J. Opt. Soc. Am. A, vol. 3, pp. 1311-1319, 1986.
50. C. H. Townes, "Spatial interferometry in the mid-infrared region," J. Astrophys. Astr., vol. 5, pp. 111-130, 1984.
51. C. H. Townes, W. C. Danchi, B. Sadoulet, and E. C. Sutton, "Long baseline spatial interferometer for the IR," Proc. SPIE, vol. 628, pp. 281-284, 1986.
52. Edward P. Wallner, "Optimal wave front correction using slope measurements," J. Opt. Soc. Am., vol. 73, pp. 1771-1776, 1983.

53. Edward P. Wallner, "Comparison of wave front sensor configurations using optimal reconstruction and correction," Proc. SPIE, vol. 351, pp. 42-53, 1982.
54. D. L. Fried, "Least-square fitting a wave front distortion estimate to an array of phase-difference measurements," J. Opt. Soc. Am., vol. 67, pp. 370-375, 1977.
55. R. H. Hudgin, "Wave front reconstruction for compensated imaging," J. Opt. Soc. Am., vol. 67, pp. 375-377, 1977.
56. Robert J. Noll, "Phase estimates from slope-type wave front sensors," J. Opt. Soc. Am., vol. 68, pp. 139-140, 1978.
57. J. Herrmann, "Least-squares wave front errors of minimum norm," J. Opt. Soc. Am., vol. 70, pp. 28-35, 1980.
58. W. H. Southwell, "Wave front estimation from wave front slope measurements," J. Opt. Soc. Am., vol. 70, pp. 998-1005, 1980.
59. K. Freischlad and C. Koliopoulos, "Wave front Reconstruction from Noisy Slope or Difference Data Using the Discrete Fourier Transform," Proc. SPIE, vol. 551, pp. 74-80, 1985.
60. J. Herrmann, "Cross coupling and aliasing in modal wave front estimation," J. Opt. Soc. Am., vol. 81, pp. 989-992, 1981.
61. R. Cubalchini, "Modal wave front estimation from phase derivative measurements," J. Opt. Soc. Am., vol. 69, pp. 972-977, 1979.
62. R. Hudgin, "Wave front compensation error due to finite corrector-element size," J. Opt. Soc. Am., vol. 67, pp. 393-395, 1977.
63. J. P. Gaffard and C. Boyer, "Adaptive optics for optimization of image resolution," Appl. Opt., vol. 26, pp. 3772-3777, 1987.
64. Darryl P. Greenwood, "Mutual coherence function of a wave front corrected by zonal adaptive optics," J. Opt. Soc. Am., vol. 69, pp. 549-554, 1979.
65. J. Y. Wang, "Optical resolution through a turbulent medium with adaptive phase compensations," J. Opt. Soc. Am., vol. 67, pp. 383-390, 1977.
66. J. Y. Wang and J. K. Markey, "Modal compensation of atmospheric turbulence phase distortion," J. Opt. Soc. Am., vol. 68, pp. 78-87, 1978.
67. J. W. Goodman, Introduction to Fourier Optics. San Francisco: McGraw-Hill Book Company, chapter 6, 1968.

68. E. S. Claflin and N. Bareket, "Configuring an electrostatic membrane mirror by least-squares fitting with analytically derived influence functions," J. Opt. Soc. Am. A, vol. 3, pp. 1833-1839, 1986.
69. P. M. Morse and H. Feshbach, Methods of Theoretical Physics, Part II. New York, NY: McGraw-Hill, 1953.
70. V. I. Tatarski, The Effects of the Turbulent Atmosphere on Wave Propagation, U.S. Dept. of Commerce, National Technical Information Service, 1971.
71. R. C. Smithson, Michael L. Peri, and Robert S. Benson, "Quantitative simulation of image correction for astronomy with a segmented active mirror," Appl. Opt., vol. 27, pp. 1615-1620, 1988.
72. R. C. Smithson and Michael L. Peri, "Partial correction of astronomical images with active mirrors," J. Opt. Soc. Am. A, vol. 6, pp. 92-97, 1989.
73. G. Megie, F. Bos, J. E. Blamont, and M. L. Chanin, "Simultaneous nighttime lidar measurements of atmospheric sodium and potassium," Planet. Space Sci., vol. 26, pp. 27-35, 1977.
74. K. H. Fricke and U. von Zahn, "Mesopause temperature derived from probing the hyperfine structure of the D<sub>2</sub> resonance line of sodium by lidar," J. Atmos. Terr. Phys., vol. 47, pp. 499-512, 1985.
75. P. G. Cardinal, P. L. Wizinowich and R. M. Measures, "Anomalous laser energy absorption associated with resonance saturation," J. Quant. Spectrosc. Radiat. Transfer, vol. 25, pp. 537-545, 1981.
76. R. M. Measures and H. Herchan, "Laser absorption under saturation conditions with allowance for spectral hole burning," J. Quant. Spectrosc. Radiat. Transfer, vol. 29, pp. 9-18, 1983.
77. R. M. Measures, Laser Remote Sensing: Fundamental and Applications, New York: John Wiley and Sons, 1984.
78. Lennox L. Cowie and Antoinette Songaila, "Atmospheric isoplanatism and astronomical image reconstruction on Mauna Kea," J. Opt. Soc. Am. A, vol. 5, pp. 1015-1022, 1988.
79. R. F. Lutomirski and R. G. Buser, "Mutual coherence function of a finite optical beam and application to coherent detection," Appl. Opt., vol. 12, pp. 2153-2160, 1973.
80. R. E. Hufnagel, in Digest of Topical Meeting on Optical Propagation Through Turbulence. Washington, DC: Optical Society of America, 1974.

81. J. A. Reagan, D. M. Byrne and B. M. Herman, "Bistatic lidar: A tool for characterizing atmospheric particulates: Part 1 The remote sensing problem," IEEE Trans. Geosci. Remote Sensing, vol. GE-20, pp. 229-235, 1982.
82. J. R. Rowlett and C. S. Gardner, "Signal processing of sodium lidar photocount data," RRL Publication No. 504, Radio Research Laboratory, Dept. of Electrical Engineering, University of Illinois, 1979.

## VITA

Byron MacMaster Welsh was born in Columbus, Mississippi, 21 January 1960. He received a Bachelor of Science degree in Electrical Engineering from Virginia Military Institute, Lexington, Virginia, May 1982. Upon graduation, he was commissioned as a lieutenant in the United States Air Force. He subsequently received a Master of Science degree in Electrical Engineering from the Air Force Institute of Technology, Wright-Patterson Air Force Base, Ohio, December 1983. In June 1986 he was promoted to the rank of captain while serving as an Avionics Systems Engineer in the Aeronautical Systems Division, Air Force Systems Command, Wright-Patterson Air Force Base, Ohio.

He is a member of the Institute of Electrical and Electronics Engineers and the International Society for Optical Engineering. He is also a member of the following honor societies: Sigma PI Sigma, Phi Kappa Phi and Eta Kappa Nu.

Captain Welsh has coauthored the following papers:

1. B. M. Welsh and J. N. Link, "Accuracy criteria for radar cross section measurements of targets consisting of multiple independent scatters," IEEE Trans. Antennas Propagat., vol. 36, pp. 1587-1593, 1988.
2. B. M. Welsh and C. S. Gardner, "Bistatic imaging lidar technique for upper atmospheric studies," Appl. Opt., vol. 28, pp. 82-88, 1989.

3. B. M. Welsh and C. S. Gardner, "Nonlinear resonant absorption effects on the design of resonance fluorescence lidars and laser guide stars," accepted for publication in Appl. Opt., July 1989.
4. B. M. Welsh and C. S. Gardner, "Performance analysis of adaptive optics systems using laser guide stars and slope sensors," accepted for publication in J. Opt. Soc. Am., July 1989.
5. C. S. Gardner, B. M. Welsh and L. A. Thompson, "Sodium laser guide star technique for adaptive imaging in astronomy," Proc. SPIE, vol. 1114, in press, 1989.
6. T. J. Kane, B. M. Welsh, C. S. Gardner, and L. A. Thompson, "Wave front detector optimization for laser guided adaptive telescopes," Proc. SPIE, vol. 1114, in press, 1989.
7. B. M. Welsh, C. S. Gardner, and L. A. Thompson, "Effects of nonlinear resonant absorption on sodium laser guide stars," Proc. SPIE, vol. 1114, in press, 1989.
8. C. S. Gardner, B. M. Welsh, and L. A. Thompson, "Design and performance analysis of adaptive optical telescopes using laser guide stars," submitted for publication to Proc IEEE, June 1989.
9. B. M. Welsh and C. S. Gardner, "Effects of turbulence induced anisoplanatism on the imaging performance of adaptive astronomical telescopes using laser guide stars," submitted for publication to J. Opt. Soc. Am., July 1989.